



# UNIVERSITÀ DEGLI STUDI DI PALERMO

Dottorato di Ricerca in Scienze Molecolari e Biomolecolari  
Dipartimento di Scienze e Tecnologie Biologiche, Chimiche e Farmaceutiche  
CHIM/06 - CHIMICA ORGANICA

## SYNTHESIS AND CHARACTERISATION OF NEW AZOLE BUILDING BLOCKS FOR FUNCTIONAL IONIC SYSTEMS

IL DOTTORE  
**ALESSIO RICCOBONO**

IL COORDINATORE  
**PATRIZIA DIANA**

IL TUTOR  
**ANDREA PACE**

CO TUTOR  
**IVANA PIBIRI  
DUNCAN W. BRUCE  
JOHN M. SLATTERY**

CICLO XXX  
ANNO CONSEGUIMENTO TITOLO 2018

# Acknowledgement

This PhD was partially supported (50%) by the Department of Chemistry of the University of York. I'm thankful to my York tutors Duncan W. Bruce and John M. Slattery who took care of me and provided expertise that greatly assisted the research of this work when I was at the University of York and of course during the whole PhD.



I'm also grateful to Rachel Bean and Adrian Whitwood for assistance with the processing of the single X-ray diffraction structure, which improved this thesis and in that line improved the data consistency significantly. My gratitude also goes to Heather Fish and Stephen Cowling, who have patiently trained me in NMR and liquid-crystals characterisation techniques, respectively.

I thank my fellow lab mates in Duncan's and John's Group, for their hospitality, for the stimulating discussions, and for all the fun we have had in the eighteenth months spent in York.

I'm also grateful to the coordinator of my PhD course Patrizia Diana and the whole Palermo's staff for their constant assistance.

I have to express enthusiastically out appreciation to my Palermo tutor Andrea Pace for sharing his pearls of wisdom with me during the course of this PhD, and Ivana Pibiri for her immense help in every aspect of this pathway. Without their, Duncan and John's wise guidance, this work would not exist, although any possible error is my own and should not tarnish the reputations of these esteemed professionals.

I would like to thank my family: my parents, my brother and my sister, for supporting me throughout my life.

Last but not the least, I would like to thank also Martina, my life partner, to have supported with pride, but also patience, all my choices in these last years.

## Summary

1. Introduction.....	4
1.1 Ionic Liquids.....	4
1.2 Liquid Crystals .....	7
1.3 Ionic Liquid Crystals.....	9
1.4 Characterisation techniques for ILCs and LCs .....	12
1.4.1 Polarized Optical Microscopy and Differential Scanning Calorimetry. ....	12
1.4.2 Small-angle X-ray and Neutron Scattering (SANS and SAXS) .....	15
1.4.3 Miller indices .....	18
1.5 Synthesis of azole compounds with perfluoroalkyl domains.....	21
1.6 Synthesis of 1,2,4-oxadiazoles .....	21
1.7 ANRORC mechanism for triazoles synthesis .....	22
2. Objective .....	26
3. Results and Discussion .....	29
3.1 Synthesis and characterisation .....	29
3.1.1 First synthetic approach.....	29
3.1.2 Quaternisation of triazole ring.....	31
3.1.3 Ethylated sub-product.....	33
3.1.4 Regiochemistry of quaternisation .....	36
3.1.5 Optimisation of the synthetic process .....	40
3.2 Crystal structure analysis .....	41
3.2.1 1,2,4-triazole and triazolium cores.....	42
3.2.2 Crystallographic analysis of triazolium triflates .....	43
3.2.3 Crystallographic analysis of triazolium bis(triflimide)s .....	46
3.2.4 Crystallographic analysis of triazolium tetrafluoroborates.....	49
3.3 Liquid Crystal Properties .....	52
3.3.1 Thermal behaviour .....	54
3.3.2 DSC analysis.....	58

3.3.3 Comparison between the thermal behaviour of pure [TRYUM-7,12][OTf] and the mixture with [EtTRYUM-7,12][OTf] .....	65
3.4 Small-angle X-Ray and Neutrons Scattering.....	65
3.4.1 Analysis of crystal phases .....	67
3.4.2 Analysis of mesophases.....	69
3.4.3 Analysis of isotropic phases .....	75
3.5 Electrochemical Impedance Spectroscopy.....	80
3.5.1 Introducing EIS .....	80
3.5.2 Instrument manufacturing and set up .....	82
3.5.3 EIS results and discussion.....	84
3.6 Further developments.....	93
3.6.1 Organogels .....	93
3.6.2 Use of triazolium salts as gelators.....	94
4. Conclusion .....	96
5. Experimental section.....	99
5.1 Material and methods.....	99
5.1.1 Polarized optical microscopy.....	99
5.1.2 Differential scanning calorimetry.....	99
5.1.3 Small-angle X-ray Scattering .....	99
5.1.4 Small-angle Neutron Scattering .....	100
5.1.5 Electrochemical characterisation.....	100
5.2 Synthesis and characterisation .....	101
5.2.1 Procedure for the synthesis of compound 2.....	101
5.2.2 General procedure for the synthesis of compounds 3-3 and 3-7 .....	101
5.2.3 Procedure for the synthesis of compound 3-7.1 .....	102
5.2.4 Procedure for the synthesis of compound 3-7.2 .....	102
5.2.5 Procedure for the synthesis of compound 3-9.....	103
5.2.6 General procedure for the synthesis of compounds 4- <i>m</i> .....	103
5.2.7 General procedure for the synthesis of compounds 5- <i>m</i> .....	104



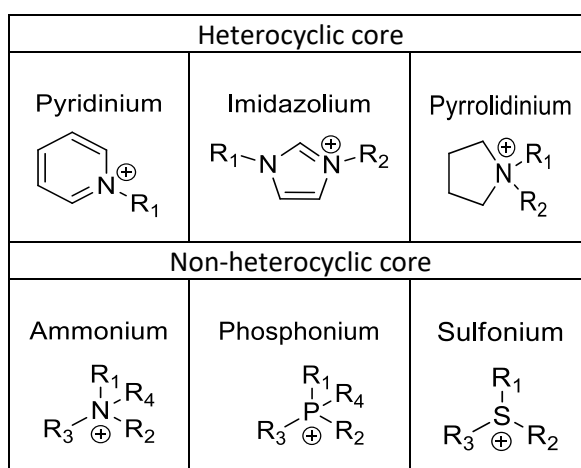
5.2.8 General procedure for the synthesis of compounds 6- <i>m</i> ,10 .....	105
5.2.9 General procedure for the synthesis of compounds 6- <i>m</i> ,12 .....	105
5.2.10 General procedure for the synthesis of compounds 6- <i>m</i> ,14 .....	106
5.2.11 Procedure for the synthesis of triazolium iodide [TRYUM-7,12][I].....	107
5.2.12 General procedure for the synthesis of triazolium trifluoromethanesulfonates [TRYUM- <i>m</i> , <i>n</i> ][OTf] .....	107
5.2.13 General procedure for the synthesis of triazolium bis((trifluoromethyl)sulfonyl)amides [TRYUM- <i>m</i> , <i>n</i> ][Tf <sub>2</sub> N] .....	109
5.2.14 General procedure for the synthesis of triazolium tetrafluoroborates [TRYUM- <i>m</i> , <i>n</i> ][BF <sub>4</sub> ] .....	111
5.3 X-ray crystallography data.....	114
Appendix A – Crystallographic structures .....	118
Crystallographic structures of Triazolium salts .....	118
Crystal Packings of Triazolium salts.....	123
Appendix B – POM Microphotographs .....	131
Appendix C – SAXS and SANS plots .....	136
Bibliography .....	166
References Summary .....	171
Figures Index .....	171
Schemes Index.....	175
Tables Index .....	176
PhD Curriculum .....	177
Academic curriculum.....	177
Conference communication.....	177

## 1. Introduction

Functional ionic systems (FISs) are charged material that have the advantage of controllable order. This might include ionic surfactants, some type of metal-organic frameworks, ionic liquids and ionic liquid crystals. The latter are a relatively new class of organic materials that recently raised scientific interest: they are defined as organic salts that lie in the boundaries of two interesting kind of materials – ionic liquids and liquid crystals.

### 1.1 Ionic Liquids

Ionic Liquids (ILs) are salts that melt below 100 °C and there has been much recent work that has investigated their use in a range of areas *e.g.* as solvents and catalyst for chemical and biocatalytic reactions<sup>1,2</sup> as well as means for optical and electrochemical sensor<sup>3</sup> as well as electrolytes for use in many electrochemical devices.<sup>4-6</sup> Typically the structures of ILs are based on a nitrogen heterocyclic core, and the classical ILs are imidazolium, pyrrolidinium and pyridinium salts,<sup>1,7</sup> although non-heterocyclic ILs, such as quaternary ammonium salts, alkyl derivatives of phosphonium and sulfonium are known (Scheme 1).<sup>7,8</sup>

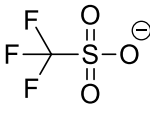
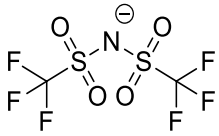
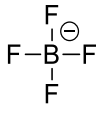
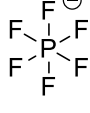
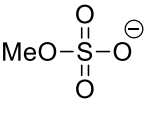
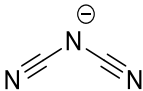
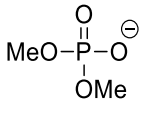


**Scheme 1.** Main cation cores of the most common ILs.

The synthesis of these salts typically involves the preparation of suitably substituted nitrogen heterocycles precursors, their quaternisation by alkylation reactions, and finally the replacement of the counterion (often halide) with suitable counterions by anion metathesis reactions. Typical anions include those containing fluorine, such as trifluoromethanesulfonate [OTf]<sup>-</sup>, bis(trifluoromethylsulfonyl)imide [Tf<sub>2</sub>N]<sup>-</sup>, tetrafluoroborate [BF<sub>4</sub>]<sup>-</sup>, hexafluorophosphate [PF<sub>6</sub>]<sup>-</sup> as well as non-fluorine-containing anions, such as methyl sulphate [MeSO<sub>4</sub>]<sup>-</sup>, dicyanamide [N(CN)<sub>2</sub>]<sup>-</sup>, dimethyl phosphate [Me<sub>2</sub>PO<sub>4</sub>]<sup>-</sup>, chloride, bromide and iodide (Scheme 2). With the exception of halide anions, the negative charge is usually distributed over several atoms.<sup>7</sup> The choice of anions is important

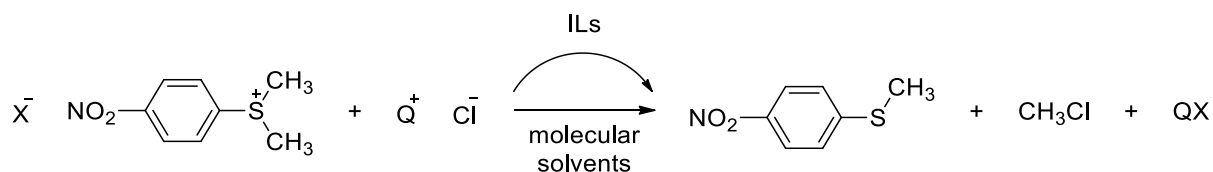
because it can strongly contribute to the tuning of the IL properties cations to get the desired physicochemical and toxicological characteristics required by the specific application.<sup>9,10</sup>

The main features supporting the classification of ILs as green solvents are their low vapour pressures and low flammability in most of the cases, for which they have been frequently considered as potential alternatives to conventional organic solvents in industrial applications.

Typical fluorinated IL anions			
Trifluoromethanesulfonate $[\text{OTf}]^-$ 	Bis(trifluoromethylsulfonyl)- imide $[\text{Tf}_2\text{N}]^-$ 	Tetrafluoroborate $[\text{BF}_4]^-$ 	Hexafluorophosphate $[\text{PF}_6]^-$ 
Typical non-fluorinated IL anions			
Methyl sulfate $[\text{MeSO}_4]^-$ 	Dicyanamide $[\text{N}(\text{CN})_2]^-$ 	Chloride, bromide, iodide $\text{Cl}^- \quad \text{Br}^- \quad \text{I}^-$	Dimethyl phosphate $[\text{Me}_2\text{PO}_4]^-$ 

**Scheme 2.** Main anion used in the most common IL systems and their abbreviations.

From a different point of view, ILs can be considered molten salts. From this perspective, electrostatic and  $\pi$ - $\pi$  interactions between the molecules of IL and/or solvent are involved in supramolecular organisation.<sup>11</sup> Variation of the cation structure significantly affects the 3D structure of the ILs<sup>11</sup> and their effect on a given reaction carried out in it. For instance, Welton *et al.* studied the  $\text{S}_{\text{N}}2$  reaction of a chloride ion with a sulfonium centre in ILs (Scheme 3) and they demonstrated that the reaction follows a different pathway to when this is carried out in molecular solvents.<sup>12</sup>

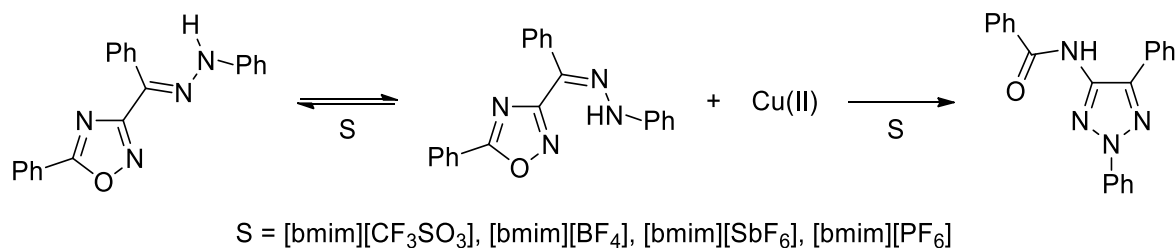


$\text{X} = \text{CF}_3\text{SO}_3, \text{N}(\text{CF}_3\text{SO}_2)_2$

**Scheme 3.**  $\text{S}_{\text{N}}2$  reaction of the trifluoromethanesulfonate and bis(trifluoromethanesulfonyl)imide salts of dimethyl-4-nitrophenylsulfonium with chloride ion.

In parallel studies, D'Anna *et al.* demonstrate also that the reaction may follow different mechanistic patterns, depending on the nature of the IL anion, as for phenylhydrazones of 3-benzoyl-5-phenyl-

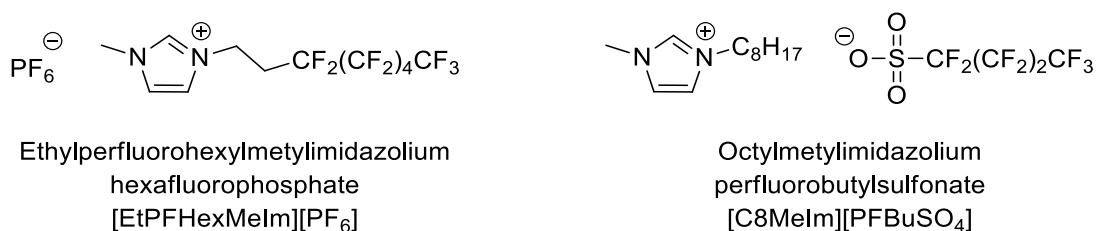
1,2,4-oxadiazole reacted in 1-butyl-3-methylimidazolium with four different counter-anion (Scheme 4).<sup>13</sup>



**Scheme 4.** *E*-/*Z*-isomerisation and rearrangement of phenylhydrazones of 3-benzoyl-5-phenyl-1,2,4-oxadiazole in the presence of CuCl<sub>2</sub> and Cu(ClO<sub>4</sub>) in four imidazolium ILs [bmim][X] (X = CF<sub>3</sub>SO<sub>3</sub>, BF<sub>4</sub>, SbF<sub>6</sub> and PF<sub>6</sub>).

Comparison with data collected in molecular solvent (*i.e.* methanol) shows that the studied reactions proceeded faster in the ILs. Specifically, in terms of yield, these reactions are affected differently by the nature of the anion of the ILs, which could exert different effects into the polymeric supramolecular fluid that ILs are.<sup>13</sup>

Fluorine-containing ILs or simply Fluorinated Ionic Liquids (FILs) have been the subject of great interest in recent years due to the wide range of properties, such as viscosity, melting point, density, conductivity, solubility, liquid range, thermal and hydrolytic stability, that can be tuned by modifying the fluorine-content of the cation or the anion.<sup>9,14,15</sup> FILs are described as a family, where fluorine chains of variable length are used in the cation or in the anion and they can be introduced replacing one or more alkyl-chains of the cation with fluoroalkyl- or perfluoroalkyl-chain as well as adding perfluoroalkyl-chain to the anion<sup>9,14,15</sup> such as the examples reported in Scheme 5.



**Scheme 5.** Examples of fluorinated ILs with fluorous domain in cation (left) and anion (right).

The first articles where a FIL was described<sup>16,17</sup> illustrates the peculiar properties that these compounds can display: notably, in addition to being a low-melting salt the reported FIL exhibits the capacity to selectively gel benzene at modest mass percentages. It's well known that ILs with longer alkyl-chain lengths (from around C6 chains) are nanostructured in the liquid phase with the formation of apolar and polar nanodomains corresponding to the apolar parts and charged polar parts of the IL.<sup>18</sup> Likewise, the fluorinated alkyl-chain present in FILs also controls the formation of fluorinated nanodomains

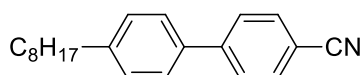
easing the accommodation of fluorinated solutes (either liquid or gases).<sup>9,19</sup> These properties make FILs excellent materials for the recovery/recycling of perfluorocarbon contaminants such as greenhouse perfluorocarbons gases and perfluoroalkyl acids of industrial effluents that are persistent, bioaccumulative.<sup>9</sup> Moreover the affinity of fluorous domain for gases such as oxygen makes also FILs good candidates as artificial blood substitutes in oxygen therapeutic preparations.<sup>9</sup>

The ILs applications in an ever-increasing number of areas require the design of new ILs with specific and tailored properties. However fundamental physical properties of ILs, such as melting point, viscosity, conductivity and other bulk properties can be predicted by relatively few methods.<sup>20,21</sup> Current methods are not perfect and need more knowledge but play an important role for future work in this area and design of new ILs.

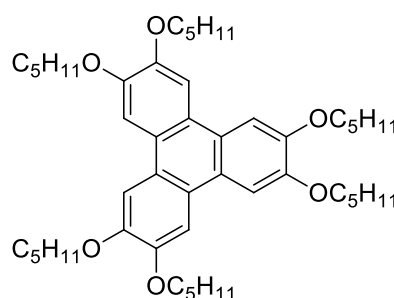
## 1.2 Liquid Crystals

Liquid crystals (LCs) are known widely as components of LC displays, yet they have other interesting properties related to their state of matter, which exists between the solid (characterised by molecular long-range order) and liquid states (characterised by fluidity). LCs represent the fourth state of matter and have properties of both solids and liquids, meaning that their physical properties are 'anisotropic' i.e., they depend upon the direction from which they are observed.<sup>22-24</sup>

Friedrich Reinitzer discovered LC properties in 1888, working on various derivatives of cholesterol which showed two melting points: they melt into a cloudy liquid and at higher temperature they melt again with a transition from the cloudy liquid to a clear one. Since Reinitzer's studies, the interest in LCs has been increasing more and more. Nowadays, LCs are well known and can be divided into thermotropic and lyotropic. Thermotropic LCs exhibit a phase transition into the LC phase as temperature is changed. This class of LC also includes metallomesogens such as alkali metal soaps, metal complexes and substituted ferrocenes, which show thermotropic behaviour.<sup>25</sup> Lyotropic LCs exhibit phase transitions as a function of both temperature and concentration of the LC molecules in a solvent (typically water).<sup>24,26</sup>



4-n-octyl-4'-cyanobiphenyl



hexapentoxytriphenylene

**Scheme 6.** Examples of historic rod-like and disk-like shaped molecules of LCs.



The finite twist angle between adjacent molecules is due to their asymmetric packing, which results in longer-range chiral order. The chirality induces a finite azimuthal twist from one layer to the next, producing a spiral twisting of the molecular axis along the layer normal (Figure 1c).<sup>27</sup>

Although this subdivision gives an idea of the main classes of LC phases, it should be noted that it is only a general classification, in fact, it is possible to distinguish several other types or subgroups of LC phases such as SmA, SmB and SmC, which are subclasses of smectic phase and many other subclasses can be described.<sup>24</sup>

In addition to calamitic molecules, discotic molecules, which have a discoid form, can produce mesophases. Just like the calamitic phases, these types of molecules can give rise to nematic phases: the nematic phases ( $N_D$ ), which are those with the smallest molecular order. In analogy to the calamitic nematic phase, there is a predominant orientational disposition in the discotic nematic, but no translational constraint exists (Figure 2a). Other discrete states characterised by both molecular orientation and translation are the columnar nematic phases ( $N_{Col}$ ) (Figure 2b) and the hexagonal columnar phase ( $Col_h$ ) (Figure 2c).<sup>22,23,28,29</sup>

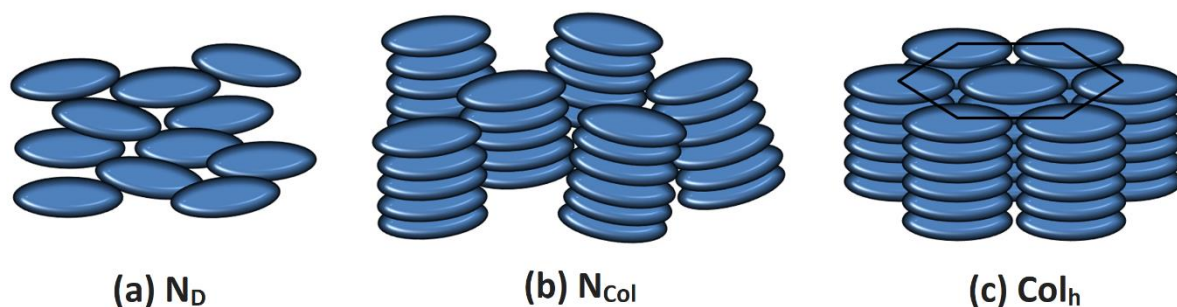


**Figure 2.** Graphical representation of molecular orientation in nematic discotic (a), nematic columnar (b) and columnar hexagonal (c) for discotic LCs.

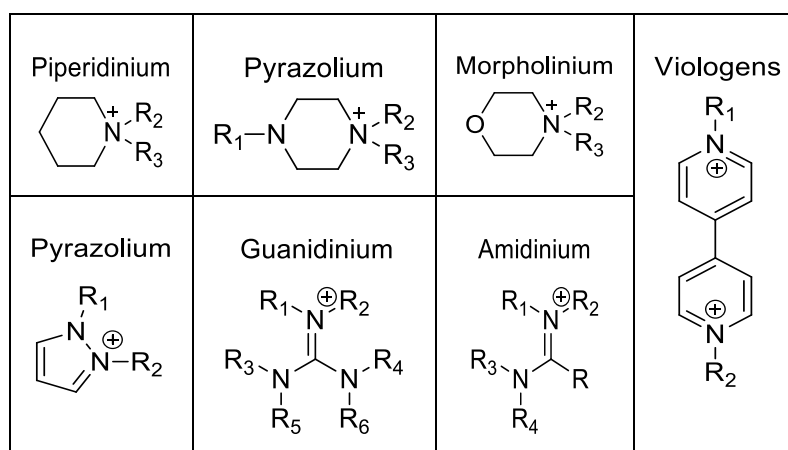
### 1.3 Ionic Liquid Crystals

In a parallel context, ionic liquid crystals (ILCs) combine many interesting features of ILs (*e.g.* low volatility and the ability to dissolve solutes with a range of polarities) as well as many attractive properties of LCs (*e.g.* their intrinsic order and anisotropy).<sup>8,9,12,13</sup>

This provides unique opportunities that can be exploited in many different fields, for example their use as electrolytes for batteries,<sup>30</sup> electrochemical sensors<sup>31,32</sup> and dye-sensitised solar cells,<sup>33</sup> as well as in water desalination as membranes,<sup>34</sup> in fuel cell, in extraction processes as solvents.<sup>22</sup> ILCs can also be used to immobilize transition metal catalysts in the liquid phase of biphasic catalytic reactions<sup>22</sup> or as alternative solvents for various organic reactions, with benefits of an enhancement of the selectivity, yield or activity of catalytic reactions.<sup>35-37</sup>

ILCs are usually composed organic salts of alkylated nitrogen-containing bases<sup>23</sup> such as imidazolium,<sup>38-42</sup> piperidinium,<sup>43</sup> piperazinium,<sup>43</sup> morpholinium,<sup>43</sup> pyrrolidinium,<sup>44</sup> pyridinium,<sup>45</sup> pyrazolium,<sup>46,47</sup> guanidinium,<sup>48</sup> bipyridinium (also known as viologens),<sup>49,50</sup> ammonium,<sup>51</sup> amidinium,<sup>52</sup> other azole/azide cations or different cations such as phosphonium<sup>22,23,53</sup> (Scheme 8). These are combined with anions that are commonly used for ILs such as halides, triflate, tetrafluoroborate, hexafluorophosphate and bis(triflimide) (Scheme 2).<sup>23,54</sup>

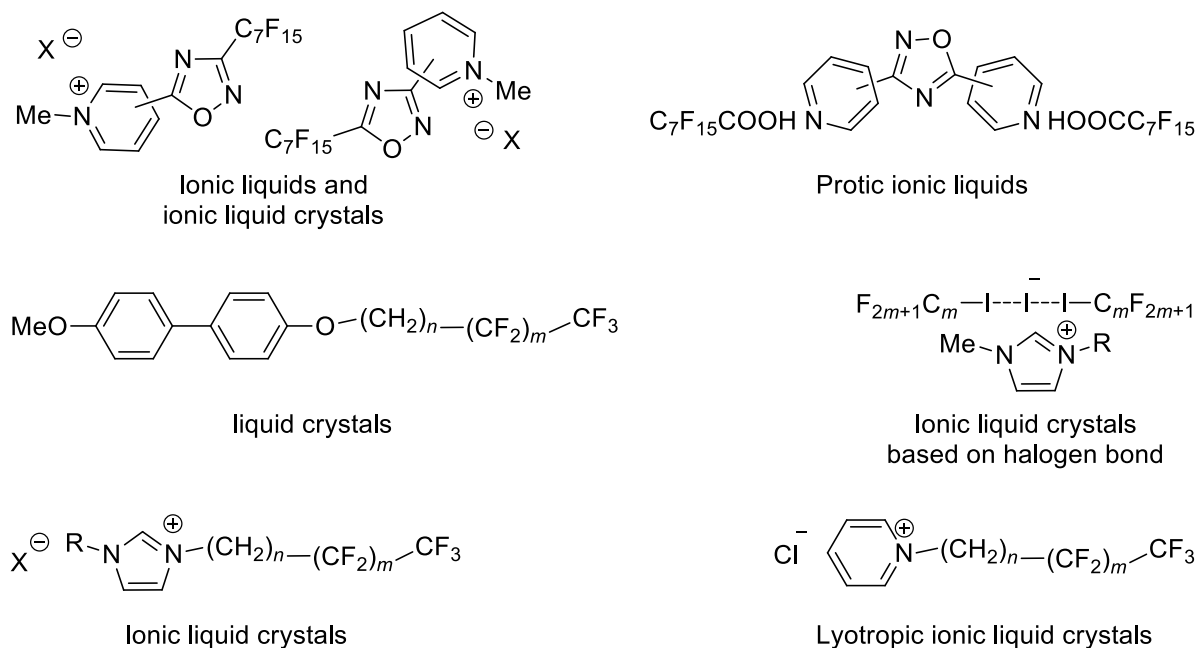
These salts usually form ILs but when one or more alkyl-chains is sufficiently long, they also exhibit mesomorphism. Since the driving force for this is micro-segregation between the hydrophobic chains and the polar ionic parts, a smectic phase (for calamitic systems) is frequently obtained.<sup>55,56</sup> Other interactions that play an important role are dipole-dipole interactions,  $\pi$ - $\pi$  stacking and Van der Waals interactions. Indeed, the introduction of specific pendant groups on the cation may induce the formation of mesophases, thus generating ILCs materials.<sup>57,58</sup> The formation of mesophases is observed more rarely for salts with bis(triflimide) anions, which are larger anions and do not normally support LC phase formation. Thus, the bis(triflimide) is not usually found in ILCs the field, with some rare exceptions.<sup>44,59-61</sup>



**Scheme 8.** Cationic azoles and azides common found in ILCs.

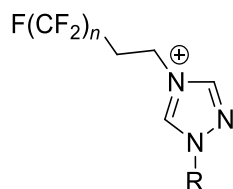
Over the past decade the properties of small fluorinated or perfluorinated systems based on heteroaromatic rings have been studied within the context of new fluorinated ILs,<sup>19,45,62</sup> protic ILs (PIL)<sup>14</sup>, ILCs,<sup>10,45,62,63</sup> lyotropic ILCs<sup>64</sup> and ILCs based on halogen bonding<sup>65</sup> have been discovered (Scheme 9). Fluorinated moieties can provide peculiar properties to the materials such as the ability of gas sorption.<sup>19</sup> In other cases LC properties have been obtained by replacing an alkyl-chain with a fluorinated chain.<sup>66</sup> Indeed, the strong segregation induced by the presence of a fluorophore domain such as the perfluoroalkyl-chain, promotes self-organisation leading to the formation of LCs or ILCs.<sup>15,66,67</sup>





**Scheme 9.** Fluorinated material showing different properties.

Triazolium salts, which form the basis of this thesis, have been reported as ILCs<sup>23,68–70</sup> and as ILs.<sup>71–73</sup> However, the perfluorinated 1,2,4-triazolium salts haven't already been reported as ILCs or ILs. *N*(4)-Polyfluoroalkyl-1,2,4-triazolium salts (Scheme 10) have been reported by Shreeve *et al.* as potential ILs and their physical properties, such as melting point, density and thermal stability have been attributed to the presence of the fluorinated domain.<sup>74</sup>



**Scheme 10.** Cationic structure of *N*(4)-polyfluoroalkyl-1,2,4-triazolium salts.

Although Shreeve's triazolium salts have been synthesized with various combinations of alkyl and perfluoroalkyl-chain length, no LCs behaviour was reported within the system. The synthesis pathway doesn't allow for the insertion of the perfluoroalkyl moiety directly into the triazolium ring and an ethylene spacer is needed in order to allow alkylation of the triazole base with a fluorinated alkylating agent.

Different synthesis strategies such as cyclisation<sup>75,76</sup> provide useful pathways to obtain perfluoroalkyl-1,2,4-triazolium salts without non-fluorinated spacers, giving access to new structures and new properties. Founded on previous work where no ILCs based on 1,2,4-triazolium salts or those with purely perfluorinated-chains have been obtained, the project will focus along these lines.

## 1.4 Characterisation techniques for ILCs and LCs

Overall, the mainly used methods of investigation in ILCs as exactly in LCs characterisation field are Polarized Optical Microscopy (POM), Differential Scanning Calorimetry (DSC) and Small-angle X-ray Scattering (SAXS).<sup>1-4,10,22,33,44,55</sup>

### 1.4.1 Polarized Optical Microscopy and Differential Scanning Calorimetry.

When a new material needs to be investigated about its mesogen behaviour, POM is usually the first technique to be performed.

Firstly, the pure sample is analysed with the microscope over a temperature range and melting point (MP) occurs from the solid phase to a fluid phase showing birefringence, which is unlike isotropic liquids since it does not appear dark in the presence of polarized light.<sup>24</sup>

As a rule, this condition highlights the presence of a mesophase, and usually keep going to heat, other transitions called clearing points (CPs) can be observed. Transition always progress to other less organised mesophases, and finally to the isotropic phase, unless any decomposition occurs at any given time.

Most of LCs and ILCs show mesophase both on heating and cooling and in this case, it is referred to enantiotropic behaviour. But if compounds show mesophase only on cooling it is referred to monotropic behaviour and generally these materials are thermodynamically more unstable, crystallizing unexpectedly from mesophase.

So secondly, following the clarification towards the isotropic liquid, or the melting in case of monotropic compounds, the sample is slowly cooled in order to re-observe the mesophase over cooling. At this stage of the analysis, molecules tend to be more effective in organizing, thus recognizing and studying some of the textures found can be a strong mean for characterisation in microscopic observation. Indeed these textures are useful in identifying mesophases and the main ones to be known are essentially two types: Schlieren texture (Figure 3a) and focal conic texture (Figure 3b)<sup>24</sup>.

Colours of textures origin from the birefringence of the material which rotate the polarized light between crossed polarizers. But in a structure with the molecular axes parallel to the substrate plane, the director orientation is perpendicular to the bounding glass plates. In this case the molecular orientation is called homeotropic and the optic axis is parallel to the direction of light propagation. So, there is no birefringence for any in-plane rotational position of the sample between crossed polarizers and in those points textures simply appears black (pseudo-isotropic).

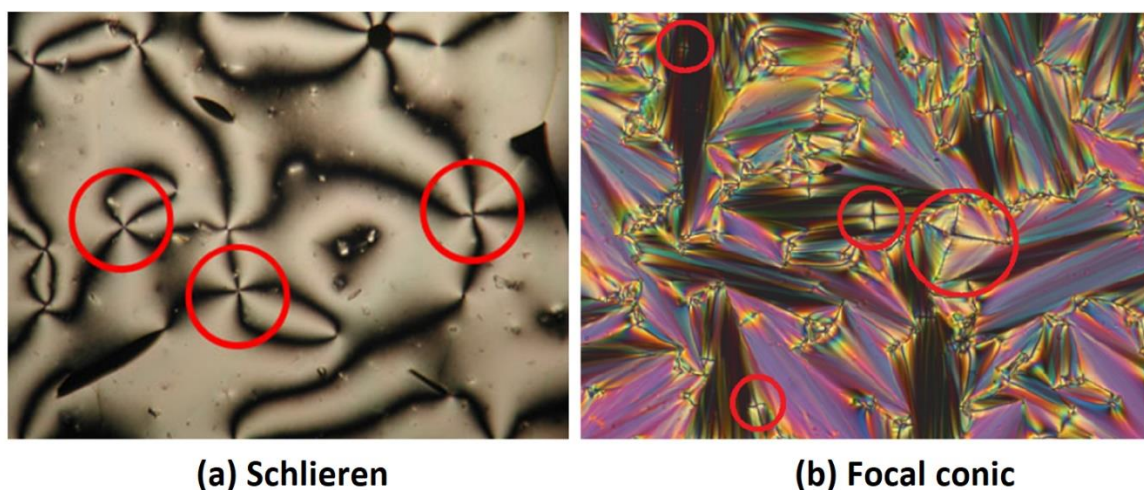


**Figure 3.** Microphotographs showing Schlieren (a) and focal conic (b) textures. Respective defects are circled in red.

Both Schlieren and focal conic textures are characterised by defects (red circled in Figure 3) namely points from which non-fractal zones are distributed to the homeotropic zones. In the Schlieren texture, a number of dark brushes (normally two or four), can be observed from defects. This condition is dictated by the way in which molecules are arranged around those points (Figure 4) and any type of defect is associated with a certain strengths ( $S$ ).

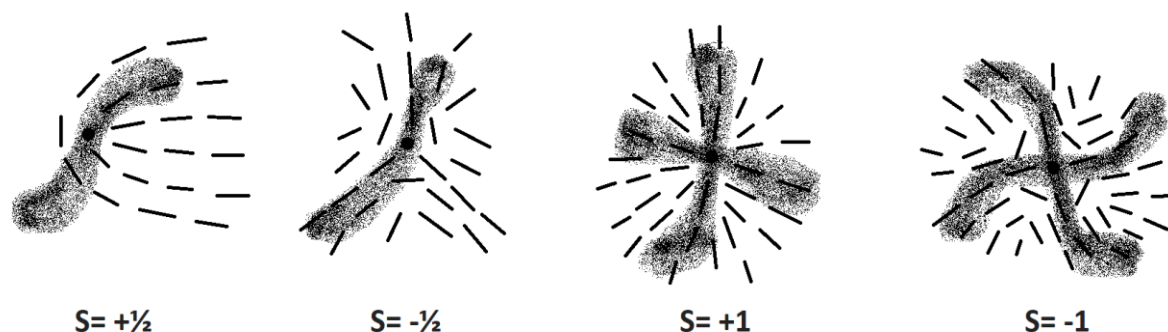


**Figure 4.** Depiction of molecule orientation around Schlieren defects with 2 and 4 brushes.

The absolute value of the strength of the disclination is obtained by dividing by 4 the number of brushes cutting a  $2\pi$  circle around the centre of a defect, i.e.  $\|S\| = \text{number of brushes}/4$ , thus  $S$  can be  $\frac{1}{2}$  or 1, while the sign of the defect strength can be obtained by rotation of the polarizers: the defect is assigned a plus (+) sign if the dark brushes rotate in the same direction as the polarizers, and a minus (-) sign if they rotate in the opposite direction.<sup>24</sup>

The defect differentiation can be a crucial factor in the identification of mesophases, in fact a Schlieren texture, is associated with mesophases of type N, N\*, N<sub>D</sub>, N<sub>COL</sub>, and in particular conditions it is associated with a subgroup of smectic, called SmC,<sup>24</sup> which show Schlieren like texture in areas with

homeotropic alignment. The analysis of the strength defects can give furthermore information, moreover the other areas around and between defects are also helpful to characterize a mesophase.

A focal conic texture also called broken fan texture is associated with mesophase with organisation in layers as precisely the smectic phases. Defects in this type of texture are characterised by dark crosses, which originate right from the organisation of the layers. Layers in smectic phases are arranged in the so-called Dupin cycloids, each containing a pair of focal cones interlinking each other. The projection of the confocal curves into the plane degenerate lines called hyperbola and ellipse (Figure 5a). The corresponding smectic layers are basically perpendicular to the substrate plane and in a top view the projections of the hyperbola with the ellipse appear as dark crosses (Figure 5b).<sup>24,26,77</sup>

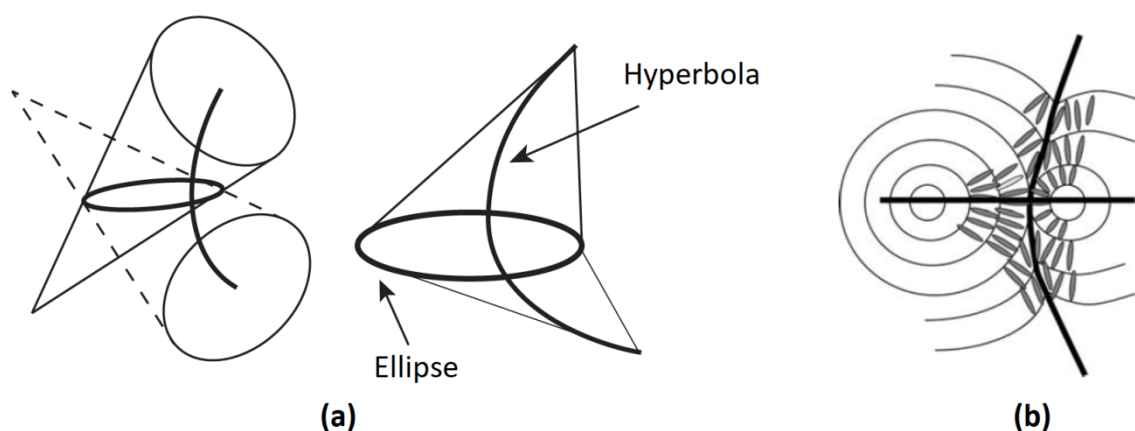


**Figure 5.** Depiction of focal conics in a Dupin cycloid (a). Schematic illustration of a focal conic defect on a top view (b).

Once the mesophases and their range of temperature have been found out by POM the sample can be analysed by DSC in order to precisely identify and confirm the temperature of transitions. Moreover DSC can measure the energy exchanged during every single event. The exchanged enthalpy of transitions can give a further clue about the nature of the mesophases and their thermodynamic stability.

When a compound is thermally investigated by DSC, it's good practice to record at least three heating and two cooling scans using a rate of 10 or 5 °C min<sup>-1</sup>, for the following reasons. When a solid is obtained from solution, it can be in a different crystalline form from the solid obtained from the melt. This can change the melting point between the first and second heating. The point of the third heating is to show that it is hopefully the same as the second. Of course, it can be the same as the first if the solid from melt and solvent are the same as well as the two cooling curves will be ideally identical. Ultimately, a too fast rate of heating/cooling can postpone or even hide one or some transition events.

### 1.4.2 Small-angle X-ray and Neutron Scattering (SANS and SAXS)

Although the DSC and POM offer a wide possibility of identifying mesophases, they alone are not enough to discriminate precisely between two possible mesophases, especially if they are similar to each other. *E.g.* the mesophase textures of SmA and SmB, show sometimes imperceptible differences, but techniques based on X-ray scattering such as SAXS can be used to achieve more clear data.

SAXS analyses the elastic scattering behaviour of X-rays when travelling through the material, recording their scattering at small angles (typically  $0.1 - 10^\circ$ , hence the 'Small-angle' in its name). It is a technique by which nanoscale density differences in a sample can be quantified. This means that it can determine nanoparticle size distributions, resolve the size and shape of (monodisperse) macromolecules, determine pore sizes, characteristic distances of partially ordered materials, and much more.

When X-rays are incident on an atom, they make the electronic cloud move as does any electromagnetic wave. The movement of these charges re-radiates waves with the same frequency, blurred slightly due to a variety of effects; this phenomenon is known as Rayleigh scattering (or elastic scattering).

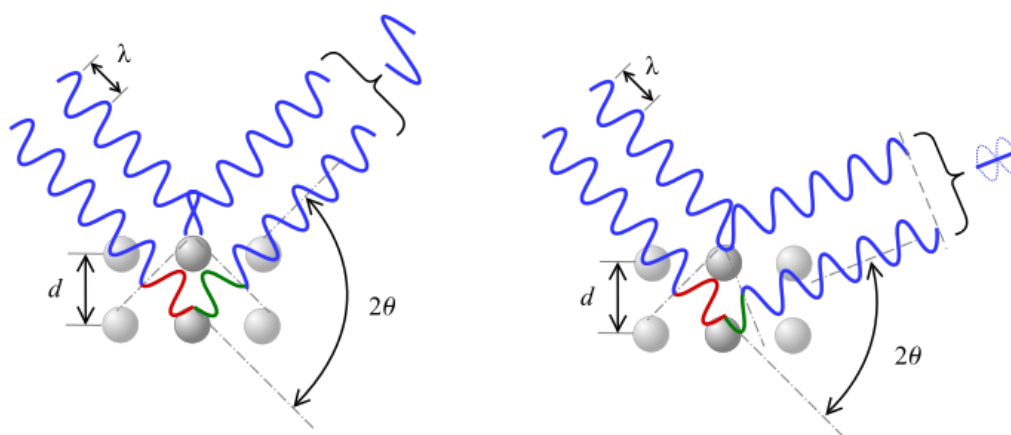


**Figure 6.** According to the  $2\theta$  deviation, the phase shift causes constructive (left figure) or destructive (right figure) interferences.

The scattered waves can themselves be scattered but this secondary scattering is assumed to be negligible. These re-emitted wave fields interfere with each other either constructively or destructively (overlapping waves either add up together to produce stronger peaks or are subtracted from each other to some degree), producing a diffraction pattern on a detector or film (Figure 6). A similar process occurs upon scattering neutron waves from the nuclei interaction with an unpaired electron, where the investigating system is called Small-angle Neutron Scattering (SANS). So, for X-rays, the scattering

arises from the electron density, whereas for neutrons, the scattering arises from the nuclear scattering length density.

The scattering power of a material is measured as Scattering Length Density (SLD) and increases with the physical density. In other words, the scattering entities are higher as tightly packed is the material and this relation is described by equation (1.1), where  $b_i$  and  $M_i$  are respectively the scattering length contributions and the atomic molar mass of the  $N$  atoms/elements of the structure involved in the scattering,  $\rho$  is the bulk density of the material and  $N_a$  is the Avogadro constant.

$$\text{SLD} = \frac{\rho \cdot N_a \sum_{i=1}^N b_i}{\sum_{i=1}^N M_i} \quad (1.1)$$

By the way, both neutron and X-ray wavelengths are comparable with inter-atomic distances ( $\sim 150$  pm) and thus are an excellent probe for this length scale.<sup>78</sup> The resulting wave interference pattern is the basis of diffraction analysis. This analysis is described by the Bragg's law (eq. 1.2), which defines the relationship between the scattering angles ( $\theta$ ) and the nanoscale density differences,  $d$ -spacing, ( $d$ ) of analysed materials at a given wavelength ( $\lambda$ ) of the incident radiation, multiplied by an integer number ( $n$ ).<sup>79</sup>

$$2d \cdot \sin \theta = n\lambda \quad (1.2)$$

SAXS experiments are conventionally reported as intensity of scattering in function of  $2\theta$  ( $^\circ$ ) and an example can be viewed in Figure 13, while SANS is reported as intensity of scattering in function of  $Q$  ( $\text{\AA}^{-1}$ ), which is a scattering vector measuring the scattering length density and defined by equation (1.3)

$$Q = \frac{4\pi \sin \frac{\theta}{2}}{\lambda} \quad (1.3)$$

For a crystalline solid or other organised material such as many LCs and ILCs, the waves are scattered from lattice planes separated by the interplanar distance  $d$ . When the scattered waves interfere constructively, they remain in phase since the difference between the path lengths of the two waves is equal to an integer multiple of the wavelength. The path difference between two waves undergoing interference is given by  $2d \cdot \sin \theta$ . The effect of the constructive or destructive interference intensifies because of the cumulative effect of reflection in successive planes of micro-organisation of material (as described by Miller notation).

About LCs and ILCs, SAXS technique is used to measure repeated distances in the supramolecular structure of a characteristic mesophase. In the simplest case of SmA phase, the diffraction spacing ( $d$ ) of the layers is approximately equal to the molecular length (Figure 7a). The same is true for SmB, but in this case the molecules laterally pack in hexagonal bundle which can be recognised if observed from a top view (Figure 7b). A smaller reflection can be recorded from the scattering of a system with

hexagonal packing. This second smaller  $d$ -space is due to repeating of lateral distances between molecules and show values usually from 4 to 6 Å. In SmC, the  $d$ -spacing is used to be usually smaller than the molecular length. This is due to the angle between the direction of levels and molecules (Figure 7c).<sup>22,23,28,29</sup>

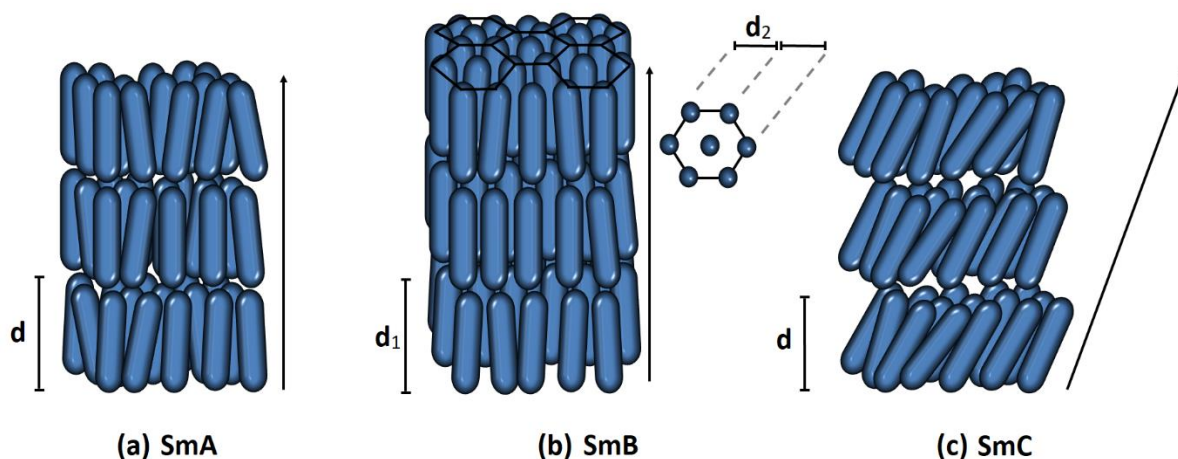


**Figure 7.** Graphic representation of molecular orientation in SmA (a), SmB (b) and SmC (c).

In any case, comparison between SAXS data and the molecular length is a powerful tool to study and understand the organisation of mesophases, especially in more complex cases involving double molecular stratification or interdigitation.

Considering a smectic system where the  $d$ -spacing equals the molecular length, every single level of the system is the same and the organisation is structured in a monolayer. This subclass of smectic phase is called SmA<sub>1</sub> (Figure 8a) and it differs from SmA<sub>2</sub> where molecules are longitudinally asymmetric and the system show a micro-molecular segregation between different domains. In SmA<sub>2</sub> the  $d$ -spacing is twice the molecular length and the organisation is structured in bi-layers (Figure 8b). A third case consists of an interdigitated bi-layer, which is called SmA<sub>D</sub> and where the  $d$ -spacing is smaller than twice the molecular length (Figure 8c).<sup>80</sup>

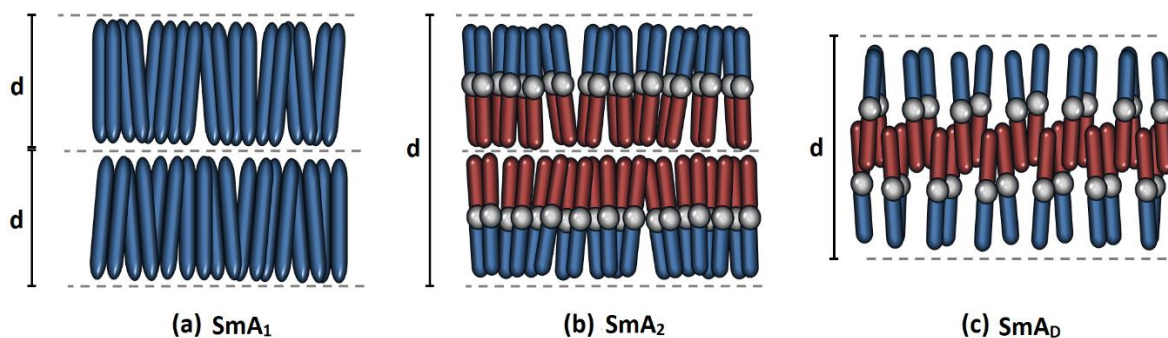


**Figure 8.** Graphical representation of molecular orientation between layers in SmA<sub>1</sub> (a), SmA<sub>2</sub> (b) and SmA<sub>D</sub> (c).



### 1.4.3 Miller indices

Miller indices consist in a notation system in crystallography and study of organised soft matter for planes in lattices. They consist in three integers  $h$ ,  $k$ , and  $\ell$  as well as they denote the family of planes orthogonal to the basis of the reciprocal lattice vectors.<sup>81</sup> The Miller indices are defined with respect to any choice of unit cell and not only with respect to primitive basis vectors, as is sometimes stated.

There are two equivalent ways to define the meaning of the Miller indices: via a point in the reciprocal lattice, or as the inverse intercepts along the lattice vectors. In either case, one needs to choose the three lattice vectors  $a_1$ ,  $a_2$ , and  $a_3$  that define the unit cell. Given these, the three primitive reciprocal lattice vectors are also determined (denoted  $b_1$ ,  $b_2$ , and  $b_3$ ).

The Miller indices are proportional to the inverses of the intercepts of the plane, in the basis of the lattice vectors. If one of the indices is zero, it means that the planes do not intersect that axis (the intercept is 'at infinity'). Considering only  $(hkl)$  planes intersecting one or more lattice points (the lattice planes), the perpendicular distance  $d$  between adjacent lattice planes is related to the (shortest) reciprocal lattice vector orthogonal to the planes.

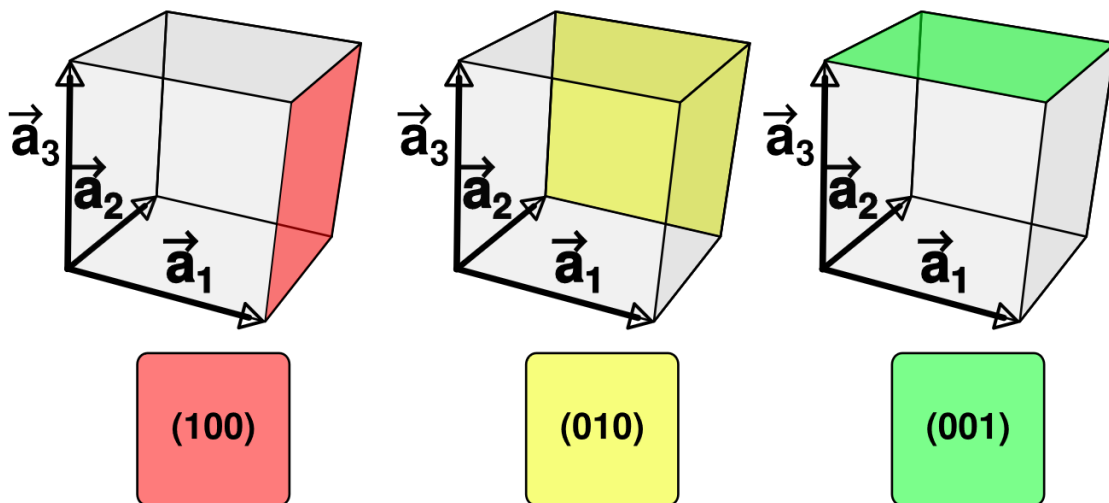


Figure 9. Planes orthogonal to the vectors with different Miller indices in cubic unit cell.

For the special case of simple cubic crystals or systems which can be simply described by a cube, the lattice vectors are orthogonal and of equal length (usually denoted  $a$ ), as are those of the reciprocal lattice. Thus, in this common case, the Miller indices simply denote normal directions in Cartesian coordinates and due to symmetry operation, the indices denote a family of directions which are equivalent, such as  $(100)$ ,  $(010)$  and  $(001)$  (Figure 9).

The plane can be also not orthogonal to the linear combination of direct lattice vectors, because the reciprocal lattice vectors need not be mutually orthogonal (Figure 10).



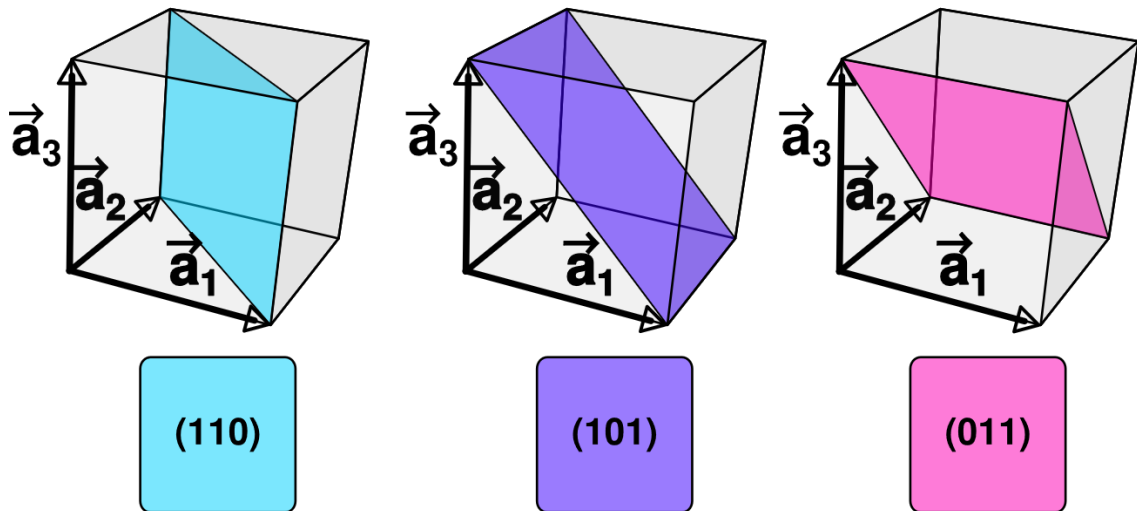


Figure 10. Planes not orthogonal to the vectors with different Miller indices in cubic unit cell.

The integers are usually written in lowest terms, i.e. their greatest common divisor should be 1. Because of the symmetry of cubic system, it is possible to change the place and sign of the integers and have equivalent directions and planes, whereby convention, negative integers are written with a bar, as in  $\bar{3}$  instead of  $-3$  (Figure 11).

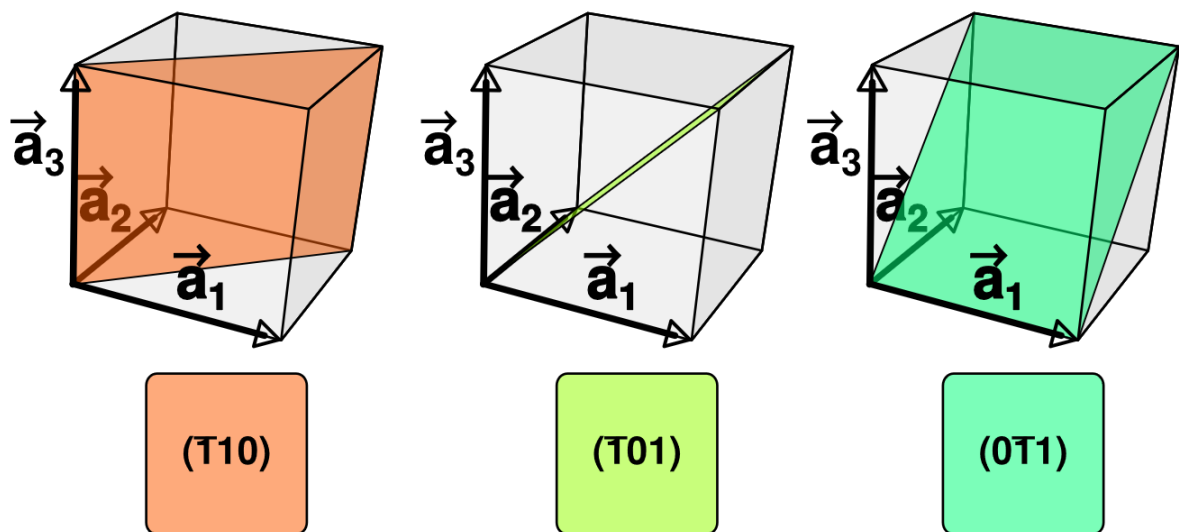
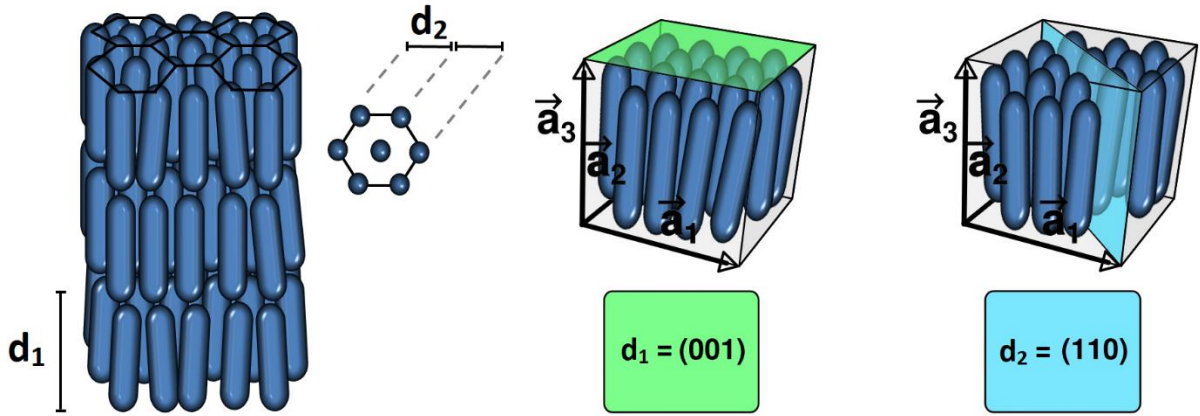


Figure 11. Planes not orthogonal to the vectors with a negative Miller index in cubic unit cell.

Considering the molecular organisation of SmB which is taken in example, layers are defined by planes which are orthogonal to the vector  $a_3$  of the unit cell chosen to describe the lattice. So, the  $d$ -spacing of layer can be indicated by a  $00l$  Miller index, as showed in Figure 12.



**Figure 12.** Description of SmB molecular organisation by Miller indices.

Figure 12 shows also a  $hk0$  plane orthogonal to the smaller  $d$ -spacing which define the distances of the characteristic lateral hexagonal packing of SmB.

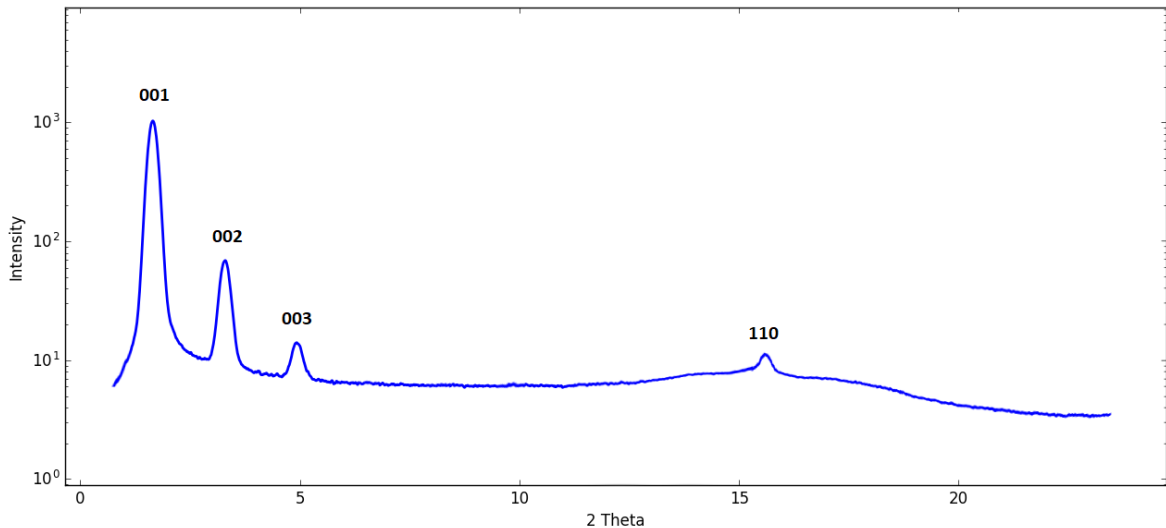


**Figure 13.** X-ray scattering of a SmB material. Miller indices denote peaks of reflections. The figure has been produced for illustrative purpose.

Figure 13 shows an example of X-ray scattering plot where a SmB material is analysed. Miller indices denote peaks:

- 001 peak consists in the lamellar  $d$ -spacing of layering;
- 002 and 003 are respectively a second and third-order reflections of the lamellar  $d$ -spacing and their value is related by equation (1.4) when expressed in Å;

$$d = d_{00\ell} \cdot \ell \quad (1.4)$$

- 110 is a minor reflection due to the hexagonal packing of SmB.

## 1.5 Synthesis of azole compounds with perfluoroalkyl domains

Despite the versatility of perfluoroalkylated azoles, most of the existing methodologies for the introduction of these fluorine-containing moieties require multistep manipulations involving expensive starting materials, and often result in low yields.<sup>82</sup>

Synthetic methods used for the synthesis of fluorinated compound generally include:

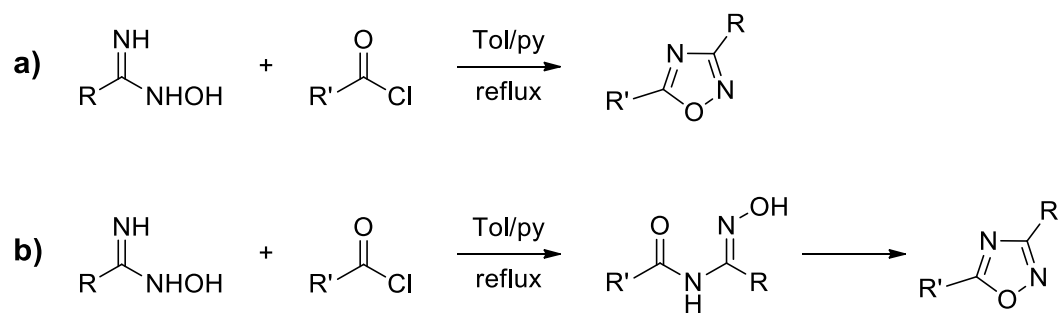
- Use of fluorinating or perfluoroalkylating reagents for the direct introduction of fluorine or perfluoroalkyl groups into the heterocyclic ring.
- Use of fluorinated precursors for the formation of new scaffold or heterocyclic ring, method known as the building block strategy.

The method of direct introduction of fluorine is not preferred for heterocyclic systems, because the fluorinated reagents are very reactive. Indeed, a high reactivity does not allow careful control of the regio- and stereo-chemical outcome of the reaction.<sup>83</sup> By contrast, the introduction of perfluoroalkyl groups is disadvantaged by the high electronegativity of fluorine, which contributes to the high kinetic barriers in nucleophilic fluorination (*e.g.* with perfluoroalkyl halides). The presence of an ethylene spacer is usually necessary to increase the alkylating ability/reactivity of these reagents.<sup>83</sup> In addition, many functional groups present in the molecule may be modified by fluorine reagents and consequently protection and subsequent deprotection of functional groups should be ensured. Other disadvantages are due to the cost, toxicity and poor availability of fluorinating reagents.

A viable alternative is represented by the building-block strategy, which allows the formation of the heterogeneous system from fluorinated precursors using cycle-addition and cycle-condensation reactions allowing also greater regio- and stereo-control. Overall, the building-block strategy is widely used for rearrangements of heterocyclic systems through chemical, thermal or photochemical processes.<sup>84,85</sup> Specifically, two viable general synthetic routes to perfluoroalkylated 1,2,4-triazoles were reported. The one-pot condensation reaction of ethyl trifluoroacetate, hydrazine, and amidines<sup>75</sup> gave 3-trifluoromethyl-1,2,4-triazoles as well as hydrazinolysis of 5-perfluoroalkyl-1,2,4-oxadiazoles<sup>76</sup> led to 3-perfluoroalkyl-1,2,4- triazoles, respectively. The latter straightforward chemistry provides the route to precursors required for the syntheses of the perfluoroalkyl triazolium salts realised in this work.

## 1.6 Synthesis of 1,2,4-oxadiazoles

The coupling between amidoxime and acyl chloride is the most commonly used method, for the synthesis of 1,2,4-oxadiazole systems. This synthesis pathway is called amidoxime route and the reaction is carried out in pyridine or toluene / pyridine at reflux, obtaining directly the oxadiazole (Scheme 11a).



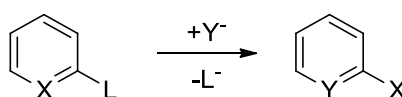
**Scheme 11.** Amidoxime route for synthesis of 1,2,4-oxadiazole.

Alternatively the open intermediate can be isolated by conducting the reaction at room temperature with successive cyclisation of the intermediate by melting to obtain the desired product (Scheme 11b).<sup>86,87</sup>

### 1.7 ANRORC mechanism for triazoles synthesis

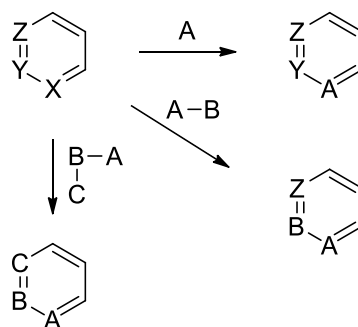
The Addition of Nucleophile, Ring Opening-Ring Closure (ANRORC) is a rearrangement where an external nucleophile attacks the heterocyclic system and determines its opening. Such attachment allows the release of an outgoing group, resulting in the closure of the ring and the formation of a new heterocycle.<sup>88</sup> Therefore, the reaction involves replacing one or more atoms of the heterocycle with one or more atoms of the nucleophile. ANRORC reactions are distinguished in two different groups:

1. Outside leaving group reactions, where the outgoing group is a ring substitute group, while the nucleophile becomes an integral part of the new heterocycle (Scheme 12). This rearrangement involves the nucleophilic attack, which causes opening of the cycle and a subsequent closure with loss of the nucleophilic group.



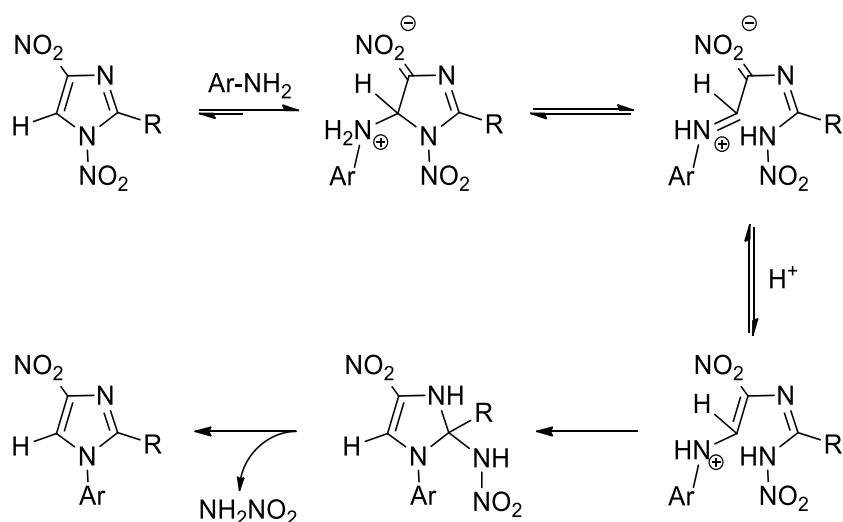
**Scheme 12.** ANRORC reaction with outside leaving group.

2. Inside leaving group reactions, in which the outgoing group is part of the heterocyclic ring. These reactions allow the formation of new heterogeneous structures by replacing one or more atoms of the starting heterocycle with one or more nucleophilic atoms (Scheme 13).



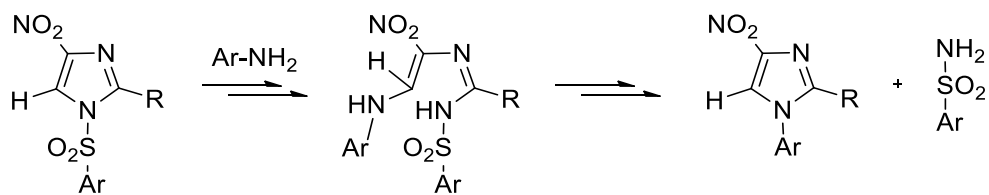
**Scheme 13.** ANRORC reactions with inside leaving group.

Van der Plas studied the so-called ANRORC mechanisms in the early 1970s, in order to explain bromopyrimidine nucleophilic substitution reactions.<sup>88</sup> Many heterogeneous systems give this type of mechanism, especially azine systems. Nonetheless, few examples of ANRORC mechanisms of pentatomic systems are known, they just work for heterocycle having strongly electron withdrawing group (EWG) as substitute. These include nitro-imidazoles (Scheme 14) and arylsulphonylnitroimidazoles (Scheme 15).



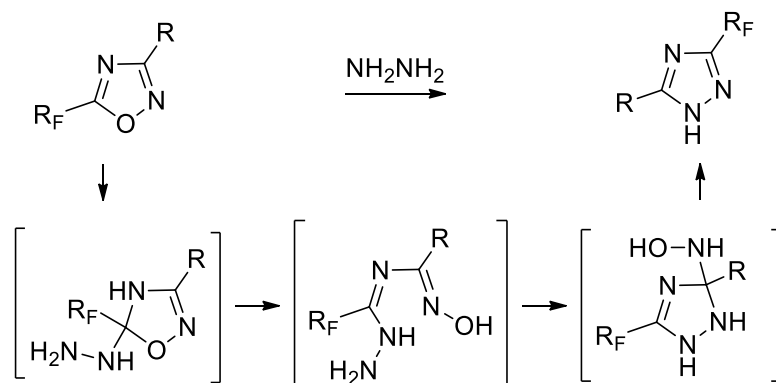
**Scheme 14.** ANRORC reaction of nitro-imidazoles.

Scheme 14 shows the 1,4-dinitroimidazole derivative, which undergoes nucleophilic attack on ring carbon 4, forming the open intermediate. The final product is obtained by an intramolecular nucleophilic addition reaction and the subsequent rapid elimination of the nitroamide. Therefore, a ring degenerate rearrangement occurs in the 1-aryl-4-nitroimidazole, with simultaneous liberation of nitramide, which decompose in nitrogen oxide and water. In another hand, the aryl-sulfonylnitroimidazoles undergo nucleophilic attack in the same manner. The reaction with aniline leading to the formation of the imidazole derivative and the elimination of aryl-sulphonamide is described in Scheme 15.



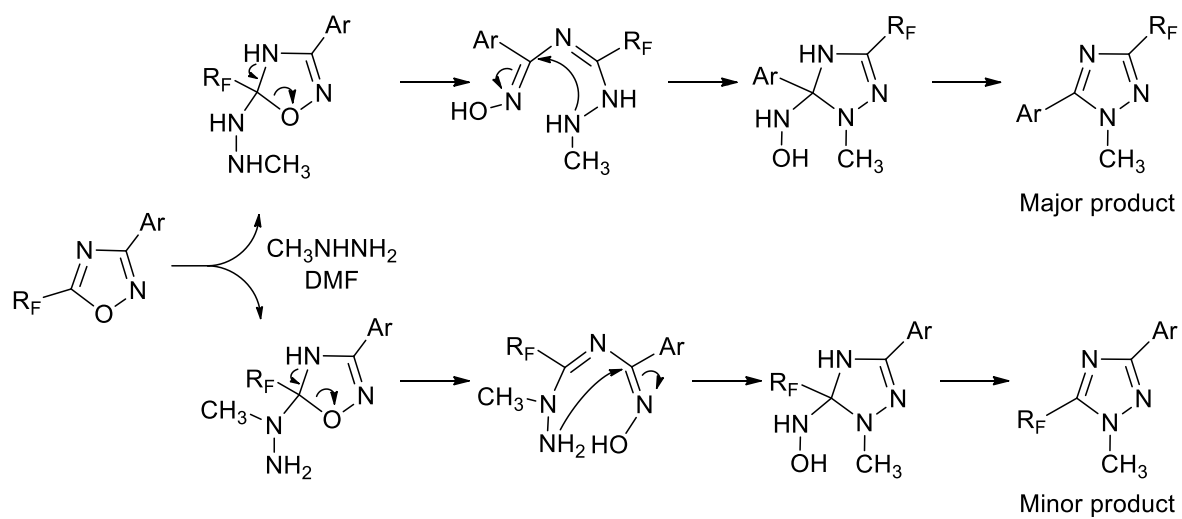
**Scheme 15.** ANRORC reaction of arylsulphonyl-nitroimidazoles.

ANRORC reaction can be operated on 1,2,4-oxadiazoles, in order to obtain triazolic derivatives. These reactions are generally conducted using 5-perfluoroalkyl-1,2,4-oxadiazoles as starting materials in the presence of hydrazines, which are bidentate nucleophiles. Reactions can be carried out in DMF at room or higher temperature, in order to obtain the respective 3-perfluoroalkyl-1,2,4-triazole.<sup>76</sup> This way, triazoles are obtained with good yield, by a very simple method from the respective oxadiazoles. Scheme 16 describes the mechanism of this ANRORC reaction and shows an initial nucleophilic addition of hydrazine to the carbon 5, which implies the opening of the ring. The next step consists in the closure of the heterocycle involving the ring carbon 3 and the second nitrogen of the bidentate nucleophile. Re-aromatization occurs due to loss of the leaving group such as hydroxylamine. The driving force of the ring interconversion has a thermodynamic nature and the most stable product is formed.



**Scheme 16.** ANRORC reaction of 5-perfluoroalkyl-1,2,4-oxadiazoles with hydrazine.

When this type of ANRORC is operated with asymmetric hydrazines such as methylhydrazine, the reaction generates two regio-isomers. The formation of two different products is due to the double possibility in the initial attachment of methylhydrazine nitrogen. The preferential initial attack by the  $\text{-NH}_2$  group to the carbon 5 causes a greater yield of 1-methyl-3-perfluoroalkyltriazole, thus 1-methyl-5-perfluoroalkyltriazole is the minor product. (Scheme 17).<sup>62,76,89,90</sup>



**Scheme 17.** ANRORC reaction of 5-perfluoralkyl-1,2,4-oxadiazoles with methylhydrazine.

## 2. Objective

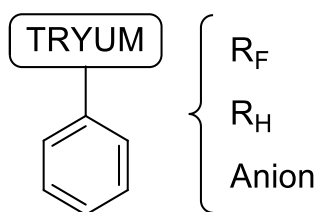
In both the ILs and ILCs fields, structural characterisation provides an important achievement to find and produce tailor-made materials or reaction media. One of the main goals in the design of a new material or bioactive molecule consists in a rationally introduction of controlled moieties to define relationships between molecular structures and macroscopic properties.

This study concerns on new mesogenic IL and ILC materials based on an 1,2,4-triazolium core. Molecular pendants and relative variables of the system were studied to present a guide on how ILCs based on these motifs can be designed with controllable properties.

In the past, a consistent job has been made to explore the chemistry leading the ILs properties, but nowadays there isn't a full understanding of the structure-activity relationship (SAR) for ILCs, especially when systems have multiple variable factors.

As reported in chapter 1, the most recent literature frames the most important elements, which mostly effect crystalline, electrically magnetic and other anisotropic properties. These include the anion in ILCs structure over than the core structure (generally heterocyclic) and pendants. Another new element consists of fluoro- or perfluoro-groups, which can be included in aliphatic chains, aromatic rings or anions.

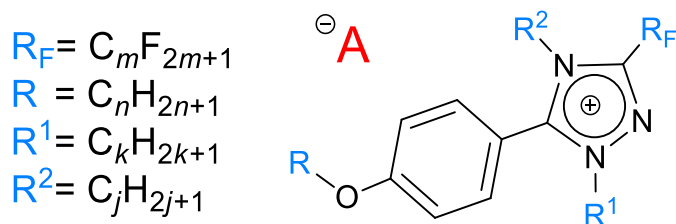
Lastly, since ILCs based on 1,2,4-triazolium (TRYUM) core has been an empty space of the literature, the new building block was designed inserting pendants and anionic counterpart in a phenyl-1,2,4-triazolium core (Scheme 18). A phenyl group is a UV-visible element, which improves and eases the synthesis process.



**Scheme 18.** Proposal building-block.

My research work involved the design and preparation of an entirely new class of ILCs and this new material system allowed a wide variability of the structure, which enables a careful control mesophase range and amphiphilicity of the ILCs phases. The molecules are based on little planar mesogen structures with two aromatic ring as molecular core: a p-alkyloxybenzene linked to 1,4-dimethyl-1,2,4-triazol-4-ium ring, where the rod-like shape has been obtained inserting in the system an alkyl-chain on one side and a perfluoroalkyl-chain on the other side (Scheme 19).



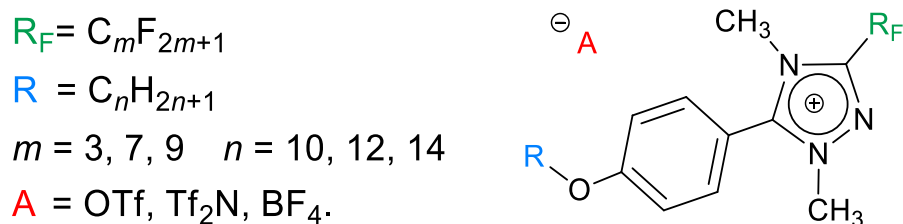


**Scheme 19.** Proposal general structure.

Therefore, a high number of variable elements generate a wider molecular library, too many combinations could be hardly managed, especially considering even the number of parameters or properties to characterize. So, the variable elements have been necessarily reduced to three, each containing three attributes, which are sufficient to define a SAR rule for the element. R, R<sub>F</sub> and A have been kept as variable elements, while R<sup>1</sup> and R<sup>2</sup> have been replaced with methyl groups, this way a molecular library containing 27 compounds comes out (Scheme 20).

Within such compromises, a perfluoro alkyl-chain has been inserted in the system, considering this one is necessary in order to give the right polarity and improve the molecular segregation within the mesomorphic behaviour. Moreover, perfluoroalkyl-chains are EWGs and their insertion is compatible with the synthetic strategy used as well as, taking advantages from this, the perfluoro chain has been linked directly to rod like core, without any CH<sub>2</sub> spacers. A careful analysis led to think that a C<sub>7</sub>F<sub>15</sub> group can provide the desiderate effect and in order to verify if the mesogen behaviour is kept also with a shorter perfluoroalkyl chain, the set of salts was replicated with a C<sub>3</sub>F<sub>7</sub> group rather the C<sub>7</sub>F<sub>15</sub> group. Besides these groups are contained in many commercial synthones such as perfluorooctanoyl and perfluorobutanoyl chloride, which are used in the synthesis. Successively the perfluoroalkyl group was elongated to C<sub>9</sub>F<sub>19</sub> in order to modify the properties of the material, expanding its LC behaviour and study the micro-segregation of the fluoruous domain with different perfluoroalkyl-chain length.

The chosen alkyl-chains are long chains with even number of carbon from 10 to 14, whilst trifluoromethanesulfonate and tetrafluoroborates have been chosen as anions as they are commonly used in literature in ILCs field, and also bis(trifluoromethane)sulfonimide where in rare case ILCs could come out also from this salts.<sup>44,59-61</sup>



**Scheme 20.** General structure.

The chosen anions generally show a low melting point trend. Indeed, their use in IL science usually leads to more potential and desirable behaviour compared to other anions such as halides. Moreover, their fluorine containing offers the opportunity of interaction with the perfluoroalkyl chain of the cations, which is on the basis of this study. For instance, they were selected with the perspective purpose to give access to suitable ILs and ILCs.

## 3. Results and Discussion

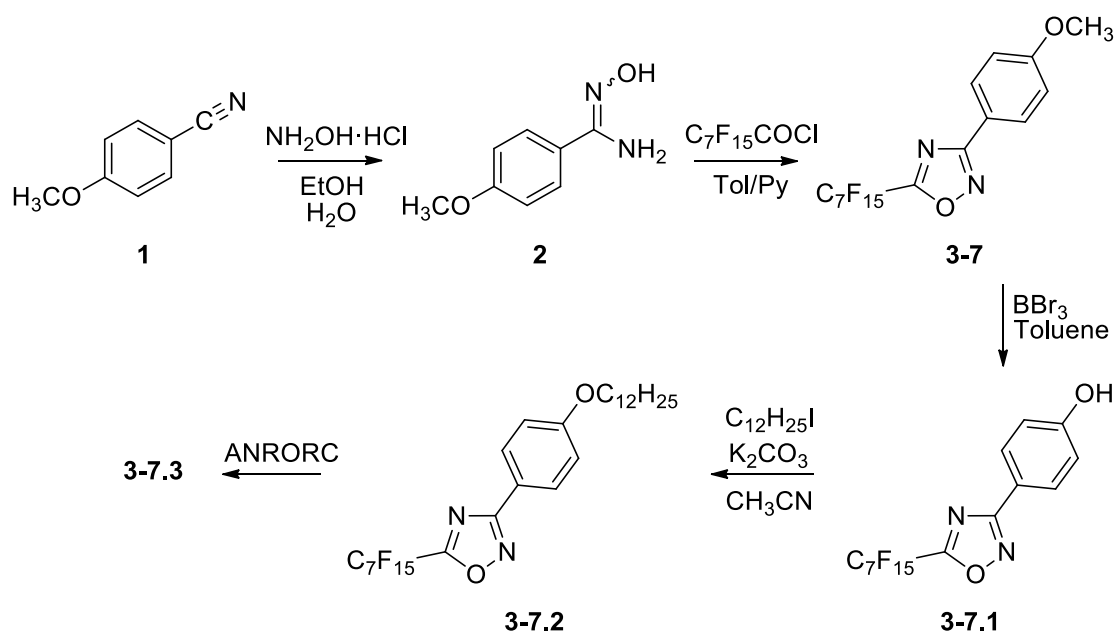
### 3.1 Synthesis and characterisation

The synthesis pathway has been designed in a way to obtain the triazolium salts by direct methylation of the corresponding neutral triazoles (3-perfluoroalkyltriazoles) and then replacing the anion by exchange metathesis, in common literature reports about similar and simpler 1,2,4-triazolium systems.<sup>82</sup>

The literature also describes the preferred methylation site of 1,2,4-triazolium systems, which leads 1,4-dimethyl-1,2,4-triazol-4-ium salts, because the N-(4) is more nucleophilic and less sterically hindered than N-(2).<sup>82</sup> The 3-perfluoroalkyltriazoles has been prepared by ANRORC-like rearrangements<sup>62,76,89,90</sup> starting from the 5-perfluoroaxadiazoles obtained in turn *via* the conventional amidoxime route.<sup>86,87</sup>

#### 3.1.1 First synthetic approach

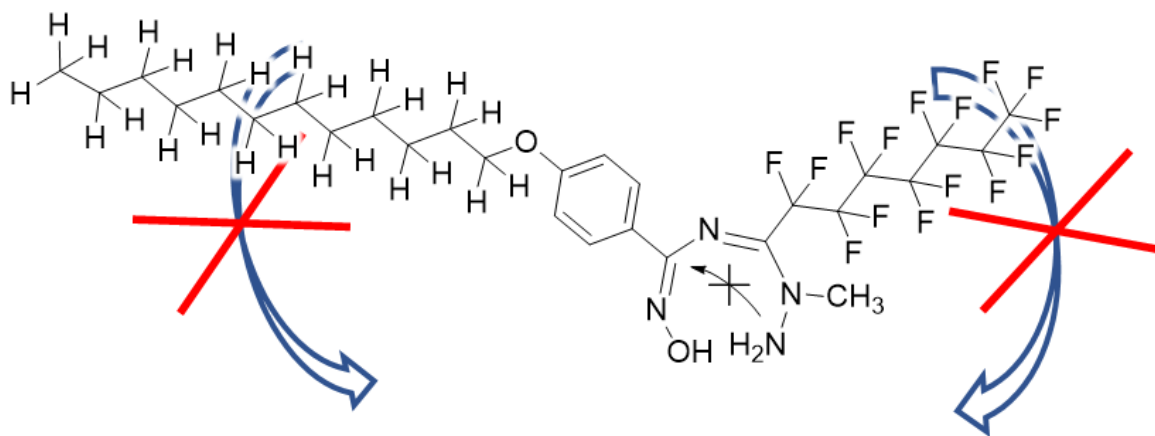
The originally proposed scheme provided for testing the ANRORC reaction on the alkylated oxadiazole 3-7.2 of Scheme 21.



**Scheme 21.** First synthetic pathway.

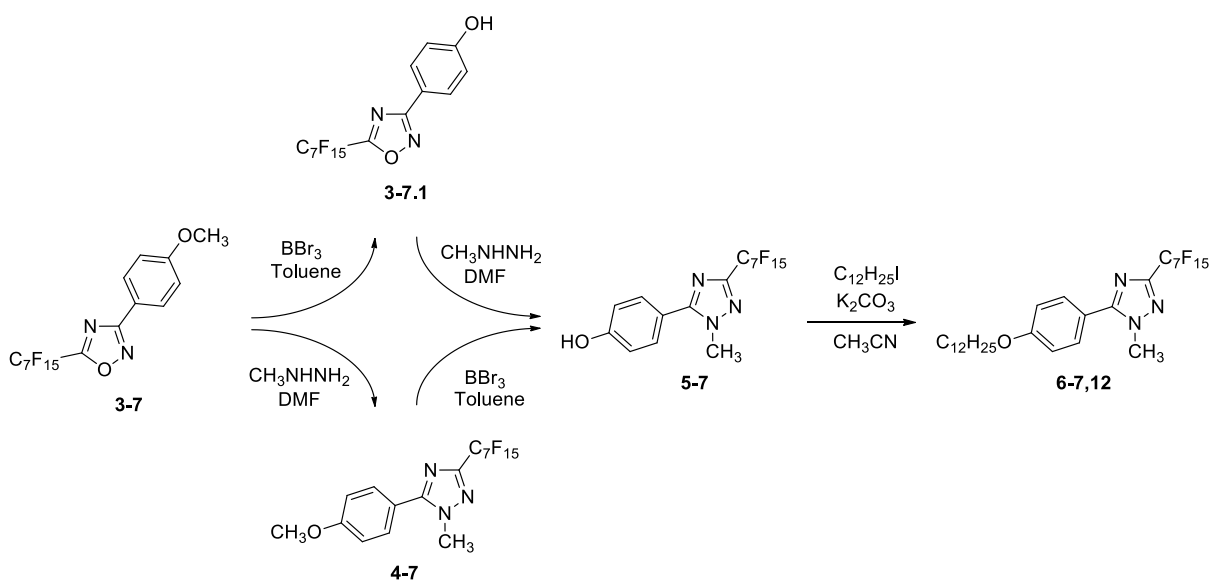
The synthetic process was carried out starting from 4-methoxybenzotrile (**1**), which was reacted with hydroxylamine under reflux on aqueous ethanol solution, obtaining the corresponding amidoxime (**2**). The latter was subsequently reacted with perfluorooctanoyl chloride in toluene, using pyridine as a base to activate the oxadiazole cyclisation. The Williamson alkylation was conducted after the cleavage of the methoxy group (by boron tribromide in toluene under reflux) and proceeded in good yield in

acetonitrile using potassium carbonate as the base and alkyl iodides or bromides as alkylating reagents (Scheme 21). Subsequently, the ANRORC transformation was tested, dissolving **3-7.2** in DMF and adding 5 and 10 mol. eq. of methyl hydrazine. Despite trying the reaction under several conditions, including at high temperature, compound **3-7.3** couldn't be isolated. Probably oxadiazole **3-7.2** isn't a good substrate for ANRORC reactions, which could be due to the long alkyl-chains, which kinetically hinder the ring closure of the reaction as showed in Scheme 22.



**Scheme 22.** Representation of kinetically hindered intermediate of reaction on **3-7.2**.

For this reason, the ANRORC reaction was moved to an earlier place in the synthesis scheme, leading the transformation into triazole from the simpler oxadiazole systems. So, the ANRORC chemistry can be performed either on compound **3-7** or **3-7.1** as well as both synthesis strategy has been tested and work fine (Scheme 23). But the pathway going through compound **4-7** shows higher yield, which was further enhanced (up to 85%) by carrying out the reaction at 110°C.



**Scheme 23.** Different pathways to obtain triazole **5-7** from oxadiazole **3-7**.

The success of the ANRORC transformation can be assessed by  $^1\text{H-NMR}$  spectroscopy, focusing on the appearance of a singlet at around 4.1 ppm corresponding to the  $\text{N-CH}_3$  group, which shows the spectrum of **5-7** (Figure 15). The Williamson etherification can be carried out successfully on triazole **5-7** in order to add the alkyl-chains to the phenolic ring.

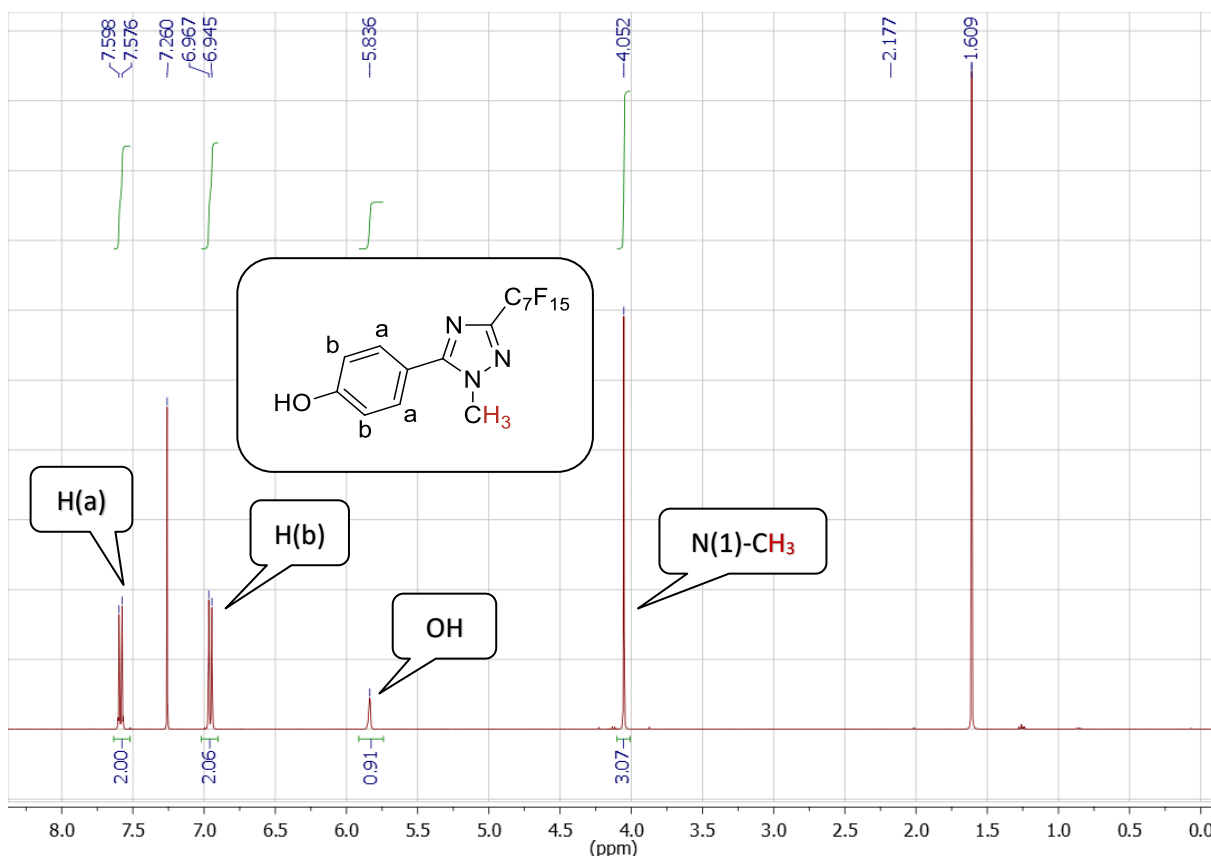
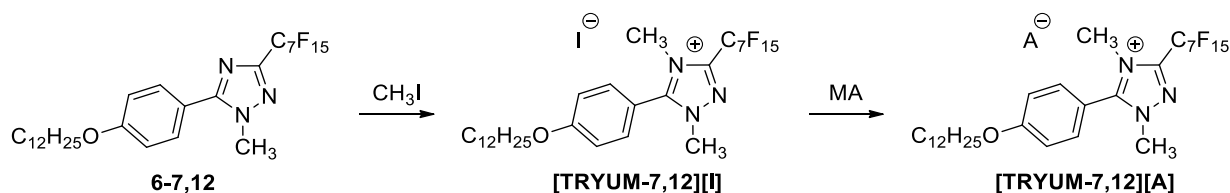


**Figure 14.**  $^1\text{H-NMR}$  spectrum in  $\text{CDCl}_3$  of compound **5-7** isolated from ANRORC reaction with **4-7** as starting material.

### 3.1.2 Quaternisation of triazole ring

Following this new synthetic route, product **6-7,12** was obtained in good yield and high purity. The next step should have initially provided for a triazole salts in the form of iodides by methylation of the core of triazoles **6-7,12** with methyl iodide. The anion would have been replaced by metathesis reaction as shown in Scheme 24.



**Scheme 24.** Methylation of triazole **6-7,12** by methyl iodide and next metathesis reactions.

The methylation with methyl iodide was attempted in several solvents (acetonitrile, ethyl acetate,

toluene, ethanol, methanol, DCM and reaction neat), heating under reflux, using a pressure vessel and or microwaves as well as other sets of conditions. These include high temperatures and pressure, long reaction time over 96 h and large excess of methyl iodide (< 45 molar equivalents).

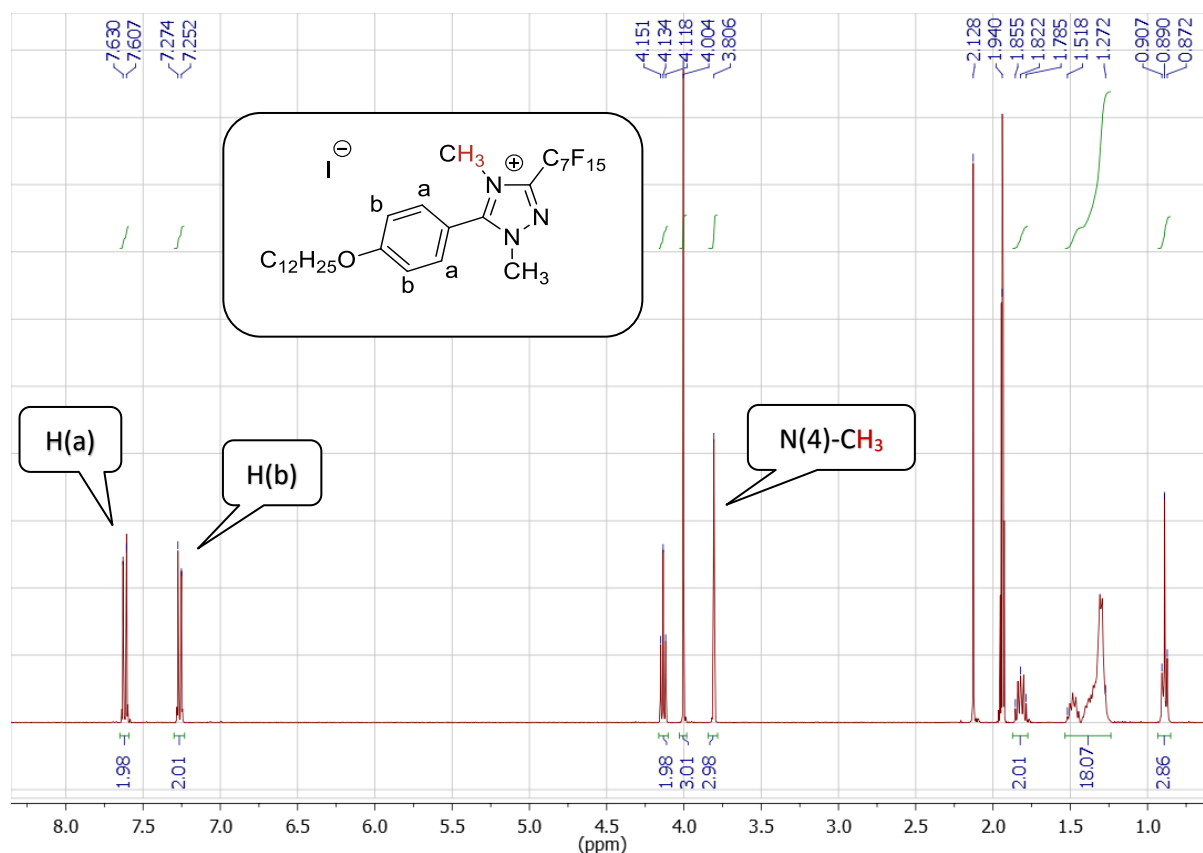
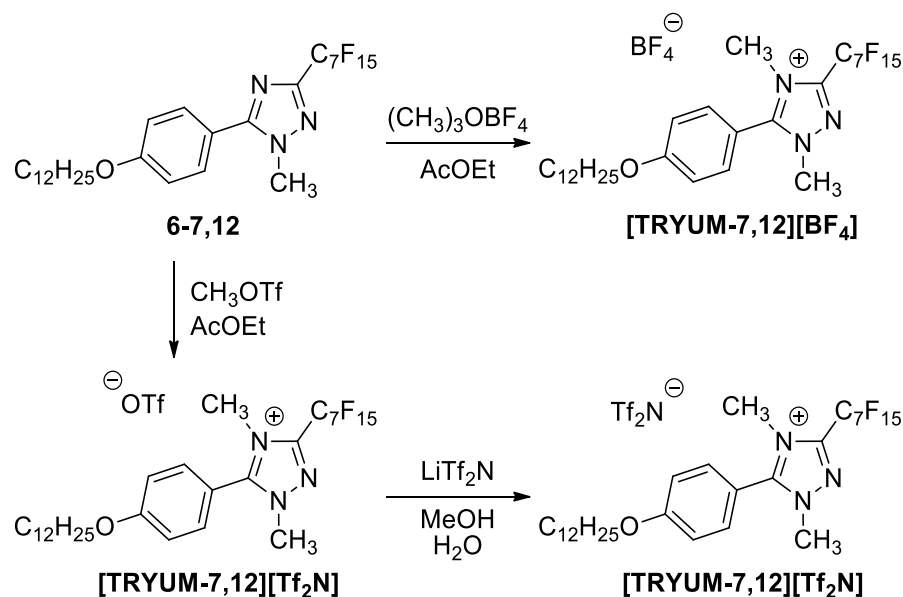


**Figure 15.** <sup>1</sup>H-NMR spectrum in CD<sub>3</sub>CN of [TRYUM-7,12][I] isolated from reaction in ethyl acetate.

The methylation can be followed by <sup>1</sup>H-NMR spectroscopy with the appearance of a singlet at around 3.8 ppm corresponding to the product. Figure 15 shows a spectrum of [TRYUM-7,12][I] isolated from a reaction carried out in ethyl acetate for 72 h. Among the conditions tried, this one represents the best for the methylation of the triazole with methyl iodide. Nevertheless, this route could not be followed since the was obtained with a yield of around 7%, as this specific triazole system evidently shows poor nucleophilic behaviour, probably due to the negative inductive effect from the perfluoroalkyl-chain.

In order to overcome this problem, the methylation of the triazole system was carried out with stronger methylating agents such as methyl triflate and trimethyloxonium tetrafluoroborate, leading directly to triflate and tetrafluoroborate salts. Bis(triflimide) salts can then be obtained by dissolving the respective triflate and lithium bis(trifluoromethane)sulfonimide (LiTf<sub>2</sub>N) in methanol and then slowly adding water in order to precipitate the less soluble [Tf<sub>2</sub>N]<sup>-</sup> salt as shown in Scheme 25.

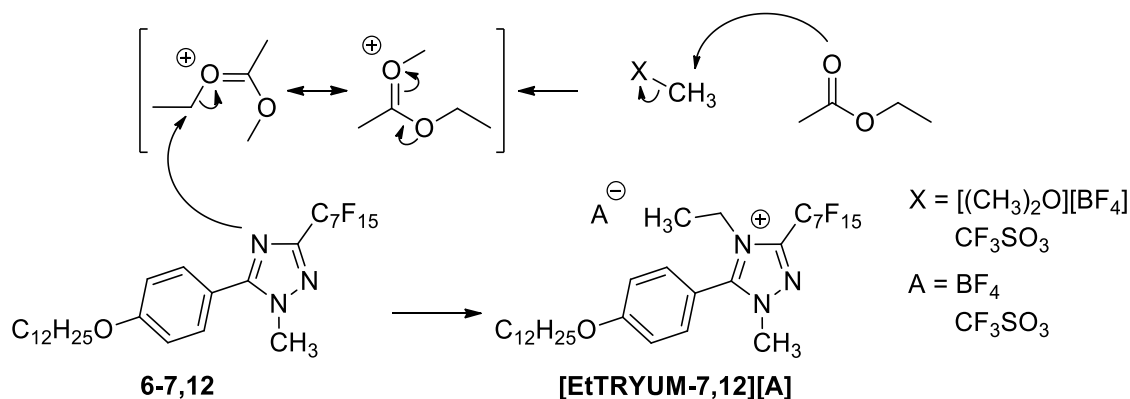


**Scheme 25.** Methylation of triazole **6-7,12** by two different methylating agent and next metathesis reaction.

### 3.1.3 Ethylated sub-product

Since the best solvent found for methylation with methyl iodide was ethyl acetate, the next methylations with the stronger methylating agents were also carried out using this solvent. However, <sup>1</sup>H-NMR spectra of **[TRYUM-7,12][OTf]**, **[TRYUM-7,12][BF<sub>4</sub>]** and **[TRYUM-7,12][Tf<sub>2</sub>N]** unexpectedly showed a small quartet at around 4.24 ppm. This was firstly confused as signal due to a residual and so, the compounds were dried under vacuum using a diffusion pump and they were then re-analysed by <sup>1</sup>H-NMR spectroscopy.

The spectra still showed the same quartet as well as revealing a splitting of some peaks such as the aromatic resonances and the singlet at 4.0 ppm, in addition to giving a surprising integration of the singlet at 3.8 ppm (*e.g.* reported in Figure 16). In fact, the signal turned out to be from an impurity in which the triazole ring is ethylated rather than methylated. This arises from reaction of the methylating agent with ethyl acetate (Scheme 26. under which conditions an ethylating agent forms).



**Scheme 26.** Proposal mechanism of ethylation by ethyl acetate interacting with methylating agent.

Thus, the methylation of **6-7,12** conducted in ethyl acetate generated a mixture of 1,4-dimethyl-1,2,4-triazol-4-ium and 4-ethyl-1-methyl-1,2,4-triazol-4-iums triflates, whose percentage was extrapolated from the integrations of the  $^1\text{H-NMR}$  spectrum in Figure 16 and the  $^{19}\text{F-NMR}$  spectrum in Figure 17.

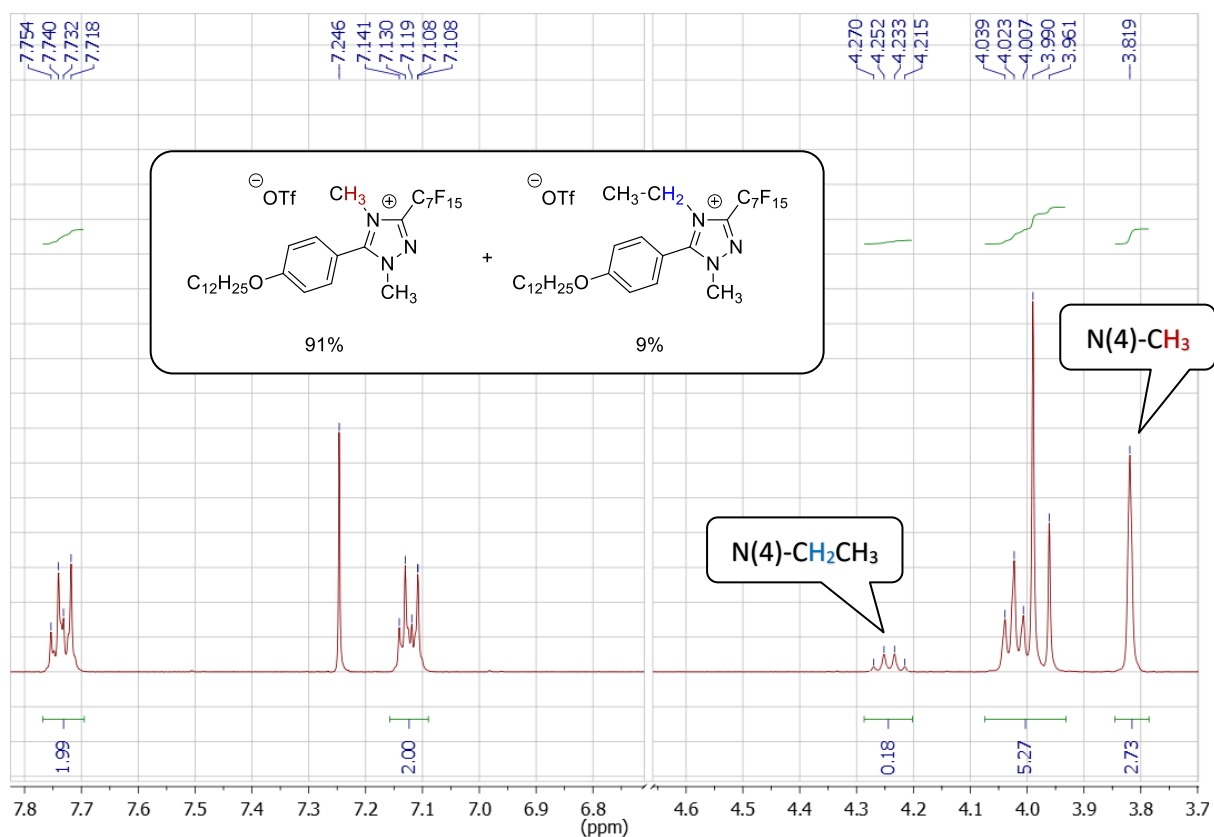


**Figure 16.**  $^1\text{H-NMR}$  spectrum cuts in  $\text{CDCl}_3$  of **[TRYUM-7,12][OTf]** isolated from reaction in ethyl acetate.

Peak at 3.82 ppm, belonging to N(1)- $\text{CH}_3$  of the **[TRYUM-7,12][OTf]**, should have integrated for three hydrogens, if it has been the unique product (the integration is compared with aromatic hydrogens of the spectrum). Instead it integrates only for 2.73 and the percentage of methylated product in the mixture is calculated from these data in equation (3.1).

$$\frac{2.73}{3.00} \cdot 100 = 91\% \quad (3.1)$$

Likewise, the signal at 4.24 ppm, belonging to N(4)- $\text{CH}_2\text{-Me}$  of **[EtTRYUM-7,12][OTf]**, should have integrated for two hydrogens, if it has been the unique product (the integration is compared with aromatic hydrogens of the spectrum). Instead it integrates only for 0.18 and the percentage of methylated product in the mixture is calculated from these data in equation (3.2).

$$\frac{0.18}{2.00} \cdot 100 = 9\% \quad (3.2)$$

A further confirmation can be provided by the  $^{19}\text{F-NMR}$  spectrum reported in Figure 17.



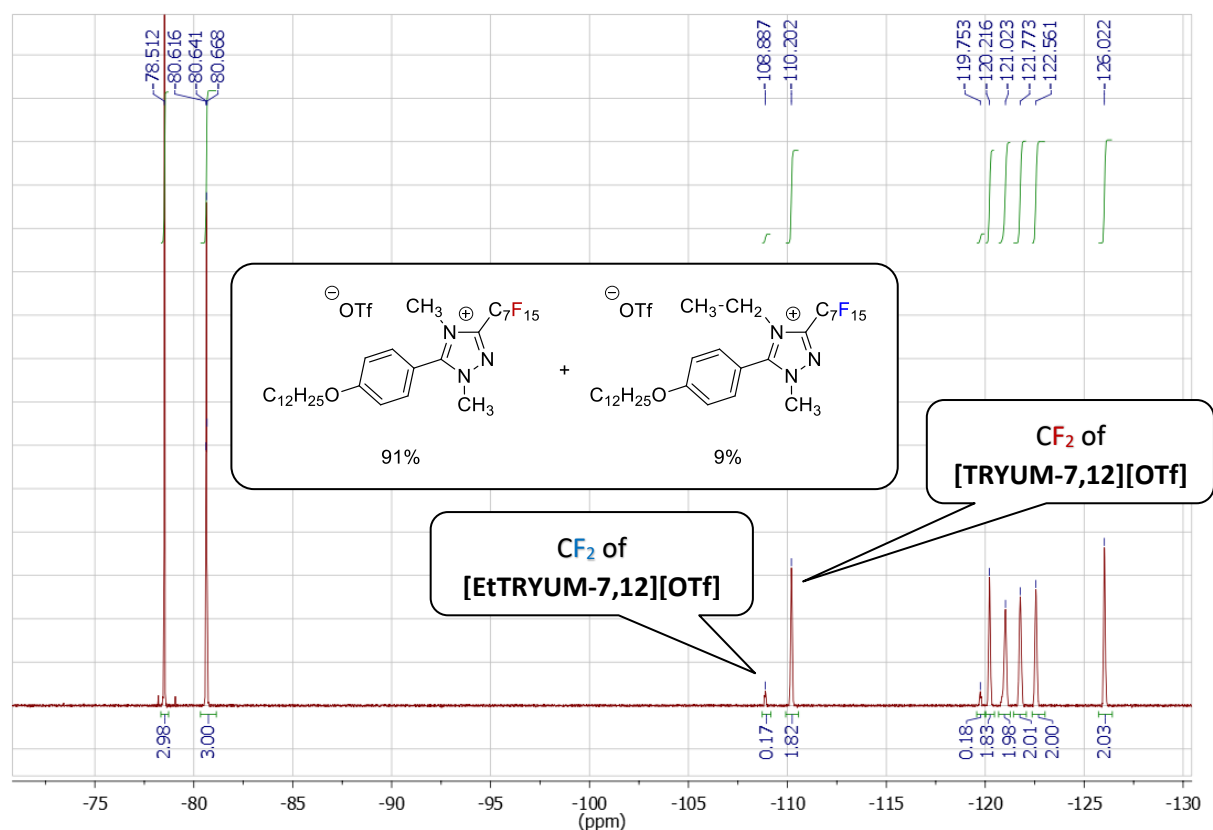


**Figure 17.**  $^{19}\text{F}$ -NMR spectrum cuts in  $\text{CDCl}_3$  of **[TRYUM-7,12][OTf]** isolated from reaction in ethyl acetate.

The signal at -110.20 ppm, belonging to a  $\text{CF}_2$  group of **[TRYUM-7,12][OTf]**, should have integrated for two fluorine atoms, if it has been the unique product. Instead it integrates only for 1.82 and the percentage of methylated product in the mixture is calculated from these data in equation (3.3).

$$\frac{1.82}{2.00} \cdot 100 = 91\% \quad (3.3)$$

Similarly, the signal at -108.89 ppm, belonging to a  $\text{CF}_2$  group of **[EtTRYUM-7,12][OTf]**, should have integrated for two fluorines, if it has been the unique product. Instead it integrates only for 0.17 and the percentage of methylated product in the mixture is calculated from these data in equation (3.4).

$$\frac{0.17}{2.00} \cdot 100 = 8.5\% \quad (3.4)$$

Overall, the methylation of compound **6-7,12** conducted in ethyl acetate generated mixture of 1,4-dimethyl-1,2,4-triazol-4-ium and 4-ethyl-1-methyl-1,2,4-triazol-4-ium triflates, in 10:1 ratio.

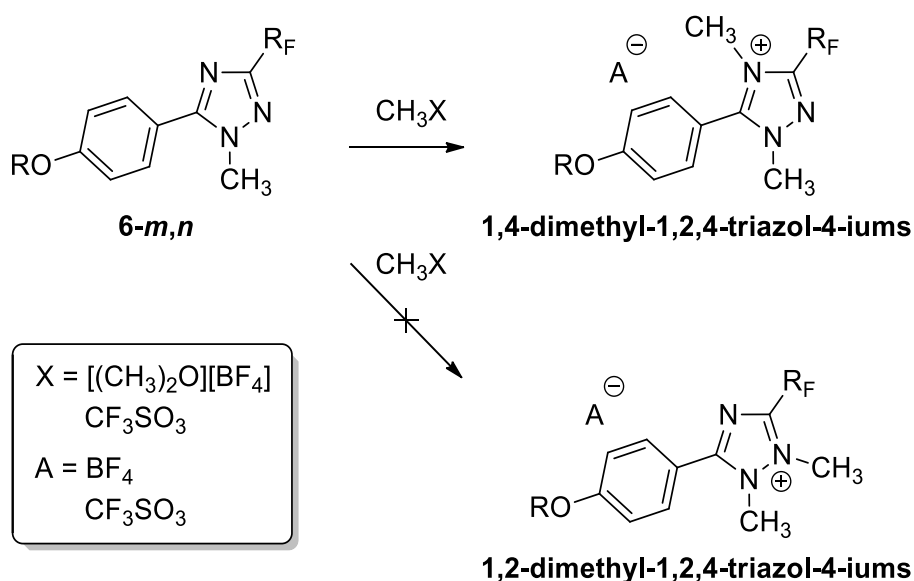
In the literature, methylation by methyl triflate or trimethyloxonium tetrafluoroborate uses solvents, such as toluene and DCM,<sup>91-93</sup> so the reactions reported in Scheme 25, were repeated in these solvents and **[TRYUM-7,12][OTf]** was isolated with no traces of **[EtTRYUM-7,12][OTf]** in both cases.

Future methylations were, therefore carried out exclusively in toluene or DCM, avoiding the formation of other ethylated sub-products.

### 3.1.4 Regiochemistry of quaternisation

The literature already suggests N(4) as the methylation site for 1,2,4-triazole system and the regiochemistry of this reaction has been confirmed by NMR techniques and single X-ray diffraction (see chapter 3.2 for the latter).

The triazolium salts are obtained from their corresponding triazole by alkylation with methylating agent, with formation of 1,4-dimethyl-1,2,4-triazol-4-iums, as illustrated in Scheme 27. This is justified by the chemical nature of N(4), which is more nucleophilic and less sterically hindered than N(2).



**Scheme 27.** Illustration of regiochemistry in the methylation of triazole ring.

To ascertain the methylation site Heteronuclear Multiple Bond Correlation (HMBC) analysis was carried out on **[TRYUM-7,12][BF<sub>4</sub>]** in CD<sub>3</sub>CN; the HMBC experiment gives coupling correlations between carbons and protons that are separated by two or three bonds.<sup>94</sup>

Figure 18 and Figure 19 show respectively the <sup>1</sup>H-<sup>13</sup>C HMBC spectrum and an expanded spectrum between 4.40 and 3.50 ppm for <sup>1</sup>H.

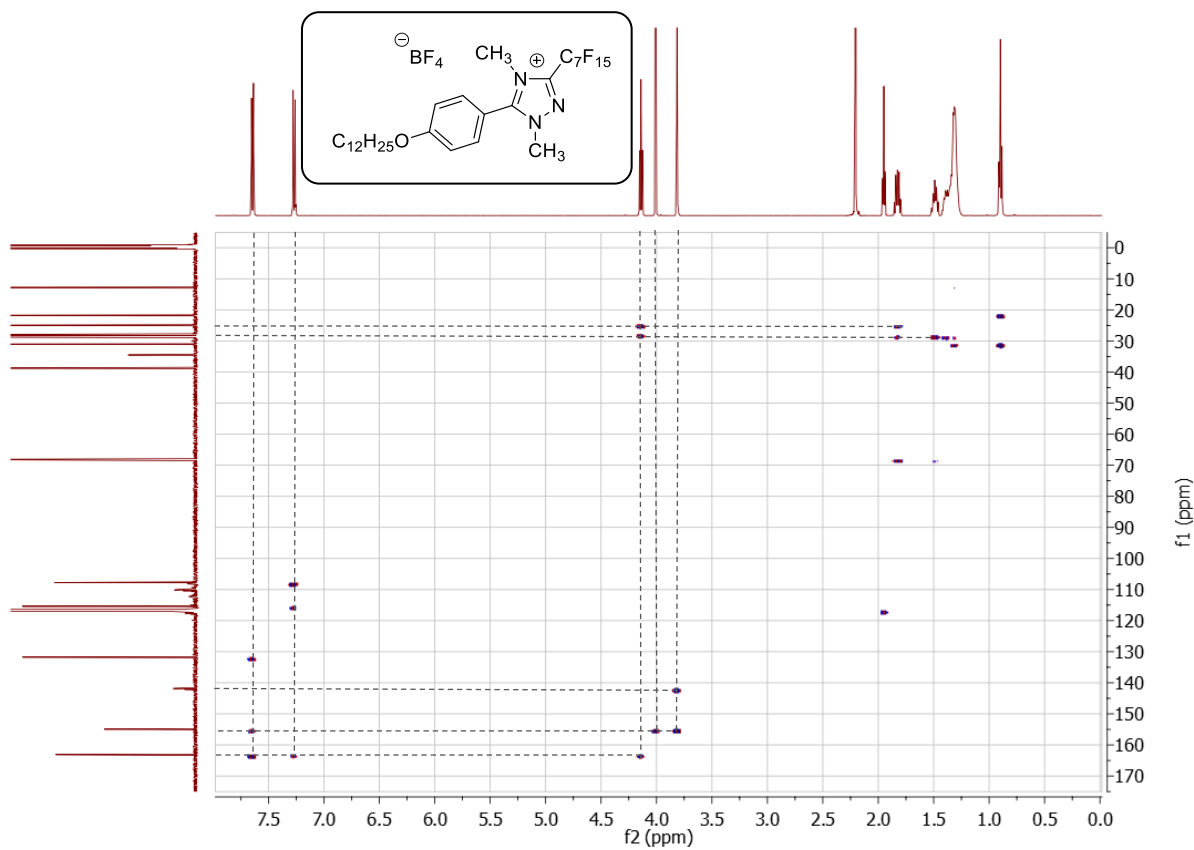


Figure 18.  $^1\text{H}$ - $^{13}\text{C}$  HMBC-NMR spectrum in CD<sub>3</sub>CN of [TRYUM-7,12][BF<sub>4</sub>].

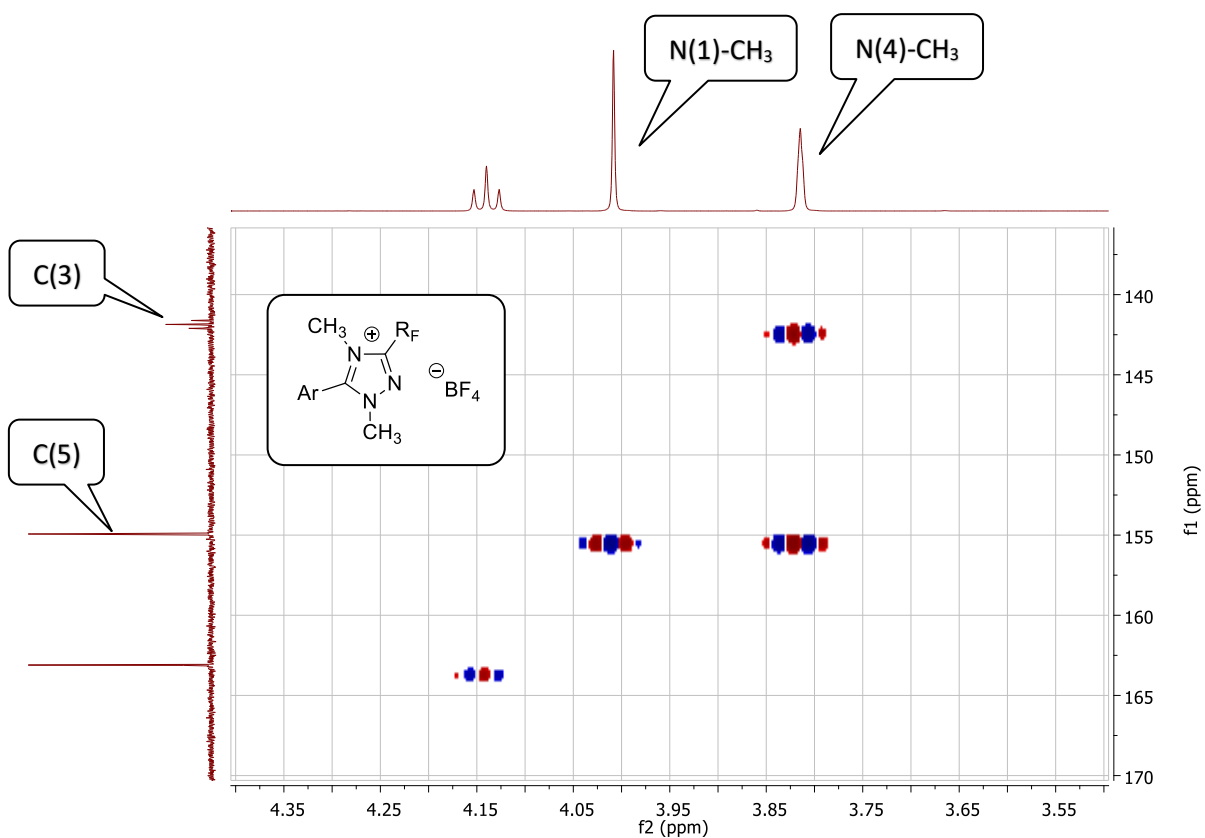
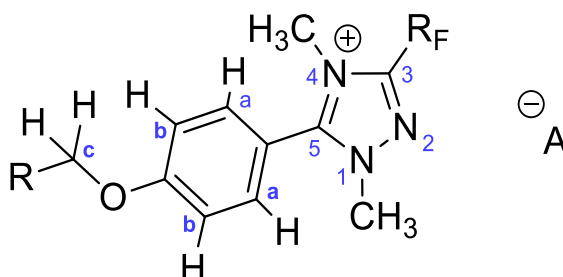


Figure 19.  $^1\text{H}$ - $^{13}\text{C}$  HMBC-NMR spectrum cut in CD<sub>3</sub>CN of [TRYUM-7,12][BF<sub>4</sub>], between 4.40 and 3.50 ppm for  $^1\text{H}$ .

Analysing spectrum cut reported in Figure 19, the structure 1,2-dimethyl-1,2,4-triazol-2-ium has been excluded at least as main isomer. Indeed, hydrogens of N(1)-methyl group couple only with C(5) (4.01, 155.62 ppm), as we could easily guess from the structure, while hydrogens of the other methyl group couple with both C(3) (3.82, 142.55 ppm) and C(5) (3.82, 155.62 ppm) as it should be for 1,4-dimethyl-1,2,4-triazol-2-ium.

Nuclear Overhauser effect (nOe) analysis also confirm the spatial conformation of the 1,4-dimethyl-1,2,4-triazol-4-ium isomer as illustrated in Scheme 28.



**Scheme 28.** Illustration of spatial conformation in 1,4-dimethyl-1,2,4-triazol-4-ium salts.

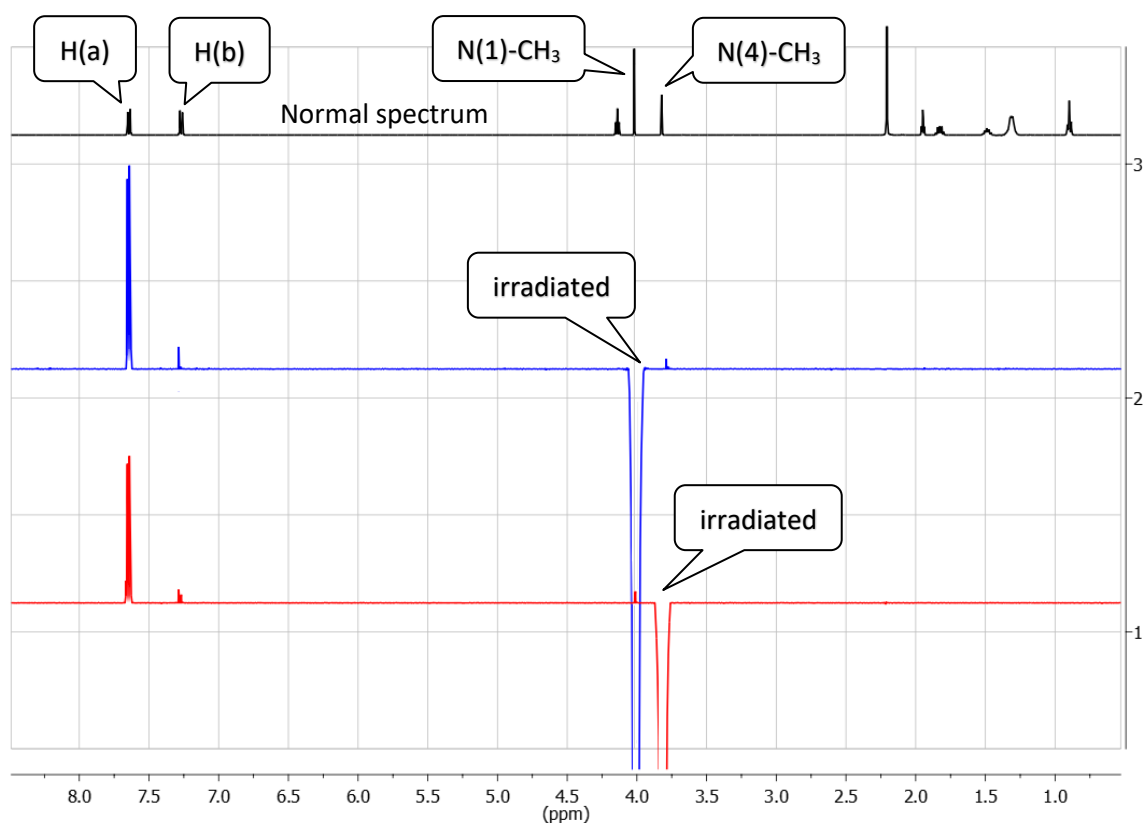


**Figure 20.** Stacking of spectra recorded on [TRYUM-7,12][BF<sub>4</sub>] in CD<sub>3</sub>CN. nOe spectrum recorded irradiating with frequency at 3.82 ppm(1, red line) and 4.01 ppm (2, blue line); <sup>1</sup>H-NMR normal spectrum (3, black line).

The nOe is the transferring of nuclear spin polarisation from one spin population to another *via* cross-relaxation through space and not through chemical bonds. The normal spin population of a specific nucleus can be altered by irradiation which causes signal intensities of other non-irradiated nuclei by dipole-dipole mechanism. From this point of view, atoms in close proximity to each other irradiated with their own frequency can give an nOe.<sup>94</sup>

Spectra reported in Figure 20 show the cross-linking relaxation when the triazolium sample was irradiated by frequencies of the two N-methyl groups. When sample is irradiated with frequency at 4.01 (N(1)-methyl group hydrogens), only the intensity of H(a) signal (7.64 ppm) is enhanced, while the other signal intensities are very lower (blue spectra of Figure 20). The low intensity signals come from at the N(4)-methyl group hydrogens (3.82 ppm) and H(b) (7.26 ppm). This means that N(1)-methyl group hydrogens are spatially close to H(a) as well as distant to H(b) and N(4) methyl group hydrogens. When sample is irradiated with frequency at 3.82 ppm (N(4)-methyl group hydrogens) instead, the intensity of H(a) signal (7.64 ppm) is enhanced too (red spectra of Figure 20). This confirm that N(4)-methyl group hydrogens are spatially close to proximal aromatic hydrogens.

Spectra reported in Figure 21 show the nOe when the triazolium sample was irradiated by frequencies of the aromatic hydrogens.

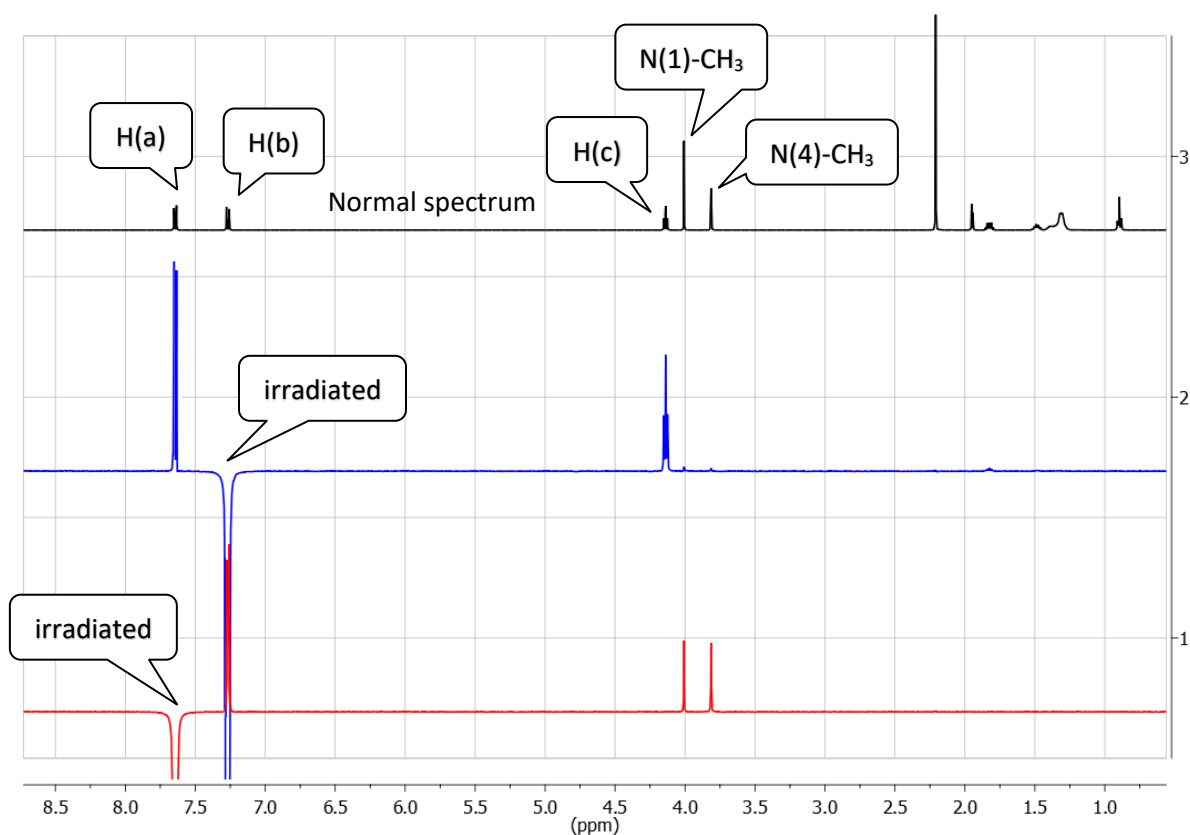
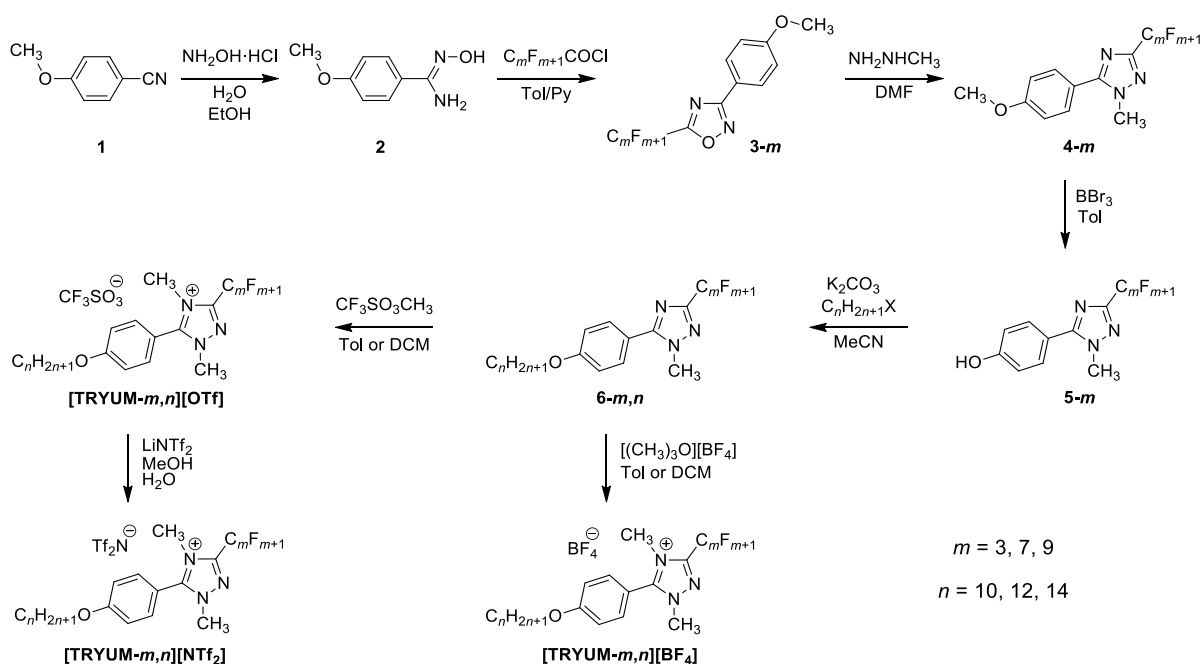


**Figure 21.** Stacking of spectra recorded on [TRYUM-7,12][BF<sub>4</sub>] in CD<sub>3</sub>CN. nOe spectrum recorded irradiating with frequency at 7.64 ppm (1, red line) and 7.26 ppm (2, blue line); <sup>1</sup>H-NMR normal spectrum (3, black line).

As further confirmation, when H(b) (7.26 ppm) are irradiated (blue spectra of Figure 20), H(a) and H(c) the first two hydrogens of the alkyl-chain resonate with high intensity signal as a singlet at 7.64 ppm and a triplet at 4.41 ppm, while both N-methyl group hydrogen at 3.82 and 4.01 ppm resonate with very low intensity. Ultimately, when H(a) (7.64 ppm) are irradiated (red spectra of Figure 20), both N-methyl group hydrogen at 3.82 and 4.01 resonate with comparable high intensity signals as well as H(b) (7.26 ppm).

### 3.1.5 Optimisation of the synthetic process

Once the problems of the quaternisation of the triazole ring were solved and the ANRONC transformation had been strategically moved within the synthesis pathway, the whole process was repeated to obtain three sets of salts (Scheme 29). Each salts set is defined by a specific perfluoroalkyl-chain length: one with a long ( $C_9F_{19}$ ), a medium ( $C_7F_{15}$ ) and a short perfluoroalkyl-chain ( $C_3F_7$ ) and consists of 9 triazolium salts, 3 triflates, 3 tetrafluoroborates and 3 bis(triflimide)s with different alkyl-chain length ( $C_{10}H_{21}$ ,  $C_{12}H_{25}$  and  $C_{14}H_{29}$ ) to give a total of 27 triazolium salts.

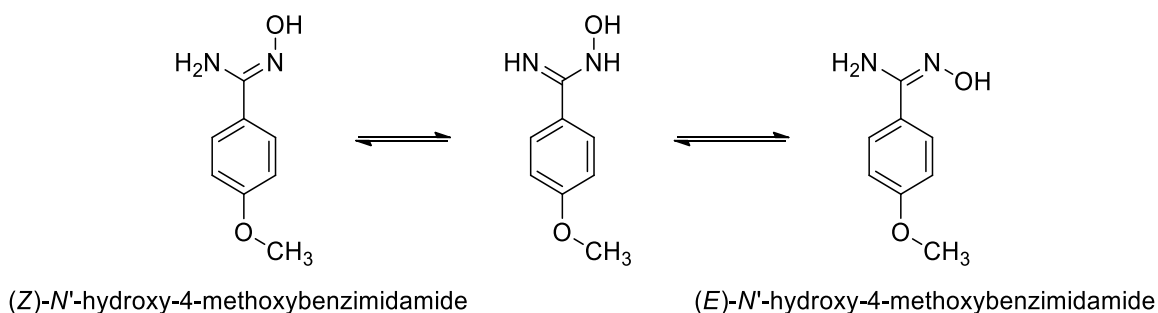


**Scheme 29.** Global synthesis process

However, while oxadiazoles **3-3** and **3-7** can be easily obtained by reacting compound **2** with the respective perfluoroalkanoyl chloride, the perfluorodecanoyl chloride is not available commercially, so adding an additional step to the synthesis of oxadiazole **3-9**. Thus, perfluorodecanoyl chloride was prepared from the perfluorodecanoic acid by reaction with oxalyl chloride in acetonitrile. After the isolation and drying of the chloride, compound **2** was added. Initially, the yield of this step was below under 20%, so the reactions were carried out under nitrogen following three cycles of vacuum/nitrogen. In order to improve the yield further, compound **2** was chromatographed isolating

an its *Z* isomer, which is more reactive toward oxadiazole cyclisation. As showed in Scheme 30, (*Z*)-*N*'-hydroxy-4-methoxybenzamidoxyime can slowly isomerize to its *E* form, going through an intermediate tautomer. So, cyclisation of oxadiazoles was performed using freshly made fractions of amidoxime and this way the yield was improved from 20 to 64%.

Similarly, demethylation of **4-m** by boron tribromide also gone much higher yields when worked under nitrogen. Another weak point of the synthesis process was the methylation of **6-m,n** by trimethyloxonium tetrafluoroborate, which is a methylating agent particularly sensitive to moisture. This step was also improved by cycles of vacuum/nitrogen and using dried toluene or DCM.



**Scheme 30.** Equilibrium between *Z* and *E* isomers of *N*'-hydroxy-4-methoxybenzamidoxyime.

Once the whole three sets of triazolium salts have been synthesised, every single compound was characterised by  $^1\text{H}$  and  $^{19}\text{F}$  NMR spectroscopy to assess the chemical structure and a preliminary purity evaluation, while combustion analysis confirmed their purity (see experimental part).

### 3.2 Crystal structure analysis

The growth of single crystals of sufficient quality for X-ray structure analysis is a common problem for compounds with long chain, since crystallisation is frequently hindered kinetically.<sup>95</sup>

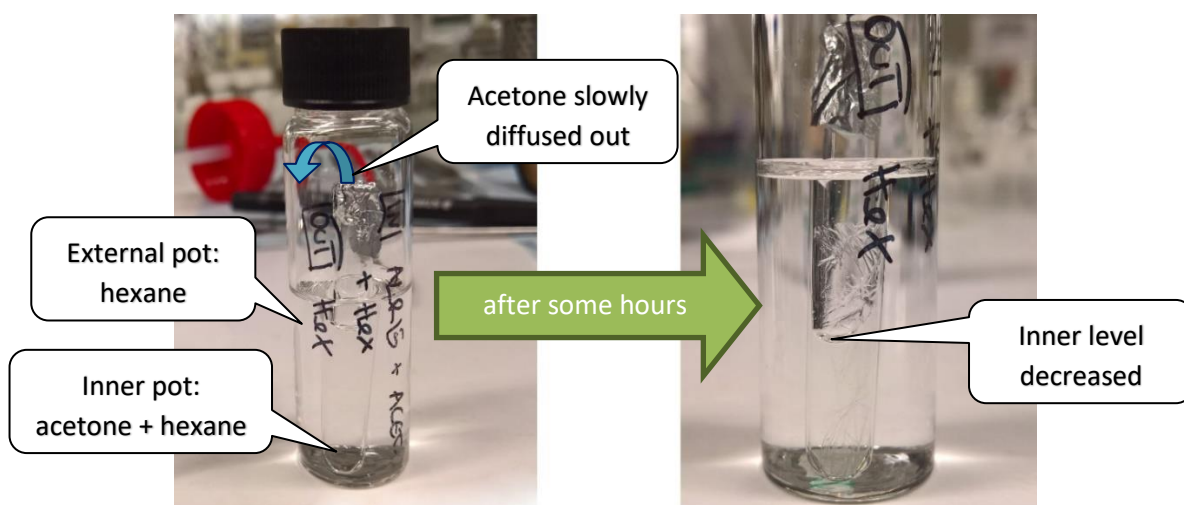
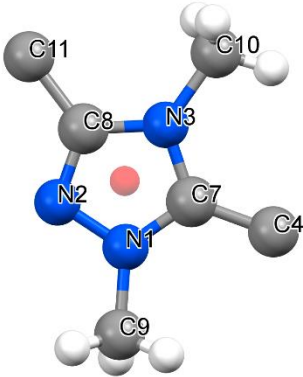


**Figure 22.** Scheme of crystal growing.

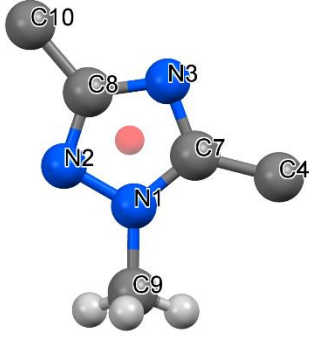
However, single crystals of the triazolium compounds can be grown successfully from an acetone solution, using hexane as anti-solvent (Figure 22). Precisely, crystals were grown by slow gas diffusion,<sup>96</sup> dissolving the sample in an inner pot with a mixture of solvent and anti-solvent as well as placing the inner pot in a bigger external pot, which contains anti-solvent.

### 3.2.1 1,2,4-triazole and triazolium cores

All the triazolium salts crystallised and analysed by X-ray diffraction show a 1,4-dimethyl-1,2,4-triazol-2-ium structure, confirming the site of the quaternisation of the triazole core as also deduced by NMR spectroscopy as described in the previous chapter.



**Triazolium core**



**Triazole core**

Atom1	Atom2	Length	Atom1	Atom2	Length		
<b>Distances</b>							
C8	N3	1.368(3)	C8	N3	1.360(4)		
N3	C7	1.351(3)	N3	C7	1.341(3)		
C7	N1	1.330(3)	C7	N1	1.344(4)		
N1	N2	1.357(3)	N1	N2	1.363(3)		
N2	C8	1.298(3)	N2	C8	1.312(4)		
C11	C8	1.502(3)	C10	C8	1.499(4)		
C7	C4	1.454(3)	C7	C4	1.466(4)		
N1	C9	1.464(3)	N1	C9	1.464(4)		
N3	C10	1.471(3)					
<b>Angles</b>							
Object1	Object2	Object3	Angle	Object1	Object2	Object3	Angle
C11	centroid	C4	146.5(8)	C10	centroid	C4	144.6(1)
C10	centroid	C9	146.5(9)				

**Figure 23.** View with ESDs of the triazolium core of [TRYUM-7,10][OTf] (left) and the triazole core of 5-9 (right). Groups in position 3- and 5- of the rings have been omitted to focus on triazolium and triazole cores, where a centroid was calculated. In this and subsequent figures, carbon atoms are coloured light grey, nitrogen atoms blue, oxygen atoms red, fluorine atoms are light green, sulfur atoms are yellow and boron atoms are pink.

Structures in Figure 23 show the triazole core of compound 5-9 and triazolium core of [TRYUM-7,10][OTf], taken as examples to compare triazolium and triazole ring features. The angle between the *N*-methyl groups (C10-Centroid-C9) as well as the angle between the lateral (C11-Centroid-C4) of



triazolium rings measure about 146.5°, slightly smaller than the analogous in the triazole core (C10-Centroid-C4: 144.6(1)°).

### 3.2.2 Crystallographic analysis of triazolium triflates

For the sake of clarity, this chapter contains the illustration of the single crystal structures that are strictly necessary for the discussion purpose. All the other crystal structures can be viewed in Appendix A, which reports the whole list of the structures collected by single X-ray diffraction.

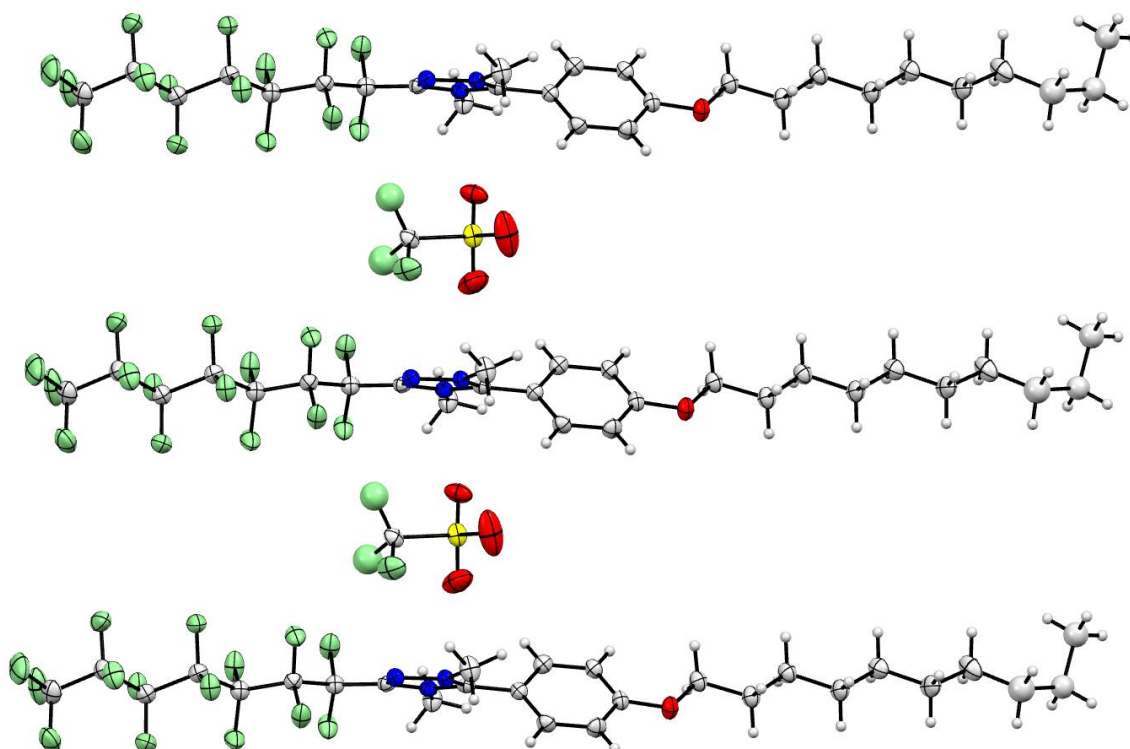


**Figure 24.** Ortep view of compound **[TRIUM-7,10][OTf]** viewed down the *b*-axis of the unit cell.

Compounds **[TRYUM-3,10][OTf]**, **[TRYUM-7,10][OTf]** and **[TRYUM-9,10][OTf]** crystallised in the monoclinic space group  $P2_1/n$  with eight formula units, in the monoclinic  $P2_1/c$  with four formula units and in the triclinic space group  $P-1$  with two formula units in the unit cell, respectively. The main crystallographic parameters are reported and compared in Table 1. In the three ionic compounds, the two chains (alkyl and perfluoroalkyl) point in the opposite direction from the phenyl triazolium core group and define a rod-like shape for the cationic entity. The conformation of the alkyl-chain is almost all *anti* in **[TRYUM-9,10][OTf]** (Figure 26) and **[TRYUM-7,10][OTf]** (Figure 24) except for the bond from the eighth to the ninth carbon, which is slightly disordered in **[TRYUM-7,10][OTf]**. By contrast, the unit cell of **[TRYUM-3,10][OTf]** shows two cations that are very different with respect to the way the chains radiate from the phenyl ring (Figure 25). There is a non-linear chain conformation and the disorder increases along the chains. Crystals of **[TRYUM-3,10][OTf]** are of poorer quality than the other two as

exemplified by the *R*-indices (Table 1). Moreover, molecular alignment and segregation is completely missing in the crystal lattice of [TRYUM-3,10][OTf], which looks to be not structure in layers.

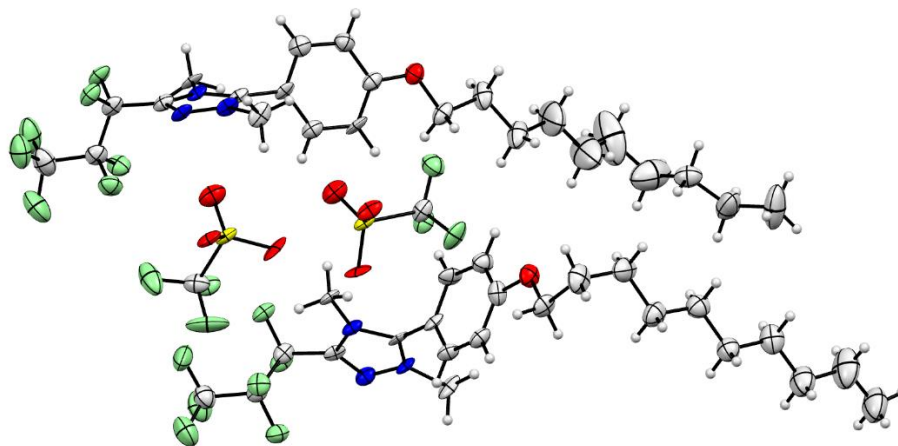


Figure 25. Ortep view of compound [TRIUM-3,10][OTf].

The perfluoroalkyl chains generally appear more linear, even if some carbon and fluorine atoms were found to be in more than one conformation in the same crystal. The perfluoroalkyl-chains and anions appear to form a fluorous domain, where the [OTf]<sup>-</sup> anions appear to be sited in a similar position relative to two cations like in [TRYUM-7,10][OTf] and [TRYUM-9,10][OTf].

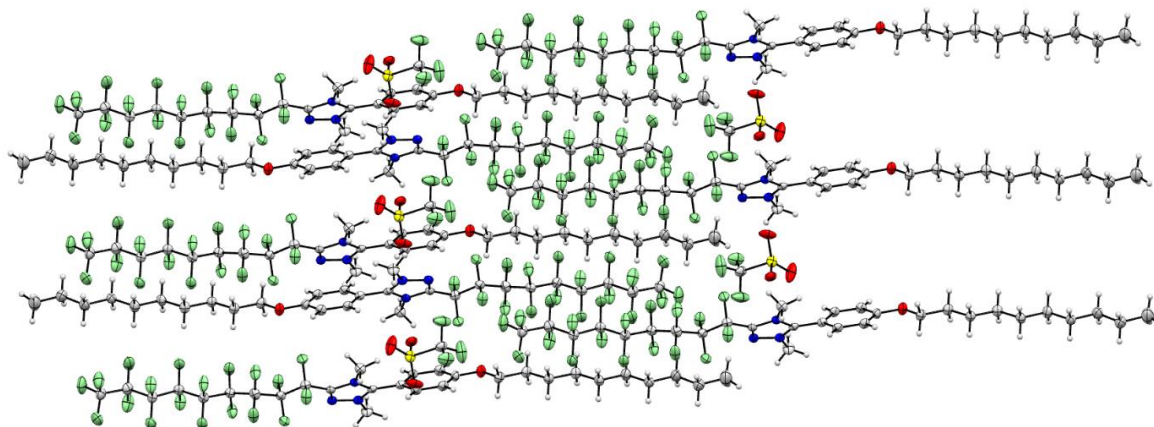
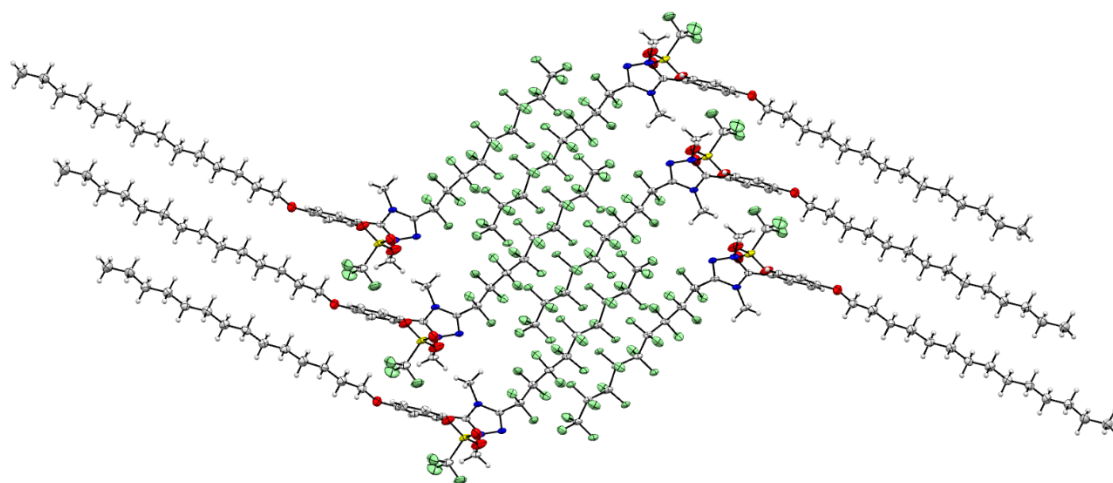


Figure 26. Crystal packing view of compound [TRIUM-9,10][OTf] along the *b*-axis of the unit cell.

Both for [TRYUM-7,10][OTf] and [TRYUM-9,10][OTf], the cations forms an interdigitated structure, but it is interesting that, despite the commonly observed situation where hydrocarbon and fluorocarbon chains phase separate at molecular level this is not the case here as is seen clearly in Figure 26.<sup>15,66,67</sup> Further, in the structure it can be seen that there is evident electrostatic interaction between cations (*i.e.* pi-pi interactions between the triazolium rings and the phenyl rings of another cation) as well as between cation and anion so that there is an alternating arrangement of the two (Figure 26 and Figure 24).

By contrast, the segregation of the fluororous domain was found to be total in [TRYUM-9,14][OTf] (Figure 27), which may suggest that the alkyl-chain length is a factor in this localised segregation. However in this salt, the two chains and the core do not define a linear motif, rather one that is, in effect, bent at the triazolium ring. It is not clear why this non-linear arrangement is preferred, but the literature reports examples of double chained ILs, where the solid-state structure changes depending upon the anion and alkyl chain length. For instance, *N,N'*-dialkylimidazolium salts exhibited linear, bent or U-shaped molecular cation structures.<sup>97</sup> Table 1 contains selected crystal data for the above salts.



**Figure 27.** Crystal packing view of compound [TRIUM-9,14][OTf]<sup>†</sup> along the *b*-axis of the unit cell. Acetone of crystallisation is omitted for clarity.

**Table 1.** Selected crystallographic properties of the triazolium triflates.

	[TRYUM-3,10][OTf]	[TRYUM-7,10][OTf]	[TRYUM-9,10][OTf]	[TRYUM-9,14][OTf] <sup>†</sup>
Space group	<i>P</i> 2 <sub>1</sub> / <i>n</i>	<i>P</i> 2 <sub>1</sub> / <i>c</i>	<i>P</i> -1	<i>P</i> -1
Crystal system	Monoclinic	Monoclinic	Triclinic	Triclinic
Unit cell dimensions / Å	<i>a</i> = 12.2678(8) <i>b</i> = 14.1723(16) <i>c</i> = 34.440(4)	<i>a</i> = 18.8350(8) <i>b</i> = 8.0827(3) <i>c</i> = 22.8945(9)	<i>a</i> = 7.9391(3) <i>b</i> = 11.5678(10) <i>c</i> = 20.8049(17)	<i>a</i> = 6.23099(17) <i>b</i> = 9.1796(4) <i>c</i> = 39.4248(14)
Unit Cell Angles / °	$\alpha$ = 90 $\beta$ = 90.660(8) $\gamma$ = 90	$\alpha$ = 90 $\beta$ = 96.376(4) $\gamma$ = 90	$\alpha$ = 82.290(7) $\beta$ = 89.720(5) $\gamma$ = 82.993(5)	$\alpha$ = 95.565(3) $\beta$ = 92.989(3) $\gamma$ = 92.795(3)
Volume / Å <sup>3</sup>	5987.4(11)	3463.9(3)	1879.1(2)	2238.04(13)
<i>Z</i>	8	4	2	2
$\rho$ / g cm <sup>-3</sup>	1.443	1.625	1.675	1.576
Final <i>R</i> factors [ <i>I</i> > 2 $\sigma$ <i>I</i> ]	<i>R</i> <sub>1</sub> = 0.1615, <i>wR</i> <sub>2</sub> = 0.3671	<i>R</i> <sub>1</sub> = 0.0485, <i>wR</i> <sub>2</sub> = 0.1245	<i>R</i> <sub>1</sub> = 0.0662, <i>wR</i> <sub>2</sub> = 0.1529	<i>R</i> <sub>1</sub> = 0.0880, <i>wR</i> <sub>2</sub> = 0.2198
<i>R</i> factors (all data)	<i>R</i> <sub>1</sub> = 0.1857, <i>wR</i> <sub>2</sub> = 0.3794	<i>R</i> <sub>1</sub> = 0.0610, <i>wR</i> <sub>2</sub> = 0.1359	<i>R</i> <sub>1</sub> = 0.0846, <i>wR</i> <sub>2</sub> = 0.1667	<i>R</i> <sub>1</sub> = 0.1033, <i>wR</i> <sub>2</sub> = 0.2274

<sup>†</sup> include acetone in the structure. The whole information is reported in the experimental section.

### 3.2.3 Crystallographic analysis of triazolium bis(triflimide)s

Triazolium bis(triflimide)s ([TRYUM-3,10][Tf<sub>2</sub>N], [TRYUM-3,14][Tf<sub>2</sub>N], [TRYUM-7,10][Tf<sub>2</sub>N], [TRYUM-7,12][Tf<sub>2</sub>N], [TRYUM-9,10][Tf<sub>2</sub>N], [TRYUM-9,12][Tf<sub>2</sub>N] and [TRYUM-9,14][Tf<sub>2</sub>N]) crystallised in the orthorhombic space group  $P2_12_12_1$  as well as in the monoclinic space groups  $P2_1$ ,  $P2_1/c$  or  $P2_1/n$  (with value of the unit cell angle  $\beta$  between 90.73 and 91.66°), always with four formula units in the unit cell. Despite the different space groups, all seven the salts have similar unit cells, with  $a$ - and  $b$ -axis value about the same, while the  $c$ -axis is particularly long (e.g. in Figure 28), increasing with length of the alkyl and perfluoroalkyl chains (Table 2). In all seven the triazolium bis(triflimide)s, the two chains (alkyl and perfluoroalkyl) of one cation point in opposite directions from the triazolium core group making an angle between 136.63 and 155.70°, and leading to bent motif. Angles were measured as shown in Figure 8 based on a centroid among the aromatic rings. Bis(triflimide)s with a C<sub>7</sub>F<sub>15</sub> chains show the smallest angle, which is greater in the other compounds with longer or shorter perfluoroalkyl-chains (Figure 29 compare angles of [TRYUM- $m$ ,10][Tf<sub>2</sub>N]).

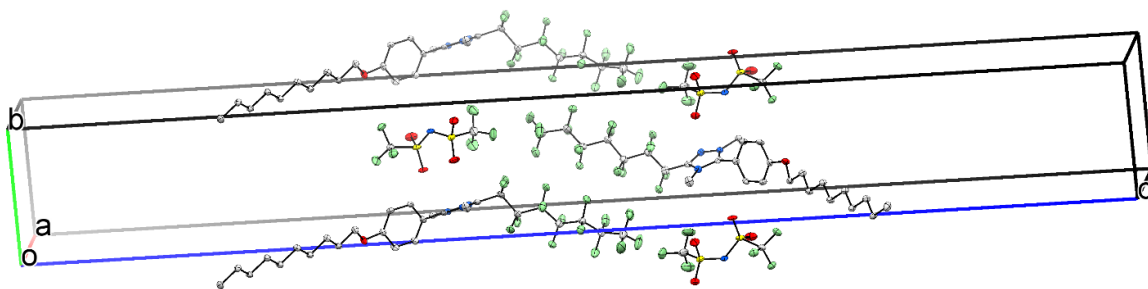


**Figure 28.** Ortep view of crystal lattice of [TRYUM-7,10][Tf<sub>2</sub>N] showing the unit cell dimensions.

The conformation of the alkyl chains is always all-*trans* regardless its length or that of the perfluoroalkyl chain. In some of the perfluoroalkyl chains, a helical arrangement of the chains was found, with both helical senses being represented. The [Tf<sub>2</sub>N]<sup>-</sup> anions were all *trans* with a dihedral angle of around 158° between the CF<sub>3</sub> groups and the nitrogen.

For all seven triazolium bis(triflimide)s in the crystals, the cations form a bilayer structure, where cations alternate sandwich-like with bis(triflimide) anions and the perfluoroalkyl chains are interdigitated (Figure 30 and Figure 31). All these compounds show a local segregation of the fluorine domain, regardless of the length of the perfluoroalkyl-chain. The bilayers formed in [TRYUM-3,10][Tf<sub>2</sub>N], [TRYUM-3,14][Tf<sub>2</sub>N], [TRYUM-7,10][Tf<sub>2</sub>N] and [TRYUM-7,12][Tf<sub>2</sub>N] are U-shaped (Figure 30, the others in Appendix A), whereas those formed in [TRYUM-9,10][Tf<sub>2</sub>N], [TRYUM-9,12][Tf<sub>2</sub>N] and [TRYUM-9,14][Tf<sub>2</sub>N] are Z-shaped. The bigger [Tf<sub>2</sub>N]<sup>-</sup> anion seems to space out the cations in these structures, which means that the potential for cation-cation pi-pi interactions is reduced. (Figure 32, the others in Appendix A).

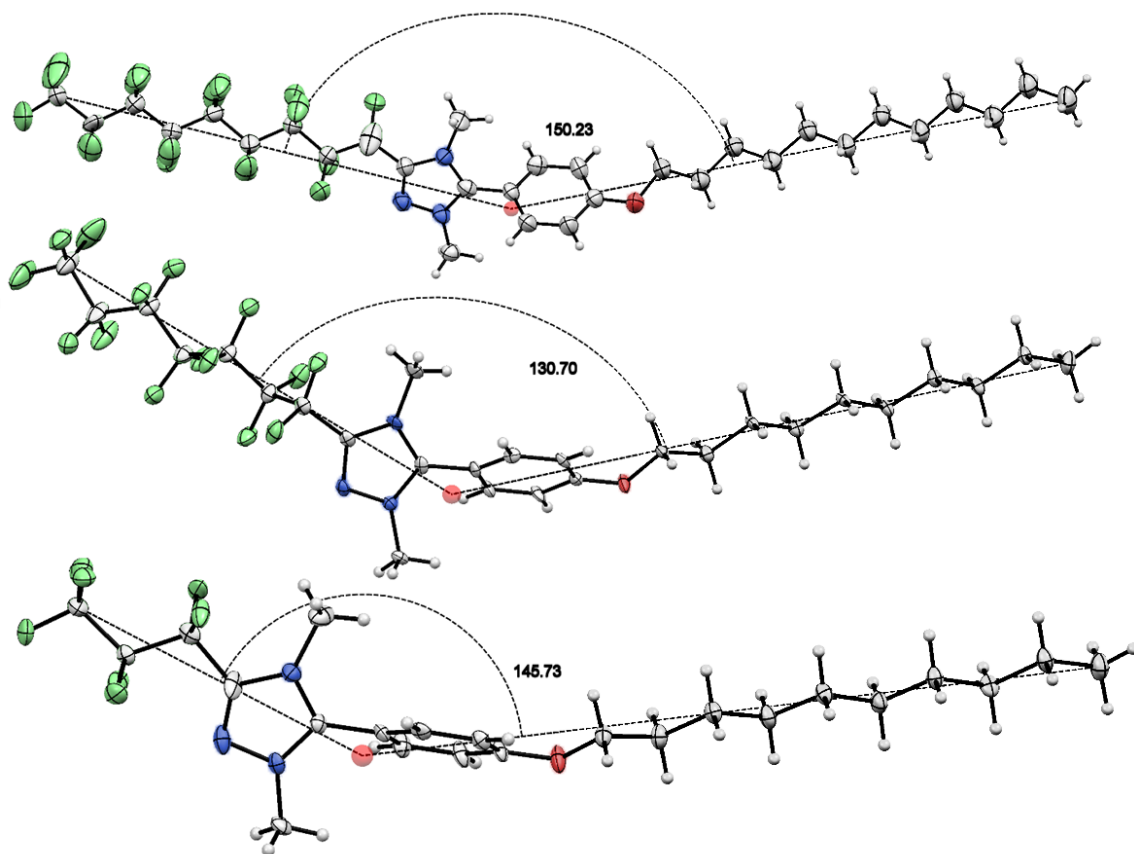


**Figure 29.** Ortep view with comparison of angles between alkyl and perfluoroalkyl-chains of triazolium bis(triflimide)s cations. Centroids are coloured red.

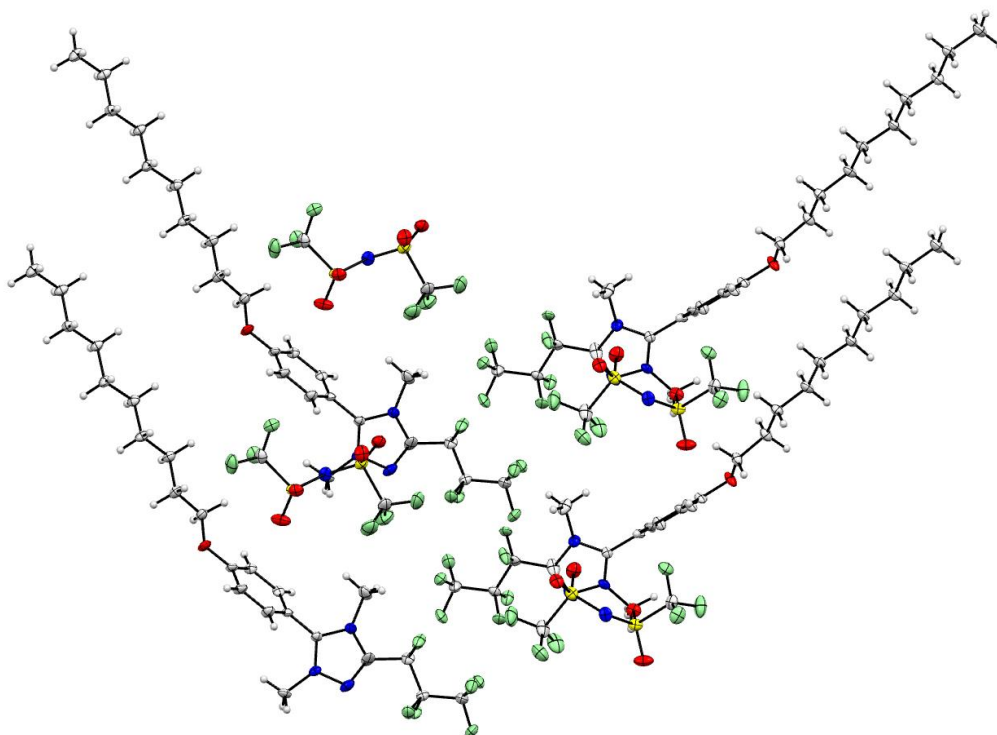


**Figure 30.** Crystal packing view of compound [TRYUM-3,10][Tf2N].

**Table 2.** Selected crystallographic properties of the triazolium bis(triflimide)s.

	[TRYUM-3,10][Tf <sub>2</sub> N]	[TRYUM-3,14][Tf <sub>2</sub> N]	[TRYUM-7,10][Tf <sub>2</sub> N]	[TRYUM-7,12][Tf <sub>2</sub> N]
Space group	<i>P</i> 2 <sub>1</sub> 2 <sub>1</sub> 2 <sub>1</sub>	<i>P</i> 2 <sub>1</sub>	<i>P</i> 2 <sub>1</sub> 2 <sub>1</sub> 2 <sub>1</sub>	<i>P</i> 2 <sub>1</sub> 2 <sub>1</sub> 2 <sub>1</sub>
Crystal system	Orthorhombic	Monoclinic	Orthorhombic	Orthorhombic
Unit cell dimensions/Å	<i>a</i> = 6.8452(4) <i>b</i> = 8.4550(4) <i>c</i> = 56.345(3)	<i>a</i> = 6.8348(3) <i>b</i> = 8.5999(4) <i>c</i> = 8.5999(4)	<i>a</i> = 6.6955(2) <i>b</i> = 8.5499(2) <i>c</i> = 68.538(2)	<i>a</i> = 6.7404(7) <i>b</i> = 8.6592(7) <i>c</i> = 71.960(6)
Unit Cell Angles/°	$\alpha$ = 90 $\beta$ = 90 $\gamma$ = 90	$\alpha$ = 90 $\beta$ = 90.931(5) $\gamma$ = 90	$\alpha$ = 90 $\beta$ = 90 $\gamma$ = 90	$\alpha$ = 90 $\beta$ = 90 $\gamma$ = 90
Volume/ Å <sup>3</sup>	3261.0(3)	3741.2(3)	3923.5(2)	4200.0(6)
<i>Z</i>	4	4	4	4
$\rho$ / g cm <sup>-3</sup>	1.586	1.482	1.657	1.592
Final <i>R</i> factors [ <i>I</i> >2 $\sigma$ ]	<i>R</i> <sub>1</sub> = 0.0563, <i>wR</i> <sub>2</sub> = 0.1166	<i>R</i> <sub>1</sub> = 0.0980, <i>wR</i> <sub>2</sub> = 0.2747	<i>R</i> <sub>1</sub> = 0.0446, <i>wR</i> <sub>2</sub> = 0.0855	<i>R</i> <sub>1</sub> = 0.0867, <i>wR</i> <sub>2</sub> = 0.1782
<i>R</i> factors (all data)	<i>R</i> <sub>1</sub> = 0.0580, <i>wR</i> <sub>2</sub> = 0.1171	<i>R</i> <sub>1</sub> = 0.1042, <i>wR</i> <sub>2</sub> = 0.2810	<i>R</i> <sub>1</sub> = 0.0516, <i>wR</i> <sub>2</sub> = 0.0886	<i>R</i> <sub>1</sub> = 0.0983, <i>wR</i> <sub>2</sub> = 0.1837
	[TRYUM-9,10][Tf <sub>2</sub> N]	[TRYUM-9,12][Tf <sub>2</sub> N]	[TRYUM-9,14][Tf <sub>2</sub> N]	
Space group	<i>P</i> 2 <sub>1</sub> / <i>c</i>	<i>P</i> 2 <sub>1</sub> / <i>c</i>	<i>P</i> 2 <sub>1</sub> / <i>n</i>	
Crystal system	Monoclinic	Monoclinic	Monoclinic	
Unit cell dimensions / Å	<i>a</i> = 6.7112(2) <i>b</i> = 8.5380(3) <i>c</i> = 71.575(3)	<i>a</i> = 6.7752(8) <i>b</i> = 8.6424(9) <i>c</i> = 74.967(9)	<i>a</i> = 6.75057(18) <i>b</i> = 8.6616(2) <i>c</i> = 78.211(2)	
Unit Cell Angles / °	$\alpha$ = 90 $\beta$ = 91.664(3) $\gamma$ = 90	$\alpha$ = 90 $\beta$ = 90.731(11) $\gamma$ = 90	$\alpha$ = 90 $\beta$ = 91.192(2) $\gamma$ = 90	
Volume / Å <sup>3</sup>	4099.6(2)	4389.3(9)	4572.1(2)	
<i>Z</i>	4	4	4	
$\rho$ / g cm <sup>-3</sup>	1.748	1.675	1.649	
Final <i>R</i> factors [ <i>I</i> >2 $\sigma$ ]	<i>R</i> <sub>1</sub> = 0.0616, <i>wR</i> <sub>2</sub> = 0.1448	<i>R</i> <sub>1</sub> = 0.1043, <i>wR</i> <sub>2</sub> = 0.2304	<i>R</i> <sub>1</sub> = 0.0716, <i>wR</i> <sub>2</sub> = 0.1385	
<i>R</i> factors (all data)	<i>R</i> <sub>1</sub> = 0.0701, <i>wR</i> <sub>2</sub> = 0.1509	<i>R</i> <sub>1</sub> = 0.1495, <i>wR</i> <sub>2</sub> = 0.2594	<i>R</i> <sub>1</sub> = 0.0872, <i>wR</i> <sub>2</sub> = 0.1472	

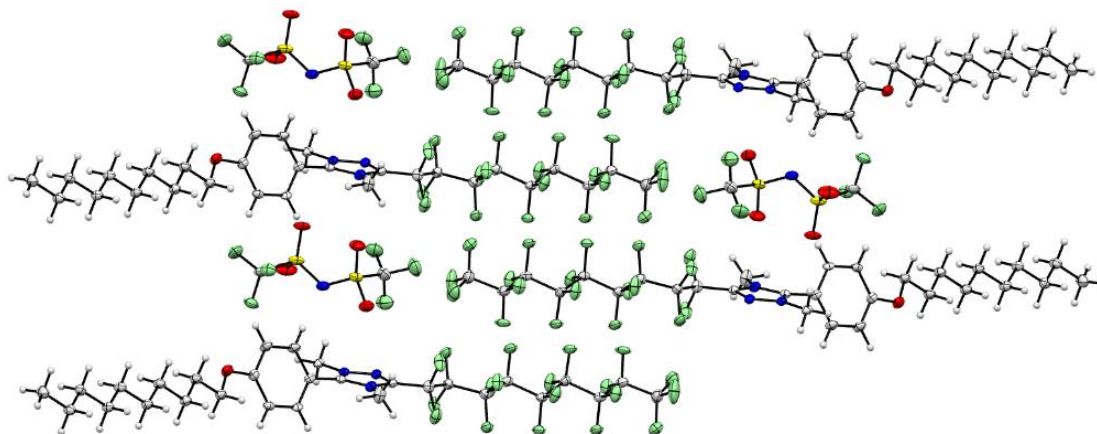


**Figure 31.** Crystal packing view of compound [TRIUM-7,12][Tf<sub>2</sub>N] along the *a*-axis of the unit cell.



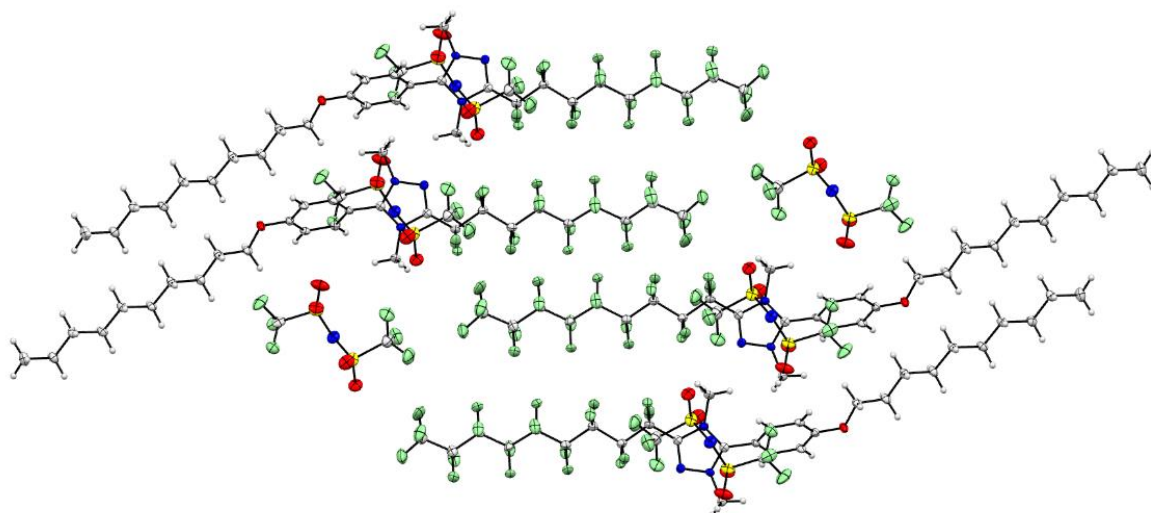


**Figure 32.** Crystal packing view of compound [TRIUM-7,12][Tf<sub>2</sub>N] along the *b*-axis of the unit cell.

### 3.2.4 Crystallographic analysis of triazolium tetrafluoroborates

Compounds [TRYUM-*m*,10][BF<sub>4</sub>] and [TRYUM-9,14][BF<sub>4</sub>] crystallised in the monoclinic system in the space group *P*2<sub>1</sub>/*c* with a value of  $\beta$  between 92.65 and 98.68°; the unit cell contained four formula units (Table 3).

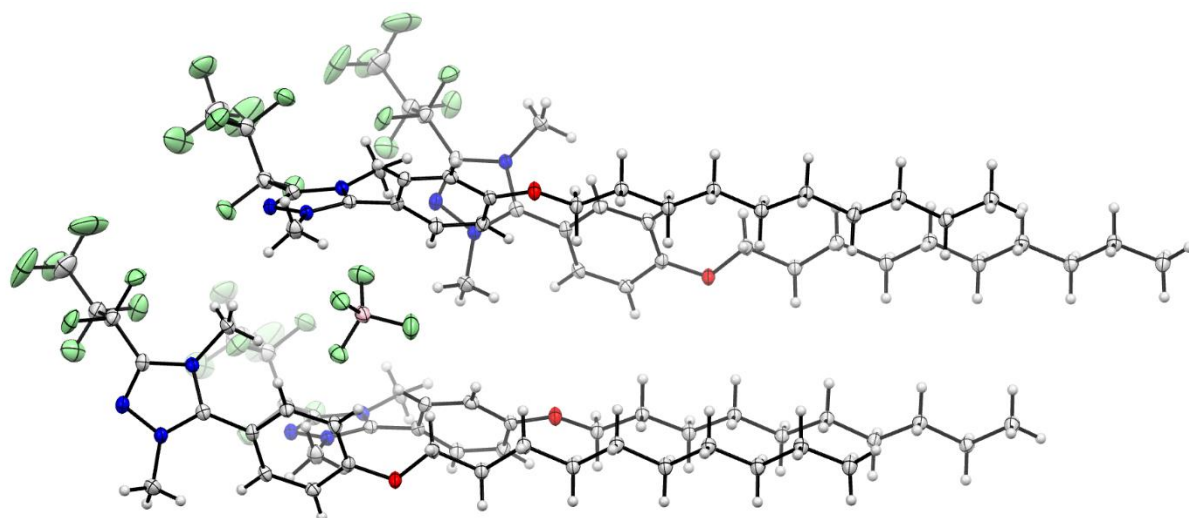


**Figure 33.** Ortep view of compound [TRIUM-3,10][BF<sub>4</sub>]<sup>+</sup>. Carbon atoms are coloured light grey, nitrogen atoms blue, oxygen atoms red, fluorine atoms are light green and boron atoms are pink. Acetone of crystallisation is omitted and depth cueing is applied, where brightness decreases along deepness.

In all the tetrafluoroborate salts, the two chains (alkyl and perfluoroalkyl) of one cation point in opposite directions with respect to the triazolium core group and make a small angle with respect to one another that is slightly smaller for [TRYUM-3,10][BF<sub>4</sub>] and [TRYUM-9,14][BF<sub>4</sub>] (Figure 33, the others in Appendix A as Figure A14, Figure A15 and Figure A16). The conformation of the alkyl-chains is always all-*trans* and the perfluoroalkyl-chains appear quite linear and show helicity, which is easily

perceptible in views orthogonal to the  $a$ -axis of the unit cell (Figure 34). However, in some cases, the disorder of the perfluoroalkyl chains was resolved as originating from the two different helical chiralities. The salts form a Z-shaped bilayer structure with angles that follow the bent shapes of cations. The perfluoroalkyl chains are always interdigitated and there is a clear and complete micro-segregation between the perfluoroalkyl and the alkyl chains regardless of the length of the perfluoroalkyl-chain (Figure 35, the others in Appendix A as Figure A30, Figure A31). While in the triflate and triflimide salts, the anions are sandwiched by the cations, in the tetrafluoroborate salts the anions appear surrounded by four cations. The main crystallographic parameters of the triazolium tetrafluoroborates are reported and compared in Table 3.

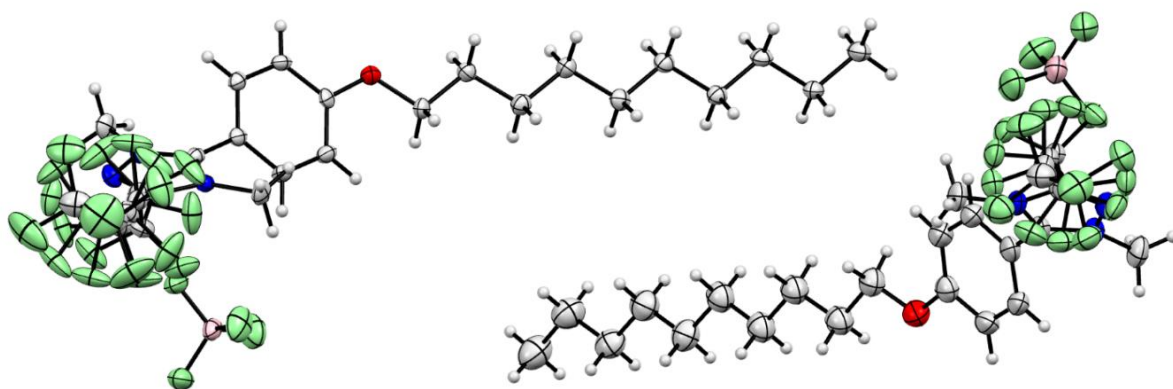


**Figure 34.** Ortep view of [TRYUM-9,10][BF<sub>4</sub>] (left) and [TRYUM-7,10][BF<sub>4</sub>] (right) along the  $a$ -axis of the unit cell.

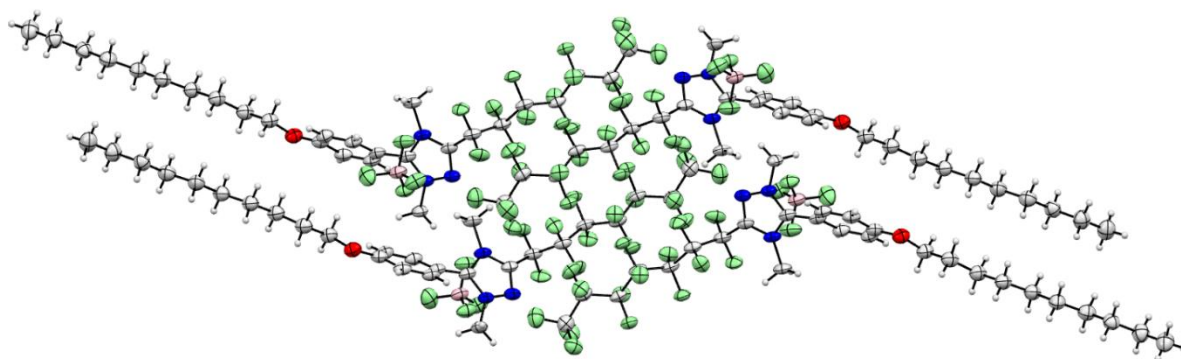


**Figure 35.** Crystal packing view of compound [TRIUM-7,10][BF<sub>4</sub>] is along the  $b$ -axis of the unit cell and hydrogens are omitted.



**Table 3.** Selected crystallographic properties of the triazolium tetrafluoroborates.

	[TRYUM-3,10][BF <sub>4</sub> ] <sup>†</sup>	[TRYUM-7,10][BF <sub>4</sub> ] <sup>†</sup>	[TRYUM-9,10][BF <sub>4</sub> ]	[TRYUM-9,14][BF <sub>4</sub> ] <sup>†</sup>
Space group	<i>P</i> <sub>2</sub> <sub>1</sub> / <i>c</i>	<i>P</i> <sub>2</sub> <sub>1</sub> / <i>c</i>	<i>P</i> <sub>2</sub> <sub>1</sub> / <i>c</i>	<i>P</i> <sub>2</sub> <sub>1</sub> / <i>c</i>
Crystal system	Monoclinic	Monoclinic	Monoclinic	Monoclinic
Unit cell dimensions / Å	<i>a</i> = 29.5005(5) <i>b</i> = 9.28574(14) <i>c</i> = 11.08372(17)	<i>a</i> = 29.930(2) <i>b</i> = 9.2437(5) <i>c</i> = 11.7255(5)	<i>a</i> = 37.0798(6) <i>b</i> = 9.45070(11) <i>c</i> = 11.29828(17)	<i>a</i> = 40.3423(12) <i>b</i> = 9.4231(3) <i>c</i> = 11.2821(4)
Unit Cell Angles / °	<i>α</i> = 90 <i>β</i> = 98.6889(15) <i>γ</i> = 90	<i>α</i> = 90 <i>β</i> = 96.553(5) <i>γ</i> = 90	<i>α</i> = 90 <i>β</i> = 98.5285(14) <i>γ</i> = 90	<i>α</i> = 90 <i>β</i> = 92.753(3) <i>γ</i> = 90
Volume / Å <sup>3</sup>	3001.36(8)	3222.8(3)	3915.48(9)	4283.9(2)
Z	4	4	4	4
<i>ρ</i> / g cm <sup>-3</sup>	1.424	1.619	1.600	1.550
Final <i>R</i> factors [ <i>I</i> > 2σ <i>I</i> ]	<i>R</i> <sub>1</sub> = 0.0392, <i>wR</i> <sub>2</sub> = 0.0959	<i>R</i> <sub>1</sub> = 0.0769, <i>wR</i> <sub>2</sub> = 0.2090	<i>R</i> <sub>1</sub> = 0.0817, <i>wR</i> <sub>2</sub> = 0.1761	<i>R</i> <sub>1</sub> = 0.0591, <i>wR</i> <sub>2</sub> = 0.1320
<i>R</i> factors (all data)	<i>R</i> <sub>1</sub> = 0.0476, <i>wR</i> <sub>2</sub> = 0.1016	<i>R</i> <sub>1</sub> = 0.0976, <i>wR</i> <sub>2</sub> = 0.2263	<i>R</i> <sub>1</sub> = 0.0847, <i>wR</i> <sub>2</sub> = 0.1774	<i>R</i> <sub>1</sub> = 0.0676, <i>wR</i> <sub>2</sub> = 0.1398

<sup>†</sup> include acetone in the structure.

The literature doesn't report many compounds similar to the triazolium salts of the present work, but 1,4,5-trimethyl-3-perfluorooctyl-1,2,4-triazolium tetrafluoroborate<sup>82</sup> was synthesised and characterised by Shreeve *et al.* (CCDC number: 235515). The salt crystallised in space group *P*<sub>2</sub><sub>1</sub>/*c* in a monoclinic unit cell. The perfluoroalkyl-chain of cation entities clearly show helicity (Figure 36, left) and there is segregation of the fluorine and hydrocarbon domains, even if there is no interdigitation of the chains (Figure 36, right). Lastly and in common with the structures described above, a single tetrafluoroborate anion seems to be surrounded by four cations (Figure 36, middle).

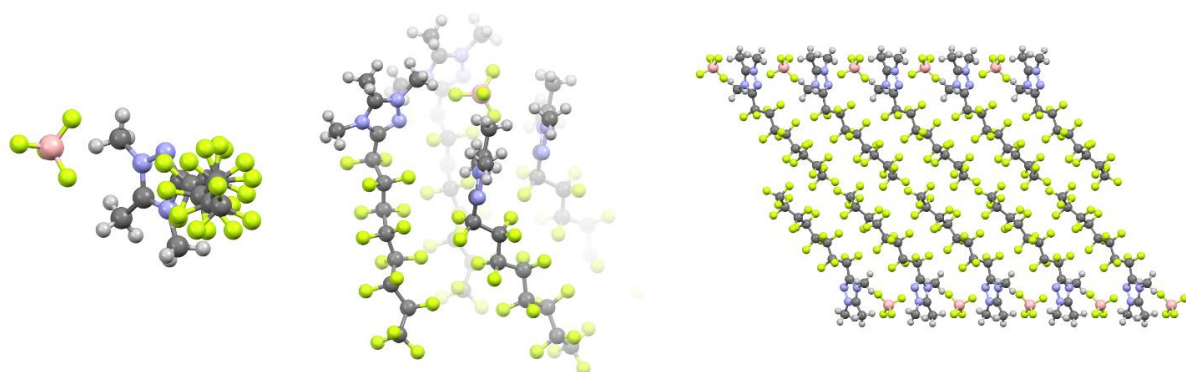


**Figure 36.** Crystal structure of 1,4,5-Trimethyl-3-perfluorooctyl-1,2,4-triazolium Tetrafluoroborate. View showing the helicity of the perfluoroheptyl-chain (left). View showing numbers of cations that surround an anion, in which depth cueing is applied, where brightness decreases along deepness (middle). View orthogonal to the *b* axis of the unit cell, which shows the segregation of the perfluoroalkyl-chain (right).

Overall, the crystal data describe a system where different moieties lead to variation in solid state geometries affecting also the system order and organisation intended as linearity and conformation of the chains as well as molecular alignment and micro-segregation in the crystal lattice.

The way the salts can pack to fill space will depend upon different factors such as size, chemical nature, electrostatics and so on, all of which derive from the nature of the cation and of the anion. While the linearity and the conformational nature of the chains seems to follow a trend with structure, it is possible that this arises from, for example, the solvent used for crystallisation and that is not necessarily an intrinsic property of the cation/anion. The following observations and comparisons between the structures of the different compounds are made in the light of these comments.

Thus, the molecular order seems to depend primarily on the anion, where triazolium triflates show the poorest chain linearity, multiple conformation of chains as well as poor local segregation of the fluorine domain. However, triazolium tetrafluoroborates and bis(triflimide)s are 'better behaved' in relation to these properties, consistent with the trend with which these compounds easily crystallise ( $[\text{OTf}]^- < [\text{BF}_4]^- < [\text{Tf}_2\text{N}]^-$ ). Indeed, within this system, the crystal lattice properties and the thermal behaviour as well as the intramolecular bending angle appear correlated with a particular anion, which also reflects on the nature of the molecular layering. The localised segregation of the fluorine domain appears most strongly correlated with the anion rather than the length of the perfluoroalkyl chain, the latter seeming to be the secondary factor. The linearity of the chains increases with the length of the perfluoroalkyl-chain as observed in all the three set of salts ( $\text{C}_3\text{F}_7 < \text{C}_7\text{F}_{15} < \text{C}_9\text{F}_{19}$ ). Lastly the molecular order, expressed as linearity and chain conformation as well as the local hydrocarbon/fluorocarbon segregation of the system, seems to increase with the alkyl chain length. ( $\text{C}_{10}\text{H}_{21} < \text{C}_{12}\text{H}_{25} < \text{C}_{14}\text{H}_{29}$ ).

### 3.3 Liquid Crystal Properties

The LC properties of the triazolium salts were characterised using a combination of POM and DSC, which allowed the characteristic optical textures obtained to be correlated with events from the thermal data. The transition temperatures, enthalpies, entropies and phase transition assignments are listed in Table 4.

**Table 4.** Transition temperatures, enthalpies and entropies obtained from the DSC traces.

Compound	Transition	$T$ (°C)	$\Delta H$ (kJ mol <sup>-1</sup> )	$\Delta S$ (J K <sup>-1</sup> mol <sup>-1</sup> )
<b>[TRYUM-3,10][OTf]</b>	Cr'-Cr	60.0	7.1	21
	Cr-Iso	101.7	21.0	56
<b>[TRYUM-3,12][OTf]</b>	Cr-Iso	91.3	48.4	133
<b>[TRYUM-3,14][OTf]</b>	Cr-Iso	73.8	38.5	111
<b>[TRYUM-3,10][Tf<sub>2</sub>N]</b>	Cr-Iso	73.1	36.7	106
<b>[TRYUM-3,12][Tf<sub>2</sub>N]</b>	Cr-Iso	76.5	54.5	156
<b>[TRYUM-3,14][Tf<sub>2</sub>N]</b>	Cr-Iso	81.1	55.4	156
<b>[TRYUM-3,10][BF<sub>4</sub>]</b>	Cr'-Cr	49.1	22.9	71
	Cr-Iso	84.1	4.4	12

[TRYUM-3,12][BF <sub>4</sub> ]	Cr'-Cr	65.0	18.6	55
	Cr-Iso	88.8	1.3	4
[TRYUM-3,14][BF <sub>4</sub> ]	Cr'-Cr	76.2	33.1	95
	Cr-Iso	96.4	2.5	7
[TRYUM-7,10][OTf]	Cr-SmA	105.6	11.5	30
	SmA-Iso	160.8	5.2	12
[TRYUM-7,12][OTf]	Cr-SmA	60.3	35.8	107
	SmA-Iso	163.5	4.9	11
[TRYUM-7,14][OTf]	Cr-SmA	52.0	19.8	61
	SmA-Iso	166.8	5.2	12
[TRYUM-7,10][Tf <sub>2</sub> N]	Cr-Iso	83.9	40.1	112
	(Iso-SmA)	(49.6)	(-2.7)	(-8)
[TRYUM-7,12][Tf <sub>2</sub> N]	Cr'-Cr	54.9	5.2	16
	Cr-Iso	86.0	40	111
	(Iso-SmA)	(72.6)	(-3.2)	(-9)
[TRYUM-7,14][Tf <sub>2</sub> N]	Cr'-Cr	78.7	10.9	31
	Cr-Iso	93.4	48.0	132
	(Iso-SmA)	(91.5)	(-4.6)	(-13)
[TRYUM-7,14][BF <sub>4</sub> ]	Cr'-Cr	67.4	20.5	60
	Cr-SmB	106.6	7.6	20
	SmB-SmA	175.9	2.1	5
	SmA-Iso	233.4	5.3	10
[TRYUM-7,12][BF <sub>4</sub> ]	Cr'-Cr	78.7	23.2	66
	Cr-SmB	115.1	7.1	18
	SmB-SmA	169.5	1.7	4
	SmA-Iso	236.6	5.0	10
[TRYUM-7,14][BF <sub>4</sub> ]	Cr''-Cr'	63.6	17.4	52
	Cr'-Cr	88.7	29.2	81
	Cr-SmB	125.2	8.6	22
	SmB-SmA	175.5	2.0	4
	SmA-Iso	237.3	5.1	10
[TRYUM-9,10][OTf]	Cr-SmA	48.6	1.5	5
	SmA-Iso	184.3	5.7	12
[TRYUM-9,12][OTf]	Cr-SmA	60.0	7.0	21
	SmA-Iso	196.0	6.8	14
[TRYUM-9,14][OTf]	Cr-SmA	69.2	13.1	38
	SmA-Iso	205.2	8.1	17
[TRYUM-9,10][Tf <sub>2</sub> N]	Cr-Iso	97.0	41.4	112
	(Iso-SmA)	(96.8)	(-3.8)	(-10)
[TRYUM-9,12][Tf <sub>2</sub> N]	Cr-SmA	97.4	44.3	120
	SmA-Iso	115.5	4.9	13
[TRYUM-9,14][Tf <sub>2</sub> N]	Cr-SmA	98.9	47.8	128
	SmA-Iso	133.2	5.7	14
[TRYUM-9,10][BF <sub>4</sub> ]	Cr'-Cr	73.2	27.9	81
	Cr-SmB	115.9	2.1	5
	SmB-SmA	139.3	9.4	23
	SmA-Iso	265.6	2.6	5
[TRYUM-9,12][BF <sub>4</sub> ]	Cr'-Cr	89.4	22.5	62
	Cr-SmB	116.7	5.0	13
	SmB-SmA	136.8	7.8	19
	SmA-Iso	268.5	1.0	2
[TRYUM-9,14][BF <sub>4</sub> ]	Cr''-Cr'	74.7	33.0	95
	Cr'-Cr	92.6	13.2	36
	Cr-SmB	116.8	3.5	9
	SmB-SmA	135.5	7.8	19
	SmA-Iso	257.7	1.3	2

Transitions refer to the 1<sup>st</sup> heating cycles (2<sup>nd</sup> heating and 1<sup>st</sup> cooling are discussed in paragraph 3.3.2).

Transition in brackets and relative value refer to transitions from isotropic on cooling for monotropic salts.

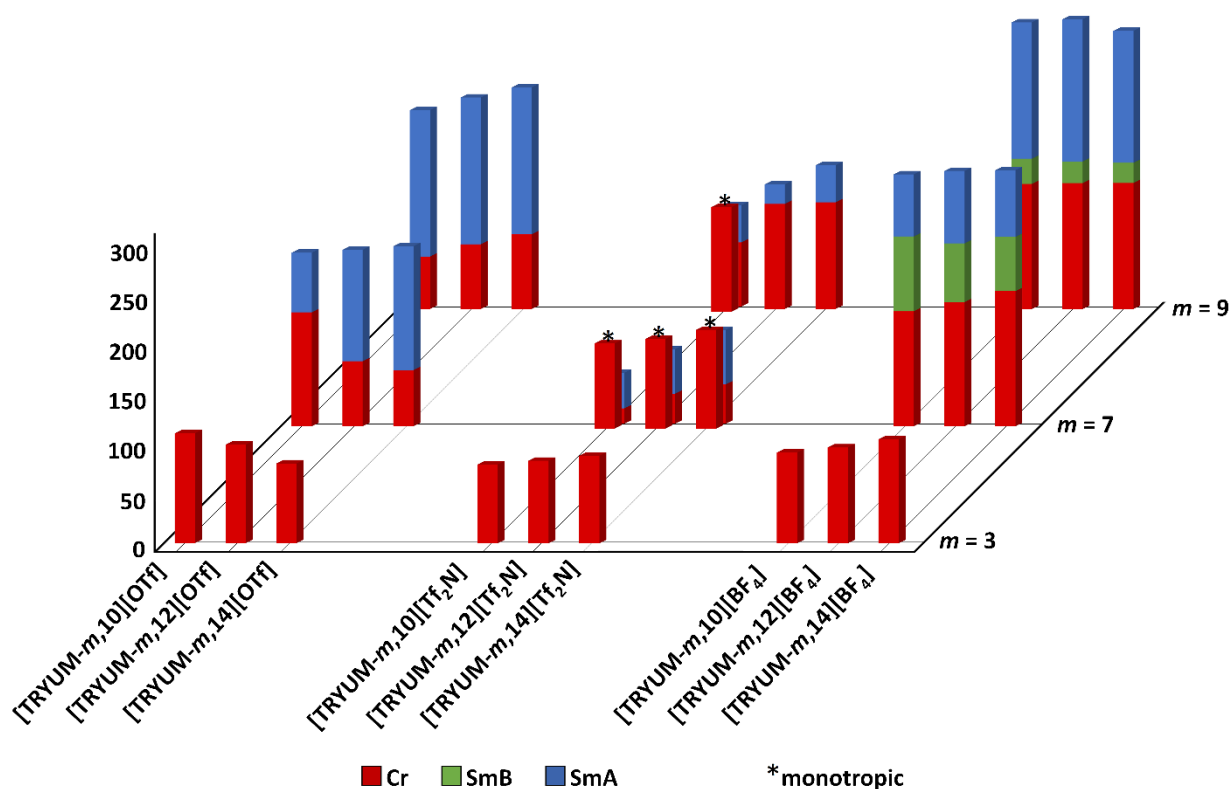


**Figure 37.** 3D Bar Chart of transition temperatures of the triazolium salts grouped by perfluoroalkyl-chain and anion.

The entire set of the 27 compounds studied allows correlation of the phase behaviour with the structural features of the salts, particularly concerning the length of perfluoroalkyl-chain, the length of the alkyl-chain and the anion. Other features affected by the perfluoroalkyl-chain length are mesophase range and stability, which are wider for longer perfluoroalkyl-chains, and as expected, the Cr-LC transition temperature (melting) are higher, since a longer perfluoroalkyl-chain reinforces lattice stability. This is clearly visible in Figure 37, a 3D histogram which highlights the effect of the perfluoroalkyl-chain length on the thermal behaviour of the triazolium salts.

### 3.3.1 Thermal behaviour

In the past, the thermal behaviour and LC properties of asymmetric 1,2,3-triazolium salts has been studied by Stappert and Mudring.<sup>68,70</sup> For many of those salts, they report SmA and SmC phases with an increase of the melting point- and clearing point-temperatures along the increasing alkyl-chain length. A break point was observed in the increase of the transition temperatures in Stappert and Mudring's salts, where a decrease in phase transition temperatures was found at longer chain lengths (14 carbons). They also reported on the influence of the anion on the ability of triazolium ILs to form mesophases.<sup>68,69</sup> The articles describe a strong promotion of LC properties with different anions, especially in LC complexity (*i.e.* replacing halides with [BF<sub>4</sub>]<sup>-</sup>). The use of the bistriflimide anion always led to transitions shifted to lower temperatures and in most of the cases no LC behaviour was observed

in this triazolium salts. The same observation can be made also in LC 1-alkyl-3-methylimidazolium salts.<sup>98</sup>

Both for ionic and non-ionic fluorinated compounds, the perfluoroalkyl- or polyfluoroalkyl-chain length is strictly related with the forming and stability of the thermotropic LC behaviour, where the fluorinated moieties are usually involved with a micro-segregation in smectic-like phases.<sup>10,45,63</sup> Not long enough fluoroalkyl chain, such as perfluoropropyl chain<sup>62</sup> usually preclude a mesogenic behaviour.

Perhaps unexpectedly for ionic compounds of the present work, the phase behaviour was dominated by the observation of the SmA phase, which was the only one observed for the [OTf]<sup>-</sup> and [Tf<sub>2</sub>N]<sup>-</sup> salts, with the mesomorphic tetrafluoroborates also showing a SmB phase below the SmA. Figure 38 shows some representative POM textures for observed mesophases obtained by heating and cooling the compounds and it can be seen that SmA phases were readily identified by their focal conic fan texture formed from the coalescence of bâtonnets.<sup>77</sup> The SmB phase was then identified by the appearance of striations across the back of the fans.

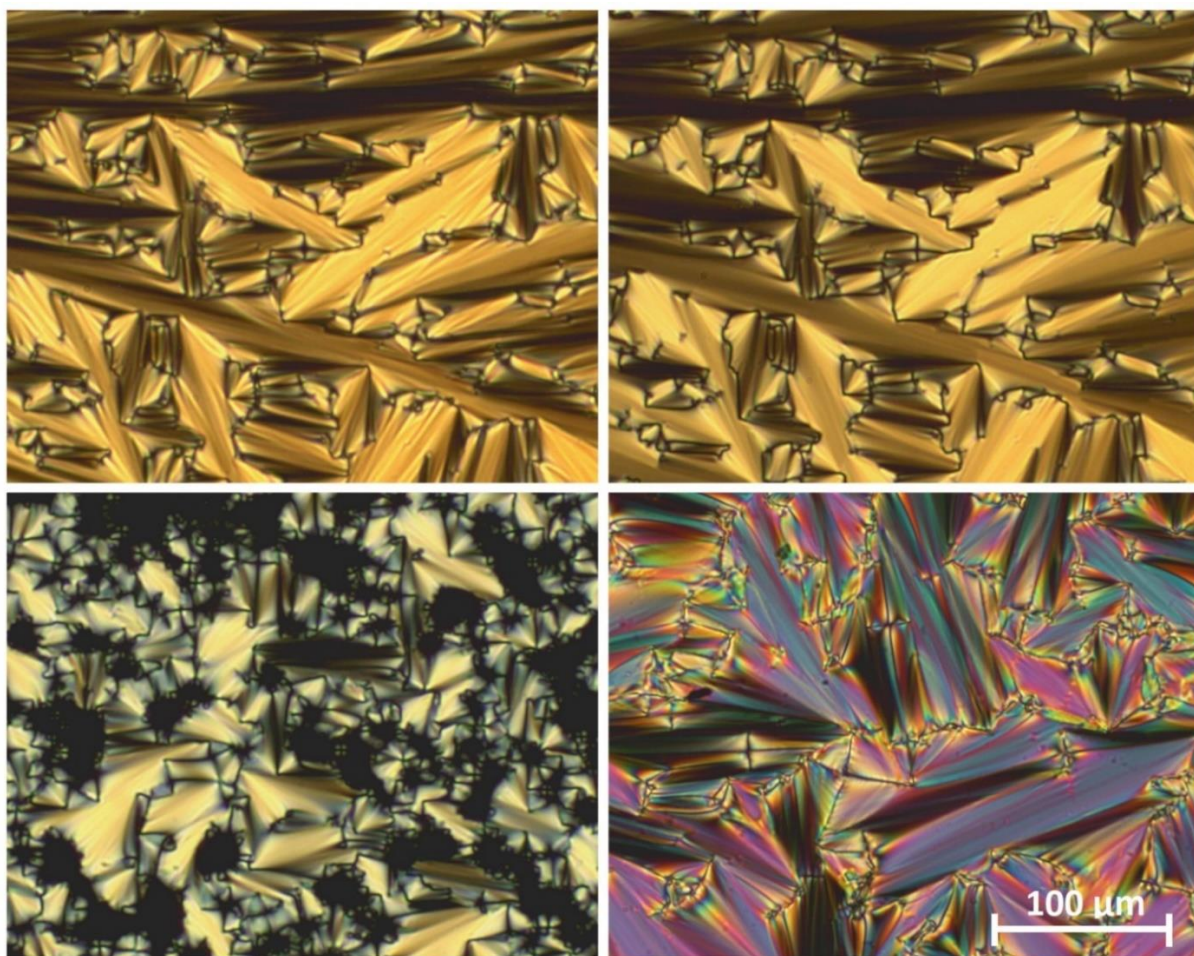


**Figure 38.** Microphotographs taken on cooling from the isotropic liquid with 100x as magnification. On top, compound [TRYUM-7,10][BF<sub>4</sub>] at 152.5°C in SmB (left) and the same sample at 183.3°C in SmA phase (right). On bottom, compound [TRYUM-7,10][Tf<sub>2</sub>N] at 49.4°C in SmA phase (left) and compound [TRYUM-7,10][OTf] at 160.1°C in SmA phase (right).

The texture of the SmA phases showed good focal conic defects and large optically isotropic zones (*e.g.* in bottom-left corner of Figure 38), so the salts were re-heated just above the clearing point and the melting in to isotropic liquid was observed without crossed polariser, in corresponding of the dark zones. This confirms the presence of dark zones with homeotropic alignment, which can be observed in SmA phases but not in the similar SmC phase.<sup>24</sup> Other picture of POM textures for observed mesophases can be viewed in Appendix B.

Looking at the effect of the structural variables, it is first of note that none of the salts with a perfluoropropyl-chain was liquid-crystalline and so the following discussion will concentrate on the remaining materials. The other point of note is that all of the bis(triflimide) salts showed a SmA phase, which was monotropic in most cases but enantiotropic in two.

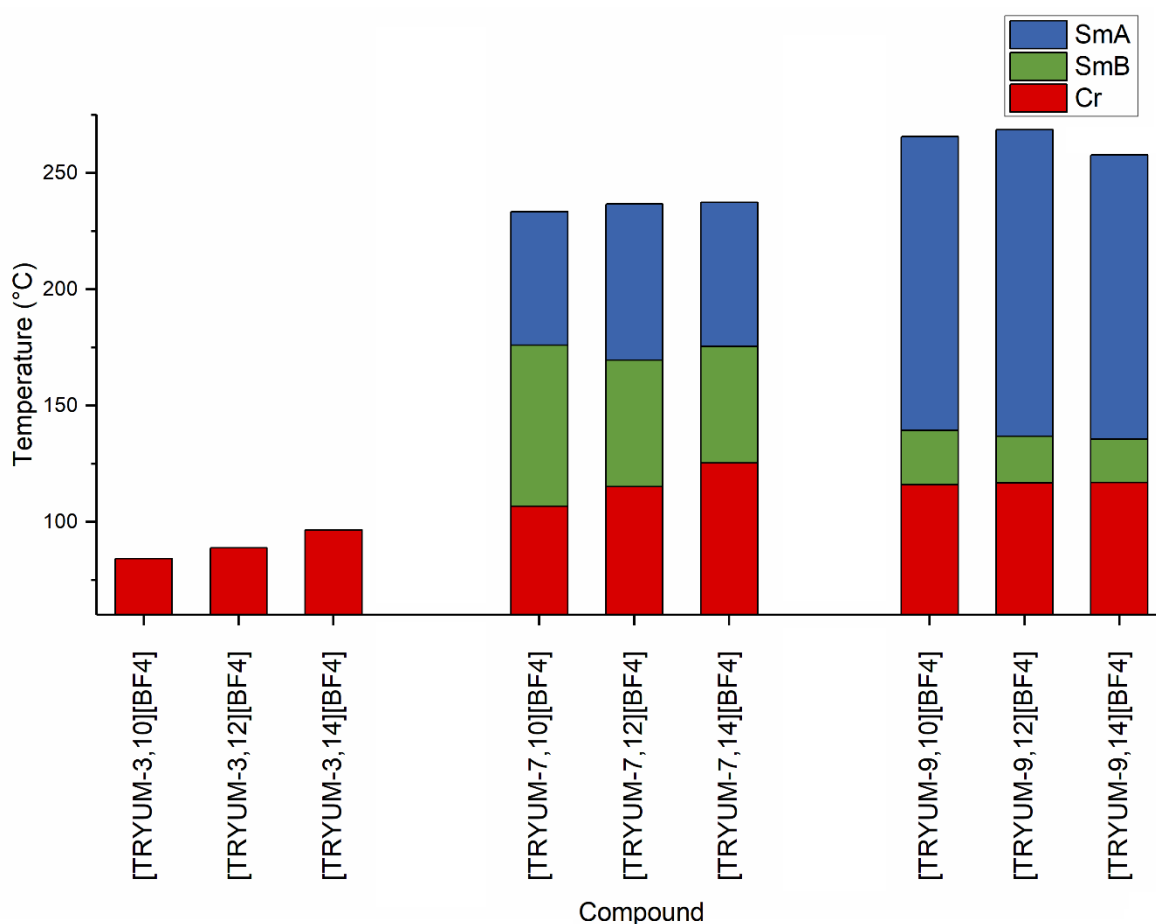


**Figure 39.** Bar chart of transition temperatures of the triazolium tetrafluoroborates grouped by perfluoroalkyl-chain.

Concentrating first on the  $[BF_4]^-$  salts, it is noticeable that the compounds containing a  $C_9F_{19}$ -chain show the most stable SmA phases, being some 25-30 °C more stable than those with a  $C_7F_{15}$ -chain (Figure 39). There is little effect of the alkyl chain length. However, in sharp contrast, the SmB phase is much less stable with the  $C_9F_{19}$ -chain and so, with broadly comparable melting points, the SmB range



is narrower where there is a C<sub>9</sub>F<sub>19</sub>-chain (ca 20 °C) compared with ca 60 °C with the C<sub>7</sub>F<sub>15</sub>-chain. In general terms, the transition temperatures are relatively insensitive to the alkyl chain length where there is a C<sub>9</sub>F<sub>19</sub>-chain and this is also true for the SmB-SmA and SmA-Iso transition temperatures in the presence of a C<sub>7</sub>F<sub>15</sub>-chain. However, for the C<sub>3</sub>F<sub>7</sub>- and the C<sub>7</sub>F<sub>15</sub>-chains, the stability of the crystal phase increases with increasing alkyl chain length.

In parallel, the [Tf<sub>2</sub>N]<sup>-</sup> salts show an increasing stability of the SmA phases with increasing perfluoroalkyl- and alkyl-chain length. Indeed, the SmA phase stability increases much more quickly than the crystal phase stability so that while all salts with a C<sub>7</sub>F<sub>15</sub> chain show a monotropic phase, two of those with a C<sub>9</sub>F<sub>19</sub> chain are enantiotropic.

Lastly, the [OTf]<sup>-</sup> salts keep the increasing trend of the SmA phase stability with both increasing perfluoroalkyl- and alkyl-chain length. Thus, the SmA phase range increases with alkyl-chain length where there is a C<sub>9</sub>F<sub>19</sub>-chain while where there is a C<sub>7</sub>F<sub>15</sub>-chain, the upward trend is less pronounced (Figure 41). This time, for the C<sub>3</sub>F<sub>7</sub>- and the C<sub>7</sub>F<sub>15</sub>-chains, the stability of the crystal phase decreases with increasing alkyl chain length. This decreasing trend turns to an increasing for the C<sub>9</sub>F<sub>19</sub>-chain.

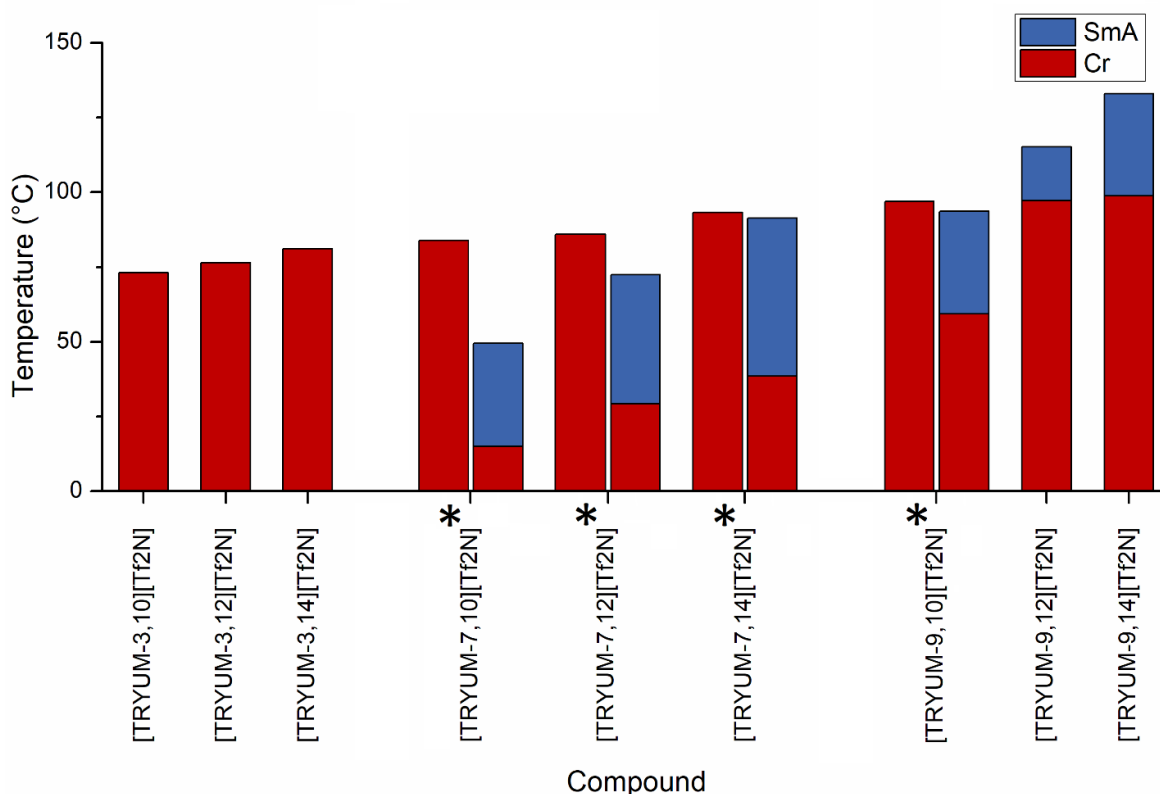


**Figure 40.** Bar chart of transition temperatures of the triazolium bis(triflimide)s grouped by perfluoroalkyl-chain. For monotropic compounds (\*) both the heating and cooling segments are shown.

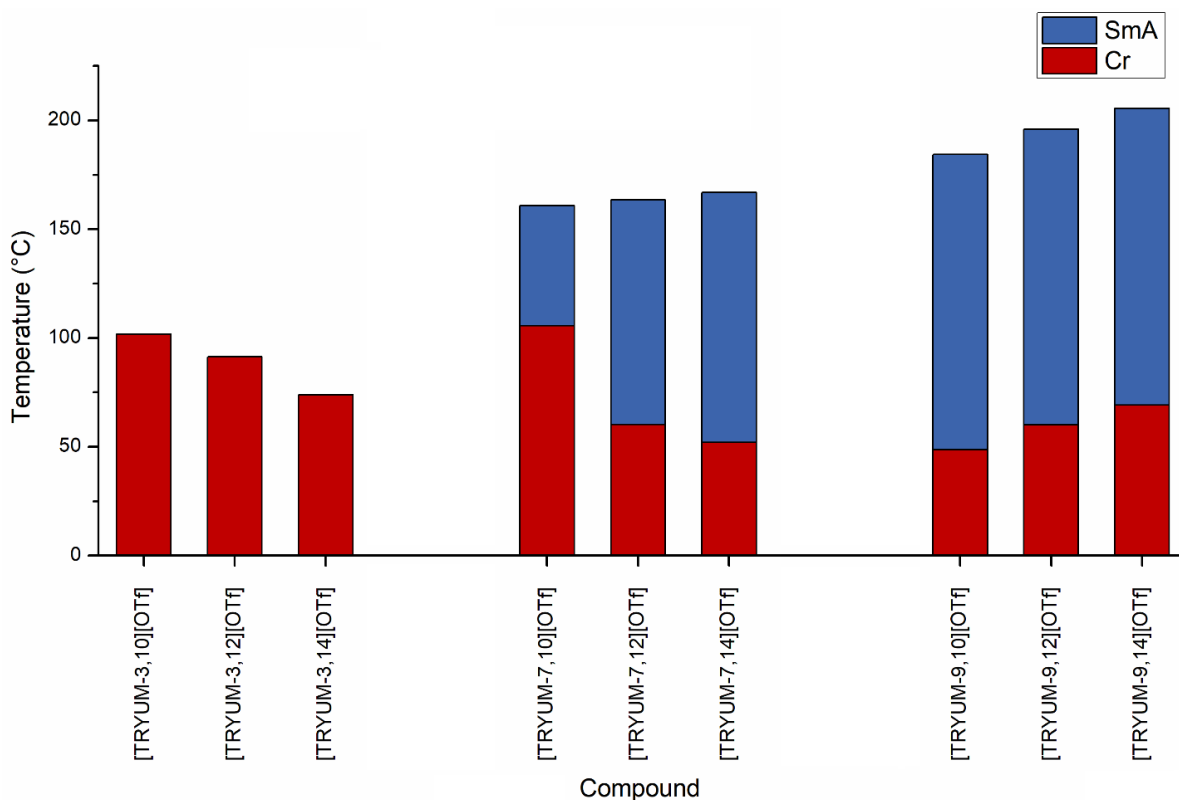


**Figure 41.** Bar chart of transition temperatures of the triazolium triflates grouped by perfluoroalkyl-chain.

### 3.3.2 DSC analysis

For the sake of clarity, representative DSC traces analyses and relative description are illustrated and compared grouping the triazolium salts with same anion and perfluoroalkyl-chain. This way, the effect of the alkyl-chain is highlighted in single DSC plot, while the effect of the anion and perfluoroalkyl-chain are provided comparing different DSC plots.

Analysing the 5-(4-(alkoxy)phenyl)-1,4-dimethyl-3-(perfluoroalkyl)-1,2,4-triazol-4-ium triflates with different alkyl-chains (decyl, **[TRYUM-*m*,10][OTf]**; dodecyl, **[TRYUM-*m*,12][OTf]**; tetradecyl, **[TRYUM-*m*,14][OTf]**) just a phase transition (melting to isotropic liquid phase) has been observed in the DSC traces for compounds with the shortest perfluoroalkyl-chain, while two phase transitions can be observed for the other triflates. Figure 42 and Figure 43 shows the DSC-traces of the second heating and first cooling cycles for all six triflates with longer perfluoroalkyl-chain. Temperature-dependent POM identifies the first transition to be the flow point (Cr→SmA) and the second one belongs to the clearing point (SmA→Iso). The cooling cycles reveal that two thermal events might overlap strongly. In addition, the DSC traces of compound **[TRYUM-7,12][OTf]**, **[TRYUM-9,12][OTf]** and **[TRYUM-9,14][OTf]** show additional thermal events between 20 and 70 °C, which can be attributed to meso-glass phase transitions.



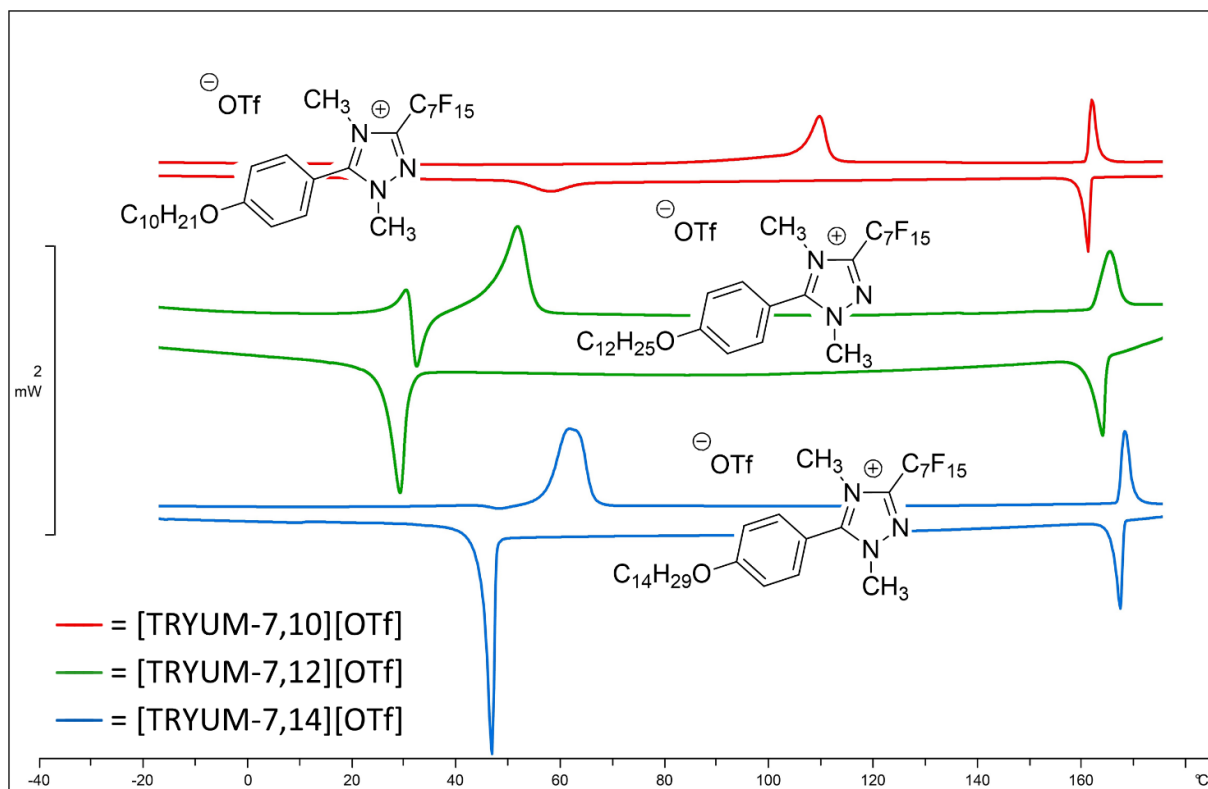


**Figure 42.** DSC traces of **[TRYUM-7,*n*][OTf]**. Traces show the 2<sup>nd</sup> heating and the 1<sup>st</sup> cooling cycles.

For the triflates an increase in the LC temperature range with the increasing chain length is observed, with an exception for compounds **[TRYUM-7,12][OTf]** and **[TRYUM-9,12][OTf]**, whose SmA phase ranges are respectively wider than compounds **[TRYUM-7,14][OTf]** and **[TRYUM-9,14][OTf]**. Compound **[TRYUM-7,10][OTf]** melts with an endothermic transition to a mesophase at 104 °C, which clears at 161 °C with a slightly smaller endothermic transition. For substance **[TRYUM-7,12][OTf]** and **[TRYUM-7,14][OTf]**, the clearing points lie at the slightly higher temperatures of respectively 165 and 168 °C, while the melting point irregularly decrease to 31 and 47 °C respectively. The roughly same regular increase of clearing points (180, 191 and 203 °C) and irregular decrease of melting points (37, 30 and 47 °C) is observed for **[TRYUM-9,*n*][OTf]**.

The thermal behaviour of the bis(triflimide)s salts is different from the triflates, which is expected considering the different size of the anion. Nevertheless, the SmA phase formation is surprisingly kept by these salts, a monotropic behaviour is observed for most of them (Figure 44 and Figure 45). For these compounds, the temperature dependent POM identifies the first transition on cooling to be the clearing point ( $L_{150} \rightarrow \text{SmA}$ ) and the second one consists of the crystallisation point ( $\text{SmA} \rightarrow \text{Cr}$ ). As expected from these salts the mesophase behaviour is less stable and within the mesophase range, without a constant cooling, crystallisations can be suddenly observed.

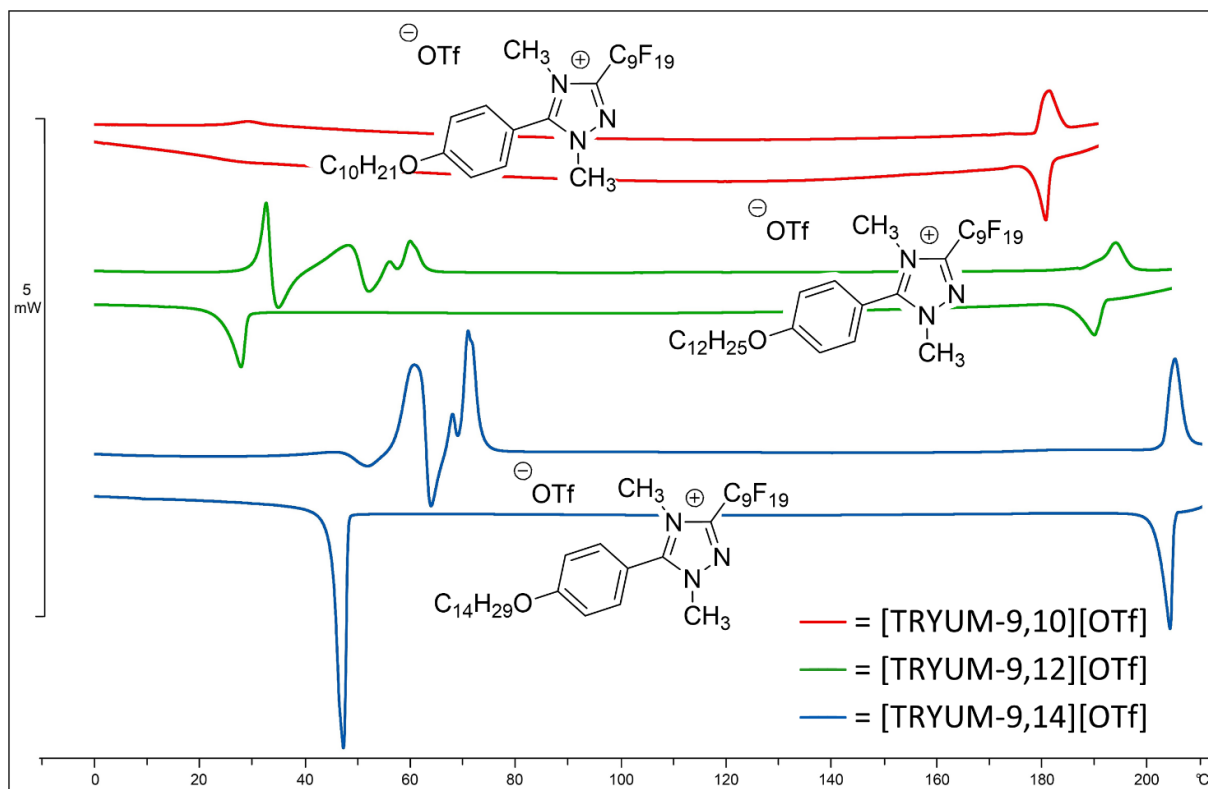


**Figure 43.** DSC traces of **[TRYUM-9,*n*][OTf]**. Traces show the 2<sup>nd</sup> heating and the 1<sup>st</sup> cooling cycles.

Compounds **[TRYUM-3,*n*][Tf<sub>2</sub>N]**, melt directly into isotropic liquid at 73, 77, 81 °C respectively and don't show a LC behaviour at all. Compounds **[TRYUM-7,*n*][Tf<sub>2</sub>N]** and **[TRYUM-9,10][Tf<sub>2</sub>N]** melt directly in to isotropic liquid with an endothermic transition at 84, 86, 92 and 97 °C respectively and clear on cooling in to a SmA phase at 50, 73, 90 and 94 °C respectively with much smaller exothermic transitions. Compounds **[TRYUM-9,12][Tf<sub>2</sub>N]** and **[TRYUM-9,14][Tf<sub>2</sub>N]** firstly melt in to SmA with smaller endothermic transitions at about 98-99 °C and they secondly clear to isotropic liquid phase at 116 and 133 °C respectively (Figure 45). For substance **[TRYUM-7,10][Tf<sub>2</sub>N]** crystallisation points lies on re-heating at -4 °C, whilst the crystallisation point of substances **[TRYUM-7,12][Tf<sub>2</sub>N]**, **[TRYUM-7,14][Tf<sub>2</sub>N]** and **[TRYUM-9,*n*][Tf<sub>2</sub>N]** appear on cooling at 29, 38, 58, 59 and 60 °C respectively (Figure 44 and Figure 45).

Overall, the increasing length of the alkyl-chain gives to the bis(triflimide)s system an always bigger stability, until it reaches an enantiotropic behaviour with the compounds **[TRYUM-9,12][Tf<sub>2</sub>N]** and **[TRYUM-9,14][Tf<sub>2</sub>N]**.

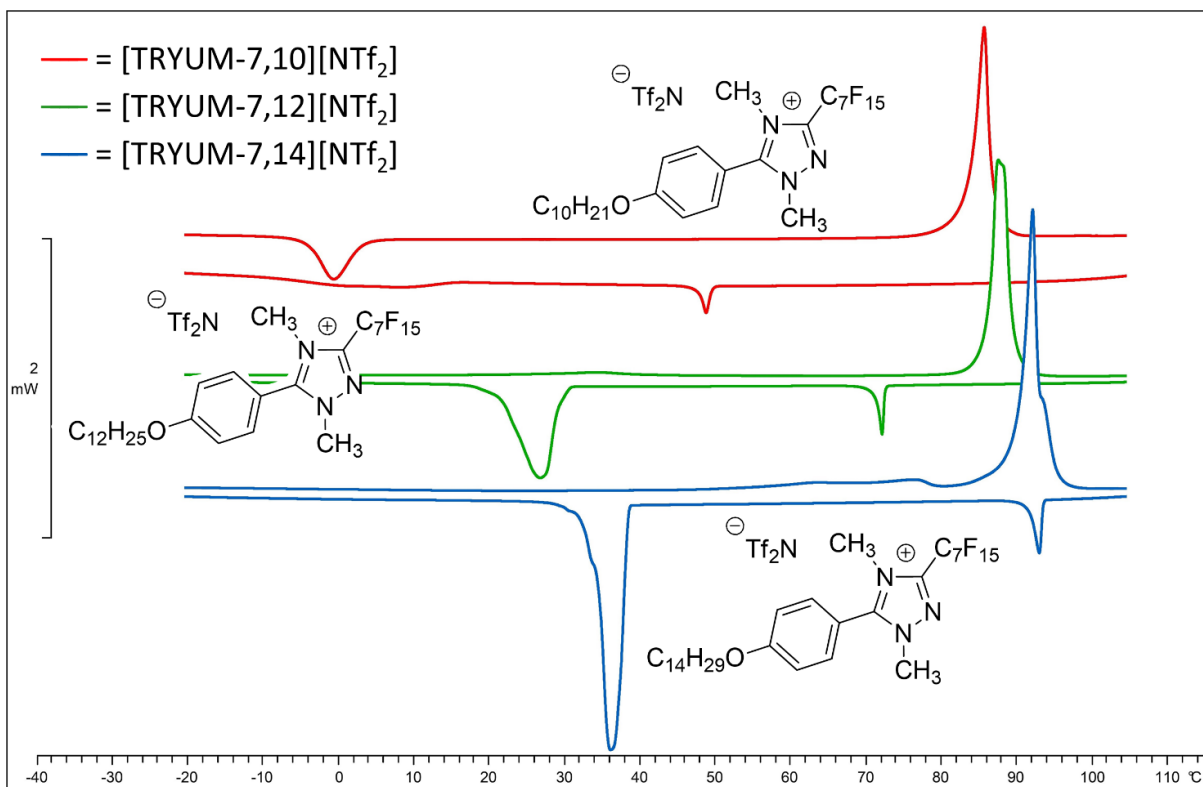


Figure 44. DSC traces of [TRYUM-7,*n*][Tf<sub>2</sub>N]. Traces show the 2<sup>nd</sup> heating and the 1<sup>st</sup> cooling cycles.

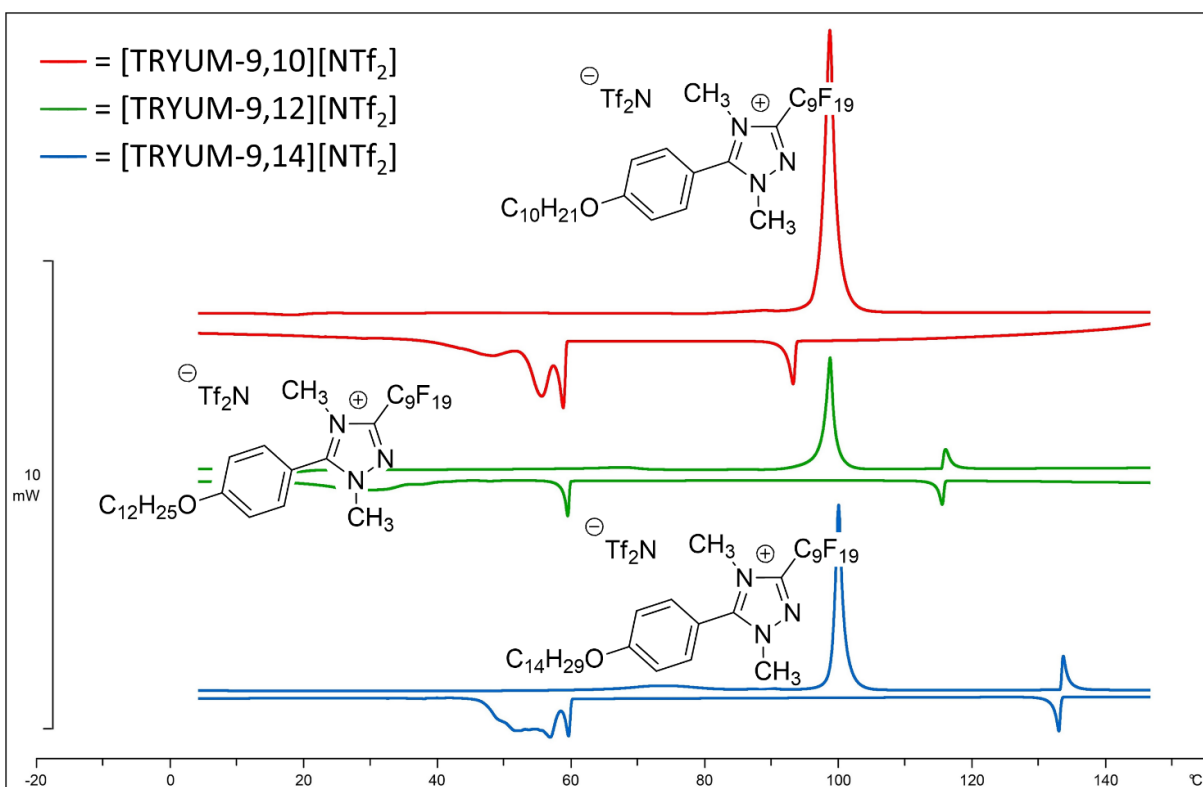
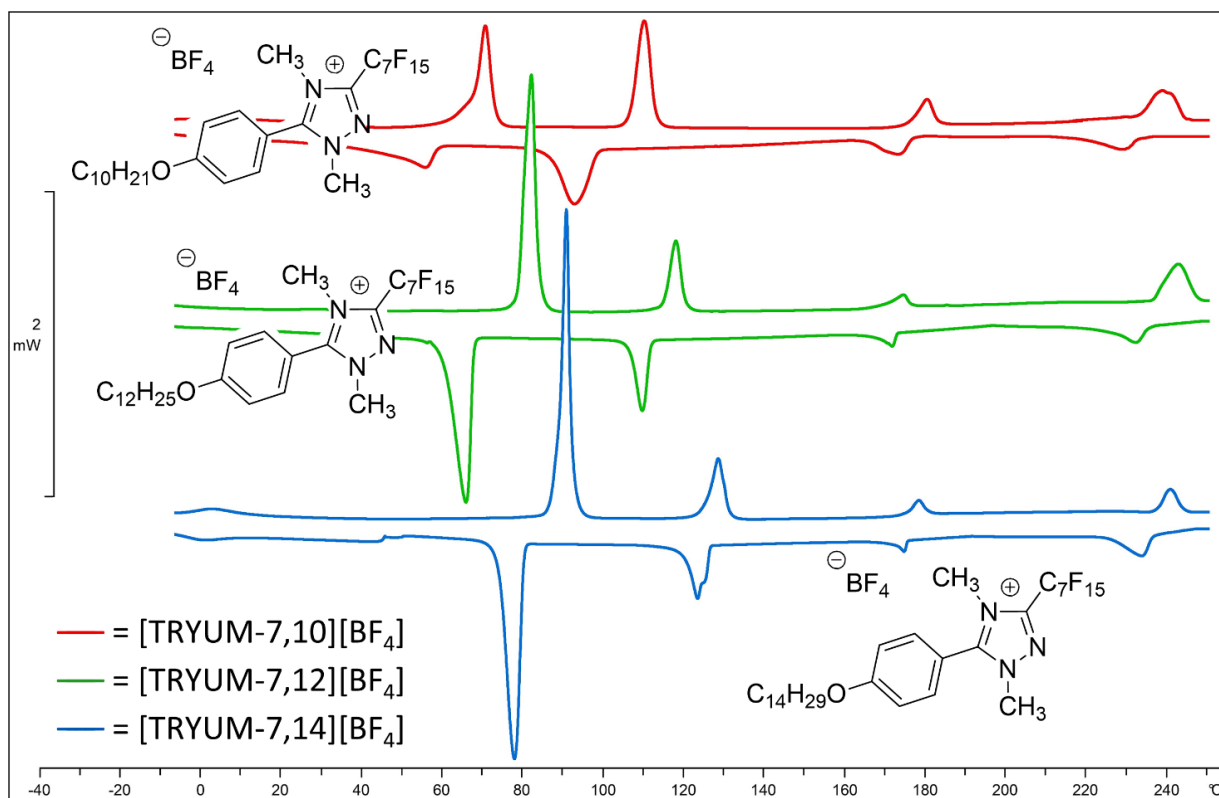


Figure 45. DSC traces of [TRYUM-9,*n*][Tf<sub>2</sub>N]. Traces show the 2<sup>nd</sup> heating and the 1<sup>st</sup> cooling cycles.

In contrast to the triflates and bis(triflimide)s, the analogous tetrafluoroborates salts [TRYUM-3,*n*][BF<sub>4</sub>], [TRYUM-7,*n*][BF<sub>4</sub>] and [TRYUM-9,*n*][BF<sub>4</sub>] exhibit a more complex phase behaviour (Figure

46 and Figure 47), where the thermal changes at lower temperature ( $T < 128$  °C) are due to a solid-solid phase transition. Compounds **[TRYUM-3,*n*][BF<sub>4</sub>]** melt directly in to isotropic liquid and do not show any mesophase. Upon heating, compounds **[TRYUM-7,*n*][BF<sub>4</sub>]** and **[TRYUM-9,*n*][BF<sub>4</sub>]** adopt a highly ordered mesophase (SmB) at about 107, 115 and 125 °C for [BF<sub>4</sub>]<sup>-</sup> salts with C<sub>7</sub>F<sub>15</sub> chain, as well as at around 117°C for [BF<sub>4</sub>]<sup>-</sup> salts with C<sub>9</sub>F<sub>19</sub> chain. The SmB phase has been characterised by POM (*e.g.* in Figure 38, top-left) and SAXS (see chapter 3.4). Compounds **[TRYUM-7,*n*][BF<sub>4</sub>]** show a transition to a SmA phase occurs at 176, 170 and 176 °C respectively (as confirmed by SAXS and POM, see below). For compounds **[TRYUM-9,*n*][BF<sub>4</sub>]** the transition to SmB phases lies at around the same temperature (117°C), whilst the transition to SmA phases lies at decreasing temperature (139, 137 and 135 °C) and this makes wider the range for SmA phases and smaller for SmB ones. All these transitions are reversible and reappear during cooling, albeit at slightly lower temperatures. Clearing points to isotropic liquid appear at very high temperatures roughly with decompositions, which interfere with the analys of these final transitions. In addition, the DSC trace of compounds **[TRYUM-7,14][BF<sub>4</sub>]** and **[TRYUM-9,14][BF<sub>4</sub>]** show one additional thermal event at lower temperatures, which can be attributed to a further solid-solid phase transition.



**Figure 46.** DSC traces of **[TRYUM-7,*n*][BF<sub>4</sub>]**. Traces show the 2<sup>nd</sup> heating and the 1<sup>st</sup> cooling cycles.

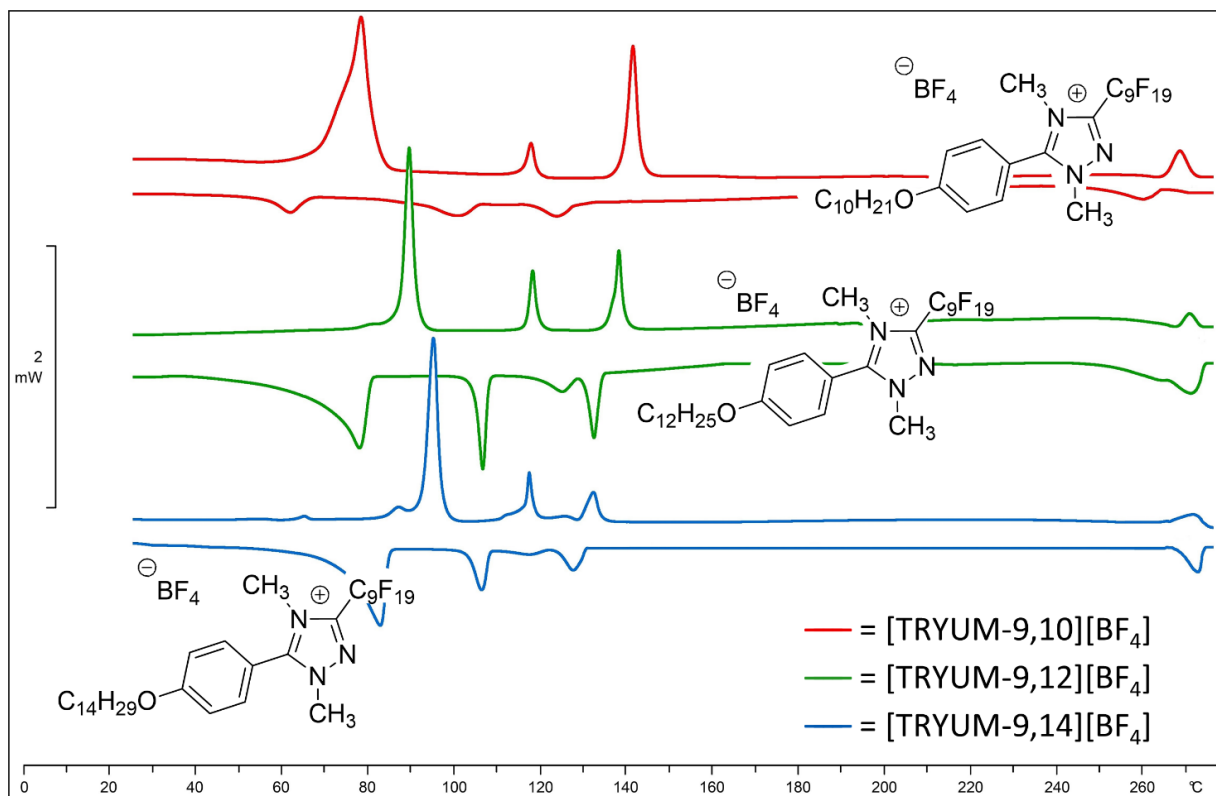


Figure 47. DSC traces of [TRYUM-9,*n*][BF<sub>4</sub>]. Traces show the 2<sup>nd</sup> heating and the 1<sup>st</sup> cooling cycles.

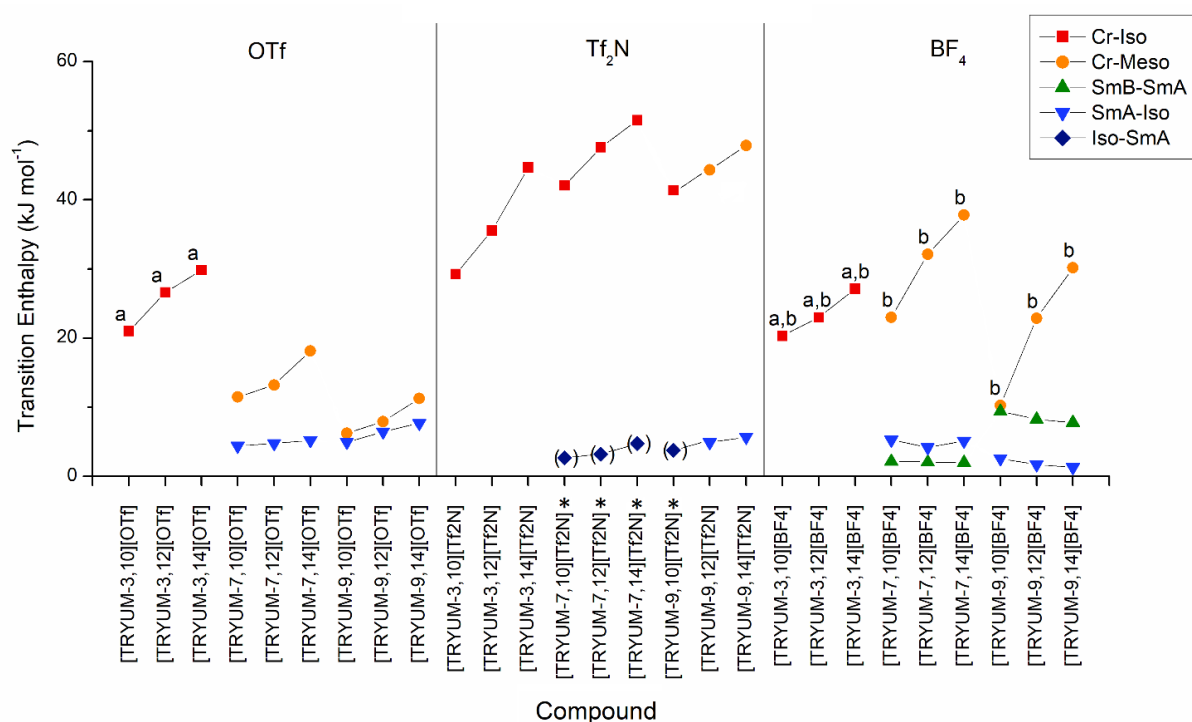


Figure 48. Transition enthalpy of the triazolium salts grouped for the anion and sub-grouped for the perfluoroalkyl-chain. For the monotropic compounds (\*), the graph shows the enthalpy absolute term of the transition from the isotropic to SmA phase and these values are reported by points in brackets. <sup>a</sup> the value refers to the first heating. <sup>b</sup> the value refers to the enthalpy sum between the transition identified as melting point and the previous event.

Figure 48 shows the transition enthalpy of the triazolium salts and highlight the correlation between the structure and this thermodynamic parameter. Generally, for each per fluorocarbon chain length, there is a clear progression in enthalpy change on melting and this is independent on whether it melts to Iso or to SmA. This implies a significant role for the chain length in all of this.

For [OTf]<sup>-</sup> and [BF<sub>4</sub>]<sup>-</sup> with C<sub>3</sub>F<sub>7</sub>-chain, very low Cr-Iso enthalpies are recorded during the 2<sup>nd</sup> heating (between 0.3 and 10 kJ mol<sup>-1</sup>). Since melting enthalpies should be very much greater, it's possible that on cooling from the melt an alternative/metastable crystal form is obtained and so it may well not be correct to express this as Cr-Iso. Furthermore, with often a large enthalpy associated with it, crystallisation can have significant kinetic factors (i.e. often supercooling). For these reasons for these compounds Cr-Iso enthalpies refer to the 1<sup>st</sup> heating and they have been marked with 'a'.

A similar issue, occur to all the [BF<sub>4</sub>]<sup>-</sup> salts where melting enthalpy is particularly low. This could be due to a first melting into a crystal smectic phase (Cr'-Cr) and so the following transition to the SmB phase (or to Iso-phase where there is C<sub>3</sub>F<sub>7</sub>-chain) does not truly represent the actual melting event. For these reasons, the melting enthalpy values of the [BF<sub>4</sub>]<sup>-</sup> salts refer to the sum between the Cr'-Cr and Cr-SmB (or Cr'-Iso where there is C<sub>3</sub>F<sub>7</sub>-chain) enthalpies and they have been marked with 'b'.

For the [OTf]<sup>-</sup> salts, the transition enthalpies increase with alkyl-chain length, but visibly decrease with the perfluoroalkyl-chains lengths. Transition enthalpy SmA-Iso are always smaller than relative melting enthalpy with values between about 5 and 10 kJ mol<sup>-1</sup> and it is almost invariant where there is a C<sub>7</sub>F<sub>15</sub>-chain.

The [Tf<sub>2</sub>N]<sup>-</sup> salts show the highest melting transition enthalpies with values between about 30 and 50 kJ mol<sup>-1</sup>. For monotropic compounds, the absolute terms of the transition enthalpies Iso-SmA always increase with the perfluoroalkyl-chains lengths. They seem to be in line with the transition enthalpy SmA-Iso of the enantiotropic compounds and they all are generally much smaller than relative melting enthalpy.

The melting enthalpies of the [BF<sub>4</sub>]<sup>-</sup> salts increase with alkyl-chain length. The transition enthalpy SmB-SmA and SmA-Iso are invariant and generally smaller than the respective melting enthalpy with an exception for **[TRYUM-9,10][BF<sub>4</sub>]**, where the SmB-SmA enthalpy show value similar to the respective melting enthalpy.

### 3.3.3 Comparison between the thermal behaviour of pure [TRYUM-7,12][OTf] and the mixture with [EtTRYUM-7,12][OTf]

Chapter 3.1.3 report about a synthesis methodology where [TRYUM-7,12][OTf] is obtained with an ethylated sub-product as impurity. A pure fraction of [TRYUM-7,12][OTf] was thermally analysed and compared with the fraction containing the ethylated impurity (9%), in order to study the properties and the difference of behaviour between the two fractions. A comparison of DSC traces shows the mixture keeps the main thermal behaviour of the pure methylated compound, with slightly differences in the transition temperatures, but with consistent change in thermal parameter of transitions (Figure 49). As discussed in the previous paragraph, the pure methylated compound show melting and clearing point point at 47 and 165 °C, while the mixture shows transition temperatures with values 42 and 15 °C lower than the respective transitions of the pure methylated compound.

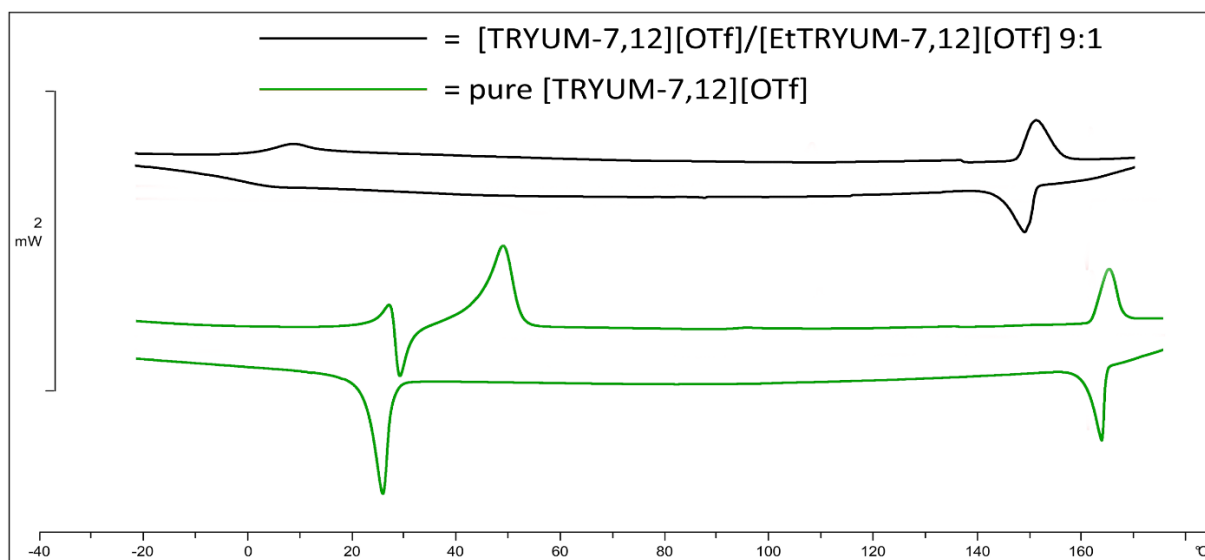


**Figure 49.** DSC traces of pure [TRYUM-7,12][OTf] and [TRYUM-7,12][OTf]/ [EtTRYUM-7,12][OTf] (9:1). Traces show the 2<sup>nd</sup> heating and the 1<sup>st</sup> cooling cycles.

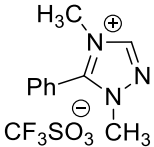
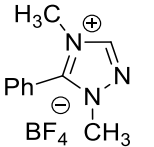
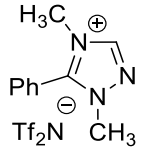
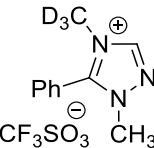
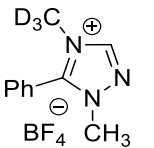
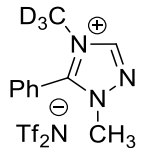
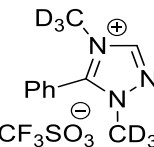
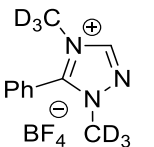
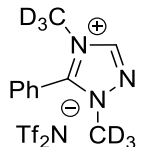
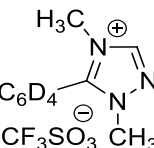
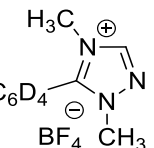
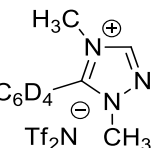
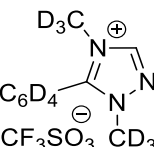
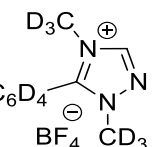
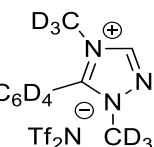
The comparison suggests the ethylated impurity affects sensibly the thermal behaviour of the triazolium salts, which were subsequently synthesised in toluene (or DCM), avoiding the formation of other ethylated sub-products.

### 3.4 Small-angle X-Ray and Neutrons Scattering

All the compounds, including ones not showing any mesophase or those ones showing only a monotropic mesophase, were studied by X-ray scattering on powder/liquid samples and representative plots are illustrated in Appendix C. Almost all compounds display a similar SAXS pattern in the mesophases with one sharp peak between 0.75 and 1.1° corresponding to (001), which relates to the distance of an interdigitated bi-layered lamella, as well as in most cases smaller second order (002), third order (003) and other smaller order peaks. Just one exception is observed in [TRYUM-7,*n*][BF<sub>4</sub>], where the first order reflection lies between 1.7 and 1.9°.

All the triazolium salts were first analysed by SAXS and later the entire set of salts, except for all the triazolium with C<sub>12</sub>H<sub>25</sub>-chain, was re-synthesised on a larger scale in order to perform SANS measurements. After a careful analysis, compounds were scaled-up with no deuteration, which wasn't required to have a sufficient contrast in SLD between the aliphatic, fluorinated and polar parts of the salts. SLDs of the triazolium salts moieties were preliminary estimated (Table 5) using the neutron scattering calculator of the National Institute of Standard and Technology (NIST). The calculations suggest average values of approximately  $3.7 \times 10^{-6} \text{ \AA}^{-2}$  for the perfluorinated-chains,  $-0.2 \times 10^{-6} \text{ \AA}^{-2}$  for the alkyl-chain and  $2.7 \times 10^{-6} \text{ \AA}^{-2}$  for the ionic core (triazolium plus phenyl ring plus [OTf]<sup>-</sup>, [Tf<sub>2</sub>N]<sup>-</sup>, or [BF<sub>4</sub>]<sup>-</sup>). This gives a good contrast between the alkyl-chain and the perfluorocarbon-chain, but little contrast between the core and the perfluorocarbon chain. Extra contrast could have been developed by adding deuterium to the phenyl ring (C<sub>6</sub>D<sub>4</sub>) and by introducing CD<sub>3</sub> groups into the triazolium ring (average SLD  $\approx 5.5 \times 10^{-6} \text{ \AA}^{-2}$ ). However, with minimal labelling suitable contrast was extracted to enable a sufficiently detailed picture of the spatial arrangement within the isotropic and LC phases without the need for time-consuming and expensive deuteration studies.

**Table 5.** Estimated SLDs values of triazolium salts moieties.

moiety	SLD ( $10^{-6} \text{ \AA}^{-2}$ )	moiety	SLD ( $10^{-6} \text{ \AA}^{-2}$ )	moiety	SLD ( $10^{-6} \text{ \AA}^{-2}$ )
C <sub>10</sub> H <sub>21</sub> O	-0.20	C <sub>12</sub> H <sub>25</sub> O	-0.21	C <sub>14</sub> H <sub>29</sub> O	-0.22
C <sub>3</sub> F <sub>7</sub>	3.87	C <sub>7</sub> F <sub>15</sub>	3.75	C <sub>9</sub> F <sub>19</sub>	3.50
	2.65		2.77		2.67
	3.44		3.74		3.22
	4.21		4.69		3.77
	3.70		4.06		3.41
	5.22		5.93		4.42

SLDs was calculated considering as density the value of the most similar compound known (*e.g.* the density of 1-decanol was used for C<sub>10</sub>H<sub>21</sub>O).



### 3.4.1 Analysis of crystal phases

X-ray scattering of the crystal phases was recorded and compared for all triazolium salts at the same reduced temperature of 0.9 and  $d$ -spacing values have been deduced by Bragg's law from  $2\theta$  values of 001 peaks. Analysis showed that all crystals increase the layer spacing with increasing alkyl and perfluoroalkyl-chain lengths (Figure 50).  $C_3F_7$  perfluoroalkyl-chained compounds regularly increase the layer spacing in the crystal structure with the increasing chain length. This is clearly visible in bis(triflimide)s ([TRYUM-3,10][Tf<sub>2</sub>N]: 28.6 Å, [TRYUM-3,12][Tf<sub>2</sub>N]: 30.5 Å, [TRYUM-3,14][Tf<sub>2</sub>N]: 32.4 Å) and tetrafluoroborates ([TRYUM-3,12][BF<sub>4</sub>]: 27.2 Å, [TRYUM-3,12][BF<sub>4</sub>]: 29.8 Å, [TRYUM-3,14][BF<sub>4</sub>]: 31.6 Å), where compounds with the same cation exhibit very similar scattering patterns. Different behaviour is exhibited by the triflates, which show a smaller and less regular layer spacing ([TRYUM-3,10][OTf]: 17.5 Å, [TRYUM-3,12][OTf]: 17.3 Å, [TRYUM-3,14][OTf]: 19.5 Å). Disorder in the crystal lattice of these compounds could explain a  $d$ -spacing different from the molecular length as discussed in chapter 3.2. None of the salts with  $C_3F_7$  perfluoroalkyl-chain show any LC behaviour and melt directly to isotropic liquids as discussed in chapter 3.3.

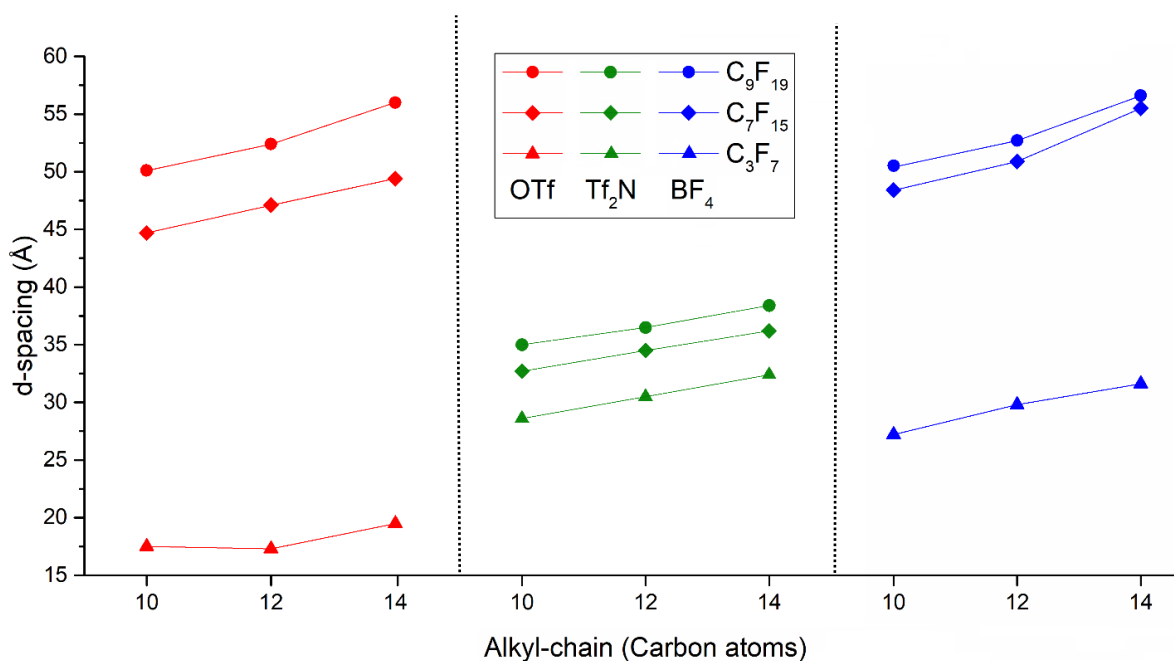


**Figure 50.** Plotting of crystal-phase  $d$ -spacing of triazolium salts at reduced temperatures (0.9) versus alkyl-chain length. Symbols denote different perfluoroalkyl-chain length, while colours denote different anions.

The distance of 32.7 Å in compound [TRYUM-7,10][Tf<sub>2</sub>N] can be identified as the smallest bilayer spacing in the crystal structure of the triazolium salts with  $C_7F_{15}$  as perfluoroalkyl-chain (Figure 50). This distance increases proportionally with the increasing chain length in the other  $C_7F_{15}$  bis(triflimide) salts ([TRYUM-7,10][Tf<sub>2</sub>N]: 32.7 Å, [TRYUM-7,12][Tf<sub>2</sub>N]: 34.5 Å, [TRYUM-7,14][Tf<sub>2</sub>N]: 36.2 Å).  $C_7F_{15}$  perfluoroalkyl-chained compounds with triflate as the anion ([TRYUM-7, $n$ ][OTf]) exhibit a regular increasing of the  $d$ -spacing with the increase of the alkyl-chain length too, but with bigger values

([TRYUM-7,10][OTf]: 44.7 Å, [TRYUM-7,12][OTf]: 47.1 Å, [TRYUM-7,14][OTf]: 49.4 Å). C<sub>7</sub>F<sub>15</sub> perfluoroalkyl-chained compounds with [BF<sub>4</sub>]<sup>-</sup> as anion show crystal pattern with *d*-spacing value similar to [TRYUM-7,*n*][OTf] and with even bigger value ([TRYUM-7,10][BF<sub>4</sub>]: 48.4 Å, [TRYUM-7,12][BF<sub>4</sub>]: 50.9 Å, [TRYUM-7,14][BF<sub>4</sub>]: 55.0 Å). Within the studied triazolium salts, the smaller anions give larger *d*-spacing, which could be counterintuitive, but this phenomenon can be explained by the way the anion affect the cation entities. Indeed, segregation and tilting of cations are strongly affected by anion as see in chapter 3.3 (see also Figure 51).

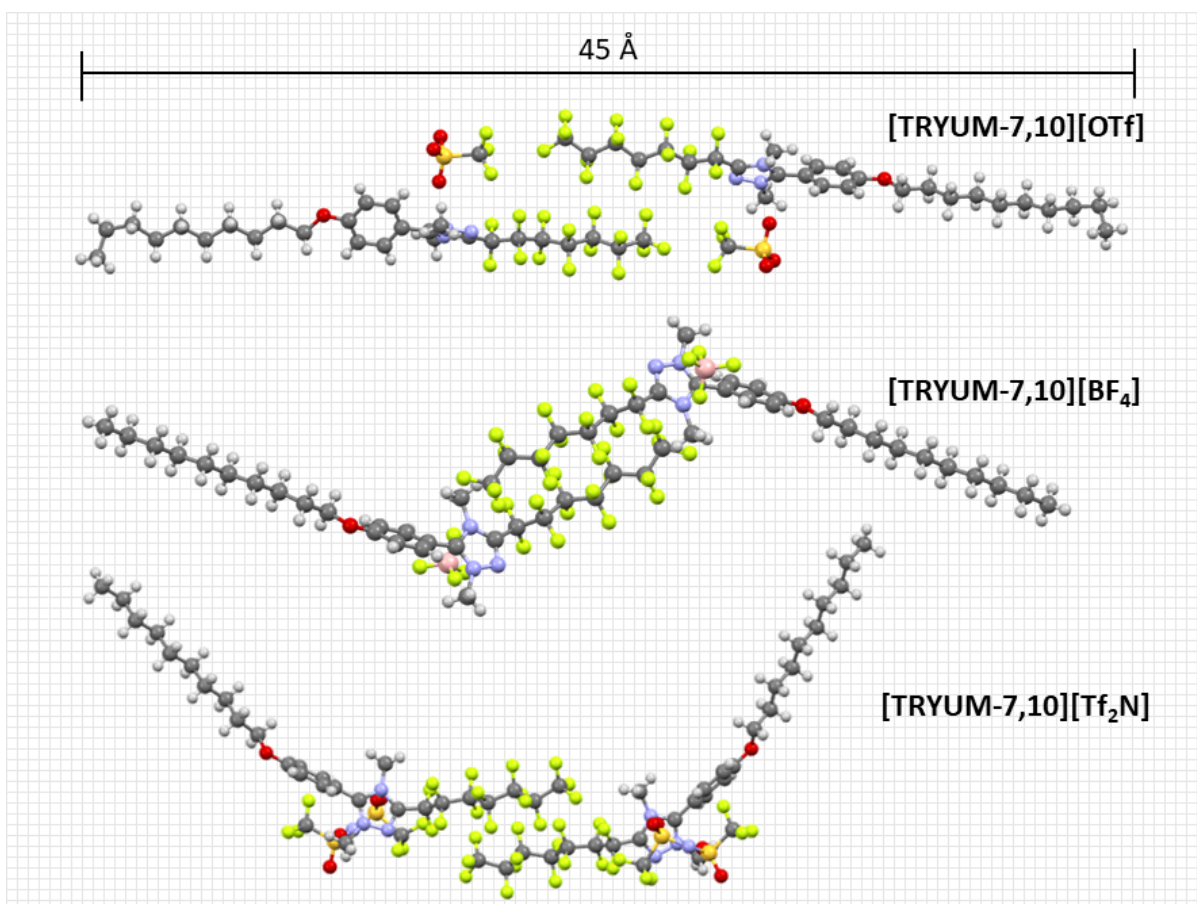


**Figure 51.** Comparison between molecular length in crystal phase of compounds [TRYUM-7,10][OTf] and [TRYUM-7,10][BF<sub>4</sub>] and [TRYUM-7,10][Tf<sub>2</sub>N].

C<sub>9</sub>F<sub>19</sub> perfluoroalkyl-chained compounds show same regular increasing *d*-spacing with the increasing alkyl-chain length in the crystal spacing and with value from 1.4 to 6.6 Å bigger than the respective C<sub>7</sub>F<sub>15</sub> perfluoroalkyl-chained compound (Figure 50). ([TRYUM-9,10][OTf]: 50.1 Å, [TRYUM-9,12][OTf]: 52.4 Å, [TRYUM-9,14][OTf]: 56.0 Å, [TRYUM-9,10][Tf<sub>2</sub>N]: 35.0 Å, [TRYUM-9,12][Tf<sub>2</sub>N]: 36.5 Å, [TRYUM-9,14][Tf<sub>2</sub>N]: 38.4 Å, [TRYUM-9,10][BF<sub>4</sub>]: 50.4 Å, [TRYUM-9,12][BF<sub>4</sub>]: 52.7 Å, [TRYUM-9,14][BF<sub>4</sub>]: 56.6 Å).

An easy comparison of *d*-spacing values either along alkyl chain, perfluoroalkyl-chain and anion is showed in the chart of Figure 50. It's interesting to notice that, both for C<sub>7</sub>F<sub>15</sub> and C<sub>9</sub>F<sub>19</sub> compounds, *d*-

spacing values are always much smaller in compounds with  $[\text{Tf}_2\text{N}]^-$  as anion. Moreover, the increasing of the  $d$ -spacing values from  $\text{C}_7\text{F}_{15}$ - to  $\text{C}_9\text{F}_{19}$ -chain is bigger for compounds with  $[\text{OTf}]^-$  as anion. This could be explained analysing the angles between alkyl and perfluoroalkyl-chains among compound as seen in chapter 3.2.

### 3.4.2 Analysis of mesophases

All mesophases show a classic scattering pattern of smectic phases, e.g. frames of X-ray scattering are reported in Figure 52.

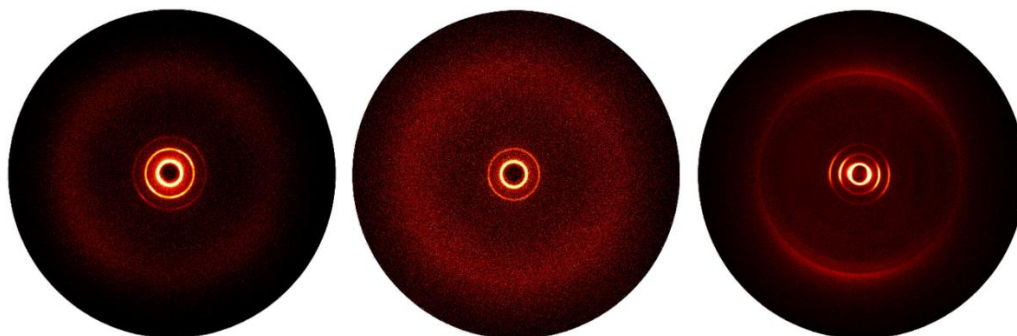


**Figure 52.** SAXS frames with the detector position at 180 mt of compounds **[TRYUM-7,12][OTf]** (left), **[TRYUM-9,12][Tf<sub>2</sub>N]** (middle) and **[TRYUM-9,12][BF<sub>4</sub>]** (right), at 82.7, 108.4 and 178.4 °C respectively.

Table 6 lists the layer spacings calculated by the Bragg's law from peak values from frame recorded in the SmA and SmB phases, using SAXS and SANS. Mesophases have been analysed at the same reduced temperature of 0.9, except for SmA phases of **[TRYUM-7,*n*][BF<sub>4</sub>]** and **[TRYUM-9,*n*][BF<sub>4</sub>]** which were recorded at the reduced temperature of 0.8 in order to avoid sample decomposition due to the high clearing point of these compounds.

**Table 6.** X-Ray, Neutrons and structural data for the mesophases of the triazolium salts.

$d_{\text{meas}}$ (Å)	$hkl$	Intensity	$d_{\text{calc}}$ (Å)	$d_{\text{neutron}}$ (Å)	Parameters
<b>[TRYUM-7,10][OTf]</b>					
36.31	001	M (br)	43.33	35.70	$T = 145 \text{ }^\circ\text{C}$ , SmA $d = 43.3 \text{ } \text{Å}$
22.34	002	S (sh)	21.67	21.97	
15.82	003	M (sh)	14.441	-	
11.22	004	VW (sh)	10.83	-	
5.8	-	VS (br)	$h_{\text{max}}$	-	
<b>[TRYUM-7,12][OTf]</b>					
46.94	001	VS (sh)	47.13	-	$T = 147 \text{ }^\circ\text{C}$ , SmA $d = 47.1 \text{ } \text{Å}$
23.53	002	M (sh)	23.56	-	
15.76	003	VW (sh)	15.71	-	
11.80	004	VW (sh)	11.78	-	
5.8	-	VS (br)	$h_{\text{max}}$	-	
<b>[TRYUM-7,14][OTf]</b>					
48.48	001	VS (sh)	48.67	45.86	$T = 150 \text{ }^\circ\text{C}$ , SmA $d = 48.7 \text{ } \text{Å}$
24.31	002	M (sh)	24.34	23.02	
16.23	003	VW (sh)	16.22	-	
12.23	004	VW (sh)	12.17	-	
5.8	-	VS (br)	$h_{\text{max}}$	-	

<b>[TRYUM-7,10][Tf<sub>2</sub>N]</b>					
39.75	001	VS (sh)	40.05	32.06	<i>T</i> = (45 °C), SmA <i>d</i> = 40.1 Å
19.92	002	M (sh)	20.03	16.28	
13.52	003	VW (sh)	13.35	-	
-	004	VW (sh)	-	-	
5.6	-	VS (br)	<i>h</i> <sub>max</sub>	-	
<b>[TRYUM-7,12][Tf<sub>2</sub>N]</b>					
41.62	001	VS (sh)	41.66	-	<i>T</i> = (66 °C), SmA <i>d</i> = 41.7 Å
20.86	002	M (sh)	20.83	-	
13.88	003	VW (sh)	13.89	-	
5.7	-	VS (br)	<i>h</i> <sub>max</sub>	-	
<b>[TRYUM-7,14][Tf<sub>2</sub>N]</b>					
43.90	001	VS (sh)	43.90	35.50	<i>T</i> = (82 °C), SmA <i>d</i> = 43.90 Å
21.94	002	M (sh)	21.95	17.9	
14.64	003	VW (sh)	14.63	-	
5.8	-	VS (br)	<i>h</i> <sub>max</sub>	-	
<b>[TRYUM-7,10][BF<sub>4</sub>]</b>					
23.60	001	S (sh)	23.73	22.12	<i>T</i> = 158 °C, SmB <i>d</i> = 23.73 Å
11.93	002	VW (sh)	11.87	-	
5.9	-	VS (br)	<i>h</i> <sub>max</sub>	-	
23.79	001	S (sh)	-	22.69	<i>T</i> = 187 °C, SmA <i>d</i> = 23.79 Å
6.1	-	VS (br)	<i>h</i> <sub>max</sub>	-	
<b>[TRYUM-7,12][BF<sub>4</sub>]</b>					
24.58	001	S (sh)	24.61	-	<i>T</i> = 153 °C, SmB <i>d</i> = 24.6 Å
12.35	002	VW (sh)	12.30	-	
8.18	003	VW (sh)	8.20	-	
6.0	-	VS (br)	<i>h</i> <sub>max</sub>	-	
24.86	001	S (sh)	24.90	-	<i>T</i> = 189 °C, SmA <i>d</i> = 24.9 Å
12.42	002	VW (sh)	12.45	-	
8.34	003	VW (sh)	8.30	-	
6.1	-	VS (br)	<i>h</i> <sub>max</sub>	-	
<b>[TRYUM-7,14][BF<sub>4</sub>]</b>					
26.50	001	S (sh)	26.51	49.85	<i>T</i> = 158 °C, SmB <i>d</i> = 26.5 Å
13.26	002	VW (sh)	13.25	24.93	
6.0	-	VS (br)	<i>h</i> <sub>max</sub>	-	
26.85	001	S (sh)	26.86	50.71	<i>T</i> = 190 °C, SmA <i>d</i> = 26.9 Å
13.44	002	VW (sh)	13.43	25.14	
5.9	-	VS (br)	<i>h</i> <sub>max</sub>	-	
<b>[TRYUM-9,10][OTf]</b>					
48.48	001	VS (sh)	48.66	46.69	<i>T</i> = 166 °C, SmA <i>d</i> = 48.7 Å
24.38	002	M (sh)	24.33	23.79	
16.17	003	VW (sh)	16.22	-	
12.23	004	VW (sh)	12.17	-	
5.9	-	VS (br)	<i>h</i> <sub>max</sub>	-	
<b>[TRYUM-9,12][OTf]</b>					
50.42	001	VS (sh)	50.41	-	<i>T</i> = 176 °C, SmA <i>d</i> = 50.4 Å
25.29	002	S (sh)	25.21	-	
16.75	003	VW (sh)	16.80	-	
5.9	-	VS (br)	<i>h</i> <sub>max</sub>	-	

<b>[TRYUM-9,14][OTf]</b>						
54.13	001	VS (sh)	54.42	51.08	$T = 185\text{ }^{\circ}\text{C}$ , SmA $d = 54.4\text{ \AA}$	
27.32	002	S (sh)	27.21	25.44		
18.16	003	VW (sh)	18.14	17.21		
5.9	-	VS (br)	$h_{\text{max}}$	-		
<b>[TRYUM-9,10][Tf<sub>2</sub>N]</b>						
42.63	001	VS (sh)	42.58	34.07	$T = (86)\text{ }^{\circ}\text{C}$ , SmA $d = 42.6\text{ \AA}$	
21.27	002	S (sh)	21.29	17.48		
-	003	S (sh)	-	-		
5.8	-	VS (br)	$h_{\text{max}}$	-		
<b>[TRYUM-9,12][Tf<sub>2</sub>N]</b>						
44.57	001	S (sh)	44.58	-	$T = 104\text{ }^{\circ}\text{C}$ , SmA $d = 44.6\text{ \AA}$	
22.29	002	VW (sh)	22.29	-		
5.8	-	VS (br)	$h_{\text{max}}$	-		
<b>[TRYUM-9,14][Tf<sub>2</sub>N]</b>						
45.96	001	VS (sh)	46.15	45.02	$T = 120\text{ }^{\circ}\text{C}$ , SmA $d = 46.2\text{ \AA}$	
23.10	002	S (sh)	23.08	22.51		
15.43	003	M (sh)	15.38	-		
5.9	-	VS (br)	$h_{\text{max}}$	-		
<b>[TRYUM-9,10][BF<sub>4</sub>]</b>						
51.30	001	VS (sh)	51.36	44.57	$T = 125\text{ }^{\circ}\text{C}$ , SmB $d = 51.4\text{ \AA}$	
25.65	002	S (sh)	25.68	25.21		
17.14	003	M (sh)	17.12	-		
12.80	004	VW (sh)	12.84	-		
10.29	005	VW (sh)	10.27	-		
8.58	006	VW (sh)	8.56	-		
5.9	-	VS (br)	$h_{\text{max}}$	-		
5.7	110	VW (sh)	-	-		
50.71	001	VS (sh)	51.18	44.37		$T = 212\text{ }^{\circ}\text{C}$ , SmA $d = 51.2\text{ \AA}$
25.51	002	VS (sh)	25.59	25.01		
17.04	003	S (sh)	17.06	-		
12.78	004	M (sh)	12.79	-		
10.33	005	VW (sh)	10.24	-		
8.58	006	VW (sh)	8.53	-		
5.9	-	VS (br)	$h_{\text{max}}$	-		
<b>[TRYUM-9,12][BF<sub>4</sub>]</b>						
53.48	001	VS (sh)	53.67	-	$T = 123\text{ }^{\circ}\text{C}$ , SmB $d = 53.7\text{ \AA}$	
26.74	002	S (sh)	26.84	-		
17.90	003	M (sh)	17.89	-		
13.50	004	VW (sh)	13.42	-		
10.76	005	VW (sh)	10.73	-		
8.93	006	VW (sh)	8.95	-		
6.0	-	VS (br)	$h_{\text{max}}$	-		
5.7	110	VW (sh)	-	-		
52.52	001	VS (sh)	52.78	-		$T = 215\text{ }^{\circ}\text{C}$ , SmA $d = 52.8\text{ \AA}$
26.34	002	S (sh)	26.39	-		
17.55	003	M (sh)	17.59	-		
13.24	004	VW (sh)	13.20	-		
10.58	005	VW (sh)	10.56	-		
8.83	006	VW (sh)	8.80	-		
6.0	-	VS (br)	$h_{\text{max}}$	-		

[TRYUM-9,14][ BF <sub>4</sub> ]					
56.20	001	VS (sh)	56.68	56.56	T = 122 °C, SmB d = 56.7 Å
28.28	002	S (sh)	28.34	28.19	
18.86	003	M (sh)	18.89	18.90	
14.22	004	VW (sh)	14.17	-	
11.38	005	VW (sh)	11.34	-	
9.44	006	VW (sh)	9.45	-	
8.14	007	VW (sh)	8.10	-	
5.9	-	VS (br)	<i>h</i> <sub>max</sub>	-	
5.7	110	VW (sh)	-	-	
55.15	001	VS (sh)	55.32	54.81	T = 206 °C, SmA d = 55.3 Å
27.66	002	S (sh)	27.66	27.49	
18.46	003	M (sh)	18.44	18.58	
13.86	004	VW (sh)	13.83	-	
11.08	005	VW (sh)	11.06	-	
9.20	006	VW (sh)	9.22	-	
5.9	-	VS (br)	<i>h</i> <sub>max</sub>	-	

$d_{\text{meas}}$  and  $d_{\text{calc}}$  are the measured and calculated diffraction spacings obtained from X-ray Scattering Data [ $d_{\text{calc}}$  is deduced from the following mathematical expressions:  $d_{00l} = 1/N_l(\sum d_{00l} \times l)$ , where  $N_l$  is the number of 00l reflections observed for the lamellar phases].  $d_{\text{neutron}}$  is the measured diffraction spacings obtained from Neutrons scattering Data.  $hkl$  are the Miller indexations of the reflections corresponding to the lamellar phases. Intensity of the sharp reflections: VS – very strong, S – strong, M – medium, VW – very weak; sh and br stand for sharp and broad reflection;  $h_{\text{max}}$  corresponds to the diffuse wide-angle scattering maximum from lateral distances between molten aliphatic tails.  $d$ : periodicity of SmA and SmB phase.

After melting from the crystal phase to the mesophase the layer distance decreases significantly by 1.4 Å in compound [TRYUM-7,10][OTf] (comparison refers to the calculated  $d$ -spacing). The 001 peak of the same compound becomes broader and less intense over the temperature range from crystal to higher temperature. In addition, the peak simultaneously moves to slightly higher  $2\theta$  values (Figure 53). This phenomenon appears both by SAXS and SANS just on this compound and since this involves only the 001 peak, but not the smaller order peaks, it justifies the large difference between the measured and the calculated values of the  $d$ -spacing at the reduced temperature for [TRYUM-7,10][OTf]. The decrease in layer spacing over temperature could occur either because of changing in interdigitation or torsional distortion of the alkyl-chains or because of tilting of the ions. The other two triflate salts with longer alkyl-chains don't show any significant decrease in  $d$ -spacing from the crystal to the mesophase (less than 0.2 Å).

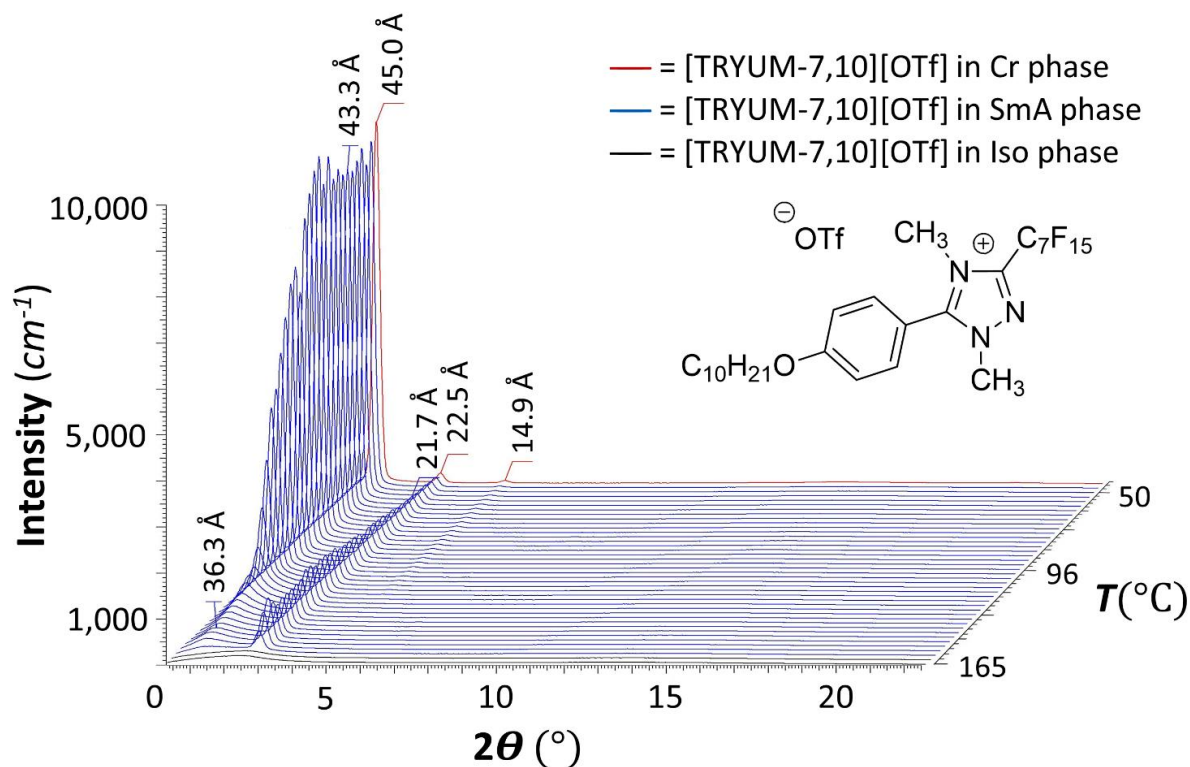


**Figure 53.** Waterfall view of X-ray scatterings recorded on compound [TRYUM-7,10][OTf] over temperatures. Frames has been recorded on cooling from isotropic liquid every 3°C.

The triflate salts with C<sub>9</sub>F<sub>19</sub> as perfluoroalkyl-chain show instead a significant decreasing of about 2-2.5 Å from the crystal to the mesophase, whilst SANS always shows *d*-spacing values 2-3 Å lower than respective SAXS values both in [TRYUM-7,*n*][OTf] and [TRYUM-9,*n*][OTf] (Figure 54). Differences between neutron and X-ray data of some compounds, could be justified by a slightly different contrast in the SAXS and SANS experiments.

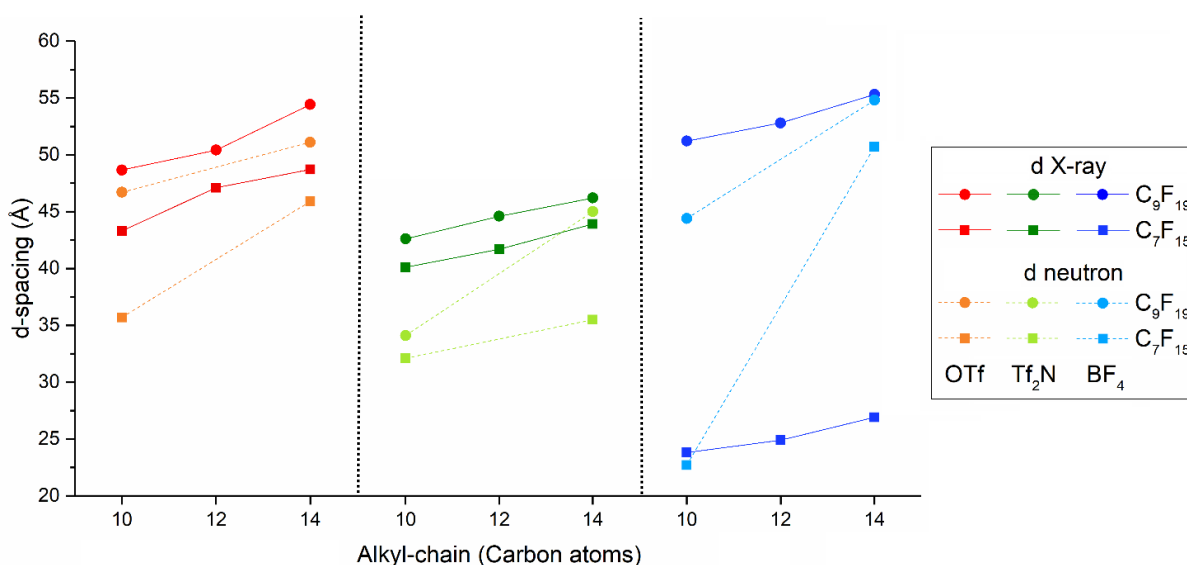


**Figure 54.** Plotting of SmA *d*-spacing of triazolium salts at reduced temperatures (0.9) versus alkyl-chain length. Symbols denote different perfluoroalkyl-chain length, colours denote different anions and irradiating source.

$C_{7F_{15}}$  perfluoroalkyl-chained compounds with  $[Tf_2N]^-$  as anion ( $[TRYUM-7,n][Tf_2N]$ ) show a quite different behaviour. This time the layer distance increases from the crystal to LC phase ( $[TRYUM-7,10][Tf_2N]$ : 40.1 Å,  $[TRYUM-7,12][Tf_2N]$ : 41.7 Å,  $[TRYUM-7,14][Tf_2N]$ : 43.9 Å). This could be due to a tilting of the molecules and the shaping of the bilayer in the solid phase, which appears highly crystalline and ordered when the anion is just  $[Tf_2N]^-$  (see chapter 3.2). The bis(triflimide) salts with  $C_9F_{19}$  perfluoroalkyl-chain can be described in the same manner, where all the layer distances are higher for 2-5 Å respectively. SANS of  $[TRYUM-9,14][Tf_2N]$  shows  $d$ -spacing values about 1.1 Å lower than the respective SAXS values, while a different diffraction pattern is showed in SANS of  $[TRYUM-7,10][Tf_2N]$ ,  $[TRYUM-7,14][Tf_2N]$  and  $[TRYUM-9,10][Tf_2N]$ , which are monotropic compounds (Figure 54). These compounds appeared visibly fluid just after the analysis and a crystallisation-like transition could be observed by naked eye. This usually means no crystallisation occurred during the analysis, but transition-like meso-glass or similar are not excluded whereas the instability of monotropic compound and the long-time of neutron irradiation in SANS experiments. In fact, a glass-like phase could justify the irregular pattern of monotropic compounds SANS, which is more similar to a crystal pattern than an LC pattern. Monotropic salts SANS shows 001 peaks with  $d$ -spacing value about 8 Å lower than respective SAXS 001 peaks. These values are more similar to the value observed in crystal phase for the respective compounds.

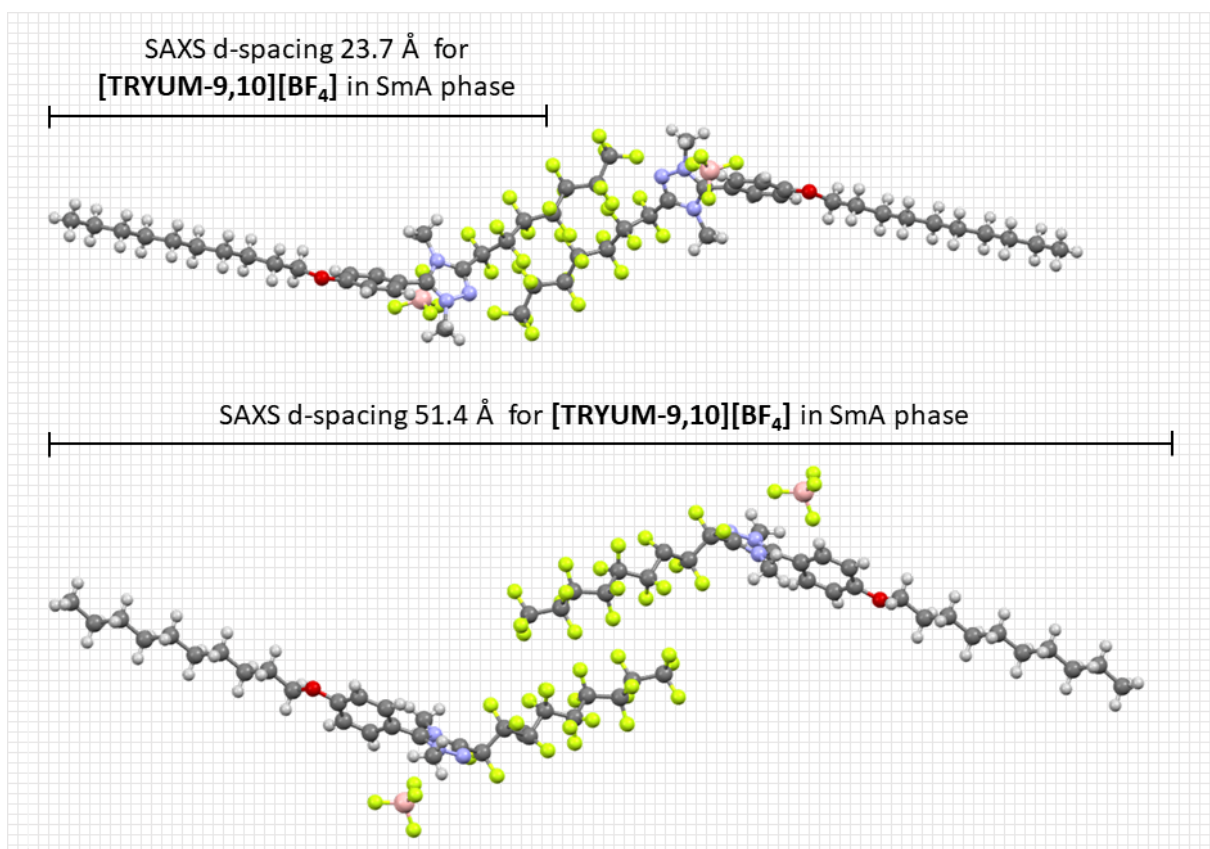


**Figure 55.** Comparison between SAXS  $d$ -spacing and crystal structure of compounds  $[TRYUM-7,10][BF_4]$  and  $[TRYUM-9,10][BF_4]$ .



The  $[\text{BF}_4]^-$  salts exhibit an increasing layer spacing upon heating from Cr to SmB and a decreasing one from SmB to SmA. This is clearly visible for  $\text{C}_9\text{F}_{19}$  perfluoroalkyl-chained  $[\text{BF}_4]^-$ , where a first order peak is always consistent with an interdigitated bi-layer. In fact, the first order peak collapses in  $\text{C}_7\text{F}_{15}$  perfluoroalkyl-chained  $[\text{BF}_4]^-$  salts (**[TRYUM-7,*n*][BF<sub>4</sub>]**) after the transition from Cr to SmB and keeps similar value along the SmA phase (Figure 54). There the 001 reflections show peak values smaller than the molecular length, thus they could describe just a section of the bi-layered structure if any other structure is possible (Figure 55). Moreover, missing a first order peak can be excluded, since second, third and following peaks has been identified as 002 and 003 and following reflections respectively. This is also observed by SANS in **[TRYUM-7,10][BF<sub>4</sub>]**, but not in **[TRYUM-7, 14][BF<sub>4</sub>]**, where the 001 peak value confirms an interdigitated bi-layer. On the contrary, the diffraction pattern of the SmA and SmB phase of **[TRYUM-9,*n*][BF<sub>4</sub>]** has got diffraction peaks with reciprocal spacing in the ratio 1 : 2 : 3 : 4 : 5 : 6 (and also : 7) by SAXS and in the ratio 1 : 2 : 3 by SANS, which suggests clearly the interdigitated bi-layered structure supposed for all the other compounds (Figure 55).

Overall, the nature of the smectic phase of **[TRYUM-7,*n*][OTf]**, **[TRYUM-7,*n*][Tf<sub>2</sub>N]**, **[TRYUM-7,*n*][BF<sub>4</sub>]**, **[TRYUM-9,*n*][OTf]**, **[TRYUM-9,*n*][Tf<sub>2</sub>N]**, and **[TRYUM-9,*n*][BF<sub>4</sub>]** was confirmed both by X-ray and neutron diffraction. Moreover, *d*-spacing values always suggest an interdigitated bi-layer identifying the mesophases as  $\text{SmA}_D$ . The small differences between the reported SAXS and SANS values are justified because X-ray and neutron interact differently with the nanoscale density differences of the analysed material. While bigger chancings suggest a different micro-organisation, which could be due to the relative long-time of SANS analysis at high temperature, especially for monotropic materials, whose SmA phases life time is doubtful. Lastly, X-ray diffraction patterns typical for smectic B phases were recorded on **[TRYUM-7,*n*][BF<sub>4</sub>]** and **[TRYUM-9,*n*][BF<sub>4</sub>]** confirming the transition between SmB and SmA phases in triazolium tetrafluoroborate.

### 3.4.3 Analysis of isotropic phases

Measurements of the isotropic phases were recorded both by SAXS and SANS (excepted for compounds with  $\text{C}_{12}\text{H}_{25}$  as alkyl-chain, which weren't scaled up) at 5-10 °C higher than the temperature of the relative transition points. The isotropic phase of **[TRYUM-9,*n*][BF<sub>4</sub>]** couldn't be analysed due to the decomposition of the material at those high temperatures.

In the isotropic liquid phase of the triazolium salts a diffraction pattern was found. This shows a broad peak between 1 and 2° characteristic of isotropic phases, but with high enough scattering intensity to suggest a residual short-range order in the phase (*e.g.* frames of X-ray scattering showed in Figure 56).

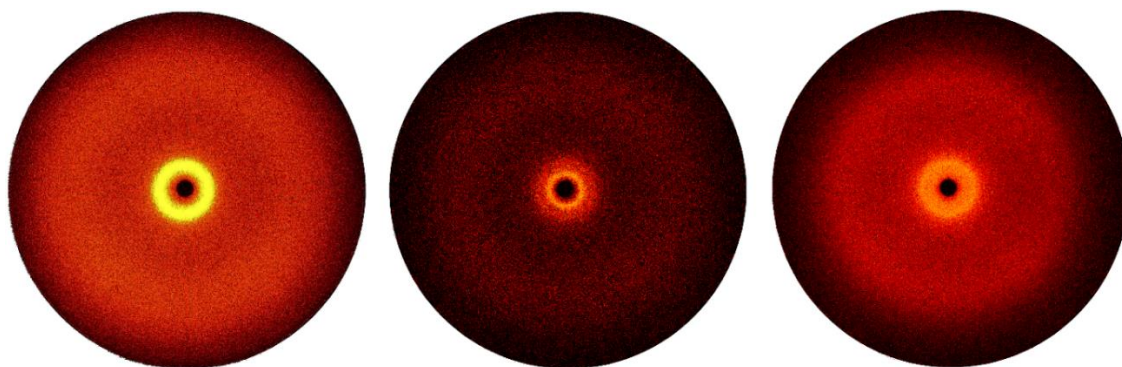


**Figure 56.** SAXS frames with the detector position at 180 mt of compounds [TRYUM-3,10][OTf] (left), [TRYUM-7,10][Tf<sub>2</sub>N] (middle) and [TRYUM-9,10][BF<sub>4</sub>] (right), at 86.1, 52.6 and 176.6 °C respectively.

The SAXS and SANS data from the isotropic phases were fit to scattering models extract the length scale of the scattering objects and the scatterer size, which relates to the periodicity in the system. SANS data were normalised by subtracting the scattering of the empty cell background using appropriate transmission measurements. Any low level of residual incoherent scattering was accounted for by a flat background term during the fitting process. The fitting of broad peaks low- $Q$  (lower than  $0.3 \text{ \AA}^{-1}$ ) was carried out by fitting to a Lorentzian peak model, where the scattering intensity  $I(q)$  is calculated by equation (3.5):

$$I(q) = \frac{\text{scale}}{\left(1 + \frac{(Q - Q_0)^2}{B}\right)} + \text{background} \quad (3.5)$$

where a peak having a height of  $I_0$  is centred at  $Q_0$  and has a half-width half-maximum of  $B$ . A correlation length, namely a  $d$ -spacing associated with this peak can be calculated from  $2\pi/Q_0$ , while the scatter size is given by  $1/B$ .

The same model was employed to fit the broad peaks of the relative SAXS data, which was performed without any background subtraction. In order to main consistency with the neutron data, the X axes of the X-ray data have been converted from  $2\theta$  to  $Q$  using equation (3.6):

$$Q = \frac{4\pi}{\lambda} \cdot \sin \frac{2\theta}{2} \quad (3.6)$$

where  $\lambda$  is the wavelength of the radiation used by instrument, expressed in  $\text{\AA}$ .

Compounds [TRYUM-7, $n$ ][OTf], [TRYUM-7, $n$ ][Tf<sub>2</sub>N], [TRYUM-9, $n$ ][Tf<sub>2</sub>N] and [TRYUM-9, $n$ ][OTf] show at low- $Q$  a broad feature that is not a usual Lorentzian peak, which seems to arise from two peaks that overlap each other. The fitting for those compounds was carried out employing a customised model which consists of two Lorentzian peaks.

Figure 57 show the different fitting between the single and the double peak model (Lorentz peak + Lorentz peak), while the fitting parameters are collected in Table 7.

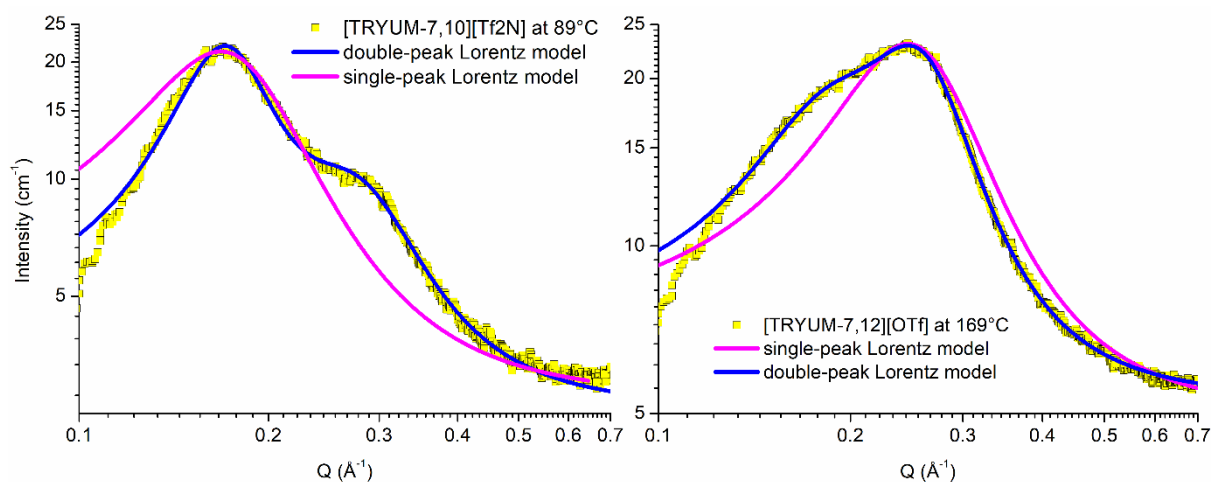


**Figure 57.** Comparison of fitting of [TRYUM-7,10][Tf<sub>2</sub>N] (left) and [TRYUM-7,12][OTf] (right) SAXS data from the isotropic liquid, between the single and double peak models.

**Table 7.** X-Ray and Neutrons fitting parameters for the isotropic phases of the triazolium salts.

Compound	T (°C)	X-ray				Neutron			
		PNPP		PNPP'		PNPP		PNPP'	
		<i>d</i> (Å)	<i>S</i> (Å)	<i>d</i> ' (Å)	<i>S</i> ' (Å)	<i>d</i> (Å)	<i>S</i> (Å)	<i>d</i> ' (Å)	<i>S</i> ' (Å)
[TRYUM-3,10][OTf]	107	22.9	15.7	-	-	24.2	11.5	-	-
[TRYUM-3,12][OTf]	96	25.6	17.5	-	-	-	-	-	-
[TRYUM-3,14][OTf]	79	28.1	22.3	-	-	27.8	25.4	-	-
[TRYUM-3,10][Tf <sub>2</sub> N]	78	22.7	11.3	-	-	25.1	7.9	-	-
[TRYUM-3,12][Tf <sub>2</sub> N]	82	25.2	13.0	-	-	-	-	-	-
[TRYUM-3,14][Tf <sub>2</sub> N]	86	28.0	15.4	-	-	28.5	12.6	-	-
[TRYUM-3,10][BF <sub>4</sub> ]	89	25.3	22.8	-	-	24.8	23.5	-	-
[TRYUM-3,12][BF <sub>4</sub> ]	94	29.2	24.4	-	-	-	-	-	-
[TRYUM-3,14][BF <sub>4</sub> ]	101	29.5	30.6	-	-	29.6	26.0	-	-
[TRYUM-7,10][OTf]	166	33.6	26.6	23.2	15.1	33.3	9.8	22.0	14.7
[TRYUM-7,12][OTf]	169	35.8	22.3	25.1	15.7	-	-	-	-
[TRYUM-7,14][OTf]	172	36.3	19.9	26.4	16.9	37.4	13.5	26.8	14.4
[TRYUM-7,10][Tf <sub>2</sub> N]	89	37.0	27.8	23.2	13.1	33.9	14.2	21.8	11.8
[TRYUM-7,12][Tf <sub>2</sub> N]	91	39.1	26.1	26.7	12.8	-	-	-	-
[TRYUM-7,14][Tf <sub>2</sub> N]	98	40.3	24.6	27.5	12.6	38.1	24.2	27.6	11.6
[TRYUM-9,10][OTf]	189	37.3	24.1	24.3	13.2	36.3	9.6	22.4	10.2
[TRYUM-9,12][OTf]	201	38.5	29.5	25.6	13.9	-	-	-	-
[TRYUM-9,14][OTf]	210	39.2	36.7	27.7	13.1	38.1	13.6	25.6	10.3
[TRYUM-9,10][Tf <sub>2</sub> N]	101	38.1	24.7	24.1	12.3	38.1	21.6	23.3	11.1
[TRYUM-9,12][Tf <sub>2</sub> N]	121	40.0	24.0	25.4	12.3	-	-	-	-
[TRYUM-9,14][Tf <sub>2</sub> N]	138	43.3	27.5	26.9	13.2	41.3	29.8	30.0	11.5

*d* and *S* are the *d*-spacing and scatter size respectively, calculated from position centre and half-width half-maximum of the first peak respectively (PNPP), while *d*' and *S*' are the *d*-spacing and scatter size, calculated from the position centre and half-width half-maximum of the eventual overlying second peak (PNPP').

When compared to the molecular length scales for the anions and cations in this system the fitted parameters in Table 7 allow a discussion of the molecular basis and structure of the isotropic liquid phase of the triazolium salts, which are basically ILs (Figure 59).

ILs frequently display three peaks (Figure 58) in small-angle scattering experiments: a peak at lower- $Q$  (usually between 0.1 and 0.5  $\text{\AA}^{-1}$ ) that is related to ion-ion distances separated by the non-polar network, the so called polar/non-polar peak (PNPP); a peak at intermediate- $Q$  (usually between 0.6 and 1.0  $\text{\AA}^{-1}$ ) that relates to the average distances between ions of the same charge, the charge ordering peak (COP); a peak at higher- $Q$  (usually between 1.0 and 1.5  $\text{\AA}^{-1}$ ) that relates to characteristic close-contact separations between ions, the so-called contact peak (CP).<sup>99</sup> The PNPP was identified by Triolo *et al.* for the first time by X-ray diffraction studies in imidazolium ILs,<sup>100</sup> and reported a dependence of the correlation distance on alkyl-chain length (PNPP position) is observed, as the chain length increases the peak sharpens, its intensity increases, and it moves to lower- $Q$  values (longer distance).

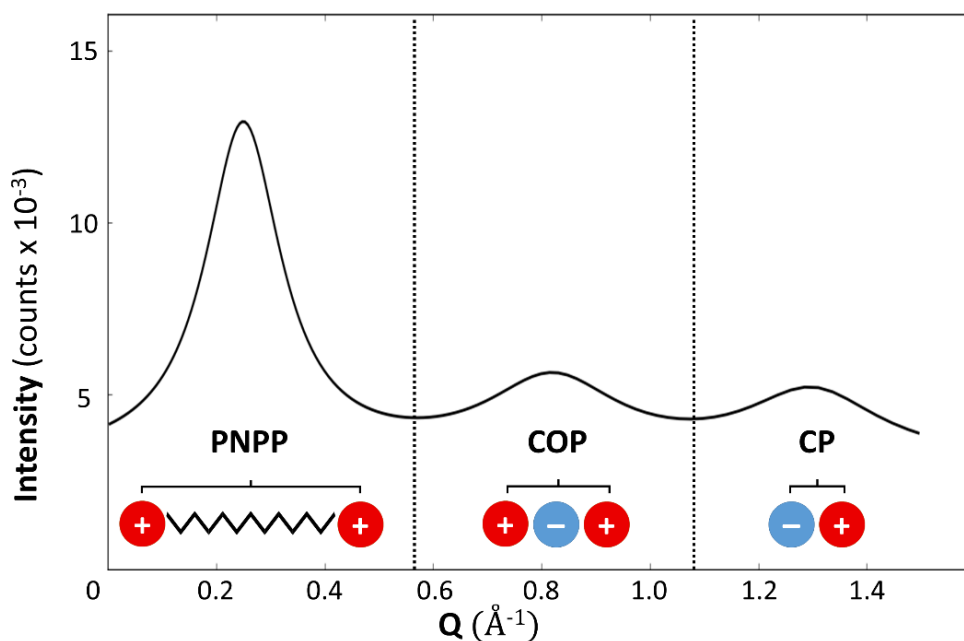


**Figure 58.** Illustrative scheme of PNPP, COP and CP in scattering of ILs isotropic states.

This is rationalised as the alkyl-chains segregating from the polar head group of the cation and the anion. The alkyl-chains do not fully interdigitate and create domains of alkyl-chains and domains of charged core and anions. X-ray diffraction studies on ILCs in their LC and isotropic states indicate that the structural ordering is similar in both, with the low- $Q$  peak intensity decreasing upon the transition into the isotropic phase. This was concluded as being due to the strong alignment effect of the LC phase being lost and not an intrinsic structural change.<sup>98,101</sup>

For most of the triazolium salts studied here, both SAXS and SANS always show a PNP peak and negligible CO and C peaks. However, for some compounds, fitting suggests a partial overlap of two

different PNPPs, so in these cases, as above mentioned parameters have been extrapolated using a double Lorentz peak model. Two PNPPs could be justified by the presence of two different domains which segregate from a central polar head. This condition would be supported by a constant value of one of the two PNPPs (PNPP and PNPP') within salts with the same perfluoroalkyl-chain. In fact, both PNPPs always increase with both increasing alkyl- and perfluoroalkyl-chain. Moreover, the inter-layer spacing of the polar network separated by the aliphatic domains doesn't fit with either of the observed *d*-spacing. Thus, a precise meaning of a second PNPP (PNPP') can't be attributed to a specific molecular description without further investigation.

However, *d*-spacing always decreases upon the transition from SmA to the isotropic phase and this can be observed comparing the SmA phases parameter with PNPP one. *d*-spacing deduced from PNPP always increase with the increasing alkyl and perfluoroalkyl-chain lengths and no big differences exist between values measured by SAXS and SANS (Figure 59). The scatter size of PNPP increase in the same manner excepted in X-ray for [TRYUM-7,*n*][OTf], [TRYUM-7,*n*][Tf<sub>2</sub>N], where the scatter size decrease with the alkyl-chain length.

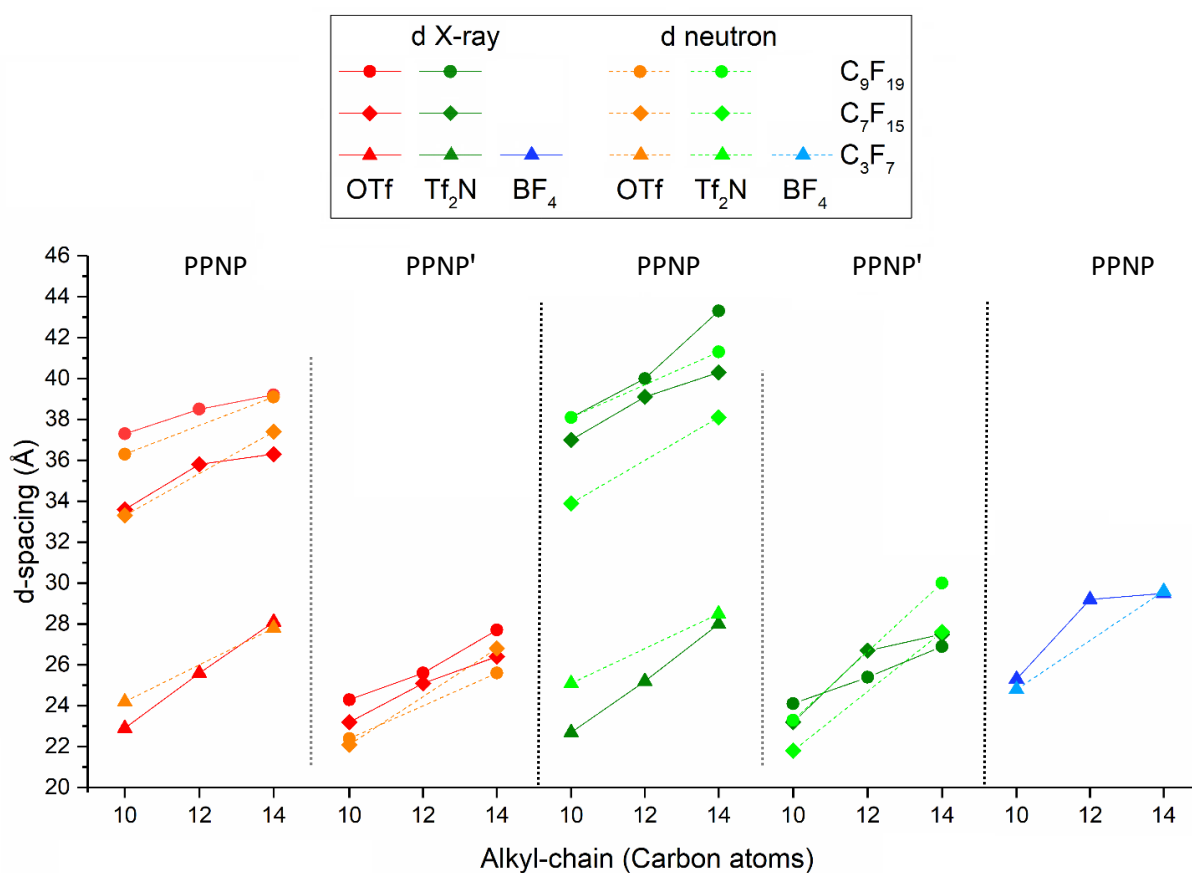


**Figure 59.** Plotting of *d*-spacing of triazolium ILs (isotropic phases) versus alkyl-chain length. Symbols denote different perfluoroalkyl-chain length, colours denote different anions and irradiating source. PNPP and PNPP' of the same salts are plotted in adjacent section.

On the contrary, only one PNPP is observed in all of the salts having C<sub>3</sub>F<sub>7</sub> as the perfluoroalkyl-chain. This is probably because perfluoro-chain length doesn't provide a sufficient scale density contrast in these compounds or more probably this is due to the lack of phase separation of the alkyl- and the perfluoroalkyl-chain in these salts in isotropic phase.

Overall, the data suggests that the length scale of the *d*-spacings get larger with increasing molecular length, which is strictly correlated to the alkyl- and perfluoroalkyl-chain lengths. This in turn induces structural changes within the polar network (since the chains are attached to charged core that are a fundamental component of the polar network). The global effect of these changes must result in an increase in the ion-ion distances separated by the non-polar and fluorinated networks, giving rise to the observed changes in PNPP position and *d*-spacing derived from this. However, based on the data available, giving an unambiguous molecular description of the origin of this effect is not possible.

### 3.5 Electrochemical Impedance Spectroscopy

We can say that the studied triazolium system has a large range of accessible properties and a degree of fine-tuning is possible by varying the constituent ions. The knowledge of other physical properties such as conductivities and viscosities can allow an easier prediction and control of IL and ILC features and is important to understand for their future applications. As, these properties are related to ion mobility and the bulk structure of the liquids, determination of these properties also gives additional insight into their fundamental behaviour. Moreover, nowadays there is a great interest to use ILs and ILCs as electrolytes for electrochemical devices or synthesis of nanorods and nanowires.<sup>102</sup> The conductivities of ILs are best deduced electrochemical impedance spectroscopy analysis.<sup>103–105</sup> The objective of EIS analysis in the present work is to investigate the electrochemical behaviour and ion mobility of triazolium salts and their potential usability in electrochemical applications.

#### 3.5.1 Introducing EIS

Electrochemical impedance spectroscopy (EIS) measures the electric properties of a medium over a range of frequencies and it is an experimental method of characterising electrochemical systems. It is based on the interaction of an external field with the electric properties of the sample, measuring the impedance (*Z*) of a system as a function of frequency (*f*). It is often used to reveal the frequency response of the system, including the energy storage and dissipation properties.<sup>106</sup> Impedance is the opposition to the flow of alternating current (AC) in a complex system. A passive complex electrical system comprises both energy dissipater (resistor and transistor) and energy storage (capacitor) elements. If the system is purely resistive, then the opposition to AC or direct current (DC) is simply resistance. Electrochemical Impedance Spectroscopy is used in a wide range of applications in several fields, such as in the paint industry to investigate the quality of coatings and to detect the presence of corrosion as well as in many biosensor systems to measure bacterial concentration and to detect

pathogens. Electrochemical Impedance Spectroscopy is also used to analyse and characterize different food products. Some examples are the assessment of food/package interactions, the analysis of milk composition, the characterisation and the determination of the freezing end-point of ice-cream mixes, the measure of meat ageing, the investigation of ripeness and quality in fruits and the determination of free acidity in olive oil.<sup>106</sup>

Data obtained by EIS is commonly expressed graphically in a Bode plot or more often as a Nyquist plot. The latter is a parametric plot of a frequency response used in automatic control and signal processing.<sup>107</sup> The Nyquist plot is named by Harry Nyquist, who was a former engineer at Bell Laboratories. In Cartesian coordinates of a Nyquist plot, the real part of the transfer function is plotted on the X axis, while the imaginary part is plotted on the Y axis (Figure 60). In EIS, Nyquist plot represents conventionally real part of impedance as  $\text{Re}(Z)$  or  $Z'$  and  $\text{Im}(Z)$  or  $Z''$  as imaginary part of impedance. The frequency is swept as a parameter and the Nyquist plot results in a diagram per frequency, which decrease from the left to the right side.

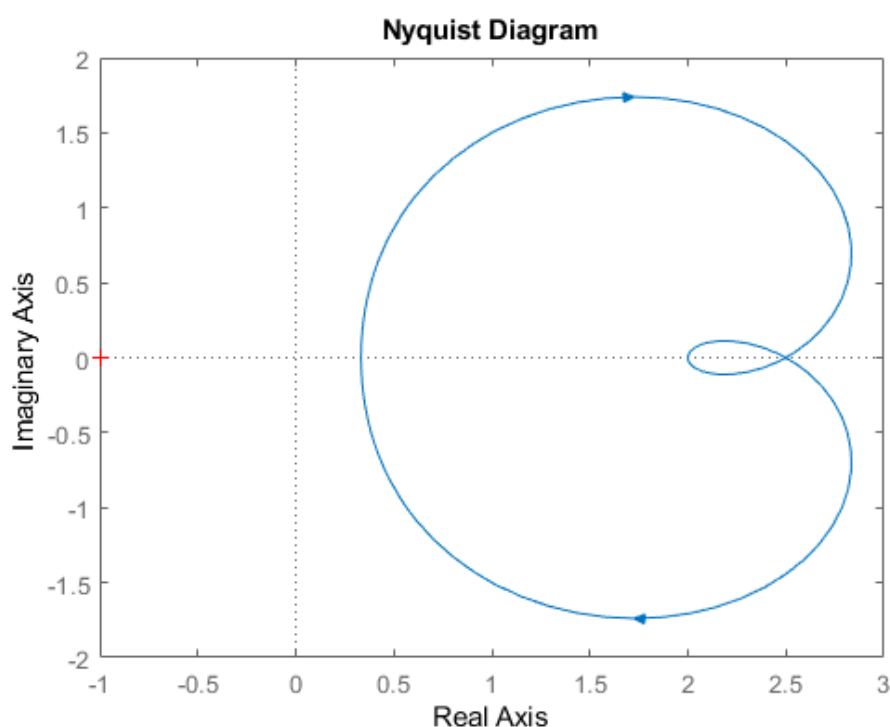


**Figure 60.** Schematic representation of a Nyquist plot.

The Nyquist plot can provide some information by the shape of the transfer function chart. For instance, the plot provides evidence on the difference between the number of poles and zeros of the transfer function by the angle at which the curve approaches the origin. In EIS one of the most common behaviour is described by a semicircle followed by straight line (proceeding to right). Moreover, on dependence by the used potentiostat as impedance analyser, the Nyquist plot allows the user to determine charge transfer resistance, double layer capacitance and Ohmic resistance.<sup>108</sup>

### 3.5.2 Instrument manufacturing and set up

To perform EIS on the LC and isotropic phases of the triazolium salts here required the design of an electrode and furnace that involved a compromise between the operational temperature limits of the instrumentation and the amount of the available or reasonably synthesisable amount of the salts. Indeed, high and controllable temperatures were required to access to some of the LC and isotropic phases of the triazolium salts. Moreover, an electrode probe must be immersed in a reasonable amount of sample, which depends on the specifics of the probe in use. After careful analysis of the necessary temperature range, to cover as many compounds as possible, as well as minimising the size of the electrode, which can be exploited to perform EIS analysis, it was decided to design and produces two tailor-made pieces of equipment for these studies.

Firstly, a platinum electrode with probe encased in borosilicate glass has been built in York. Round tubing was used to produce the probe, which has a 0.7 cm internal diameter, on which two 0.4 x 0.4 cm platinum plates were attached diametrically opposite each other using an epoxy adhesive with high temperature resistance. The structural performance of the adhesive is to 175 °C and this represent an important limit temperature, which exclude the investigation of some compounds or their phases. The two electrode plates define a volume called electrode cell, which usually is sited in a separated chamber on the tip of the electrode probe. The top edges of the platinum plates were welded to platinum wires linked in turn to copper cables for connection to the potentiostat. Electrode probe and plates sizes provide a minimum operating volume not over 0.112 mL, which is a good compromise to use the triazolium salts obtained from the scale-up synthesis earlier mentioned. Secondly, a bigger size of round tubing has been used to produce a flat-bottomed sample holder, which fits perfectly the probe size. This electrode was tested by measuring the resistance of a standard solution and an already characterised ILs whose conductivity have been reported in the literature.

EIS experiments on the triazolium salts were performed by an EC-Lab SP-150 potentiostat with five cables in its interface: two for the worker electrode (WE/CA1 and REF1, which are red), two for the counter electrode (CE/CA2 and REF2, which are blue) and one for the reference electrode (REF3, which is white). For these experiments, the platinum electrode has been used as worker electrode and no other electrode has been used as counter or reference probe. This way, the electrode and the potentiostat were configurated *via* crocodile clamps, connecting the CE/CA2 (blue), REF3 (blue), and REF2 (white) each independently of each other to one of the electrode plate of the cell as well as the WE/CA1 (red) and REF1 (red) independently of each other to the other electrode plate of the cell, as the instrument manual recommends to set up this kind of experiment (Figure 62 right).



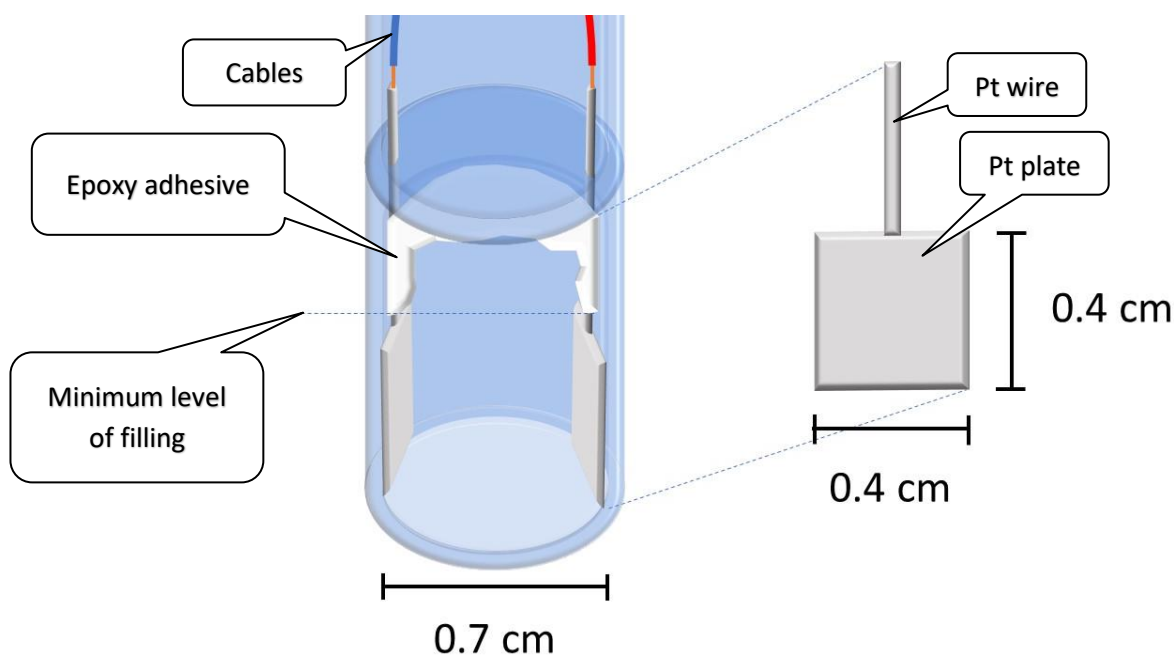


**Figure 61.** Illustration of the chamber of the platinum electrode. Sizes of the cell are reported.

EIS experiments were performed inside a Faraday cage in order to avoid interferences from external sources of electromagnetic waves. During a first analysis at room temperature, the electrode working was found to be affected by the filling level of sample holder. This was because any amount of sample over the platinum plates influences the electrode working and measurements were not reproducible. This was due to the small sizes of plates, which are comparable in surface area of the platinum wires above them, which apparently contribute to the measurement. This problem was solved by coating the platinum wires with the epoxy adhesive, in order to electrically insulate their surfaces. This way, the measurements with the probe are not affected by extra filling in the probe chamber and are reproducible, as long as the platinum plates are completely submerged by the sample (Figure 61).

In addition to the electrochemical cell, a thermal-block able to heat the sample holder of the electrode probe was produced (Figure 62, left). The heating system consists of an aluminium and brass block, where a electrical resistance heaters and a temperature sensor have been inserted and these have been linked in turn to a temperature controller. Ultimately, the sides and bottom of the thermal-block was coated with insulating material in order to preserve the bench work and the user as well as to avoid heat dissipation and enhance the heating performance.

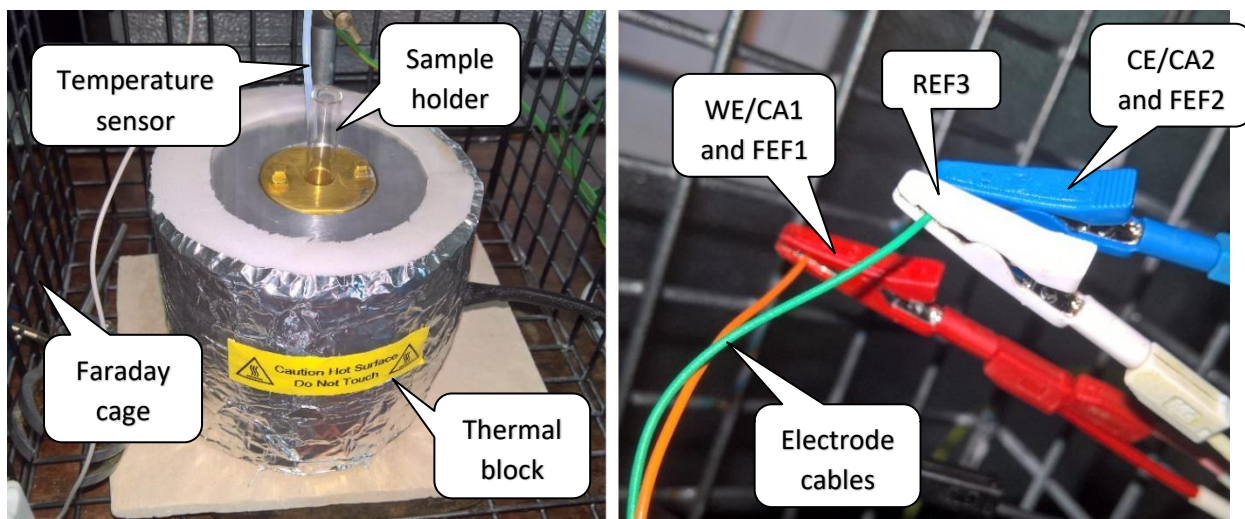


**Figure 62.** Thermo-block with sample holder in relative slot (left) and cable configuration (right).

### 3.5.3 EIS results and discussion

Platinum electrode probe features were deduced by measuring the resistance of reference solutions of aqueous potassium chloride (5000 and 12880  $\mu\text{S cm}^{-1}$ ) and already known ILs. The ILs used as references were dodecyl-methylimidazolium bis(trifluoromethanesulfonyl) imide ( $[\text{C}_{12}\text{mim}][\text{Tf}_2\text{N}]$ ) and ethyl-methylimidazolium bis(trifluoromethanesulfonyl) imide ( $[\text{C}_2\text{mim}][\text{Tf}_2\text{N}]$ ), whose conductivities are reported in the literature.<sup>109–111</sup>

The cell constant ( $k_c$ ) of the probe was calculated from the measured resistance ( $R_1$ ) and conductivity ( $\sigma$ ) of the reference solutions, using the second Ohm's law reported in equations (3.7):

$$R_1 = \rho \frac{l}{a} \quad (3.7)$$

where  $\rho$  is the resistivity or the specific resistance of the material as well as  $a$  and  $l$  are the activated surface area of the of the platinum plates of the electrode and the distances between those respectively. While equations (3.8) and (3.9) define  $k_c$  and describe the relation between  $\rho$  and  $\sigma$ .

$$k_c = \frac{l}{a} \quad (3.8)$$

$$\rho = \frac{1}{\sigma} \quad (3.9)$$

Measured  $k_c$  values are reproducible and reasonably comparable with  $k_c$  values calculated from the plates dimensions. Samples and references have been measured after equilibration at the desired temperature. Each measurement has been recorded with an amplitude of 120, 240, 300, 400 or 500 mV and over a frequency window from 1 Hz to 1 MHz. Samples were analysed within LC and/or isotropic phases over a range of temperatures, collecting 4 or 5 points of conductivity/temperature in accordance with the temperature limits of the instrumentation and the sample phases.

Conductivity values are always calculated by Ohm’s law from the relative measured resistances, which are extrapolated from the Nyquist plot by fitting to a model of an equivalent circuit described as

$\frac{R_1}{Q_1 + Q_2/R_2}$ , whose relation in function of impedance is reported in equation (3.10),

$$Z(f) = \frac{R_1(1 + (i2\pi f)^{\alpha_1} Q_1 R_2 + (i2\pi f)^{\alpha_2} Q_2 R_2)}{1 + (i2\pi f)^{\alpha_2} Q_2 R_2 + (i2\pi f)^{\alpha_1} Q_1 (R_2 + R_1(1 + (i2\pi f)^{\alpha_2} Q_2 R_2))} \quad (3.10)$$

where  $\alpha_1 = \alpha_2$ ;  $i$  is an imaginary number;  $R_1$ ,  $Q_1$  and  $Q_2$  are resistances of the resistor and constant phase elements respectively of the equivalent circuit as well as  $R_2$ , which represents the resistance made by the analysed material (Examples of Nyquist plot and relative fitting are reported in Figure 63 and Figure 64).

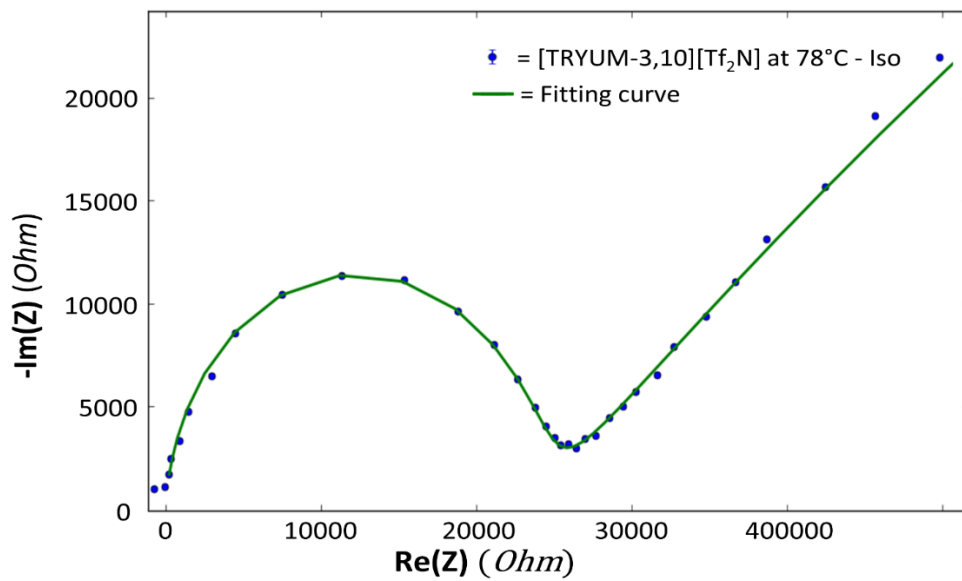


Figure 63. Nyquist plot of EIS measurement on [TRYUM-3,10][Tf<sub>2</sub>N] at 78°C and relative fitting.

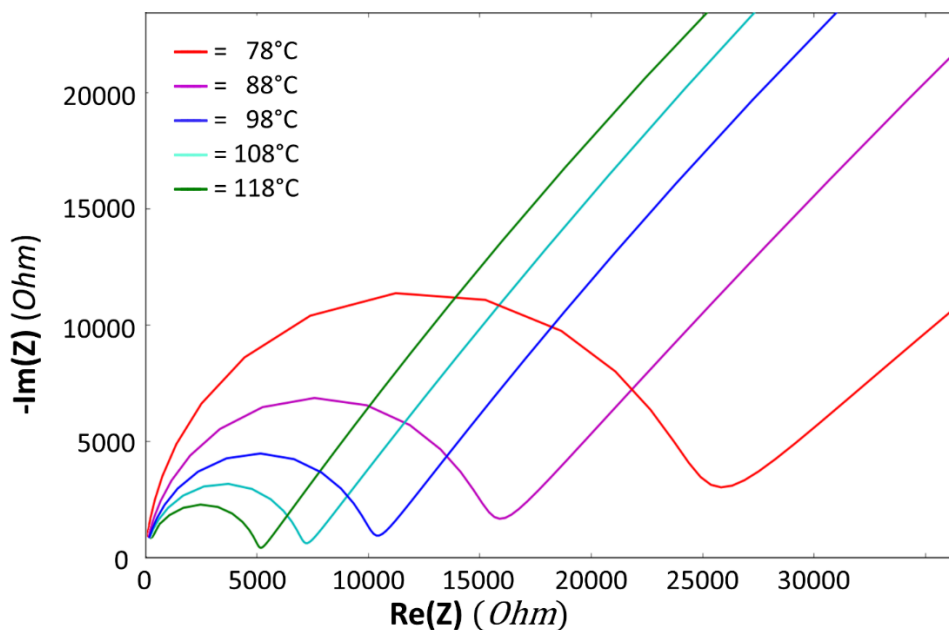


Figure 64. Nyquist plot of fitted EIS of [TRYUM-3,10][Tf<sub>2</sub>N] over a range of temperatures.

The sample conductivities were found to increase exponentially with temperature. Indeed, conductivity of the same samples have been collected at different temperatures, plotted in chart as a function of the temperature and fitted to the exponential equations (3.11) and (3.12), in order to extrapolate energy parameters such as the activation energy ( $E_a$ ).

$$\sigma = A \cdot e^{-\frac{E_a}{RT}} \quad (3.11)$$

$$\sigma = B \cdot e^{-\frac{C}{T-T_0}} \quad (3.12)$$

Equation (3.11) is Arrhenius law, where  $R = 8.31 \text{ J K}^{-1} \text{ mol}^{-1}$  and  $T$  is expressed in Kelvins; while equation (3.12) is the Vogel-Fulcher-Tammann (VFT) relationship for glass-forming liquids, where  $B$  is proportional to the concentration of carrier ions,  $C$  is the pseudo activation energy for ion conduction, and  $T_0$  is the ideal glass transition temperature  $T_g$ .<sup>112,113</sup> The conductivities values of analysed compounds at different reduced temperatures have been extrapolated from the fitting parameters, in order to compare conductivities between compounds despite the different temperature ranges for each phase. Table 8 shows conductivity values obtained from EIS measurements and relative fitting parameters, while a plot of triazolium salt conductivities as function of temperature is shown in Figure 65.

**Table 8.** Conductivity and fitting data for the LC and isotropic phases of the triazolium salts.

$\sigma$ ( $\mu\text{S cm}^{-1}$ )	$T$ ( $^{\circ}\text{C}$ )	Parameters
<b>[TRYUM-3,10][OTf]</b>		
53.6	107	$P = \text{Iso}$
106.0	118	$A = 2.78 \cdot 10^{10} \mu\text{S cm}^{-1}$ , $E_a = 63 \text{ kJ mol}^{-1}$ , $R^2_{\text{Arr}} = 0.9990$
172.1	128	$B = 8.84 \cdot 10^5 \mu\text{S cm}^{-1}$ , $C = 1499 \text{ K}$ , $T_0 = 225.5 \text{ K}$ ,
264.1	137	$R^2_{\text{VFT}} = 0.9999$
399.9	147	
<b>[TRYUM-3,14][OTf]</b>		
10.5	79	$P = \text{Iso}$
24.5	89	$A = 3.74 \cdot 10^{12} \mu\text{S cm}^{-1}$ , $E_a = 77 \text{ kJ mol}^{-1}$ , $R^2_{\text{Arr}} = 0.9983$
56.2	99	$B = 3.31 \cdot 10^5 \mu\text{S cm}^{-1}$ , $C = 1015 \text{ K}$ , $T_0 = 255.2 \text{ K}$ ,
112.6	109	$R^2_{\text{VFT}} = 0.9999$
211.7	120	
<b>[TRYUM-3,10][Tf<sub>2</sub>N]</b>		
141.2	78	$P = \text{Iso}$
215.5	88	$A = 3.39 \cdot 10^8 \mu\text{S cm}^{-1}$ , $E_a = 43 \text{ kJ mol}^{-1}$ , $R^2_{\text{Arr}} = 0.9995$
323.9	98	$B = 9.30 \cdot 10^5 \mu\text{S cm}^{-1}$ , $C = 1668 \text{ K}$ , $T_0 = 161.9 \text{ K}$ ,
466.5	108	$R^2_{\text{VFT}} = 0.9999$
648.0	118	
<b>[TRYUM-3,14][Tf<sub>2</sub>N]</b>		
171.8	86	$P = \text{Iso}$
269.4	96	$A = 1.24 \cdot 10^9 \mu\text{S cm}^{-1}$ , $E_a = 47 \text{ kJ mol}^{-1}$ , $R^2_{\text{Arr}} = 0.9993$
403.5	106	$B = 2.15 \cdot 10^6 \mu\text{S cm}^{-1}$ , $C = 1829 \text{ K}$ , $T_0 = 165 \text{ K}$ ,
607.7	116	$R^2_{\text{VFT}} = 0.9999$
852.0	126	

<b>[TRYUM-3,10][BF<sub>4</sub>]</b>		
14.4	89	$P = \text{Iso}$
31.0	99	$A = 9.69 \cdot 10^{11} \mu\text{S cm}^{-1}, E_a = 75 \text{ kJ mol}^{-1}, R^2_{\text{Arr}} = 0.9993$
62.7	109	$B = 2.79 \cdot 10^6 \mu\text{S cm}^{-1}, C = 1778 \text{ K}, T_0 = 216.2 \text{ K},$
113.9	119	$R^2_{\text{VFT}} = 0.9999$
196.8	129	
<b>[TRYUM-3,14][BF<sub>4</sub>]</b>		
20.9	102	$P = \text{Iso}$
38.0	111	$A = 1.22 \cdot 10^{11} \mu\text{S cm}^{-1}, E_a = 70 \text{ kJ mol}^{-1}, R^2_{\text{Arr}} = 0.9991$
64.7	121	$B = 6.59 \cdot 10^6 \mu\text{S cm}^{-1}, C = 2388 \text{ K}, T_0 = 187.3 \text{ K},$
104.7	131	$R^2_{\text{VFT}} = 0.9982$
178.9	141	
<b>[TRYUM-7,10][OTf]</b>		
11.8	111	$P = \text{SmA}$
21.1	121.5	$A = 7.97 \cdot 10^9 \mu\text{S cm}^{-1}, E_a = 65 \text{ kJ mol}^{-1}, R^2_{\text{Arr}} = 0.9996$
34.0	131	$B = 6.88 \cdot 10^5 \mu\text{S cm}^{-1}, C = 2010 \text{ K}, T_0 = 201.7 \text{ K},$
52.2	141	$R^2_{\text{VFT}} = 0.9990, \sigma_{\text{Red}} = 63.5 \mu\text{S cm}^{-1} (145 \text{ }^\circ\text{C})$
82.8	151	
442.8	165	$P = \text{Iso}$
492.3	170	$A = 1.12 \cdot 10^8 \mu\text{S cm}^{-1}, E_a = 45 \text{ kJ mol}^{-1}, R^2_{\text{Arr}} = 0.9962$
562.3	175	$B = 4.14 \cdot 10^6 \mu\text{S cm}^{-1}, C = 2905 \text{ K}, T_0 = 121.4 \text{ K},$
653.6	180	$R^2_{\text{VFT}} = 0.9957$
749.4	185	
<b>[TRYUM-7,14][OTf]</b>		
30.7	125	$P = \text{SmA}$
49.7	135	$A = 1.10 \cdot 10^{10} \mu\text{S cm}^{-1}, E_a = 65 \text{ kJ mol}^{-1}, R^2_{\text{Arr}} = 0.9999$
79.5	145	$B = 2.81 \cdot 10^5 \mu\text{S cm}^{-1}, C = 2464 \text{ K}, T_0 = 182.9 \text{ K},$
122.2	155	$R^2_{\text{VFT}} = 0.9999, \sigma_{\text{Red}} = 98.6 \mu\text{S cm}^{-1} (150 \text{ }^\circ\text{C})$
445.8	170	$P = \text{Iso}$
514.2	175	$A = 1.57 \cdot 10^8 \mu\text{S cm}^{-1}, E_a = 47 \text{ kJ mol}^{-1}, R^2_{\text{Arr}} = 0.9998$
591.4	180	$B = 4.09 \cdot 10^5 \mu\text{S cm}^{-1}, C = 1547 \text{ K}, T_0 = 216.5 \text{ K},$
673.5	185	$R^2_{\text{VFT}} = 0.9995$
775.1	190	
<b>[TRYUM-7,10][Tf<sub>2</sub>N]</b>		
108.7	89	$P = \text{Iso}$
182.8	99	$A = 8.66 \cdot 10^8 \mu\text{S cm}^{-1}, E_a = 48 \text{ kJ mol}^{-1}, R^2_{\text{Arr}} = 0.9983$
262.8	109	$B = 5.17 \cdot 10^5 \mu\text{S cm}^{-1}, C = 1422 \text{ K}, T_0 = 194.0 \text{ K},$
400.9	119	$R^2_{\text{VFT}} = 0.9991$
558.0	129	
<b>[TRYUM-7,14][Tf<sub>2</sub>N]</b>		
140.9	98	$P = \text{Iso}$
216.7	108	$A = 1.59 \cdot 10^8 \mu\text{S cm}^{-1}, E_a = 43 \text{ kJ mol}^{-1}, R^2_{\text{Arr}} = 0.9991$
301.3	118	$B = 3.46 \cdot 10^5 \mu\text{S cm}^{-1}, C = 1445 \text{ K}, T_0 = 185.7 \text{ K},$
423.3	128	$R^2_{\text{VFT}} = 0.9997$
568.5	138	
<b>[TRYUM-7,10][BF<sub>4</sub>]</b>		
3.0	121	$P = \text{SmB}$
4.3	131	$A = 2.16 \cdot 10^9 \mu\text{S cm}^{-1}, E_a = 67 \text{ kJ mol}^{-1}, R^2_{\text{Arr}} = 0.9976$
6.6	141	$B = 1.54 \cdot 10^6 \mu\text{S cm}^{-1}, C = 3161 \text{ K}, T_0 = 157.4 \text{ K},$
10.8	151	$R^2_{\text{VFT}} = 0.9962, \sigma_{\text{Red}} = 14.8 \mu\text{S cm}^{-1} (158 \text{ }^\circ\text{C})$
17.1	161	

<b>[TRYUM-7,14][BF<sub>4</sub>]</b>		
16.0	135	$P = \text{SmB}$
22.7	144	$A = 3.71 \cdot 10^{10} \mu\text{S cm}^{-1}, E_a = 74 \text{ kJ mol}^{-1}, R^2_{\text{Arr}} = 0.9961$
35.1	154	$B = 1.95 \cdot 10^7 \mu\text{S cm}^{-1}, C = 3536 \text{ K}, T_0 = 159.4 \text{ K},$
55.1	164	$R^2_{\text{VFT}} = 0.9944, \sigma_{\text{Red}} = 43.5 \mu\text{S cm}^{-1} (158 \text{ }^\circ\text{C})$
91.9	174	
<b>[TRYUM-9,10][OTf]</b>		
1.7	84	$P = \text{SmA}$
3.7	94	$A = 3.09 \cdot 10^{10} \mu\text{S cm}^{-1}, E_a = 70 \text{ kJ mol}^{-1}, R^2_{\text{Arr}} = 0.9998$
6.9	104	$B = 1.98 \cdot 10^6 \mu\text{S cm}^{-1}, C = 2518 \text{ K}, T_0 = 177.6 \text{ K},$
12.0	114	$R^2_{\text{VFT}} = 0.9992, \sigma_{\text{Red}} = 148.2 \mu\text{S cm}^{-1} (166 \text{ }^\circ\text{C})$
20.2	124	
34.4	134	
<b>[TRYUM-9,14][OTf]</b>		
1.5	84	$P = \text{SmA}$
2.8	94	$A = 1.88 \cdot 10^{10} \mu\text{S cm}^{-1}, E_a = 69 \text{ kJ mol}^{-1}, R^2_{\text{Arr}} = 0.9999$
5.4	104	$B = 5.61 \cdot 10^5 \mu\text{S cm}^{-1}, C = 2117 \text{ K}, T_0 = 194.2 \text{ K},$
9.6	114	$R^2_{\text{VFT}} = 0.9997, \sigma_{\text{Red}} = 222.6 \mu\text{S cm}^{-1} (185 \text{ }^\circ\text{C})$
16.4	124	
27.1	134	
<b>[TRYUM-9,10][Tf<sub>2</sub>N]</b>		
134.5	102	$P = \text{Iso}$
208.4	112.5	$A = 2.09 \cdot 10^8 \mu\text{S cm}^{-1}, E_a = 44 \text{ kJ mol}^{-1}, R^2_{\text{Arr}} = 0.9987$
298.9	122	$B = 1.16 \cdot 10^5 \mu\text{S cm}^{-1}, C = 1018 \text{ K}, T_0 = 224.4 \text{ K},$
411.5	132	$R^2_{\text{VFT}} = 0.9999$
555.5	142	
<b>[TRYUM-9,14][Tf<sub>2</sub>N]</b>		
93.7	105	$P = \text{SmA}$
107.6	111	$A = 1.50 \cdot 10^7 \mu\text{S cm}^{-1}, E_a = 38 \text{ kJ mol}^{-1}, R^2_{\text{Arr}} = 0.9898$
127.8	117.5	$B = 1.06 \cdot 10^5 \mu\text{S cm}^{-1}, C = 1504 \text{ K}, T_0 = 165.9 \text{ K},$
153.6	123.5	$R^2_{\text{VFT}} = 0.9870, \sigma_{\text{Red}} = 141.7 \mu\text{S cm}^{-1} (120 \text{ }^\circ\text{C})$
187.3	129	
405.8	138	$P = \text{Iso}$
465.5	144	$A = 7.45 \cdot 10^7 \mu\text{S cm}^{-1}, E_a = 42 \text{ kJ mol}^{-1}, R^2_{\text{Arr}} = 0.9903$
539.9	150	$B = 3.00 \cdot 10^5 \mu\text{S cm}^{-1}, C = 1418 \text{ K}, T_0 = 197.9 \text{ K},$
634.9	156	$R^2_{\text{VFT}} = 0.9873$
779.3	162	
<b>[TRYUM-9,10][BF<sub>4</sub>]</b>		
4.5	121	$P = \text{SmB}$
4.9	126	$A = 8.72 \cdot 10^4 \mu\text{S cm}^{-1}, E_a = 32 \text{ kJ mol}^{-1}, R^2_{\text{Arr}} = 0.9800$
5.5	131	$B = 1.81 \cdot 10^4 \mu\text{S cm}^{-1}, C = 2741 \text{ K}, T_0 = 64.7 \text{ K},$
6.4	136	$R^2_{\text{VFT}} = 0.9793, \sigma_{\text{Red}} = 4.9 \mu\text{S cm}^{-1} (125 \text{ }^\circ\text{C})$
17.7	145	$P = \text{SmA}$
24.1	155	$A = 4.20 \cdot 10^7 \mu\text{S cm}^{-1}, E_a = 51 \text{ kJ mol}^{-1}, R^2_{\text{Arr}} = 0.9918$
30.7	165	$B = 1.27 \cdot 10^6 \mu\text{S cm}^{-1}, C = 3476 \text{ K}, T_0 = 109.8 \text{ K},$
42.2	175	$R^2_{\text{VFT}} = 0.9903, \sigma_{\text{Red}} = 235.2 \mu\text{S cm}^{-1} (239 \text{ }^\circ\text{C})$
60.6	185	

[TRYUM-9,14][ BF <sub>4</sub> ]		
6.5	141	$P = \text{SmA}$
10.4	151	$A = 1.41 \cdot 10^9 \mu\text{S cm}^{-1}, E_a = 66 \text{ kJ mol}^{-1}, R^2_{\text{Arr}} = 0.9995$
15.3	161	$B = 3.75 \cdot 10^5 \mu\text{S cm}^{-1}, C = 2367 \text{ K}, T_0 = 199.4 \text{ K},$
23.2	171	$R^2_{\text{VFT}} = 0.9985, \sigma_{\text{Red}} = 183.3 \mu\text{S cm}^{-1} (232 \text{ }^\circ\text{C})$
35.0	181	

$\sigma$  is the calculated conductivity at the respective temperature ( $T$ ) deduced by the second Ohm's law from the measured resistance.  $P$  is the phase within the material was analysed.  $A$  and activation energy ( $E_a$ ) are parameters deduced from the fitting of the conductivity data with the Arrhenius equation:  $\sigma = A \cdot e^{-E_a/RT}$ , where  $R = 8.31 \text{ JK}^{-1}\text{mol}^{-1}$  and  $T$  is expressed in K.  $B$ ,  $C$  and  $T_0$  are parameters deduced from the fitting of the conductivity data with the Vogel-Fulcher-Tammann (VFT) equation:  $\sigma = B \cdot e^{-C/(T-T_0)}$ .  $R^2_{\text{Arr}}$  and  $R^2_{\text{VFT}}$  are the constants of determination for the fitting with the Arrhenius and VFT equations respectively.  $\sigma_{\text{Red}}$  is the conductivity at the reduced temperature of 0.9, deduced using the fitted parameters.

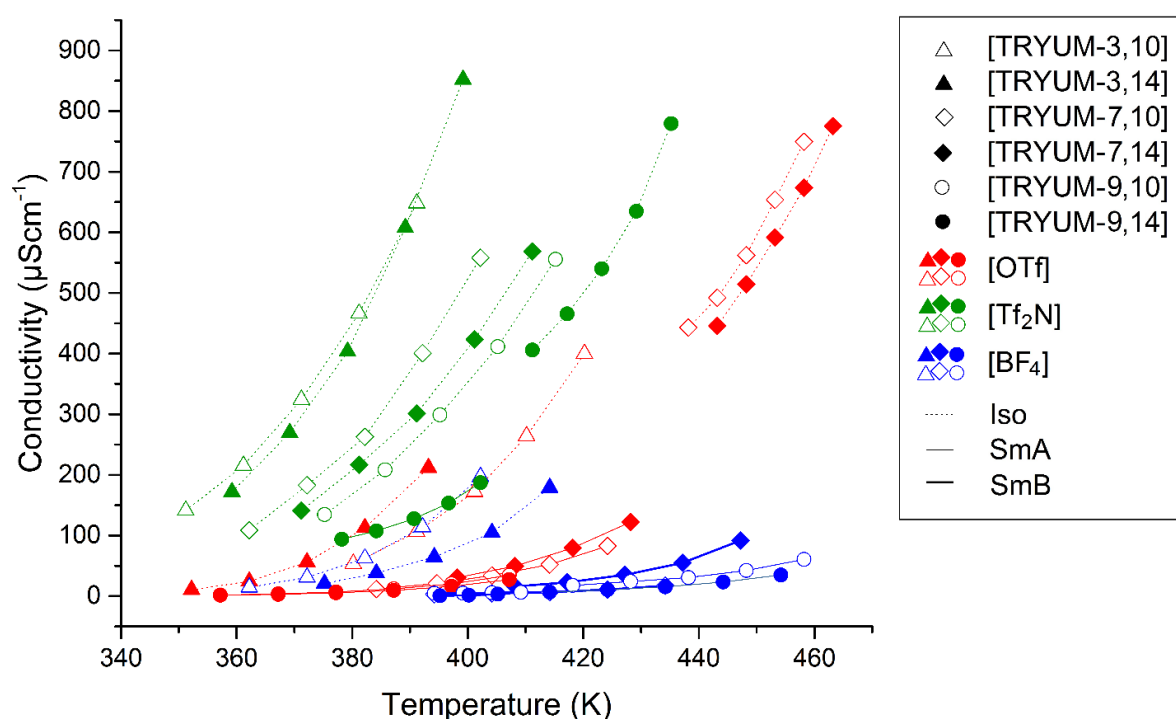


**Figure 65.** A plot of triazolium salt conductivities as function of temperature.

The data clearly suggest that the highest conductivities are shown by bis(triflimide)s and this is reasonable, because it is known that ILs containing the  $[\text{Tf}_2\text{N}]^-$  anion exhibit relatively low viscosities and high conductivity when combined with other cations. This has been attributed to the partially delocalised charge in the anion which reduces the strength of anion-cation interactions, thus imparting flexibility into the structure and allowing higher ion mobility.<sup>104</sup> This is, however, somewhat offset by the larger size of the  $[\text{Tf}_2\text{N}]^-$  anion, which reduces ion mobility. Trying to compare triazolium salts with same cation but with different anions in reasonably comparable temperature, it can be noted that ILs containing the  $[\text{BF}_4]^-$  anion show the lowest conductivities. ILs containing the  $[\text{OTf}]^-$  show conductivities intermediate between  $[\text{Tf}_2\text{N}]^-$  and  $[\text{BF}_4]^-$  salts. This can also be justified on the basis of the degree of charge delocalisation of the ions, with the  $[\text{OTf}]^-$  anion being intermediate between the

other two kinds of anions in terms of its size and charge density. In line with the molecular mobility, which generally decreases with the increasing molecular size, the conductivity decreases with the increasing alkyl-chain length and even more with the increasing perfluoroalkyl-chain length. The latter is a stiff moieties, which could decrease the ability of the cations to move through the liquid.

Within different phases of the same compound, the conductivity seems to increase as the compound moves between the LC phases and the isotropic liquid. This effect could be covered by the exponential relation between conductivity and temperature, since existing field of isotropic phases always lies at higher temperature. However, comparing parameters extrapolated from fitting with Arrhenius ( $A$ ) or VFT ( $B$ ) equations such as the  $E_a$ , the conductivity profile changes after the phase transition. This appears clear when focusing on the fitted parameters (Figure 66) of SmA and Isotropic phases of the analysed salts (*i.e.* [TRYUM-7,10][OTf], [TRYUM-7,14][OTf] and [TRYUM-9,14][Tf<sub>2</sub>N]) as well as the fitted parameters of SmB and SmA phases of the [BF<sub>4</sub>]<sup>-</sup> salts (*i.e.* [TRYUM-7,14][BF<sub>4</sub>] and [TRYUM-9,10][BF<sub>4</sub>]).

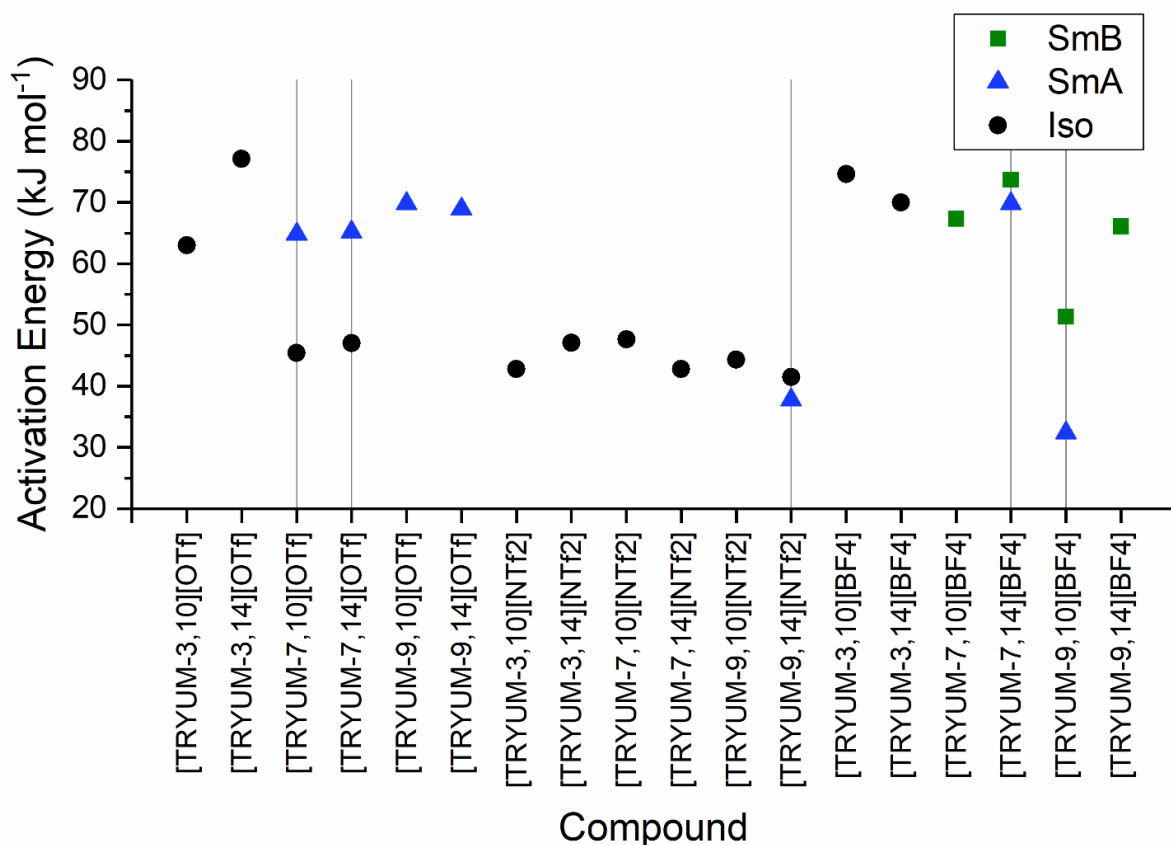


**Figure 66.** A plot of the extrapolated triazolium salt activation energies as function of the structure.

Within the same compound, the  $E_a$  usually decreases from SmB to SmA and from SmA to Iso phases. This can be translated as an increasing conductivity profile from SmB to SmA and Iso phases, with an exception for [TRYUM-9,14][Tf<sub>2</sub>N], which is the unique enantiotropic bis(triflimide) salt that allowed



conductivity measurements in the SmA phase. However, not only the  $E_a$  can be used to compare and describe the conductivity of the salts in the different phases. It is also possible to compare the extrapolated conductivities at the same reduced temperature (Figure 67). Although, the triflate salts seem to describe a trend in function of the molecular length, but this trend could be led by the difference in the absolute temperatures. At the same way, the conductivity of [TRYUM-9,10][BF<sub>4</sub>] is higher in SmA than SmB phase, but again the reduced temperature corresponds to very different absolute temperatures. In these terms, a comparison between the extrapolated conductivities at the same absolute temperature could be more useful.

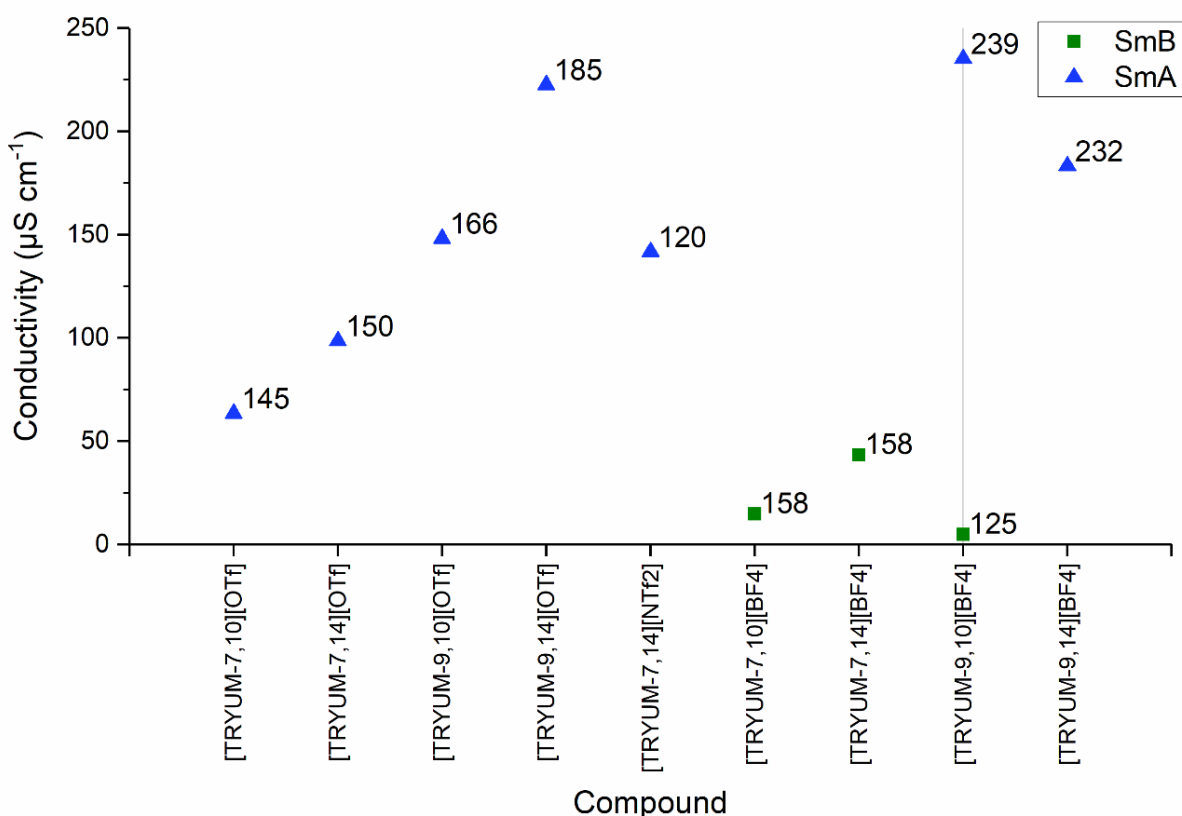


**Figure 67.** A plot of the extrapolated triazolium salt conductivities at the same reduced temperature. The point labels indicate the respective absolute temperature (°C) referred to the reduced temperature (0.9).

A plot of the extrapolated conductivities at the same absolute temperature allow a complete comparison, which involve also the isotropic phase (Figure 68). The temperature of 100 °C was chosen for the plot, since the most of the triazolium salts show LC or isotropic phase at this temperature. Nevertheless, some extrapolated conductivities showed in the plot are virtual, *i.e.* they belong to phases that are physically incongruent with the temperature. However, at the absolute temperature of 100 °C the bis(triflimide) salts show the highest conductivities, with decreasing trend with molecular weight. The SmA conductivities of the triflate salts and the SmB conductivities of the tetrafluoroborate salt are invariant. Generally, the Iso conductivities are higher than the SmA conductivities as well as

the SmA conductivities are higher than the SmB conductivities, with an exception for **[TRYUM-9,14][Tf<sub>2</sub>N]**, as mentioned during comparison of the activation energies.

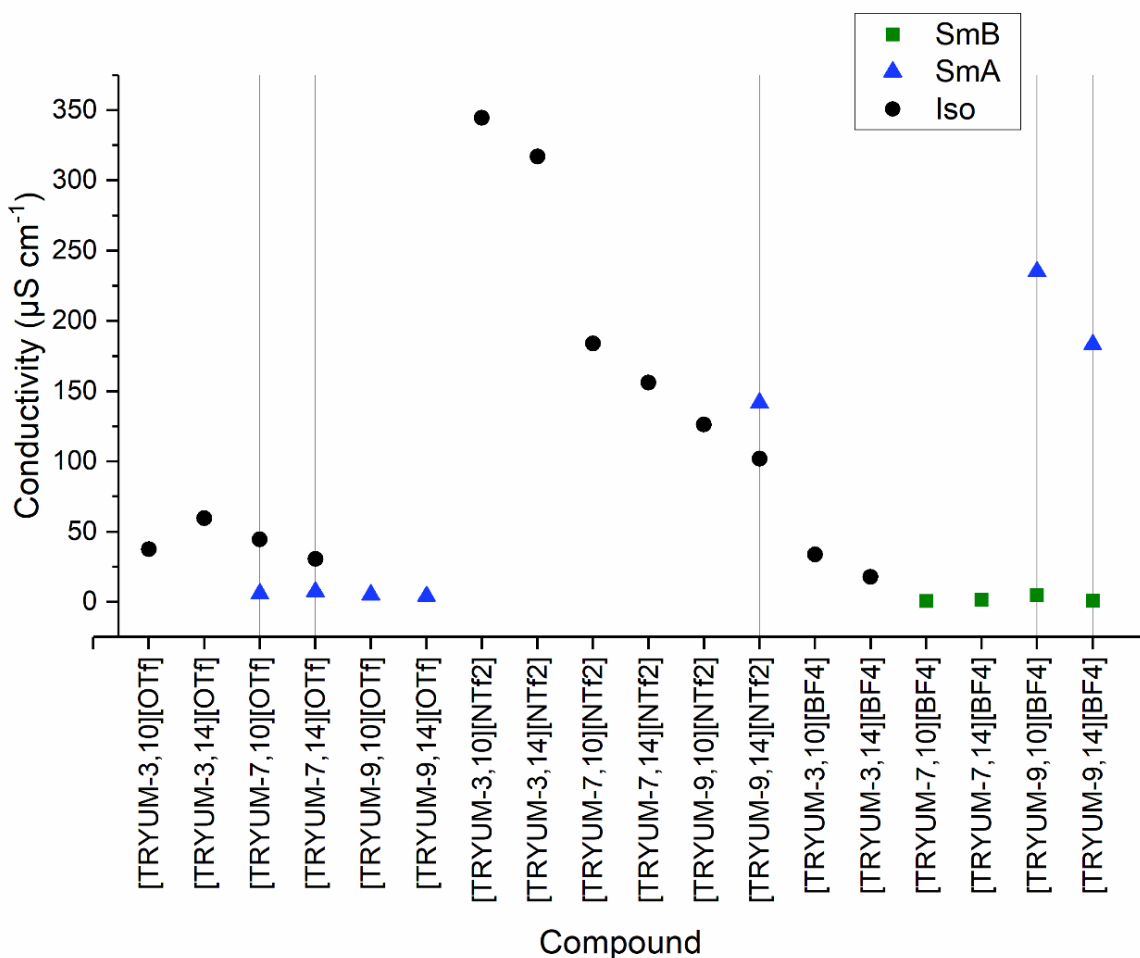


**Figure 68.** A plot of the extrapolated triazolium salt conductivities at the same absolute temperature (100 °C).

Briefly, in line with the decreasing viscosity, the conductivity of triazolium salts increases over transitions from SmB to SmA and from SmA to Isotropic phases. This suggests that molecular order of the triazolium phases gives viscous phases, which decrease the ion mobility, and don't lead to any enhancement of the conductivity, in this system. However, during EIS measurements, no alignment of the samples was performed through the electrode plates. Indeed, the alignment could show an enhancement of the conductivity along one direction in the more ordered LC phases,<sup>114</sup> which could potentially explain the countertrend observed for **[TRYUM-9,14][Tf<sub>2</sub>N]**.

Overall, triazolium salts presented in this work show relatively low conductivity values compared with other materials commonly used in opto-electric devices such as dye-sensitised solar cells.<sup>5,115,116</sup> Nevertheless, the absolute conductivity may be not important for other applications as semiconductor or as anisotropic fluid means for conductivity dopants. In any case, here is reported a careful characterisation of the triazolium phases, which will facilitate their application in the future. Moreover,

the conductivity studies allowed to understand the ion mobility as function of the anion, the alkyl- and the perfluoroalkyl-chain, as well as the phase of the system. This is powerful fundamental insight into the dynamics in this system that complements the synthetic and the phase range data really well. Whereby, the system can be specifically tuned in order to match the desiderate combination of LC and conductivity properties.

### 3.6 Further developments

During some crystallisation attempts to purify or to obtain single crystals suitable for XRD analysis, some triazolium salts showed gelling properties when mixed with some solvents.

For instance, salts such as **[TRYUM-7,10][BF<sub>4</sub>]**, **[TRYUM-7,14][BF<sub>4</sub>]**, **[TRYUM-7,14][OTf]**, and **[TRYUM-3,10][BF<sub>4</sub>]** gelled when mixed with specific ratio (around 1:5) of DCM or ethyl acetate and hexane, giving quite homogeneous and transparent gels (e.g. Figure 69).

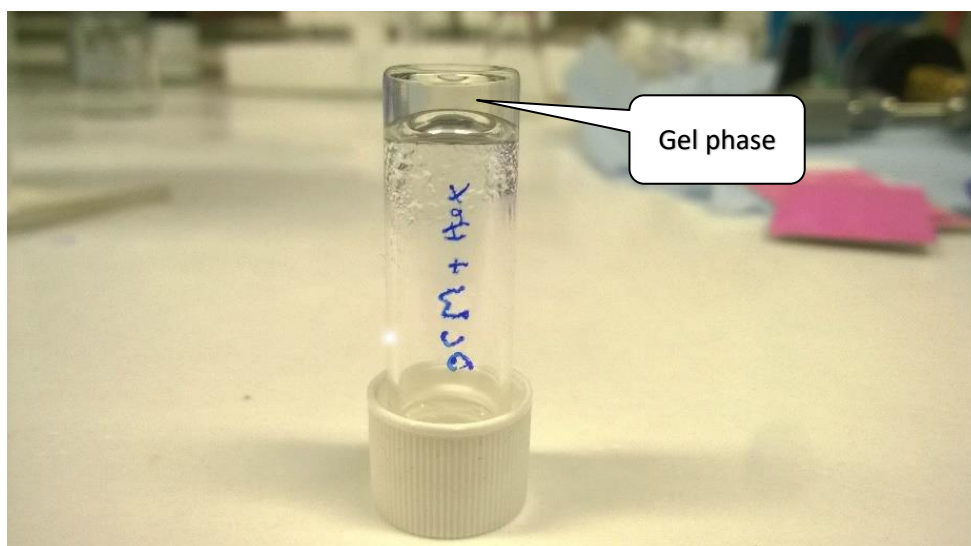


**Figure 69.** Gel phase obtained mixing **[TRYUM-7,10][BF<sub>4</sub>]** with DCM and hexane.

After this peculiar behaviour had been noticed, triazolium salts were tested in order to study this behaviour and assess any relationship with anion/cation structure and the formation of gels, as well as to assess the suitability of triazolium salts as gelators for environment or gas storing application.

#### 3.6.1 Organogels

An organogel is a class of gel composed of a liquid organic phase within a three-dimensional, cross-linked network. Organogel networks can form in two ways. The first is classic gel network formation via polymerisation. This mechanism converts a precursor solution of monomers with various reactive sites into polymeric chains that grow into a single covalently-linked network. At a critical concentration (the gel point), the polymeric network becomes large enough so that on the macroscopic scale, the solution starts to exhibit gel-like physical properties: an extensive continuous solid network, no steady-

state flow, and solid-like rheological properties.<sup>117</sup> However, organogels based on ‘low molecular weight gelators’ can also be designed to form gels via self-assembly. Secondary forces, such as van der Waals interactions or hydrogen bonding, cause monomers to cluster into a non-covalently bonded network that retains organic solvent, and as the network grows, it exhibits gel-like physical properties.<sup>118</sup> Both gelation mechanisms lead to gels characterised as organogels.

Organogels are useful in applications such as drug delivery mediums for topical and oral pharmaceuticals<sup>119</sup> as well as for cosmetics cleaning materials for art conservation.<sup>120</sup>

The capacity of fluorinated material to gel specific solvent (*i.e.* benzene) is known since the report of the first FIL.<sup>17</sup> Specifically, organogels containing fluorine groups have raised the interest of scientific community for their sorption properties suitable in gel materials used as gas storage.<sup>121</sup>

### 3.6.2 Use of triazolium salts as gelators

Gels obtained by mixing triazolium salts with hexane are not stable in open system, as expectable considering the high volatility of such solvent. Indeed, when they are leaved in open system they, the structure of the gel collapse: it liquefys in some minutes first and a precipitation of solids is followed. The observed gelling properties of the triazolium salts has been attributed to the interaction with the alkane hexane. Due to the polarity of the salts, which are not soluble in non-polar hydrocarbons such as hexane, a second solvent was necessary to mix the triazolium salts with alkanes. Indeed, once the gelator, the alkane and a second solvent such as DCM are homogenously mixed, the more volatile DCM slowly evaporated leaving in contact the other two components.

**Table 9.** Scheme of gelation test of triazolium compounds in heptane.

Compound	0.5 mg ml <sup>-1</sup>	1 mg ml <sup>-1</sup>	2 mg ml <sup>-1</sup>	4 mg ml <sup>-1</sup>	6 mg ml <sup>-1</sup>	10 mg ml <sup>-1</sup>
[TRYUM-3,10][BF <sub>4</sub> ]	-	S	G	GP	GP	-
[TRYUM-9,10][BF <sub>4</sub> ]	-	-	S	G	GP	-
[TRYUM-7,10][BF <sub>4</sub> ]	S	G	G	G	G	G
[TRYUM-7,12][BF <sub>4</sub> ]	-	S	G	G	GP	GP
[TRYUM-7,14][BF <sub>4</sub> ]	-	S	G	G	GP	-
[TRYUM-7,10][OTf]	-	P	P	P	P	P
[TRYUM-7,14][OTf]	-	-	P	P	P	-
[TRYUM-9,10][OTf]	-	-	P	P	-	-
[TRYUM-3,10][Tf <sub>2</sub> N]	-	P	P	P	-	-
[TRYUM-7,10][Tf <sub>2</sub> N]	-	P	P	P	P	-
[TRYUM-7,10][Tf <sub>2</sub> N]	-	P	P	P	P	-
[TRYUM-9,10][Tf <sub>2</sub> N]	-	P	P	P	P	-

S, G, P and GP are solution, gel, precipitate and gel with precipitate states respectively.

Other gels more stable in open atmospheric system were obtained replacing hexane with less volatile alkanes. For instance, gels stable for hours (to two days) has been obtained with several concentration

of **[TRYUM-7,*n*][BF<sub>4</sub>]** in heptane, where 1 mg/mL has been identified as the MGC. Despite the fact they are relatively stable in an open vessel, the volatility of heptane (whose boiling point is about 103°C) makes the gel volume visibly reduce over some hours. If on the one hand the volatility of heptane makes less stable the gels, on the other hand it makes easier the obtaining of xerogels by lyophilisation, so this property may be of some use in future studies.

Since **[TRYUM-7,10][BF<sub>4</sub>]** has been found to be the best gelator in combination with heptane (*i.e.* among the triazolium salts tested, it showed the smallest MGC and the best quality of gel in terms of stability and homogeneity), it was tested for gelation with decane (boiling point 174°C), giving very stable gel at atmospheric pressure and room temperature. 4 mg/mL has been identified as the MGC for **[TRYUM-7,10][BF<sub>4</sub>]** in decane, and the gel resulted stable in an open vessel for more than 2 weeks.

Further developments are in progress and in future, the organogel properties of the triazolium salts will be fully characterised.

## 4. Conclusion

Considering the increasing applications of functional organic salts in the field of innovative materials, this work represents the first systematic approach to evaluate the effect of key structural features of triazolium based salts on their physicochemical properties including phase organization, conductivity and gelation ability.

Considering the simultaneous presence of alkyl and perfluoroalkyl chains, the explored matrix of variable structural parameters concerned the length of the two chains as well as the nature of the anion. This rational setup allowed for a three-dimensional structure-property correlation based on twenty-seven salts where each variable was explored by considering three values. Specifically, long ( $C_9F_{19}$ ), medium ( $C_7F_{15}$ ) and short ( $C_3F_7$ ) perfluoroalkyl chains were differently enough to produce an effect on the investigated properties. These effects were evident even at shorter chain lengths with respect to the non-fluorinated alkyl chains which were explored as  $C_{10}H_{21}$ ,  $C_{12}H_{25}$ , and  $C_{14}H_{29}$ . This difference is due to a well known feature of perfluorinated chains, which present a major order compared to the corresponding alkyl chains, caused by conformational arrangement of fluoromethylene groups. Such aspects were confirmed also by single X-ray data which, in some cases, highlighted some helicity in the fluorinated moiety. As for the third variable, explored counter anions considered triflates, tetrafluoroborates and bis(triflimides), which differ in size and electronic properties thus affecting interionic interactions.

A synthetic strategy has been designed and implemented to allow the synthesis of the entire series of salts based on 5-(4-(alkyloxy)phenyl)-1,4-dimethyl-3-(perfluoroalkyl)-1,2,4-triazol-4-ium. Such strategy exploits ANRORC reactivity of readily available 5-perfluoroalkyl-1,2,4-oxadiazoles as versatile synthons for fluorinated triazolic systems.

The methylation process for quaternisation of 1,2,4-triazole derivatives has been thoroughly investigated from the regioselectivity point of view and optimised in terms of yields. In this context NMR spectroscopic and single X-ray measurements confirmed methylation at the N(4) of the triazole ring.

The phase behaviour of these compounds was preliminarily studied and LC properties of this new family of salts were studied by thermal analysis and microscopic investigation as a function of the salts highlighting structural elements for the modulation of tunable properties. Specifically, all triazolium salts with long and medium perfluoroalkyl chains have been classified as ILCs due to their mesophasic behaviour, shown also by bis(triflimides) salts. On the other hand, results showed that shorter perfluoroalkyl chain ( $C_3F_7$ ) was not sufficient to maintain a mesogenic behaviour and related salts have been classified as ILs. Along the series, a large number of single X-ray crystal structures were obtained. Collected crystal data permitted a good characterisation of the structural and organisation changes

that arose as a function of structural changes in the cation and anion. Organisation properties of the material was studied on crystal, meso- and isotropic-phases over temperature by SAXS characterisation. Eighteen out of twenty-seven compounds were reproduced scaling-up the synthesis in order to obtain bigger amount of material, which was enough to carry out further experiments such as SANS and conductivity analysis. No deuteration was required, as the non-deuterated materials had SLD differences between the different parts of the salts with sufficient contrast for SANS. Temperature-dependent small-angle neutron scattering was measured on the SANS2D diffractometers at the ISIS Pulsed Neutron Source (STFC Rutherford Appleton Laboratory - Didcot, U.K.). A comparison between SANS and SAXS data, as well as fitting of data based on Lorentzian models integrated the structure-properties correlation analysis. Moreover, the investigation of electrochemical properties as a function of temperature required the design and setup of a tailor-made heating block and electrode probe. These were manufactured and used at the University of York to study the conductivity and ionic mobility properties of the materials as a function of phase behaviour.

Crystallographic, small-angle scattering and electrochemical data identified the ways that a range of properties changed as the nature of the anion and cation in the salts changed. These include the order and the structuring of the micro-organisation as well as the micro-segregation of fluorine domain as well as the ionic mobility and conductivity in function of the kind of anion, perfluoroalkyl and alkyl-chain length.

In summary, it was observed that the thermal and other behaviour of the triazolium salts strongly depends on the anion and highlighted the following trends. Crystal order and conductivity within the mesomorphic and isotropic phases are depending on the anion size with the largest anion ( $[\text{Tf}_2\text{N}]^-$ ) showing the highest ionic mobility and the highest order in the crystal phase. Counterwise, bis(triflimide)s presented less pronounced LC properties, as confirmed by scattering data showing a more compact arrangement in the crystal with respect to mesophase, an opposite behaviour with respects to salts with a different anion. In turn, salts with the  $[\text{OTf}]^-$  anion, had an intermediate ionic mobility and improved LC properties. On the contrary, the crystal phase of triazolium triflate salts were the most disordered, while the mesophases were found to be more compacted than the crystalline phases. Finally, triazolium compounds with  $[\text{BF}_4]^-$  anion showed the lowest ionic mobility and conductivity as well as the most complex LC behaviour, while all the other properties are intermediate between triazolium  $[\text{Tf}_2\text{N}]^-$  and  $[\text{OTf}]^-$  properties. Additionally, tetrafluoroborate salts were the most suitable for generating transparent gel phase when in conjunction with apolar hydrocarbons.

Both alkyl and perfluoroalkyl chain lengths are able to influence the molecular micro-segregation and spatial order in phases, albeit with lesser effect than the anion. Overall, longer perfluoroalkyl chains increase the mesophase range and stability, as well as the structural order, but decrease the ionic

mobility and conductivity. For instance, perfluoropropyl-chain is not long enough to provide any LC properties. On the other hand, mesophases stability is less dependent on alkyl chain length, but it slightly widens or shifts to higher temperatures for longer alkyl groups which also slightly decreases the ionic mobility and conductivity.

In conclusion, reported study represents the first step of the rationalization of physical and electrochemical features of ionic materials based on hybrid hydro/fluoro-carburic scaffolds. The studied model system considered chain lengths and anion types as main factors to investigate. Nevertheless, chain arrangements along the semirigid bi-aryl core would be a very interesting parameter to explore in further studies. For instance, changes in the nature of the five-membered heterocyclic core or substitution of the phenyl moiety expand the scope of present, opening the way to a variety of heteroaromatic analogues.



## 5. Experimental section

### 5.1 Material and methods

Flash chromatography was performed using silica gel (200-400 mesh) and mixtures of ethyl acetate and light petroleum (fraction boiling in the range 40-60°C) in various ratios as eluents. All other starting materials and solvents were purchased from standard commercial sources and were used without further purification. No protective atmosphere was required during the synthesis unless stated otherwise.

Solution-state NMR spectra were recorded on a JEOL ECS spectrometer operating at 400 MHz ( $^1\text{H}$ ), 376 MHz ( $^{19}\text{F}$ ) as solutions in  $\text{CDCl}_3$  or  $\text{CD}_3\text{CN}$ , unless stated otherwise. One dimensional  $^1\text{H}$  NOE NMR experiments were performed on a Bruker AVANCE 500 spectrometer operating at 500 MHz ( $^1\text{H}$ ), 125.6 MHz ( $^{13}\text{C}\{^1\text{H}\}$ ) at a temperature of 298 K and on samples in solution in  $\text{CDCl}_3$ .

CHN analysis were carried out on an Exter Analytical Inc. CE-440 Elemental Analyzer.

Single crystal XRD experiments were carried out on a SuperNova Eos diffractometer. The crystal was kept at 110.05(10) K during data collection, using  $\text{CuK } \alpha$  ( $\lambda = 1.54184 \text{ \AA}$ ) as radiation.

#### 5.1.1 Polarized optical microscopy

Polarised optical microscopy was performed on a Zeiss Axioskop 40Pol microscope using a Mettler FP82HT hot-stage controlled by a Mettler FP90 central processor. Photomicrographs were captured via an InfinityX-21 MP digital camera mounted atop the microscope. Images were recorded at a magnification of 100x, and 200x during heating and cooling of the samples which were placed between two cover slips. Heating and cooling rates were 0.1-10  $\text{K min}^{-1}$ .

#### 5.1.2 Differential scanning calorimetry

Differential scanning calorimetry parameters were determined on a Mettler DSC822<sup>e</sup> thermal analyser fitted with an autosampler operating with Mettler Stare software and calibrated before use against an indium standard (onset =  $156.55 \pm 0.2 \text{ }^\circ\text{C}$ ,  $\Delta H = 28.45 \pm 0.40 \text{ J g}^{-1}$ ). Samples were prepared in 40  $\mu\text{L}$  aluminium light crucibles, using an XS105 as analytical balance, and analysis were carried out with a rate of  $10 \text{ }^\circ\text{C min}^{-1}$  for each sample under a  $\text{N}_2$  flux of  $60 \text{ cm}^3 \text{ min}^{-1}$ .

#### 5.1.3 Small-angle X-ray Scattering

Temperature-dependent small-angle X-ray scattering experiments were performed using a Bruker D8 Discover instrument equipped with a temperature-controlled, bored graphite rod furnace, custom built at the University of York. The radiation used was copper  $\text{K}\alpha$  ( $\lambda = 1.54056 \text{ \AA}$ ) from a 1  $\mu\text{S}$  microfocus source. Diffraction patterns were recorded on a 2048 x 2048 pixel Bruker VANTEC 500 area detector. Samples were filled into 1.0 mm capillary tubes and aligned with a pair of 1 T magnets. Diffraction

patterns were collected as a function of temperature and data processed using the DIFFRAC.EVA software.

#### 5.1.4 Small-angle Neutron Scattering

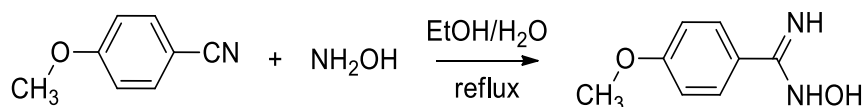
Temperature-dependent small-angle neutron scattering data were measured at the SANS2D diffractometer at the ISIS Pulsed Neutron Source (STFC Rutherford Appleton Laboratory, Didcot, U.K.). SANS2D is a time-of-flight instruments and uses neutrons with an incident wavelength of  $2.2 \text{ \AA} < \lambda < 14 \text{ \AA}$ , and with the  $1 \text{ m}^2$  detector offset sideways and vertically by 150 mm, the resulting Q range was  $0.006 \text{ \AA}^{-1} < Q < 0.7 \text{ \AA}^{-1}$ . Appropriate normalisation using site-specific procedures gave the absolute cross section  $I(Q)(\text{cm}^{-1})$  as a function of the momentum transfer  $Q (\text{\AA}^{-1})$ . Measurements of the samples (no deuteration was needed to provide the necessary contrast), were collected as a function of temperature, after 30 minutes of equilibration time and the material was placed in Hellma quartz cuvettes with a path length of 1 mm, which allows an incident beam diameter of 12 mm.

#### 5.1.5 Electrochemical characterisation

Platinum electrodes were used for the electrochemical characterisation of the triazolium ILs by impedance spectroscopy. The dependence of conductivity from the electrochemical cell potential was investigated using a computer-controlled potentiostat (SP-150 with EC-Lab<sup>®</sup> software package) through impedance measurements. The impedance spectra were measured in the frequency range from 1.0 Hz to 1.0 MHz with AC potential amplitude of 120, 240, 300, 400 and 500 mV at specific temperatures controlled by an aluminium/brass furnace custom built at the University of York. Impedance spectra were measured at the following polarisation potential: -10 V. Laboratory made electrochemical cell was used in all electrochemical experiments. Cell parameters are the following: volume — 0.112 mL, electrode area —  $0.4 \times 0.4 \text{ cm}$ , and distance between anode and cathode (Pt plates) — 0.7 cm. Pt wire was used as a reference electrode. According to Ohm's law, the resistance R for the above circuit is given by  $R = \rho \cdot \ell / A$ , where  $\rho$  is the resistivity (also called specific electrical resistance) of the solution (in  $\Omega \text{ cm}$ ),  $\ell$  — distance between electrode (in cm) and A — the cross-sections area of electrodes (in  $\text{cm}^2$ ). The electrodes were used without additional polishing. The active area of the electrodes was determined with conductivity standard solutions ( $12880$  and  $5000 \mu\text{S cm}^{-1}$ ) solution before impedance measurements. Impedance data of the triazolium ILs and ILCs were analysed using the complex plane Nyquist plot.

## 5.2 Synthesis and characterisation

### 5.2.1 Procedure for the synthesis of compound 2

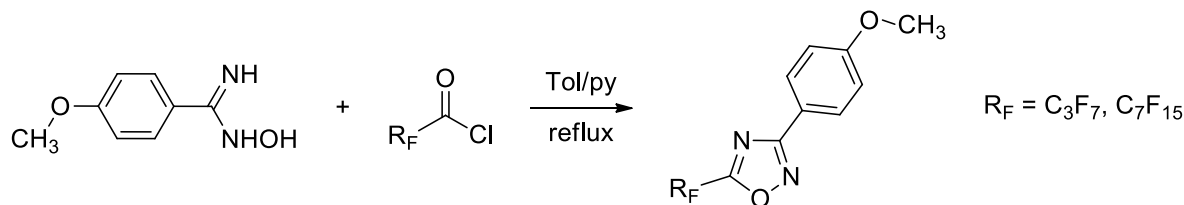


4-Methoxybenzonitrile (4.100 g; 30.79 mmol) was dissolved in EtOH (60 mL) in a 250 mL round-bottomed flask. Separately NaOH (2.460 g; 2.0 mol eq.) was dissolved in an amount of water as small as possible in another flask, using ice to help the dissolution, and NH<sub>2</sub>OH·HCl (4.280 g; 2.0 mol eq) was added. The solutions were blended together and heated under reflux for 6 h and the reaction was monitored by TLC (petroleum ether and ethyl acetate 5:1). Ethanol was removed under vacuum, water (100 mL) was added and the precipitate was filtered under vacuum, washing with cold water. The Z-isomer was isolated by chromatography using petroleum ether and ethyl acetate 1:2. Yield = 55%.

#### (Z)-N'-Hydroxy-4-methoxybenzimidamide

Colourless solid. <sup>1</sup>H NMR (400 MHz, DMSO)  $\delta$ : 9.49 (s, 1H), 7.62 (d, *J* = 8.8 Hz, 2H), 6.92 (d, *J* = 8.8 Hz, 2H), 5.73 (s, 2H), 3.76 (s, 3H).

### 5.2.2 General procedure for the synthesis of compounds 3-3 and 3-7



N'-Hydroxy-4-methoxybenzimidamide (**2**) (2.450 g, 14.8 mmol) was dissolved in toluene (75 ml) in a 250 ml round-bottomed flask. Next pyridine (2 mL) and perfluorobutanoyl chloride or perfluorooctanoyl chloride (1.5 mol eq.) were added. The obtained solution was heated under reflux for 5-7 h and the reaction was monitored by TLC (petroleum ether and ethyl acetate 50:1). Following the reflux, the mixture was dried under vacuum, water (100 mL) was added, pH was adjusted to 4-5 with a dilute HCl solution and the organic compounds were extracted with ethyl acetate (3 x 40 mL). After this the organic phases were dried with Na<sub>2</sub>SO<sub>4</sub> and compounds **3-3** and **3-7** were isolated by chromatography using petroleum ether/ethyl acetate 5:1 as eluents. Yields = 64-83%.

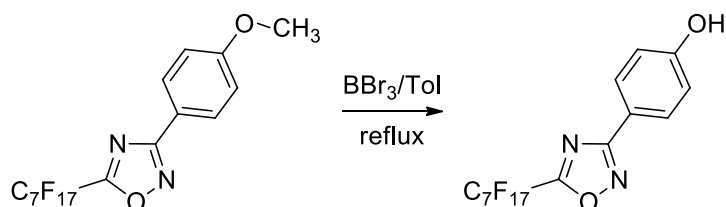
#### 3-(4-Methoxyphenyl)-5-(perfluoropropyl)-1,2,4-oxadiazole (3-3)

Colourless solid. <sup>1</sup>H NMR (300 MHz, CDCl<sub>3</sub>)  $\delta$ : 8.07 (AA'XX', *J* = 8.9 Hz, 2H), 7.02 (AA'XX', *J* = 8.9 Hz, 2H, Ar), 3.89 (s, 3H).

### 3-(4-methoxyphenyl)-5-(perfluoroheptyl)-1,2,4-oxadiazole (3-7)

Colourless solid.  $^1\text{H}$  NMR (400 MHz,  $\text{CDCl}_3$ )  $\delta$ : 8.07 (AA'XX',  $J = 8.9$  Hz, 2H), 7.02 (AA'XX',  $J = 8.9$  Hz, 2H, Ar), 3.89 (s, 3H).

#### 5.2.3 Procedure for the synthesis of compound 3-7.1

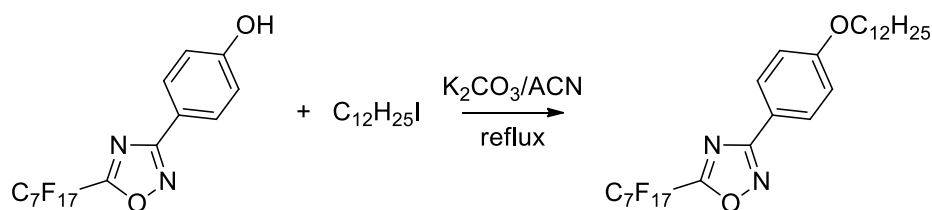


Oxadiazole **3-7** (0.12 g, 0.23 mmol) was dissolved in toluene (60 mL) in a 250 mL 3-neck round-bottomed flask and after this and  $\text{BBr}_3$  in heptane (6 mL in each) were added. The mixtures were heated under reflux for 3.5 h and the reaction was monitored by TLC (petroleum ether and ethyl acetate 5:1). After this, water (15 mL) was added and the mixture was heated for another hour. After this the mixture was dried under vacuum, further water (50 mL) was added, pH was adjusted to neutral with a dilute NaOH solution and it was extracted with ethyl acetate (25 mL x 3). The organic phase was dried with  $\text{Na}_2\text{SO}_4$  and the compounds **3-7.1** was isolated by chromatography using petroleum ether/ethyl acetate 5:1 and 2:1 as eluents. Yields = 74%

### 4-(5-(Perfluoroheptyl)-1,2,4-oxadiazol-3-yl)phenol (3-7.1)

Colourless solid.  $^1\text{H}$  NMR (300 MHz,  $\text{CDCl}_3$ )  $\delta$ : 7.59 (AA'XX',  $J = 8.8$  Hz, 2H), 6.96 (AA'XX',  $J = 8.8$  Hz, 2H), 5.84 (s, 1H).

#### 5.2.4 Procedure for the synthesis of compound 3-7.2

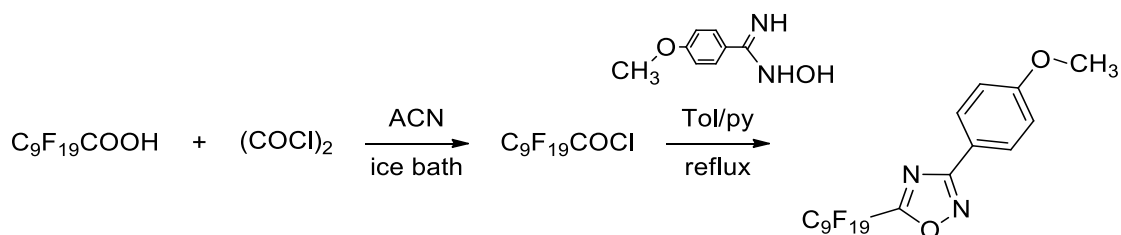


Oxadiazole **3-7.1** (0.11 g, 0.16 mmol) was dissolved in  $\text{CH}_3\text{CN}$  (15 mL) in a 100 mL round-bottomed flask as well as  $\text{K}_2\text{CO}_3$  (3 mol eq.) and 1-bromododecane were added (1.5 mol eq.). The obtained mixture was heated at 80 °C for 6 h and after cooling, was dried under vacuum, water was added, pH was adjusted to neutral with a dilute HCl solution and the organic compounds were extracted with ethyl acetate (25 mL x 3). The organic phase was dried with  $\text{Na}_2\text{SO}_4$  and the compounds **3-7.2** were isolated by chromatography using petroleum ether/ethyl acetate 20:1 and 5:1 as eluents. Yields = 89%.

### 3-(4-(Dodecyloxy)phenyl)-5-(perfluoroheptyl)-1,2,4-oxadiazole (3-7.2)

Colourless solid.  $^1\text{H}$  NMR (400 MHz,  $\text{CDCl}_3$ )  $\delta$ : 7.64 (AA'XX',  $J = 8.6$  Hz, 2H), 7.02 (AA'XX',  $J = 8.6$  Hz, 2H), 4.02 (t,  $J = 6.5$  Hz, 2H), 1.82 (p,  $J = 6.4$  Hz, 2H), 1.57 – 1.10 (m, 18H), 0.88 (t,  $J = 6.5$  Hz, 3H).

### 5.2.5 Procedure for the synthesis of compound 3-9

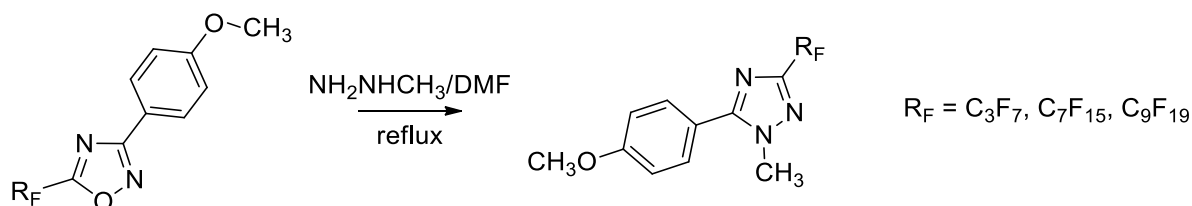


The acid  $\text{C}_9\text{F}_{19}\text{COOH}$  (6 g, 11.671 mmol) was degassed in a 3-neck 250 mL round-bottomed flask with three cycles and vacuum nitrogen, and then dried acetonitrile (about 60 mL) was added by cannula under vacuum along with a drop of DMF. After this the flask was put on ice bath and  $(\text{COCl})_2$  (3 eq. mol) was added dropwise with bubbling and the formation of a white solid took place. The mixture was left on ice bath stirring for 2 h and after this the solvent was removed by cannula filtration under nitrogen, washing the product with cold acetonitrile and drying under vacuum. *N'*-hydroxy-4-methoxybenzimidamide (**2**) (1.8 g, 10.89 mmol) was added and the solid mixture was degassed with three cycles of vacuum and nitrogen. After this dried toluene (70 mL) was added by cannula under vacuum, along with pyridine (2 mL) and the mixture was heated under reflux overnight under nitrogen. After cooling, water (100 mL) was added and the organic compounds were extracted with ethyl acetate (3 x 50 mL). After this the organic phases were dried with  $\text{Na}_2\text{SO}_4$  and compound **3-9** was isolated by chromatography using petroleum ether/ethyl acetate 5:1 as eluents. Yields = 64%

#### 3-(4-Methoxyphenyl)-5-(perfluorononyl)-1,2,4-oxadiazole (3-9)

Colourless solid.  $^1\text{H}$  NMR (400 MHz,  $\text{CDCl}_3$ )  $\delta$ : 8.07 (AA'XX',  $J = 8.7$  Hz, 1H), 7.02 (AA'XX',  $J = 8.7$  Hz, 1H), 3.89 (s, 2H).

### 5.2.6 General procedure for the synthesis of compounds 4-m



The compounds **3-3** (2.700 g, 7.84 mmol), **3-7** (2.700 g, 4.96 mmol) and **3-9** (2.700 g, 4.19 mmol) were dissolved separately in DMF (6 mL) in small round-bottomed flasks and methylhydrazine (5 mol eq.) was added to each tube. The solution was stirred and heated at 150 °C for 1.5-2.5 h and the reaction was monitored by TLC (petroleum ether/ethyl acetate 5:1). After cooling, water was added (100 mL), pH was adjusted to neutral with HCl solution and the organic compounds were extracted with diethyl ether (40 mL x 3). Then the organic phase was dried with  $\text{Na}_2\text{SO}_4$  and the compounds **4-m** were isolated and purified by chromatography (using petroleum ether/ethyl acetate 5:1). Yields = 74-86%

### 5-(4-Methoxyphenyl)-1-methyl-3-(perfluoropropyl)-1,2,4-triazole (4-3)

Colourless solid.  $^1\text{H}$  NMR (300 MHz,  $\text{CDCl}_3$ )  $\delta$ : 7.65 (AA'XX',  $J = 8.8$  Hz, 2H), 7.04 (AA'XX',  $J = 8.8$  Hz, 2H), 4.06 (s, 3H), 3.88 (s, 3H).

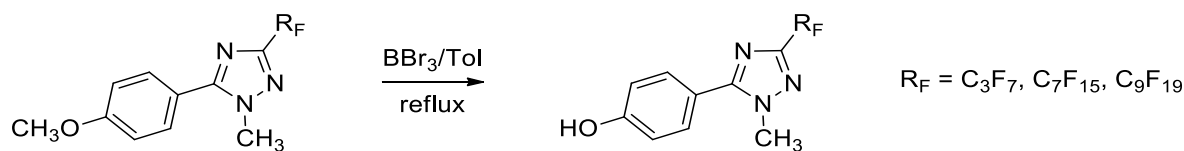
### 5-(4-Methoxyphenyl)-1-methyl-3-(perfluoroheptyl)-1,2,4-triazole (4-7)

Colourless solid.  $^1\text{H}$  NMR (400 MHz,  $\text{CDCl}_3$ )  $\delta$ : 7.66 (AA'XX',  $J = 8.8$  Hz, 2H), 7.04 (AA'XX',  $J = 8.8$  Hz, 2H), 4.06 (s, 3H), 3.88 (s, 3H).

### 5-(4-Methoxyphenyl)-1-methyl-3-(perfluorononyl)-1,2,4-triazole (4-9)

Colourless solid.  $^1\text{H}$  NMR (400 MHz,  $\text{CDCl}_3$ )  $\delta$ : 7.66 (AA'XX',  $J = 8.9$  Hz, 1H), 7.04 (AA'XX',  $J = 8.8$  Hz, 1H), 4.06 (s, 1H), 3.88 (s, 2H).  $^{19}\text{F}$  NMR (376 MHz,  $\text{CDCl}_3$ )  $\delta$ : -80.65 (t,  $J = 10.0$  Hz), -112.31 (s), -121.29 (s), -121.64 – -121.95 (m), -122.62 (s), -126.01 (s).

## 5.2.7 General procedure for the synthesis of compounds 5-m



The triazoles **4-3** (2.500 g, 7.00 mmol), **4-7** (2.500 g, 4.49 mmol) and **4-9** (2.500 g, 3.80 mmol) were separately degassed with three cycles vacuum and nitrogen in 250 mL 3-neck round-bottomed flasks and after this dried toluene (90 mL in each) and  $\text{BBr}_3$  in heptane (6 mL in each) were added respectively by cannula under vacuum and by syringes. The mixture was heated under reflux for 3.5 h and the reactions were monitored by TLC (petroleum ether and ethyl acetate 5:1). After this, water was added (30 mL) to the mixtures which were heated for another hour. After cooling, the mixture was dried under vacuum, further water was added (70 mL), and the organic compounds were extracted with ethyl acetate (40 mL x 3). The organic phase was dried with  $\text{Na}_2\text{SO}_4$  and the compounds **5-m** were isolated by chromatography using petroleum ether/ethyl acetate 5:1 and 2:1 as eluents. Yields = 87-94%

### 4-(1-Methyl-3-(perfluoropropyl)-1,2,4-triazol-5-yl)phenol (5-3)

Colourless solid.  $^1\text{H}$  NMR (300 MHz,  $\text{CDCl}_3$ )  $\delta$ : 7.51 (AA'XX',  $J = 7.8$  Hz, 2H), 7.09 (s, 1H), 6.86 (AA'XX',  $J = 7.8$  Hz, 2H), 4.05 (s, 3H).

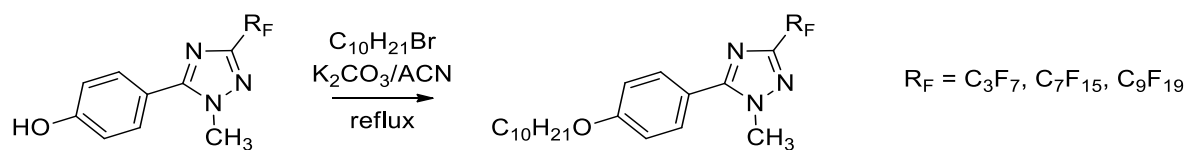
### 4-(1-methyl-3-(perfluoroheptyl)-1,2,4-triazol-5-yl)phenol (5-7)

Colourless solid.  $^1\text{H}$  NMR (400 MHz,  $\text{CDCl}_3$ )  $\delta$ : 7.59 (AA'XX',  $J = 8.8$  Hz, 2H), 6.96 (AA'XX',  $J = 8.8$  Hz, 2H), 5.84 (s, 1H), 4.06 (s, 3H).

### 4-(1-methyl-3-(perfluorononyl)-1,2,4-triazol-5-yl)phenol (5-9)

Colourless solid.  $^1\text{H}$  NMR (400 MHz,  $\text{CDCl}_3$ )  $\delta$ : 7.51 (AA'XX',  $J = 8.5$  Hz, 1H), 6.88 (AA'XX',  $J = 8.6$  Hz, 1H), 4.04 (s, 1H), 4.06 (s, 3H).

### 5.2.8 General procedure for the synthesis of compounds 6-m,10



The triazoles **5-3** (0.70 g, 2.04 mmol), **5-7** (0.70 g, 1.29 mmol) and **5-9** (0.70 g, 1.09 mmol) were dissolved separately in acetonitrile (10-15 mL) in 100 mL round-bottomed flasks as well as  $K_2CO_3$  (3 mol eq.) and 1-bromodecane were added (2 mol eq.). The obtained mixture was heated at 80 °C for 6-14 h and the reaction was monitored by TLC (petroleum ether and ethyl acetate 5:1). After cooling, the mixture was dried under vacuum, water was added (50 mL), pH was adjusted to neutral with a diluted HCl solution and organic compounds were extracted with ethyl acetate (30 mL x 3). The organic phase was dried with  $MgSO_4$  and the compounds **6-m,10** were isolated by chromatography using petroleum ether/ethyl acetate 20:1 and 5:1 as eluents. Yields = 87-97%.

#### 5-(4-(Decyloxy)phenyl)-1-methyl-3-(perfluoropropyl)-1,2,4-triazole (6-3,10)

Colourless solid.  $^1H$  NMR (300 MHz,  $CDCl_3$ )  $\delta$ : 7.64 (AA'XX',  $J = 8.4$  Hz, 2H), 6.96 (AA'XX',  $J = 8.4$  Hz, 2H), 4.17 – 3.92 (m, 5H), 1.82 (p,  $J = 6.4$  Hz, 2H,  $CH_2$ ), 1.55 – 1.17 (m, 14H), 0.88 (t,  $J = 5.5$  Hz, 3H,  $CH_3$ ).

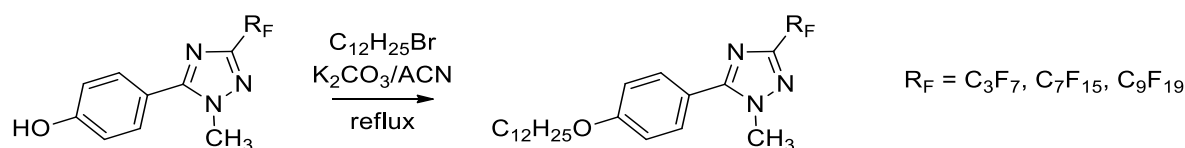
#### 5-(4-(Decyloxy)phenyl)-1-methyl-3-(perfluoroheptyl)-1,2,4-triazole (6-7,10)

Colourless solid.  $^1H$  NMR (400 MHz,  $CDCl_3$ )  $\delta$ : 7.64 (AA'XX',  $J = 8.7$  Hz, 2H), 7.02 (AA'XX',  $J = 8.7$  Hz, 2H), 4.12 – 3.91 (m, 5H), 1.82 (p,  $J = 6.4$  Hz, 2H), 1.53 – 1.13 (m, 14H), 0.88 (t,  $J = 6.6$  Hz, 3H).

#### 5-(4-(Decyloxy)phenyl)-1-methyl-3-(perfluorononyl)-1,2,4-triazole (6-9,10)

Colourless solid.  $^1H$  NMR (400 MHz,  $CDCl_3$ )  $\delta$ : 7.64 (AA'XX',  $J = 8.8$  Hz, 2H), 7.02 (AA'XX',  $J = 8.8$  Hz, 2H), 4.06 (s, 3H), 4.02 (t,  $J = 6.6$  Hz, 2H), 1.82 (p,  $J = 6.4$  Hz, 2H), 1.53 – 1.23 (m, 14H), 0.88 (t,  $J = 6.9$  Hz, 3H).

### 5.2.9 General procedure for the synthesis of compounds 6-m,12



The triazoles **5-3** (0.70 g, 2.04 mmol), **5-7** (0.70 g, 1.29 mmol) and **5-9** (0.70 g, 1.09 mmol) were dissolved separately in acetonitrile (10-15 mL) in 100 mL round-bottomed flasks as well as  $K_2CO_3$  (3 mol eq.) and 1-bromododecane were added (2 mol eq.). The obtained mixture was heated at 80°C for 6-14 h and the reaction was monitored by TLC (petroleum ether and ethyl acetate 5:1). After cooling, the mixture was dried under vacuum, water was added (50 mL), pH was adjusted to neutral with a diluted HCl solution and organic compounds were extracted with ethyl acetate (30 mL x 3). The organic phase was dried with  $MgSO_4$  and the compounds **6-m,12** were isolated by chromatography using petroleum ether/ethyl acetate 20:1 and 5:1 as eluents. Yields = 91-95%.

### 5-(4-(Dodecyloxy)phenyl)-1-methyl-3-(perfluoropropyl)-1,2,4-triazole (6-3,12)

Colourless solid.  $^1\text{H}$  NMR (300 MHz,  $\text{CDCl}_3$ )  $\delta$ : 7.64 (AA'XX',  $J = 8.3$  Hz, 2H), 6.96 (AA'XX',  $J = 8.3$  Hz, 2H), 4.16 – 3.87 (m, 5H), 1.81 (p,  $J = 6.4$  Hz, 2H), 1.55 – 1.17 (m, 18H), 0.88 (t,  $J = 5.7$  Hz, 3H).

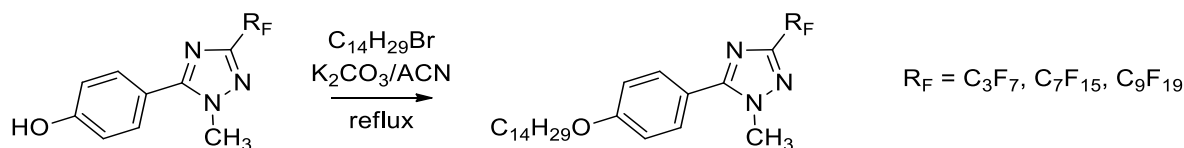
### 5-(4-(Dodecyloxy)phenyl)-1-methyl-3-(perfluoroheptyl)-1,2,4-triazole (6-7,12)

Colourless solid.  $^1\text{H}$  NMR (400 MHz,  $\text{CDCl}_3$ )  $\delta$ : 7.64 (AA'XX',  $J = 8.6$  Hz, 2H), 7.02 (AA'XX',  $J = 8.6$  Hz, 2H), 4.06 (s, 3H), 4.02 (t,  $J = 6.5$  Hz, 2H), 1.82 (p,  $J = 6.4$  Hz, 2H), 1.57 – 1.10 (m, 18H), 0.88 (t,  $J = 6.5$  Hz, 3H).

### 5-(4-(Dodecyloxy)phenyl)-1-methyl-3-(perfluorononyl)-1,2,4-triazole (6-9,12)

Colourless solid.  $^1\text{H}$  NMR (400 MHz,  $\text{CDCl}_3$ )  $\delta$ : 7.64 (AA'XX',  $J = 8.7$  Hz, 2H), 7.02 (AA'XX',  $J = 8.7$  Hz, 2H), 4.06 (s, 3H), 4.02 (t,  $J = 6.6$  Hz, 2H), 1.82 (p,  $J = 6.4$  Hz, 2H), 1.53 – 1.22 (m, 18H), 0.88 (t,  $J = 6.9$  Hz, 2H).

## 5.2.10 General procedure for the synthesis of compounds 6-*m*,14



The triazoles **5-3** (0.70 g, 2.04 mmol), **5-7** (0.70 g, 1.29 mmol) and **5-9** (0.70 g, 1.09 mmol) were dissolved separately in acetonitrile (10-15 mL) in 100 mL round-bottomed flasks as well as  $\text{K}_2\text{CO}_3$  (3 mol eq.) and 1-bromotetradecane were added (2 mol eq.). The obtained mixture was heated at  $80^\circ\text{C}$  for 6-14 h and the reaction was monitored by TLC (petroleum ether and ethyl acetate 5:1). After cooling, the mixture was dried under vacuum, water (50 mL) was added, pH was adjusted to neutral with a diluted HCl solution and organic compounds were extracted with ethyl acetate (30 mL x 3). The organic phase was dried with  $\text{MgSO}_4$  and the compounds **6-*m*,14** were isolated by chromatography using petroleum ether/ethyl acetate 20:1 and 5:1 as eluents. Yields= 83-96%.

### 1-Methyl-3-(perfluoropropyl)-5-(4-(tetradecyloxy)phenyl)-1,2,4-triazole (6-3,14)

Colourless solid.  $^1\text{H}$  NMR (300 MHz,  $\text{CDCl}_3$ )  $\delta$ : 7.64 (AA'XX',  $J = 8.8$  Hz, 2H), 7.02 (AA'XX',  $J = 8.8$  Hz, 2H), 4.06 (s, 3H), 4.02 (t,  $J = 6.5$  Hz, 2H), 1.81 (p,  $J = 6.4$  Hz, 2H), 1.55 – 1.18 (m, 22H), 0.88 (t,  $J = 6.6$  Hz, 3H).

### 1-Methyl-3-(perfluoroheptyl)-5-(4-(tetradecyloxy)phenyl)-1,2,4-triazole (6-7,14)

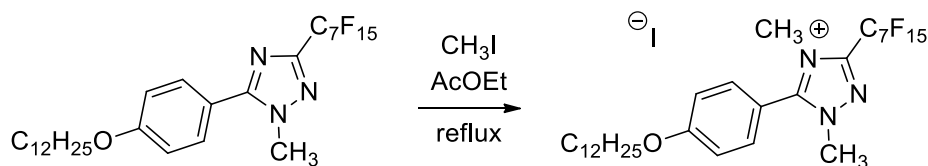
Colourless solid.  $^1\text{H}$  NMR (400 MHz,  $\text{CDCl}_3$ )  $\delta$ : 7.64 (AA'XX',  $J = 8.7$  Hz, 2H), 7.02 (AA'XX',  $J = 8.7$  Hz, 2H), 4.05 (s, 3H), 4.01 (t,  $J = 6.5$  Hz, 2H), 1.81 (p,  $J = 6.4$  Hz, 2H), 1.57 – 1.13 (m, 22H), 0.88 (t,  $J = 6.7$  Hz, 3H).

### 1-Methyl-3-(perfluorononyl)-5-(4-(tetradecyloxy)phenyl)-1,2,4-triazole (6-9,14)

Colourless solid.  $^1\text{H}$  NMR (400 MHz,  $\text{CDCl}_3$ )  $\delta$ : 7.64 (AA'XX',  $J = 8.8$  Hz, 1H), 7.02 (AA'XX',  $J = 8.8$  Hz, 1H), 4.06 (s, 3H), 4.01 (t,  $J = 6.5$  Hz, 2H), 1.81 (p,  $J = 6.4$  Hz, 2H), 1.56 – 1.12 (m, 1H), 0.88 (t,  $J = 6.7$  Hz, 1H).



### 5.2.11 Procedure for the synthesis of triazolium iodide [TRYUM-7,12][I]

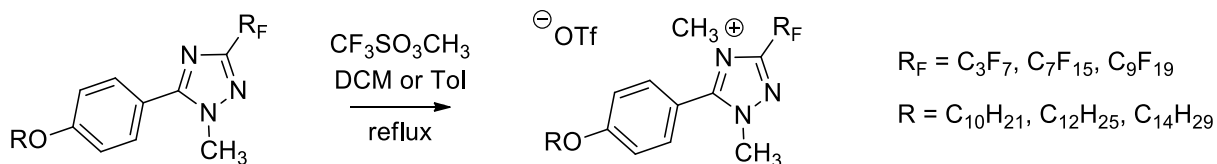


Triazoles **6-7,12** (0.10 g) was dissolved in ethyl acetate (10 mL) in small pressure vessel and  $\text{CH}_3\text{I}$  (30 mol eq.) was added. The mixture was stirred and heated at 110 °C for total 72 h. The reaction was monitored by TLC (petroleum ether and ethyl acetate 5:1 and 1:1). After cooling, water (50 mL) was added at the mixture, which was dried, pH was adjusted to neutral, and the organic compounds were extracted with ethyl acetate (25 mL x 3). The organic phase was dried with  $\text{Na}_2\text{SO}_4$  and the compound **[TRYUM-7,12][I]** was isolated by chromatography using petroleum ether / ethyl acetate 5:1 and 1:1 as eluents. Yields = 7%

### 5-(4-(Dodecyloxy)phenyl)-1,4-dimethyl-3-(perfluoroheptyl)-1,2,4-triazol-4-ium trifluoromethanesulfonate ([TRYUM-7,12][I])

Colourless solid.  $^1\text{H}$  NMR (400 MHz,  $\text{CD}_3\text{CN}$ )  $\delta$ : 7.62 (AA'XX',  $J$  = 9.0 Hz, 2H), 7.26 (AA'XX',  $J$  = 8.9 Hz, 2H), 4.13 (t,  $J$  = 6.5 Hz, 2H), 4.00 (s, 3H), 3.81 (s, 3H), 1.82 (p,  $J$  = 7.0 Hz, 2H), 1.62 – 1.21 (m, 18H), 0.87 (t,  $J$  = 6.8 Hz, 3H).

### 5.2.12 General procedure for the synthesis of triazolium trifluoromethanesulfonates [TRYUM-*m,n*][OTf]



The triazoles **6-*m,n*** were separately dissolved in toluene in small round-bottomed flasks and  $\text{CF}_3\text{SO}_3\text{CH}_3$  (15 mol eq.) was added. The mixture was stirred and heated at 60 °C for total 4-6 h. The reaction was monitored by TLC (petroleum ether and ethyl acetate 5:1 and 1:1). After cooling, water (50 mL) was added at the mixture, which was dried, pH was adjusted to neutral, and the organic compounds were extracted with DCM (30 mL x 3). The organic phase was dried with  $\text{MgSO}_4$  and the compounds **[TRYUM-*m,n*][OTf]** were isolated by chromatography using petroleum ether / ethyl acetate 5:1 and 1:1 as eluents. Yields = 76-92%. Combustion analysis performed on triazolium triflates is reported in Table 10.

### 5-(4-(Decyloxy)phenyl)-1,4-dimethyl-3-(perfluoropropyl)-1,2,4-triazol-4-ium trifluoromethanesulfonate ([TRYUM-3,10][OTf])

Colourless solid.  $^1\text{H}$  NMR (300 MHz,  $\text{CD}_3\text{CN}$ )  $\delta$ : 7.64 (AA'XX',  $J$  = 8.9 Hz, 2H, Ar), 7.26 (AA'XX',  $J$  = 8.9 Hz, 2H), 4.13 (t,  $J$  = 6.5 Hz, 2H), 4.00 (s, 3H), 3.80 (s, 3H), 1.80 (p,  $J$  = 6.4 Hz, 2H), 1.52 – 1.30 (m, 14H), 0.89

(t,  $J = 6.4$  Hz, 3H).  $^{19}\text{F}$  NMR (376 MHz,  $\text{CDCl}_3$ )  $\delta$ : -78.56 (s), -79.63 (t,  $J = 10.0$  Hz), -109.51 – -112.48 (m), -123.91 – -125.61 (m).

Anal. Calcd. for  $\text{C}_{24}\text{H}_{31}\text{F}_{10}\text{N}_3\text{O}_4\text{S}$ : C, 44.51; H, 4.83; N, 6.49. Found: C, 44.21; H, 4.89; N, 6.33.

**5-(4-(Dodecyloxy)phenyl)-1,4-dimethyl-3-(perfluoropropyl)-1,2,4-triazol-4-ium trifluoromethanesulfonate ([TRYUM-3,12][OTf])**

Colourless solid.  $^1\text{H}$  NMR (300 MHz,  $\text{CD}_3\text{CN}$ )  $\delta$ : 7.66 (AA'XX',  $J = 8.9$  Hz, 2H), 7.28 (AA'XX',  $J = 8.9$  Hz, 2H), 4.15 (t,  $J = 6.5$  Hz, 2H), 4.03 (s, 3H), 3.83 (s, 3H), 1.84 (p,  $J = 6.4$  Hz, 2H), 1.62 – 1.21 (m, 18H), 0.91 (t,  $J = 6.6$  Hz, 3H).  $^{19}\text{F}$  NMR (376 MHz,  $\text{CDCl}_3$ )  $\delta$ : -78.56 (s), -79.63 (t,  $J = 10.0$  Hz), -109.51 – -112.48 (m), -123.91 – -125.61 (m).

Anal. Calcd. for  $\text{C}_{26}\text{H}_{35}\text{F}_{10}\text{N}_3\text{O}_4\text{S}$ : C, 46.22; H, 5.22; N, 6.22. Found: C, 46.06; H, 5.19; N, 6.18.

**1,4-Dimethyl-3-(perfluoropropyl)-5-(4-(tetradecyloxy)phenyl)-1,2,4-triazol-4-ium trifluoromethanesulfonate ([TRYUM-3,14][OTf])**

Colourless solid.  $^1\text{H}$  NMR (300 MHz,  $\text{CD}_3\text{CN}$ )  $\delta$ : 7.63 (AA'XX',  $J = 8.9$  Hz, 2H), 7.26 (AA'XX',  $J = 8.9$  Hz, 2H), 4.13 (t,  $J = 6.5$  Hz, 2H), 4.00 (s, 3H), 3.80 (s, 3H), 1.81 (p,  $J = 6.4$  Hz, 2H), 1.59 – 1.21 (m, 22H), 0.88 (t,  $J = 6.6$  Hz, 3H).  $^{19}\text{F}$  NMR (376 MHz,  $\text{CDCl}_3$ )  $\delta$ : -78.56 (s), -79.63 (t,  $J = 10.0$  Hz), -109.51 – -112.48 (m), -123.91 – -125.61 (m).

Anal. Calcd. for  $\text{C}_{28}\text{H}_{39}\text{F}_{10}\text{N}_3\text{O}_4\text{S}$ : C, 47.79; H, 5.59; N, 5.97. Found: C, 47.71; H, 5.90; N, 5.41.

**5-(4-(Decyloxy)phenyl)-1,4-dimethyl-3-(perfluoroheptyl)-1,2,4-triazol-4-ium trifluoromethanesulfonate ([TRYUM-7,10][OTf])**

Colourless solid.  $^1\text{H}$  NMR (400 MHz,  $\text{CDCl}_3$ )  $\delta$ : 7.80 (AA'XX',  $J = 8.4$  Hz, 2H), 7.16 (AA'XX',  $J = 8.4$  Hz, 2H), 4.21 – 3.97 (m, 5H), 3.88 (s, 3H), 1.84 (p,  $J = 6.4$  Hz, 2H), 1.94 – 1.74 (m, 14H), 0.88 (t,  $J = 6.8$  Hz, 3H).  $^{19}\text{F}$  NMR (376 MHz,  $\text{CDCl}_3$ )  $\delta$ : -78.56 (s), -80.69 (t,  $J = 9.9$  Hz), -110.21 (s), -120.23 (s), -121.06 (s), -121.81 (s), -122.60 (s), -126.06 (s).

Anal. Calcd. for  $\text{C}_{28}\text{H}_{31}\text{F}_{18}\text{N}_3\text{O}_4\text{S}$ : C, 39.68; H, 3.69; N, 4.96. Found: C, 39.57; H, 3.63; N, 4.88.

**5-(4-(Dodecyloxy)phenyl)-1,4-dimethyl-3-(perfluoroheptyl)-1,2,4-triazol-4-ium trifluoromethanesulfonate ([TRYUM-7,12][OTf])**

Colourless solid.  $^1\text{H}$  NMR (400 MHz,  $\text{CDCl}_3$ )  $\delta$ : 7.80 (AA'XX',  $J = 8.9$  Hz, 2H), 7.13 (AA'XX',  $J = 8.9$  Hz, 2H), 4.22 – 3.91 (m, 5H), 3.83 (s, 3H), 1.81 (p,  $J = 6.4$  Hz, 2H), 1.62 – 1.21 (m, 18H), 0.87 (t,  $J = 6.8$  Hz, 3H).  $^{19}\text{F}$  NMR (376 MHz,  $\text{CDCl}_3$ )  $\delta$ : -78.65 (s), -80.79 (t,  $J = 9.9$  Hz), -110.40 (s), -120.27 (s), -121.16 (s), -121.89 (s), -122.68 (s), -126.16 (t,  $J = 14.9, 7.0$  Hz).

Anal. Calcd. for  $\text{C}_{30}\text{H}_{35}\text{F}_{18}\text{N}_3\text{O}_4\text{S}$ : C, 41.15; H, 4.03; N, 4.80. Found: C, 41.43; H, 4.09; N, 4.64.

**1,4-Dimethyl-3-(perfluoroheptyl)-5-(4-(tetradecyloxy)phenyl)-1,2,4-triazol-4-ium trifluoromethanesulfonate ([TRYUM-7,14][OTf])**

Colourless solid.  $^1\text{H}$  NMR (400 MHz,  $\text{CDCl}_3$ )  $\delta$ : 7.80 (AA'XX',  $J = 8.2$  Hz, 2H), 7.15 (AA'XX',  $J = 8.2$  Hz, 2H), 4.06 – 4.04 (m, 5H), 3.86 (s, 3H), 1.85 (p,  $J = 6.4$  Hz, 2H), 1.46 – 1.21 (m, 22H), 0.87 (t,  $J = 6.6$  Hz, 3H,  $\text{CH}_3$ ).  $^{19}\text{F}$  NMR (376 MHz,  $\text{CDCl}_3$ )  $\delta$ : -78.58 (s), -80.69 (t,  $J = 9.9$  Hz), -110.21 (s), -120.23 (s), -121.07 (s), -121.81 (s), -122.60 (s), -126.08 (t,  $J = 14.9, 7.0$  Hz).

Anal. Calcd. for C<sub>32</sub>H<sub>39</sub>F<sub>18</sub>N<sub>3</sub>O<sub>4</sub>S: C, 42.53; H, 4.35; N, 4.65. Found: C, 42.35; H, 4.24; N, 4.65.

### 5-(4-(Decyloxy)phenyl)-1,4-dimethyl-3-(perfluorononyl)-1,2,4-triazol-4-ium trifluoromethanesulfonate ([TRYUM-9,10][OTf])

Colourless solid. <sup>1</sup>H NMR (400 MHz, CDCl<sub>3</sub>) δ: 7.79 (AA'XX', *J* = 8.8 Hz, 2H), 7.16 (AA'XX', *J* = 8.8 Hz, 2H), 4.15 – 3.97 (m, 5H), 3.88 (s, 2H), 1.83 (p, *J* = 6.4 Hz, 2H), 1.56 – 1.20 (m, 14H), 0.88 (t, *J* = 6.8 Hz, 3H). <sup>19</sup>F NMR (376 MHz, CDCl<sub>3</sub>) δ: -78.59 (s), -80.78 (t, *J* = 10.0 Hz), -110.27 (s), -120.26 (s), -121.12 (s), -121.37 – -122.25 (m), -122.73 (s), -126.16 (s).

Anal. Calcd. for C<sub>30</sub>H<sub>31</sub>F<sub>22</sub>N<sub>3</sub>O<sub>4</sub>S: C, 38.02; H, 3.30; N, 4.43 Found: C, 37.91; H, 3.32; N, 4.29.

### 5-(4-(Dodecyloxy)phenyl)-1,4-dimethyl-3-(perfluorononyl)-1,2,4-triazol-4-ium trifluoromethanesulfonate ([TRYUM-9,12][OTf])

Colourless solid. <sup>1</sup>H NMR (400 MHz, CDCl<sub>3</sub>) δ: 7.80 (AA'XX', *J* = 8.9 Hz, 2H), 7.13 (AA'XX', *J* = 8.9 Hz, 2H), 4.21 – 3.90 (m, 5H), 3.82 (s, 3H), 1.80 (p, *J* = 6.4 Hz, 2H), 1.61 – 1.21 (m, 18H), 0.87 (t, *J* = 6.8 Hz, 3H). <sup>19</sup>F NMR (376 MHz, CDCl<sub>3</sub>) δ: -78.65 (s), -80.79 (t, *J* = 9.9 Hz), -110.40 (s), -120.27 (s), -121.16 (s), -121.89 (s), -122.68 (s), -126.16 (t, *J* = 14.9, 7.0 Hz).

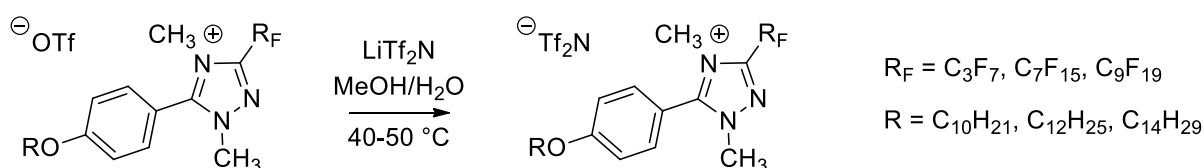
Anal. Calcd. for C<sub>32</sub>H<sub>35</sub>F<sub>22</sub>N<sub>3</sub>O<sub>4</sub>S: C, 39.39; H, 3.62; N, 4.31. Found: C, 39.49; H, 3.64; N, 4.22.

### 1,4-Dimethyl-3-(perfluorononyl)-5-(4-(tetradecyloxy)phenyl)-1,2,4-triazol-4-ium trifluoromethanesulfonate ([TRYUM-9,14][OTf])

Colourless solid. <sup>1</sup>H NMR (400 MHz, CDCl<sub>3</sub>) δ: 7.79 (AA'XX', *J* = 8.5 Hz, 2H), 7.16 (AA'XX', *J* = 4.2 Hz, 2H), 4.07 – 4.05 (m, 5H), 3.88 (s, 2H), 1.82 (p, *J* = 6.4 Hz, 2H), 1.55 – 1.08 (m, 22H), 0.87 (t, *J* = 6.6 Hz, 3H). <sup>19</sup>F NMR (376 MHz, CDCl<sub>3</sub>) δ: -78.56 (s), -80.70 (s), -110.24 (s), -120.24 (s), -121.03 (s), -121.33 – -122.15 (m), -122.67 (s), -126.10 (s).

Anal. Calcd. for C<sub>34</sub>H<sub>39</sub>F<sub>22</sub>N<sub>3</sub>O<sub>4</sub>S: C, 40.68; H, 3.92; N, 4.19. Found: C, 40.54; H, 3.90; N, 4.12.

## 5.2.13 General procedure for the synthesis of triazolium bis((trifluoromethyl)sulfonyl)amides [TRYUM-*m,n*][Tf<sub>2</sub>N]



The triazolium salts [TRYUM-*m,n*][OTf] were dissolved in amounts of MeOH as small as possible to dissolve them (3-10 mL) in a glass vessel and LiTf<sub>2</sub>N (2.5 mol eq.) was added. The mixture was stirred for 0.5 h at 40-50 °C and just after water was added dropwise, until permanent suspension was formed. After this the mixture was stirred for further 2 h and the solid was filtrated under vacuum washing with water. Yields = 72-86%. Combustion analysis performed on triazolium bis(triflimide)s is reported in Table 10.

**5-(4-(Decyloxy)phenyl)-1,4-dimethyl-3-(perfluoropropyl)-1,2,4-triazol-4-ium bis((trifluoromethyl)sulfonyl)amide ([TRYUM-3,10][Tf<sub>2</sub>N])**

Colourless solid. <sup>1</sup>H NMR (300 MHz, CDCl<sub>3</sub>) δ: 7.71 (AA'XX', *J* = 8.9 Hz, 2H), 7.17 (AA'XX', *J* = 8.9 Hz, 2H), 4.12 – 4.04 (m, 5H), 3.86 (s, 3H), 1.84 (p, *J* = 6.4 Hz), 1.52 – 1.28 (m, 14H), 0.88 (t, *J* = 6.6 Hz, 3H). <sup>19</sup>F NMR (376 MHz, CDCl<sub>3</sub>) δ: -79.63 (t, *J* = 10.0 Hz), -80.71 (s), -109.51 – -112.48 (m), -123.91 – -125.61 (m).

Anal. Calcd. for C<sub>25</sub>H<sub>31</sub>F<sub>13</sub>N<sub>4</sub>O<sub>5</sub>S<sub>2</sub>: C, 38.56; H, 4.01; N, 7.20. Found: C, 39.16; H, 4.10; N, 6.90.

**5-(4-(Dodecyloxy)phenyl)-1,4-dimethyl-3-(perfluoropropyl)-1,2,4-triazol-4-ium bis((trifluoromethyl)sulfonyl)amide ([TRYUM-3,12][Tf<sub>2</sub>N])**

Colourless solid. <sup>1</sup>H NMR (300 MHz, CDCl<sub>3</sub>) δ: 7.71 (AA'XX', *J* = 8.8 Hz, 2H), 7.28 (AA'XX', *J* = 8.8 Hz, 2H), 4.20 – 4.00 (m, 5H), 3.87 (s, 3H), 1.87 (p, *J* = 6.4 Hz, 2H), 1.53-1.19 (m, 18H), 0.88 (t, *J* = 6.6 Hz, 3H, CH<sub>3</sub>). <sup>19</sup>F NMR (376 MHz, CDCl<sub>3</sub>) δ: -79.63 (t, *J* = 10.0 Hz), -80.71 (s), -109.51 – -112.48 (m), -123.91 – -125.61 (m).

Anal. Calcd. for C<sub>27</sub>H<sub>35</sub>F<sub>13</sub>N<sub>4</sub>O<sub>5</sub>S<sub>2</sub>: C, 40.20; H, 4.37; N, 6.95. Found: C, 40.19; H, 4.34; N, 6.78.

**1,4-Dimethyl-3-(perfluoropropyl)-5-(4-(tetradecyloxy)phenyl)-1,2,4-triazol-4-ium bis((trifluoromethyl)sulfonyl)amide ([TRYUM-3,14][Tf<sub>2</sub>N])**

Colourless solid. <sup>1</sup>H NMR (300 MHz, CDCl<sub>3</sub>) δ: 7.71 (AA'XX', *J* = 8.9 Hz, 2H), 7.17 (AA'XX', *J* = 8.9 Hz, 2H), 4.12 – 4.04 (m, 5H), 3.86 (s, 3H), 1.84 (p, *J* = 6.4 Hz, 2H), 1.52 – 1.28 (m, 22H), 0.88 (t, *J* = 6.6 Hz, 3H). <sup>19</sup>F NMR (376 MHz, CDCl<sub>3</sub>) δ: -79.02 (s) -79.63 (t, *J* = 10.0 Hz), -80.71 (s), -109.51 – -112.48 (m), -123.91 – -125.61 (m).

Anal. Calcd. for C<sub>29</sub>H<sub>39</sub>F<sub>13</sub>N<sub>4</sub>O<sub>5</sub>S<sub>2</sub>: C, 41.73; H, 4.71; N, 6.71. Found: C, 42.07; H, 4.77; N, 6.54.

**5-(4-(Decyloxy)phenyl)-1,4-dimethyl-3-(perfluoroheptyl)-1,2,4-triazol-4-ium bis((trifluoromethyl)sulfonyl)amide ([TRYUM-7,10][Tf<sub>2</sub>N])**

Colourless solid. <sup>1</sup>H NMR (400 MHz, CDCl<sub>3</sub>) δ: 7.71 (AA'XX', *J* = 8.9 Hz, 2H), 7.21 (AA'XX', *J* = 8.9 Hz, 2H), 4.11 (s, 1H), 4.08(t, *J* = 6.5 Hz, 5H), 3.92 (s, 3H), 1.84 (p, *J* = 6.4 Hz, 2H), 1.95 – 1.73 (m, 14H), 0.88 (t, *J* = 6.9 Hz, 3H). <sup>19</sup>F NMR (376 MHz, CDCl<sub>3</sub>) δ: -80.71 (s), -81.98 (t, *J* = 10.1 Hz), -111.38 (s), -121.20 (s), -121.74 (s), -122.71 (s), -123.50 (s), -126.98 (s).

Anal. Calcd. for C<sub>29</sub>H<sub>31</sub>F<sub>21</sub>N<sub>4</sub>O<sub>5</sub>S<sub>2</sub>: C, 35.59; H, 3.19; N, 5.72. Found: C, 35.68; H, 3.13; N, 5.55.

**5-(4-(Dodecyloxy)phenyl)-1,4-dimethyl-3-(perfluoroheptyl)-1,2,4-triazol-4-ium bis((trifluoromethyl)sulfonyl)amide ([TRYUM-7,12][Tf<sub>2</sub>N])**

Colourless solid. <sup>1</sup>H NMR (300 MHz, CD<sub>3</sub>CN) δ: 7.61 (AA'XX', *J* = 8.9 Hz, 2H), 7.26 (AA'XX', *J* = 8.9 Hz, 2H), 4.13 (t, *J* = 6.5 Hz, 2H) 4.00 (s, 3H), 3.80 (s, 3H), 1.79 (p, *J* = 6.4 Hz, 2H), 1.57 – 1.19 (m, 18H), 0.89 (t, *J* = 6.6 Hz, 3H). <sup>19</sup>F NMR (376 MHz, CD<sub>3</sub>CN) δ: -80.71 (s), -81.98 (t, *J* = 10.1 Hz), -111.02 (s), -121.21 (s), -121.74 (s), -122.71 (s), -123.51 (s), -126.998 (s).

Anal. Calcd. for C<sub>31</sub>H<sub>35</sub>F<sub>21</sub>N<sub>4</sub>O<sub>5</sub>S<sub>2</sub>: C, 36.98; H, 3.50; N, 5.57. Found: C, 37.01; H, 3.39; N, 5.20.

**1,4-Dimethyl-3-(perfluoroheptyl)-5-(4-(tetradecyloxy)phenyl)-1,2,4-triazol-4-ium bis((trifluoromethyl)sulfonyl)amide ([TRYUM-7,14][Tf<sub>2</sub>N])**

Colourless solid. <sup>1</sup>H NMR (400 MHz, CDCl<sub>3</sub>) δ: 7.71 (AA'XX', *J* = 8.9 Hz, 2H), 7.16 (AA'XX', *J* = 8.9 Hz, 2H), 4.13 – 4.00 (m, 5H), 3.85(s, 3H), 1.83 (p, *J* = 7.0 Hz, 2H), 1.50 – 1.26 (m, 22H), 0.88 (t, *J* = 6.6 Hz, 3H). <sup>19</sup>F NMR (376 MHz, CD<sub>3</sub>CN) δ: -79.01 (s), -80.74 (t, *J* = 10.1 Hz), -110.25 (s), -120.23 (s), -121.09 (s), -121.88 (s), -122.63 (s), -126.12 (s).

Anal. Calcd. for C<sub>33</sub>H<sub>39</sub>F<sub>21</sub>N<sub>4</sub>O<sub>5</sub>S<sub>2</sub>: C, 38.30; H, 3.80; N, 5.41. Found: C, 38.63; H, 3.84; N, 5.09.

**5-(4-(Decyloxy)phenyl)-1,4-dimethyl-3-(perfluorononyl)-1,2,4-triazol-4-ium bis((trifluoromethyl)sulfonyl)amide ([TRYUM-9,10][Tf<sub>2</sub>N])**

Colourless solid. <sup>1</sup>H NMR (400 MHz, CDCl<sub>3</sub>) δ: 7.71 (AA'XX', *J* = 8.8 Hz, 2H), 7.18 (AA'XX', *J* = 8.8 Hz, 2H), 4.25 – 4.01 (m, 5H), 3.88 (s, 2H), 1.84 (p, *J* = 6.4 Hz, 2H), 1.52 – 1.18 (m, 14H), 0.88 (t, *J* = 6.6 Hz, 3H). <sup>19</sup>F NMR (376 MHz, CDCl<sub>3</sub>) δ: -78.94 (s), -80.70 (t, *J* = 9.9 Hz), -110.14 (s), -120.20 (s), -121.00 (s), -121.46 – -122.23 (m, *J* = 82.7 Hz), -126.09 (td, *J* = 15.0, 6.1 Hz).

Anal. Calcd. for C<sub>31</sub>H<sub>31</sub>F<sub>25</sub>N<sub>4</sub>O<sub>5</sub>S<sub>2</sub>: C, 34.52; H, 2.90; N, 5.19. Found: C, 34.36; H, 2.79; N, 5.06.

**5-(4-(Dodecyloxy)phenyl)-1,4-dimethyl-3-(perfluorononyl)-1,2,4-triazol-4-ium bis((trifluoromethyl)sulfonyl)amide ([TRYUM-9,12][Tf<sub>2</sub>N])**

Colourless solid. <sup>1</sup>H NMR (400 MHz, CD<sub>3</sub>CN) δ: 7.71 (AA'XX', *J* = 8.9 Hz, 2H), 7.17 (AA'XX', *J* = 9.0 Hz, 2H), 4.27 – 3.97 (m, 5H), 3.86 (s, 2H), 1.83 (p, *J* = 6.4 Hz, 2H), 1.52 – 1.11 (m, 18H), 0.88 (t, *J* = 6.6 Hz, 3H). <sup>19</sup>F NMR (376 MHz, CD<sub>3</sub>CN) δ: -79.00 (s), -80.77 (t, *J* = 10.0 Hz), -110.17 (s), -120.24 (s), -121.06 (s), -121.54 – -122.36 (m, *J* = 83.4 Hz), -122.73 (s), -126.15 (td, *J* = 14.6, 6.5 Hz).

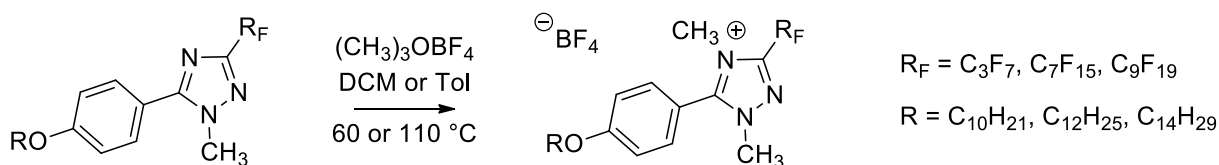
Anal. Calcd. for C<sub>33</sub>H<sub>35</sub>F<sub>25</sub>N<sub>4</sub>O<sub>5</sub>S<sub>2</sub>: C, 35.81; H, 3.19; N, 5.06. Found: C, 36.00; H, 3.19; N, 4.84.

**1,4-Dimethyl-3-(perfluorononyl)-5-(4-(tetradecyloxy)phenyl)-1,2,4-triazol-4-ium bis((trifluoromethyl)sulfonyl)amide ([TRYUM-9,14][Tf<sub>2</sub>N])**

Colourless solid. <sup>1</sup>H NMR (400 MHz, CDCl<sub>3</sub>) δ: 7.71 (AA'XX', *J* = 8.9 Hz, 2H), 7.16 (AA'XX', *J* = 8.9 Hz, 2H), 4.13-4.00 (m, 5H), 3.85(s, 3H), 1.83 (p, *J* = 7.0 Hz, 2H), 1.50-1.26 (m, 22H), 0.88 (t, *J* = 6.6 Hz, 3H). <sup>19</sup>F NMR (376 MHz, CD<sub>3</sub>CN) δ: -79.01 (s), -80.74 (t, *J* = 10.1 Hz), -110.25 (s), -120.23 (s), -121.09 (s), -121.88 (s), -122.63 (s), -126.12 (s).

Anal. Calcd. for C<sub>35</sub>H<sub>39</sub>F<sub>25</sub>N<sub>4</sub>O<sub>5</sub>S<sub>2</sub>: C, 37.04; H, 3.46; N, 4.94. Found: C, 37.09; H, 3.39; N, 4.78.

**5.2.14 General procedure for the synthesis of triazolium tetrafluoroborates [TRYUM-*m,n*][BF<sub>4</sub>]**



The triazoles **6-*m,n*** were dissolved in DCM (5-8 mL) in a Fischer-Porter vessel and (CH<sub>3</sub>)<sub>3</sub>O<sub>3</sub>BF<sub>4</sub> (20 mol eq.) was added. The mixtures were stirred and heated at 60 °C for total 4-6 d. The reaction was

monitored by TLC (petroleum ether and ethyl acetate 5:1 and 1:1). After cooling the mixture was dried, water (50 mL) was added, pH was adjusted to neutral, and the organic compounds were extracted with ethyl acetate (30 mL x 3). The organic phase was dried with MgSO<sub>4</sub> and the compounds [TRYUM-*m,n*][BF<sub>4</sub>] were isolated by chromatography using petroleum ether / ethyl acetate 5:1 and 1:1 as eluents. Yields = 42-56%. Combustion analysis performed on triazolium tetrafluoroborates is reported in Table 10.

**5-(4-(Decyloxy)phenyl)-1,4-dimethyl-3-(perfluoropropyl)-1,2,4-triazol-4-ium tetrafluoroborate ([TRYUM-3,10][BF<sub>4</sub>])**

Colourless solid. <sup>1</sup>H NMR (400 MHz, CDCl<sub>3</sub>) δ: 7.63 (AA'XX', *J* = 8.8 Hz, 2H), 7.26 (AA'XX', *J* = 8.8 Hz, 2H), 4.04 (t, *J* = 6.5 Hz), 4.01 (s, 3H), 3.84 (s, 3H), 1.83 (p, *J* = 6.4 Hz, 2H), 1.54 – 1.17 (m, 14H), 0.88 (t, *J* = 6.4 Hz, 3H). <sup>19</sup>F NMR (376 MHz, CDCl<sub>3</sub>) δ: -79.63 (t, *J* = 10.0 Hz), -109.51 – -112.48 (m), -123.91 – -125.61 (m), -155.39 (s), -155.44 (s).

Anal. Calcd. for C<sub>23</sub>H<sub>31</sub>BF<sub>11</sub>N<sub>3</sub>O: C, 47.20; H, 5.34; N, 7.18. Found: C, 46.99; H, 5.30; N, 7.02.

**5-(4-(Dodecyloxy)phenyl)-1,4-dimethyl-3-(perfluoropropyl)-1,2,4-triazol-4-ium tetrafluoroborate ([TRYUM-3,12][BF<sub>4</sub>])**

Colourless solid. <sup>1</sup>H NMR (400 MHz, CD<sub>3</sub>CN) δ: 7.746 (AA'XX', *J* = Hz, 2H), 7.12 (AA'XX', *J* = 8.9 Hz, 2H), 4.15 (t, *J* = 6.5 Hz, 2H), 3.98 (s, 3H), 3.82 (s, 3H), 1.82 (p, *J* = 6.4 Hz, 2H), 1.52 – 1.27 (m, 18H), 0.88 (t, *J* = 6.8 Hz, 3H). <sup>19</sup>F NMR (376 MHz, CDCl<sub>3</sub>) δ: -79.69 (t, *J* = 10.0 Hz), -110.00 – -113.02 (m), -124.50 – -126.13 (m), -155.35 (s), -155.40 (s).

Anal. Calcd. for C<sub>25</sub>H<sub>35</sub>BF<sub>11</sub>N<sub>3</sub>O: C, 48.95; H, 5.75; N, 6.85. Found: C, 49.01; H, 5.83; N, 6.23.

**1,4-Dimethyl-3-(perfluoropropyl)-5-(4-(tetradecyloxy)phenyl)-1,2,4-triazol-4-ium tetrafluoroborate ([TRYUM-3,14][BF<sub>4</sub>])**

Colourless solid. <sup>1</sup>H NMR (300 MHz, CD<sub>3</sub>CN) δ: 7.74 (AA'XX', *J* = 8.9 Hz, 2H), 7.13 (AA'XX', *J* = 8.9 Hz, 2H), 4.04 (t, *J* = 6.5 Hz, 2H), 4.00 (s, 3H), 3.80 (s, 3H), 1.82 (p, *J* = 6.4 Hz, 2H), 1.52 – 1.17 (m, 22H), 0.88 (t, *J* = 6.8 Hz, 3H). <sup>19</sup>F NMR (376 MHz, CDCl<sub>3</sub>) δ: -79.67 (t, *J* = 10.0 Hz, 3F, CF<sub>3</sub>), -110.17 – -112.37 (m, 2F, CF<sub>2</sub>), -123.98 – -126.63 (m, 2F, CF<sub>2</sub>), -155.38 (s), -155.44 (s).

Anal. Calcd. for C<sub>27</sub>H<sub>39</sub>BF<sub>11</sub>N<sub>3</sub>O: C, 50.56; H, 6.13; N, 6.55. Found: C, 50.77; H, 6.20; N, 6.14.

**5-(4-(Decyloxy)phenyl)-1,4-dimethyl-3-(perfluoroheptyl)-1,2,4-triazol-4-ium tetrafluoroborate ([TRYUM-7,10][BF<sub>4</sub>])**

Colourless solid. <sup>1</sup>H NMR (500 MHz, CD<sub>3</sub>CN) δ: 7.64 (dt, *J* = 8.5 Hz, 2.5 Hz, 2H), 7.27 (dt, *J* = 8.5 Hz, 2.5 Hz, 2H), 4.14 (t, *J* = 6.5 Hz, 2H), 4.01 (s, 3H), 3.81 (s, 3H), 1.83 (p, *J* = 6.5 Hz, 2H), 1.54 – 1.25 (m, 14H), 0.90 (t, *J* = 6.9 Hz, 3H). <sup>19</sup>F NMR (471 MHz, CD<sub>3</sub>CN) δ: -81.47 (tt, *J* = 10.1 Hz, 2.3 Hz), -109.00 – -111.64 (m), -120.67 – -120.81 (m), -121.20 – -121.36 (m), -122.23 (s), -123.02 (s), -126.45 – -126.56 (m), -152.09 (s), -152.15 (s). <sup>13</sup>C NMR (126 MHz, CDCl<sub>3</sub>) δ: 164.65 (s), 156.47 (s), 143.40 (t, *J* = 31.0 Hz), 133.30 (s), 116.93 (s), 111.67 (t, *J* = 34.1 Hz), 109.27 (s), 69.67 (s), 40.32 (s), 36.06 (s), 32.57 (s), 30.21 (d, *J* = 1.6 Hz), 29.96 (d, *J* = 3.5 Hz), 29.60 (s), 26.52 (s), 23.33 (s), 14.32 (s), 1.23 (dp, *J* = 41.5, 20.8 Hz). <sup>11</sup>B NMR (160 MHz, CD<sub>3</sub>CN) δ: -1.25 (s).

Anal. Calcd. for C<sub>27</sub>H<sub>31</sub>BF<sub>19</sub>N<sub>3</sub>O: C, 41.29; H, 3.98; N, 5.35. Found: C, 40.97; H, 3.94; N, 5.12.

**5-(4-(Dodecyloxy)phenyl)-1,4-dimethyl-3-(perfluoroheptyl)-1,2,4-triazol-4-ium tetrafluoroborate ([TRYUM-7,12][BF<sub>4</sub>])**

Colourless solid. <sup>1</sup>H NMR (400 MHz, CDCl<sub>3</sub>) δ: 7.74 (AA'XX', *J* = 8.9 Hz, 2H), 7.14 (AA'XX', *J* = 8.9 Hz, 2H), 4.03 (t, *J* = 6.5 Hz, 2H), 4.00 (s, 3H), 3.84 (s, 3H), 1.82 (p, *J* = 6.4 Hz, 2H), 1.52 – 1.14 (m, 18H), 0.88 (t, *J* = 6.8 Hz, 3H). <sup>19</sup>F NMR (376 MHz, CDCl<sub>3</sub>) δ: -80.74 (t, *J* = 9.9 Hz), -109.15 – -111.81 (m), -120.33 (s), -121.12 (s), -121.85 (s), -122.65 (s), -126.13 (td, *J* = 15.0, 7.0 Hz), -155.35 (s), -155.40 (s).

Anal. Calcd. for C<sub>29</sub>H<sub>35</sub>BF<sub>19</sub>N<sub>3</sub>O: C, 42.82; H, 4.34; N, 5.17. Found: C, 43.10; H, 4.34; N, 5.17.

**1,4-Dimethyl-3-(perfluoroheptyl)-5-(4-(tetradecyloxy)phenyl)-1,2,4-triazol-4-ium tetrafluoroborate ([TRYUM-7,14][BF<sub>4</sub>])**

Colourless solid. <sup>1</sup>H NMR (400 MHz, CDCl<sub>3</sub>) δ: 7.74 (AA'XX', *J* = 8.4 Hz, 2H), 7.12 (AA'XX', *J* = 8.4 Hz, 2H), 4.02 (t, *J* = 6.5 Hz, 2H), 3.98 (s, 3H), 3.81 (s, 3H), 1.81 (p, *J* = 6.4 Hz), 1.52 – 1.22 (m, 22H), 0.87 (t, *J* = 6.8 Hz, 3H). <sup>19</sup>F NMR (376 MHz, CDCl<sub>3</sub>) δ: -80.81 (t, *J* = 9.8 Hz), -110.46 (s), -120.37 (s), -121.22 (s), -121.92 (s), -122.73 (s), -126.21 (td, *J* = 15.1, 7.1 Hz), -155.43 (s), -155.48 (s).

Anal. Calcd. for C<sub>31</sub>H<sub>39</sub>BF<sub>19</sub>N<sub>3</sub>O: C, 44.25; H, 4.67; N, 4.99. Found: C, 43.64; H, 4.57; N, 7.74.

**5-(4-(Decyloxy)phenyl)-1,4-dimethyl-3-(perfluorononyl)-1,2,4-triazol-4-ium tetrafluoroborate ([TRYUM-9,10][BF<sub>4</sub>])**

Colourless solid. <sup>1</sup>H NMR (400 MHz, CDCl<sub>3</sub>) δ: 7.74 (AA'XX', *J* = 8.5 Hz, 2H), 7.12 (AA'XX', *J* = 8.5 Hz, 2H), 4.03 (t, *J* = 6.4 Hz, 2H), 3.98 (s, 3H), 3.82 (s, 3H), 1.84 (p, *J* = 6.4 Hz, 2H), 1.53 – 1.20 (m, 14H), 0.88 (t, *J* = 6.6 Hz, 3H). <sup>19</sup>F NMR (376 MHz, CDCl<sub>3</sub>) δ: -80.87 (t, *J* = 9.9 Hz), -110.47 (s), -120.37 (s), -121.60 – -122.35 (m), -122.81 (s), -126.24 (s), -155.28 (s), -155.36 (s).

Anal. Calcd. for C<sub>29</sub>H<sub>31</sub>BF<sub>23</sub>N<sub>3</sub>O: C, 39.34; H, 3.53; N, 4.75. Found: C, 39.48; H, 3.57; N, 4.62.

**5-(4-(Dodecyloxy)phenyl)-1,4-dimethyl-3-(perfluorononyl)-1,2,4-triazol-4-ium tetrafluoroborate ([TRYUM-9,12][BF<sub>4</sub>])**

Colourless solid. <sup>1</sup>H NMR (400 MHz, CDCl<sub>3</sub>) δ: 7.74 (AA'XX', *J* = 8.8 Hz, 2H), 7.11 (AA'XX', *J* = 8.8 Hz, 2H), 4.02 (t, *J* = 6.5 Hz, 2H), 3.96 (s, 3H), 3.80 (s, 3H), 1.81 (p, *J* = 6.4 Hz, 2H), 1.50 – 1.25 (m, 18H), 0.87 (t, *J* = 6.8 Hz, 1H). <sup>19</sup>F NMR (376 MHz, CDCl<sub>3</sub>) δ: -80.95 (t, *J* = 10.0 Hz), -110.38 – -110.69 (m), -120.41 (s), -121.25 (s), -121.82 (s), -122.07 (s), -122.87 (s), -126.27 – -126.37 (m), -155.43 (s), -155.49 (s).

Anal. Calcd. for C<sub>31</sub>H<sub>35</sub>BF<sub>23</sub>N<sub>3</sub>O: C, 40.76; H, 3.86; N, 4.60. Found: C, 40.68; H, 3.82; N, 4.59.

**1,4-Dimethyl-3-(perfluorononyl)-5-(4-(tetradecyloxy)phenyl)-1,2,4-triazol-4-ium tetrafluoroborate ([TRYUM-9,14][BF<sub>4</sub>])**

Colourless solid. <sup>1</sup>H NMR (400 MHz, CDCl<sub>3</sub>) δ: 7.73 (AA'XX', *J* = 8.8 Hz, 2H), 7.16 (AA'XX', *J* = 8.9 Hz, 2H), 4.18 – 3.96 (m, 5H), 3.88 (s, 3H), 1.83 (p, *J* = 6.4 Hz), 1.52 – 1.13 (m, 22H), 0.88 (t, *J* = 6.8 Hz, 3H). <sup>19</sup>F NMR (376 MHz, CDCl<sub>3</sub>) δ: -80.67 (t, *J* = 9.9 Hz), -110.38 (s), -120.27 (s), -120.99 (s), -121.58 (s), -121.83 (s), -122.65 (s), -125.96 – -126.34 (m), -155.25 (s), -155.30 (s).

Anal. Calcd. for C<sub>33</sub>H<sub>39</sub>BF<sub>23</sub>N<sub>3</sub>O: C, 42.10; H, 4.18; N, 4.46. Found: C, 41.93; H, 4.17; N, 4.39.

**Table 10.** CHN Analysis results for the triazolium salts.

Compound	Experimental Analysis Found / (Required) %					
	C		H		N	
[TRYUM-3,10][OTf]	44.21	(44.51)	4.89	(4.83)	6.33	(6.49)
[TRYUM-3,12][OTf]	46.06	(46.22)	5.19	(5.22)	6.18	(6.22)
[TRYUM-3,14][OTf]	47.71	(47.79)	5.90	(5.59)	5.41	(5.97)
[TRYUM-3,10][Tf2N]	39.16	(38.56)	4.10	(4.01)	6.90	(7.20)
[TRYUM-3,12][Tf2N]	40.19	(40.20)	4.34	(4.37)	6.78	(6.95)
[TRYUM-3,14][Tf2N]	42.07	(41.73)	4.77	(4.71)	6.54	(6.71)
[TRYUM-3,10][BF4]	46.99	(47.29)	5.30	(5.34)	7.02	(7.18)
[TRYUM-3,12][BF4]	49.01	(48.95)	5.83	(5.75)	6.23	(6.85)
[TRYUM-3,14][BF4]	50.77	(50.56)	6.20	(6.13)	6.14	(6.55)
[TRYUM-7,10][OTf]	39.57	(39.68)	3.63	(3.69)	4.88	(4.96)
[TRYUM-7,12][OTf]	41.43	(41.15)	4.09	(4.03)	4.64	(4.80)
[TRYUM-7,14][OTf]	42.35	(42.53)	4.24	(4.35)	4.65	(4.65)
[TRYUM-7,10][Tf2N]	35.68	(35.59)	3.13	(3.19)	5.55	(5.72)
[TRYUM-7,12][Tf2N]	37.01	(36.98)	3.39	(3.50)	5.20	(5.57)
[TRYUM-7,14][Tf2N]	38.63	(38.30)	3.84	(3.80)	5.09	(5.41)
[TRYUM-7,14][BF4]	40.97	(41.29)	3.94	(3.98)	5.12	(5.35)
[TRYUM-7,12][BF4]	43.10	(42.82)	4.34	(4.34)	5.17	(5.17)
[TRYUM-7,14][BF4]	43.64	(44.25)	4.57	(4.67)	7.74	(4.99)
[TRYUM-9,10][OTf]	37.91	(38.02)	3.32	(3.30)	4.29	(4.43)
[TRYUM-9,12][OTf]	39.49	(39.39)	3.64	(3.62)	4.22	(4.31)
[TRYUM-9,14][OTf]	40.54	(40.68)	3.90	(3.92)	4.12	(4.19)
[TRYUM-9,10][Tf2N]	34.36	(34.52)	2.79	(2.90)	5.06	(5.19)
[TRYUM-9,12][Tf2N]	36.00	(35.81)	3.19	(3.19)	4.84	(5.06)
[TRYUM-9,14][Tf2N]	37.09	(37.04)	3.39	(3.46)	4.78	(4.94)
[TRYUM-9,10][BF4]	39.48	(39.34)	3.57	(3.53)	4.62	(4.75)
[TRYUM-9,12][BF4]	40.68	(40.76)	3.82	(3.86)	4.59	(4.60)
[TRYUM-9,14][BF4]	41.93	(42.10)	4.17	(4.18)	4.39	(4.46)

### 5.3 X-ray crystallography data

Suitable crystals of reported compounds were selected using oil on 200 micrometre micro-mount and mounted on a SuperNova Eos diffractometer. The crystals were kept at 110.00(10) K during data collection. Using Olex2,<sup>122</sup> the structures were solved with the ShelXT<sup>123</sup> structure solution program using Intrinsic Phasing and refined with the ShelXL<sup>124</sup> refinement package using Least Squares minimisation.

Crystal Data for C<sub>18</sub>H<sub>8</sub>F<sub>19</sub>N<sub>3</sub>O [5-9] (*M* = 643.27 g mol<sup>-1</sup>): monoclinic, space group P2<sub>1</sub>/n (no. 14), *a* = 6.0924(2) Å, *b* = 39.8499(12) Å, *c* = 8.8230(2) Å, *β* = 91.068(3)°, *V* = 2141.70(11) Å<sup>3</sup>, *Z* = 4, *T* = 110.00(10) K, *μ*(CuKα) = 2.224 mm<sup>-1</sup>, *D*<sub>calc</sub> = 1.995 g/cm<sup>3</sup>, 15340 reflections measured (8.876° ≤ 2θ ≤ 134.154°), 3829 unique (*R*<sub>int</sub> = 0.0391, *R*<sub>sigma</sub> = 0.0287) which were used in all calculations. The final *R*<sub>1</sub> was 0.0505 (*I* > 2σ(*I*)) and *wR*<sub>2</sub> was 0.1133 (all data).



Crystal Data for  $C_{24}H_{31}F_{11}N_3O_3S$  [[**TRYUM-3,10**][**OTf**]] ( $M = 650.58 \text{ g mol}^{-1}$ ): monoclinic, space group  $P2_1/n$  (no. 14),  $a = 12.2678(8) \text{ \AA}$ ,  $b = 14.1723(16) \text{ \AA}$ ,  $c = 34.440(4) \text{ \AA}$ ,  $\beta = 90.660(8)^\circ$ ,  $V = 5987.4(11) \text{ \AA}^3$ ,  $Z = 8$ ,  $T = 110.00(10) \text{ K}$ ,  $\mu(\text{CuK}\alpha) = 2.514 \text{ mm}^{-1}$ ,  $D_{\text{calc}} = 1.443 \text{ g/cm}^3$ , 20605 reflections measured ( $7.678^\circ \leq 2\theta \leq 142.528^\circ$ ), 11276 unique ( $R_{\text{int}} = 0.0786$ ,  $R_{\text{sigma}} = 0.0996$ ) which were used in all calculations. The final  $R_1$  was 0.1615 ( $I > 2\sigma(I)$ ) and  $wR_2$  was 0.3794 (all data).

Crystal Data for  $C_{28}H_{31}F_{18}N_3O_4S$  [[**TRYUM-7,10**][**OTf**]] ( $M = 847.62 \text{ g mol}^{-1}$ ): monoclinic, space group  $P2_1/c$  (no. 14),  $a = 18.8350(8) \text{ \AA}$ ,  $b = 8.0827(3) \text{ \AA}$ ,  $c = 22.8945(9) \text{ \AA}$ ,  $\beta = 96.376(4)^\circ$ ,  $V = 3463.9(3) \text{ \AA}^3$ ,  $Z = 4$ ,  $T = 110.05(10) \text{ K}$ ,  $\mu(\text{CuK}\alpha) = 2.102 \text{ mm}^{-1}$ ,  $D_{\text{calc}} = 1.625 \text{ g/cm}^3$ , 17893 reflections measured ( $7.772^\circ \leq 2\theta \leq 134.158^\circ$ ), 6188 unique ( $R_{\text{int}} = 0.0319$ ,  $R_{\text{sigma}} = 0.0326$ ) which were used in all calculations. The final  $R_1$  was 0.0485 ( $I > 2\sigma(I)$ ) and  $wR_2$  was 0.1359 (all data).

Crystal Data for  $C_{30}H_{31}F_{22}N_3O_4S$  [[**TRYUM-9,10**][**OTf**]] ( $M = 947.64 \text{ g mol}^{-1}$ ): triclinic, space group  $P-1$  (no. 2),  $a = 7.9391(3) \text{ \AA}$ ,  $b = 11.5678(10) \text{ \AA}$ ,  $c = 20.8049(17) \text{ \AA}$ ,  $\alpha = 82.290(7)^\circ$ ,  $\beta = 89.720(5)^\circ$ ,  $\gamma = 82.993(5)^\circ$ ,  $V = 1879.1(2) \text{ \AA}^3$ ,  $Z = 2$ ,  $T = 109.95(10) \text{ K}$ ,  $\mu(\text{Cu K}\alpha) = 2.169 \text{ mm}^{-1}$ ,  $D_{\text{calc}} = 1.675 \text{ g/cm}^3$ , 10985 reflections measured ( $7.77^\circ \leq 2\theta \leq 134.124^\circ$ ), 6665 unique ( $R_{\text{int}} = 0.0360$ ,  $R_{\text{sigma}} = 0.0545$ ) which were used in all calculations. The final  $R_1$  was 0.0662 ( $I > 2\sigma(I)$ ) and  $wR_2$  was 0.1667 (all data).

Crystal Data for  $C_{37}H_{45}F_{22}N_3O_5S$  [[**TRYUM-9,14**][**OTf**]] ( $M = 1061.82 \text{ g mol}^{-1}$ ): triclinic, space group  $P-1$  (no. 2),  $a = 6.23099(17) \text{ \AA}$ ,  $b = 9.1796(4) \text{ \AA}$ ,  $c = 39.4248(14) \text{ \AA}$ ,  $\alpha = 95.565(3)^\circ$ ,  $\beta = 92.989(3)^\circ$ ,  $\gamma = 92.795(3)^\circ$ ,  $V = 2238.04(13) \text{ \AA}^3$ ,  $Z = 2$ ,  $T = 110.00(10) \text{ K}$ ,  $\mu(\text{CuK}\alpha) = 1.905 \text{ mm}^{-1}$ ,  $D_{\text{calc}} = 1.576 \text{ g/cm}^3$ , 13942 reflections measured ( $6.77^\circ \leq 2\theta \leq 134.154^\circ$ ), 7968 unique ( $R_{\text{int}} = 0.0407$ ,  $R_{\text{sigma}} = 0.0601$ ) which were used in all calculations. The final  $R_1$  was 0.0880 ( $I > 2\sigma(I)$ ) and  $wR_2$  was 0.2274 (all data).

Crystal Data for  $C_{25}H_{31}F_{13}N_4O_5S_2$  [[**TRYUM-3,10**][**Tf<sub>2</sub>N**]] ( $M = 778.66 \text{ g mol}^{-1}$ ): orthorhombic, space group  $P2_12_12_1$  (no. 19),  $a = 6.8452(4) \text{ \AA}$ ,  $b = 8.4550(4) \text{ \AA}$ ,  $c = 56.345(3) \text{ \AA}$ ,  $V = 3261.0(3) \text{ \AA}^3$ ,  $Z = 4$ ,  $T = 110.00(10) \text{ K}$ ,  $\mu(\text{CuK}\alpha) = 2.563 \text{ mm}^{-1}$ ,  $D_{\text{calc}} = 1.586 \text{ g/cm}^3$ , 29641 reflections measured ( $9.418^\circ \leq 2\theta \leq 134.14^\circ$ ), 5800 unique ( $R_{\text{int}} = 0.0395$ ,  $R_{\text{sigma}} = 0.0317$ ) which were used in all calculations. The final  $R_1$  was 0.0563 ( $I > 2\sigma(I)$ ) and  $wR_2$  was 0.1171 (all data).

Crystal Data for  $C_{29}H_{39}F_{13}N_4O_5S_2$  [[**TRYUM-3,14**][**Tf<sub>2</sub>N**]] ( $M = 834.76 \text{ g mol}^{-1}$ ): monoclinic, space group  $P2_1$  (no. 14),  $a = 6.8348(3) \text{ \AA}$ ,  $b = 8.5999(4) \text{ \AA}$ ,  $c = 63.658(3) \text{ \AA}$ ,  $V = 3741.2(3) \text{ \AA}^3$ ,  $Z = 4$ ,  $T = 110.00(10) \text{ K}$ ,  $\mu(\text{CuK}\alpha) = 1.54184 \text{ mm}^{-1}$ ,  $D_{\text{calc}} = 1.482 \text{ g/cm}^3$ , 21029 reflections measured ( $6.944^\circ \leq 2\theta \leq 134.152^\circ$ ), 10458 unique ( $R_{\text{int}} = 0.0528$ ,  $R_{\text{sigma}} = 0.0607$ ) which were used in all calculations. The final  $R_1$  was 0.0980 ( $I > 2\sigma(I)$ ) and  $wR_2$  was 0.2810 (all data).

Crystal Data for  $C_{29}H_{31}N_4O_5F_{21}S_2$  [[**TRYUM-7,10**][**Tf<sub>2</sub>N**]] ( $M = 978.70 \text{ g mol}^{-1}$ ): orthorhombic, space group  $P2_12_12_1$  (no. 19),  $a = 6.6955(2) \text{ \AA}$ ,  $b = 8.5499(2) \text{ \AA}$ ,  $c = 68.538(2) \text{ \AA}$ ,  $V = 3923.5(2) \text{ \AA}^3$ ,  $Z = 4$ ,  $T = 110.00(10) \text{ K}$ ,  $\mu(\text{CuK}\alpha) = 2.573 \text{ mm}^{-1}$ ,  $D_{\text{calc}} = 1.657 \text{ g/cm}^3$ , 18397 reflections measured ( $7.74^\circ \leq 2\theta \leq 134.134^\circ$ ), 6928 unique ( $R_{\text{int}} = 0.0327$ ,  $R_{\text{sigma}} = 0.0420$ ) which were used in all calculations. The final  $R_1$  was 0.0446 ( $I > 2\sigma(I)$ ) and  $wR_2$  was 0.0886 (all data).

Crystal Data for  $C_{31}H_{35}F_{21}N_4O_5S_2$  [[**TRYUM-7,12**][**Tf<sub>2</sub>N**]] ( $M = 1006.75 \text{ g mol}^{-1}$ ): orthorhombic, space group  $P2_12_12_1$  (no. 19),  $a = 6.7404(7) \text{ \AA}$ ,  $b = 8.6592(7) \text{ \AA}$ ,  $c = 71.960(6) \text{ \AA}$ ,  $V = 4200.0(6) \text{ \AA}^3$ ,  $Z = 4$ ,  $T = 110.00(10) \text{ K}$ ,  $\mu(\text{CuK}\alpha) = 2.514 \text{ mm}^{-1}$ ,  $D_{\text{calc}} = 1.592 \text{ g/cm}^3$ , 13238 reflections measured ( $7.37^\circ \leq 2\theta \leq 134.138^\circ$ ), 6861 unique ( $R_{\text{int}} = 0.0341$ ,  $R_{\text{sigma}} = 0.0608$ ) which were used in all calculations. The final  $R_1$  was 0.0867 ( $I > 2\sigma(I)$ ) and  $wR_2$  was 0.1837 (all data).

Crystal Data for  $C_{31}H_{31}F_{25}N_4O_5S_2$  [[**TRYUM-9,10**][**Tf<sub>2</sub>N**]] ( $M = 1078.72 \text{ g mol}^{-1}$ ): monoclinic, space group  $P2_1/c$  (no. 14),  $a = 6.7112(2) \text{ \AA}$ ,  $b = 8.5380(3) \text{ \AA}$ ,  $c = 71.575(3) \text{ \AA}$ ,  $\beta = 91.664(3)^\circ$ ,  $V = 4099.6(2) \text{ \AA}^3$ ,  $Z = 4$ ,  $T = 110.00(10) \text{ K}$ ,  $\mu(\text{CuK}\alpha) = 2.674 \text{ mm}^{-1}$ ,  $D_{\text{calc}} = 1.748 \text{ g/cm}^3$ , 14305 reflections measured ( $7.414^\circ \leq 2\theta \leq 134.158^\circ$ ), 7264 unique ( $R_{\text{int}} = 0.0456$ ,  $R_{\text{sigma}} = 0.0589$ ) which were used in all calculations. The final  $R_1$  was 0.0616 ( $I > 2\sigma(I)$ ) and  $wR_2$  was 0.1509 (all data).

Crystal Data for  $C_{33}H_{35}F_{25}N_4O_5S_2$  [[**TRYUM-9,12**][**Tf<sub>2</sub>N**]] ( $M = 1106.77 \text{ g mol}^{-1}$ ): monoclinic, space group  $P2_1/c$  (no. 14),  $a = 6.7752(8) \text{ \AA}$ ,  $b = 8.6424(9) \text{ \AA}$ ,  $c = 74.967(9) \text{ \AA}$ ,  $\beta = 90.731(11)^\circ$ ,  $V = 4389.3(9) \text{ \AA}^3$ ,  $Z = 4$ ,  $T = 110.00(10) \text{ K}$ ,  $\mu(\text{CuK}\alpha) = 2.514 \text{ mm}^{-1}$ ,  $D_{\text{calc}} = 1.675 \text{ g/cm}^3$ , 13874 reflections measured ( $7.076^\circ \leq 2\theta \leq 134.15^\circ$ ), 7800 unique ( $R_{\text{int}} = 0.0336$ ,  $R_{\text{sigma}} = 0.0784$ ) which were used in all calculations. The final  $R_1$  was 0.1043 ( $I > 2\sigma(I)$ ) and  $wR_2$  was 0.2594 (all data).

Crystal Data for  $C_{36}H_{45}BF_{23}N_3O_2$  [[**TRYUM-9,14**][**Tf<sub>2</sub>N**]] ( $M = 999.56 \text{ g mol}^{-1}$ ): monoclinic, space group  $P2_1/c$  (no. 14),  $a = 40.3423(12) \text{ \AA}$ ,  $b = 9.4231(3) \text{ \AA}$ ,  $c = 11.2821(4) \text{ \AA}$ ,  $\beta = 92.753(3)^\circ$ ,  $V = 4283.9(2) \text{ \AA}^3$ ,  $Z = 4$ ,  $T = 110.00(14) \text{ K}$ ,  $\mu(\text{CuK}\alpha) = 1.484 \text{ mm}^{-1}$ ,  $D_{\text{calc}} = 1.550 \text{ g/cm}^3$ , 39137 reflections measured ( $8.778^\circ \leq 2\theta \leq 142.732^\circ$ ), 8204 unique ( $R_{\text{int}} = 0.0339$ ,  $R_{\text{sigma}} = 0.0226$ ) which were used in all calculations. The final  $R_1$  was 0.0591 ( $I > 2\sigma(I)$ ) and  $wR_2$  was 0.1398 (all data).

Crystal Data  $C_{26}H_{37}BF_{11}N_3O_2$  [[**TRYUM-3,10**][**BF<sub>4</sub>**]] ( $M = 643.39 \text{ g mol}^{-1}$ ): monoclinic, space group  $P2_1/c$  (no. 14),  $a = 29.5005(5) \text{ \AA}$ ,  $b = 9.28574(14) \text{ \AA}$ ,  $c = 11.08372(17) \text{ \AA}$ ,  $\beta = 98.6889(15)^\circ$ ,  $V = 3001.36(8) \text{ \AA}^3$ ,  $Z = 4$ ,  $T = 110.00(10) \text{ K}$ ,  $\mu(\text{CuK}\alpha) = 2.674 \text{ mm}^{-1}$ ,  $D_{\text{calc}} = 1.424 \text{ g/cm}^3$ , 22329 reflections measured ( $9.098^\circ \leq 2\theta \leq 142.286^\circ$ ), 7264 unique ( $R_{\text{int}} = 0.0311$ ,  $R_{\text{sigma}} = 0.0247$ ) which were used in all calculations. The final  $R_1$  was 0.0392 ( $I > 2\sigma(I)$ ) and  $wR_2$  was 0.1016 (all data).

Crystal Data for  $C_{27}H_{31}BF_{19}N_3O$  [[**TRYUM-7,10**][**BF<sub>4</sub>**]] ( $M = 785.36 \text{ g mol}^{-1}$ ): monoclinic, space group  $P2_1/c$  (no. 14),  $a = 29.930(2) \text{ \AA}$ ,  $b = 9.2437(5) \text{ \AA}$ ,  $c = 11.7255(5) \text{ \AA}$ ,  $\beta = 96.553(5)^\circ$ ,  $V = 3222.8(3) \text{ \AA}^3$ ,  $Z = 4$ ,  $T = 110.05(10) \text{ K}$ ,  $\mu(\text{CuK}\alpha) = 1.585 \text{ mm}^{-1}$ ,  $D_{\text{calc}} = 1.619 \text{ g/cm}^3$ , 10892 reflections measured ( $8.922^\circ \leq 2\theta \leq 134.188^\circ$ ), 5692 unique ( $R_{\text{int}} = 0.0339$ ,  $R_{\text{sigma}} = 0.0436$ ) which were used in all calculations. The final  $R_1$  was 0.0769 ( $I > 2\sigma(I)$ ) and  $wR_2$  was 0.2263 (all data).

Crystal Data for  $C_{32}H_{37}BF_{23}N_3O_2$  [[**TRYUM-9,10**][**BF<sub>4</sub>**]] ( $M = 943.45 \text{ g mol}^{-1}$ ): monoclinic, space group  $P2_1/c$  (no. 14),  $a = 37.0798(6) \text{ \AA}$ ,  $b = 9.45070(11) \text{ \AA}$ ,  $c = 11.29828(17) \text{ \AA}$ ,  $\beta = 98.5285(14)^\circ$ ,  $V = 3915.48(9) \text{ \AA}^3$ ,  $Z = 4$ ,  $T = 110.00(10) \text{ K}$ ,  $\mu(\text{CuK}\alpha) = 1.586 \text{ mm}^{-1}$ ,  $D_{\text{calc}} = 1.600 \text{ g/cm}^3$ , 20003 reflections measured ( $7.232^\circ \leq 2\theta \leq 134.136^\circ$ ), 6997 unique ( $R_{\text{int}} = 0.0318$ ,  $R_{\text{sigma}} = 0.0239$ ) which were used in all calculations. The final  $R_1$  was 0.0817 ( $I > 2\sigma(I)$ ) and  $wR_2$  was 0.1774 (all data).

Crystal Data for  $C_{36}H_{45}BF_{23}N_3O_2$  [[**TRYUM-9,14**][**BF<sub>4</sub>**]] ( $M = 999.56 \text{ g mol}^{-1}$ ): monoclinic, space group  $P2_1/c$  (no. 14),  $a = 40.3423(12) \text{ \AA}$ ,  $b = 9.4231(3) \text{ \AA}$ ,  $c = 11.2821(4) \text{ \AA}$ ,  $\beta = 92.753(3)^\circ$ ,  $V = 4283.9(2) \text{ \AA}^3$ ,  $Z = 4$ ,  $T = 110.00(14) \text{ K}$ ,  $\mu(\text{CuK}\alpha) = 1.484 \text{ mm}^{-1}$ ,  $D_{\text{calc}} = 1.550 \text{ g/cm}^3$ , 39137 reflections measured ( $8.778^\circ \leq 2\theta \leq 142.732^\circ$ ), 8204 unique ( $R_{\text{int}} = 0.0339$ ,  $R_{\text{sigma}} = 0.0226$ ) which were used in all calculations. The final  $R_1$  was 0.0591 ( $I > 2\sigma(I)$ ) and  $wR_2$  was 0.1398 (all data).

## Appendix A – Crystallographic structures

All reported crystal structures are represented in Ortep view. Thermal ellipsoids size encloses 50% probability of finding the electron density of the atom.<sup>125</sup> The colour labelling scheme is as follows: carbon (light grey), nitrogen (blue), fluorine (light green), oxygen (red), sulphur (yellow) and boron (pink).

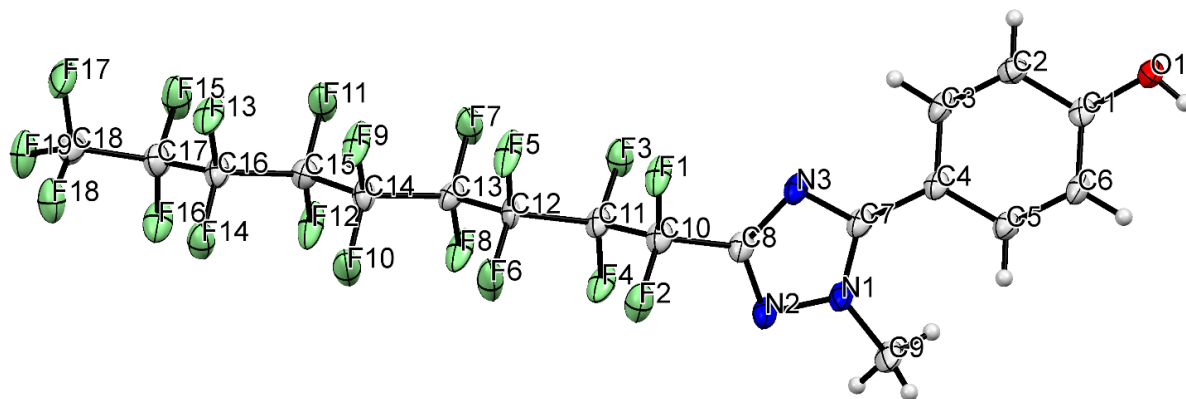


Figure A1. Ortep view of compound 5-9.

## Crystallographic structures of Triazolium salts

Marked compound structures (†) include acetone and several structures show some atoms in different conformational position in crystals. Acetone and some duplicates of conformational atoms have been omitted for clarity. For the same reason, Ortep views show just carbon atoms labels.

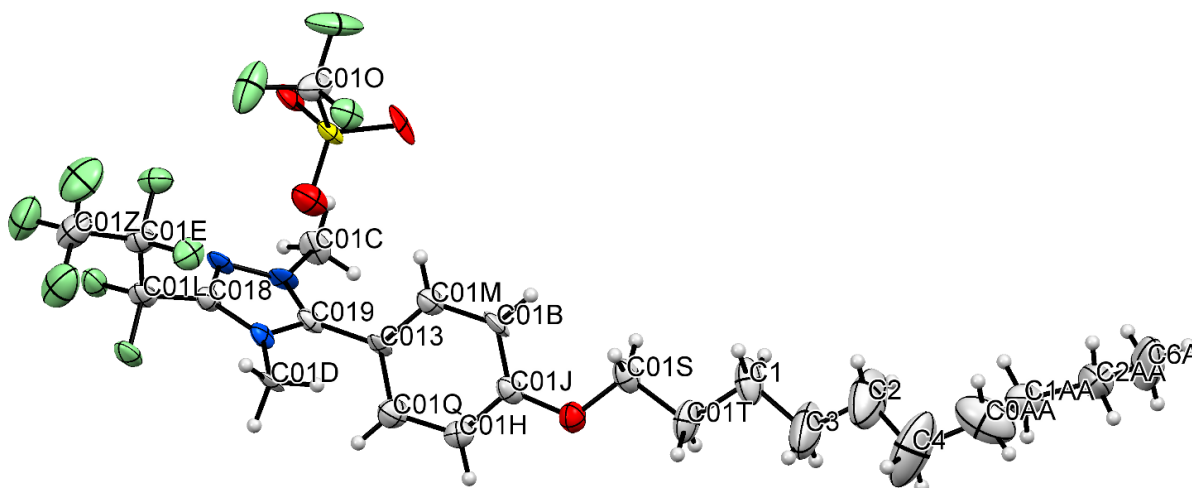


Figure A2. Ortep view of compound [TRIUM-3,10][OTf]. The unite cell contains two cations which are very different with respect to the way the chains come off the phenyl ring. For the sake of clarity, one of the two cations is omitted.

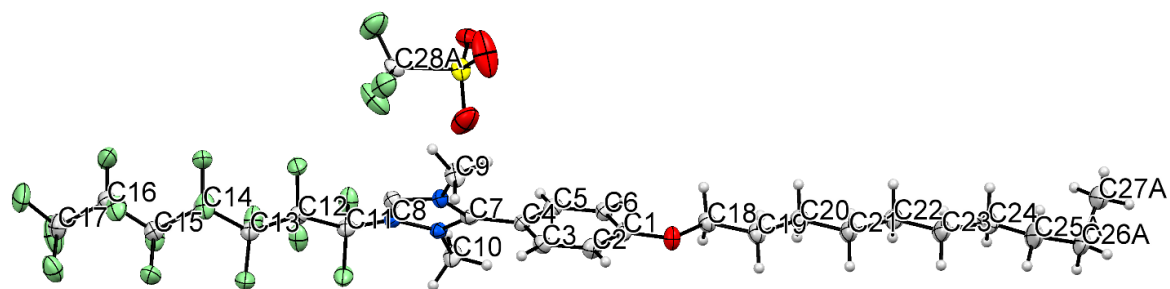


Figure A3. Ortep view of compound [TRIUM-7,10][OTf].

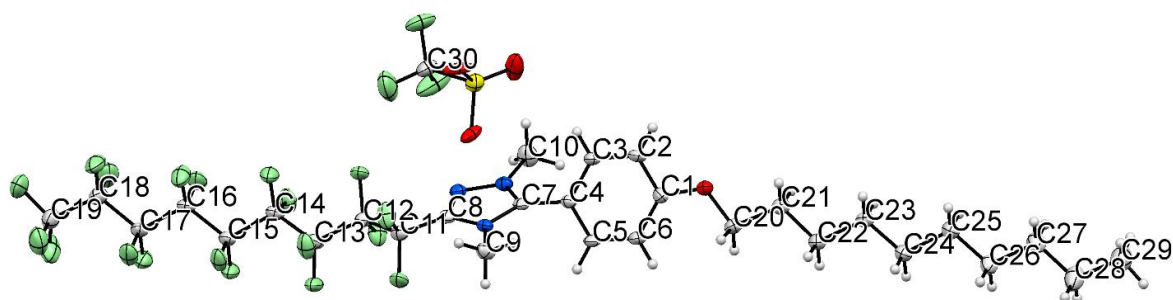


Figure A4. Ortep view of compound [TRIUM-9,10][OTf].

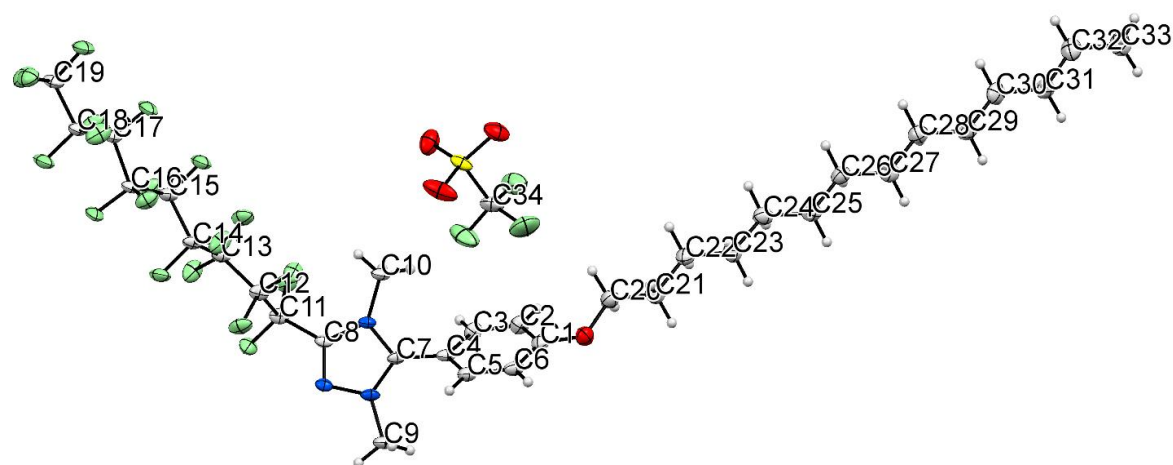


Figure A5. Ortep view of compound [TRIUM-9,14][OTf]<sup>†</sup>.

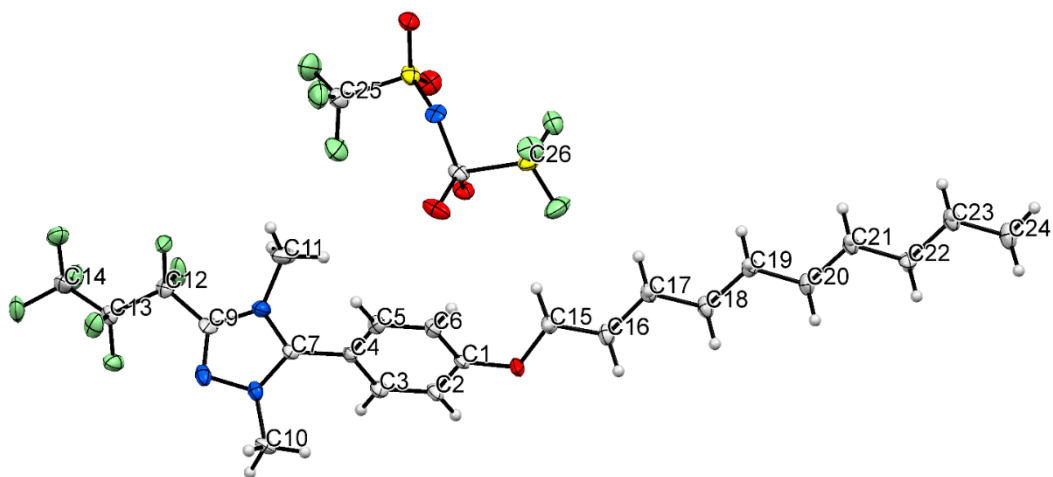


Figure A6. Ortep view of compound [TRIUM-3,10][Tf<sub>2</sub>N].

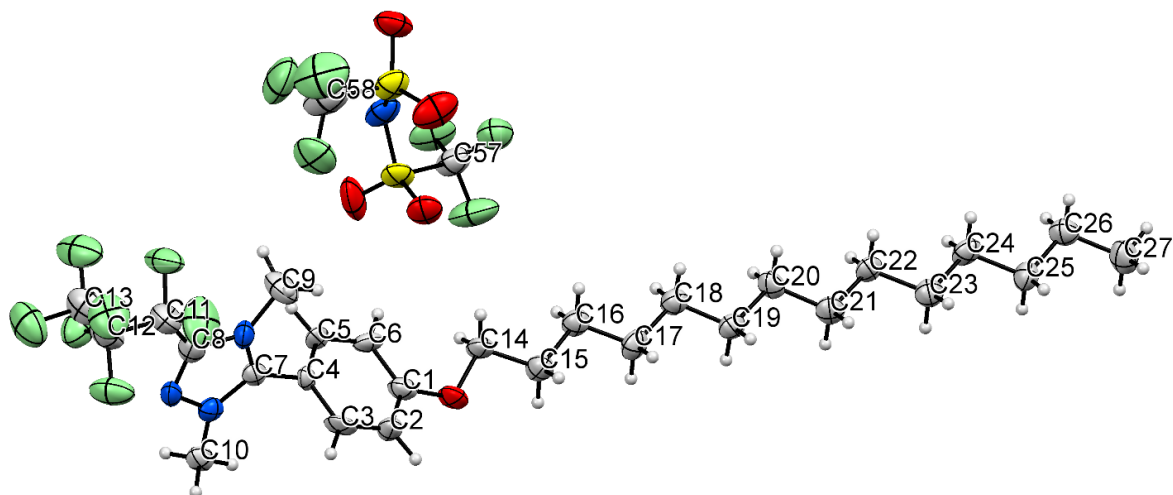


Figure A7. Ortep view of compound [TRIUM-3,14][Tf<sub>2</sub>N].

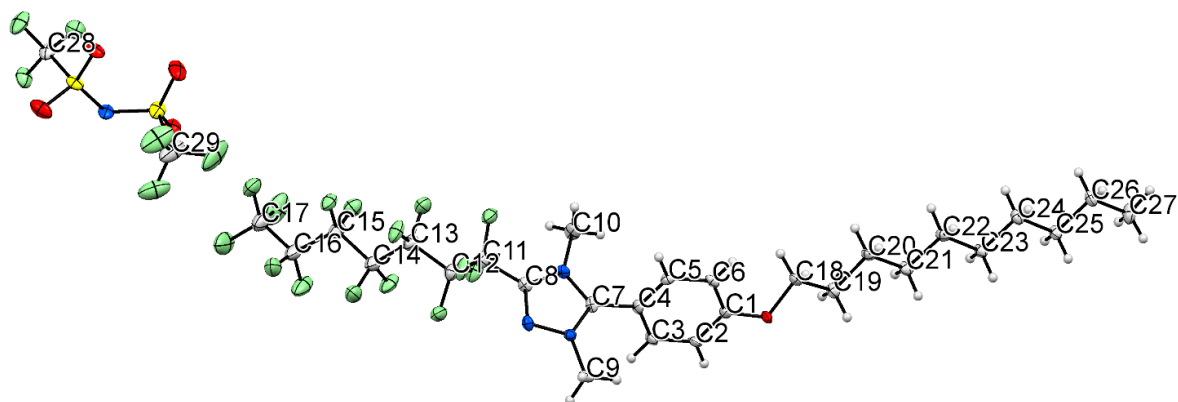


Figure A8. Ortep view of compound [TRIUM-7,10][Tf<sub>2</sub>N].

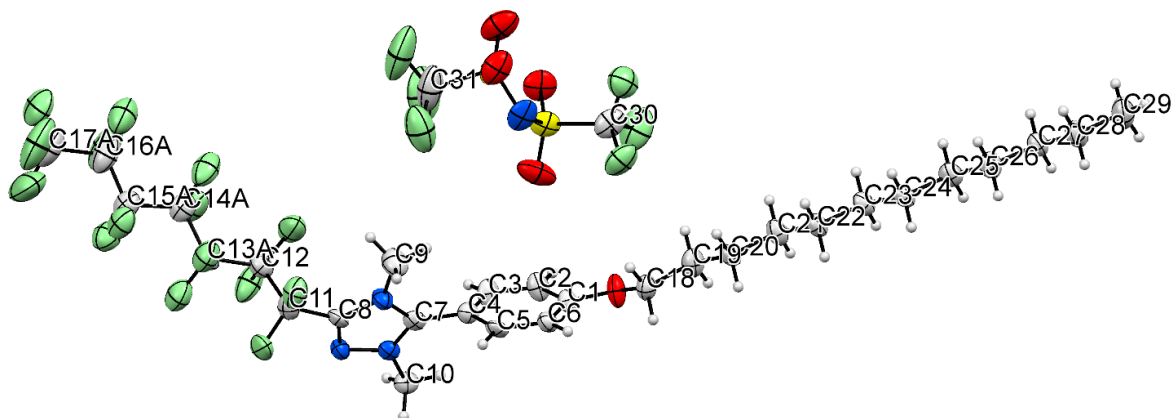


Figure A9. Ortep view of compound [TRIUM-7,12][Tf<sub>2</sub>N].

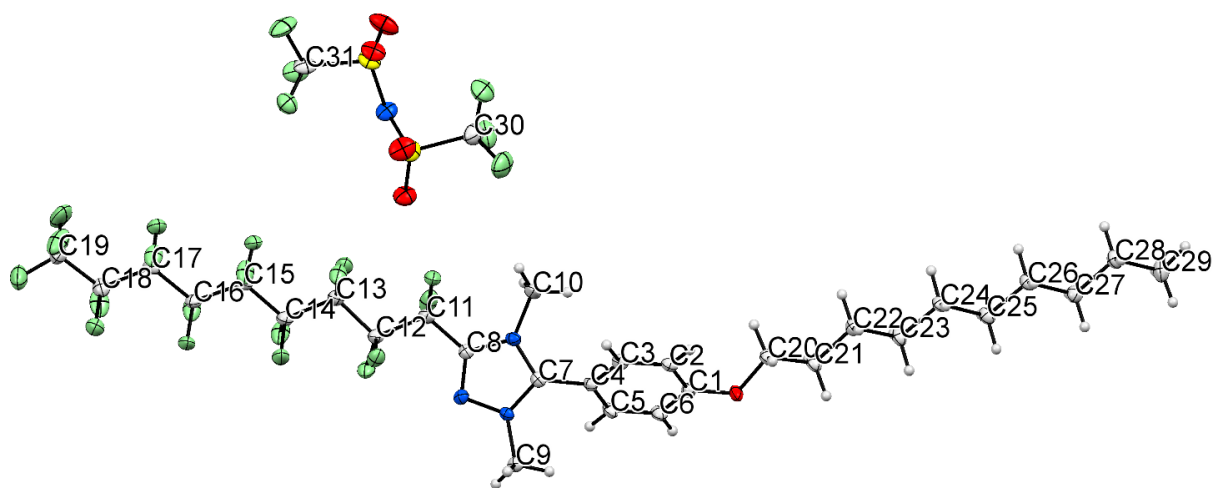


Figure A10. Ortep view of compound [TRIUM-9,10][Tf<sub>2</sub>N].

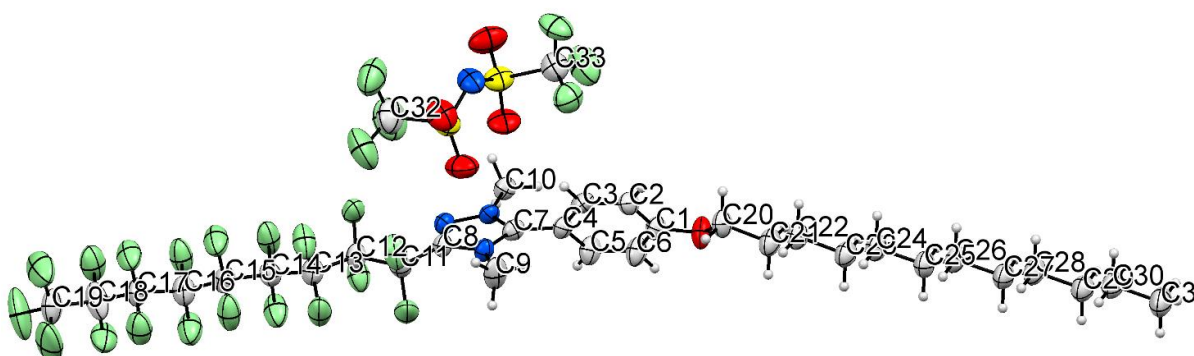


Figure A11. Ortep view of compound [TRIUM-9,12][Tf<sub>2</sub>N].

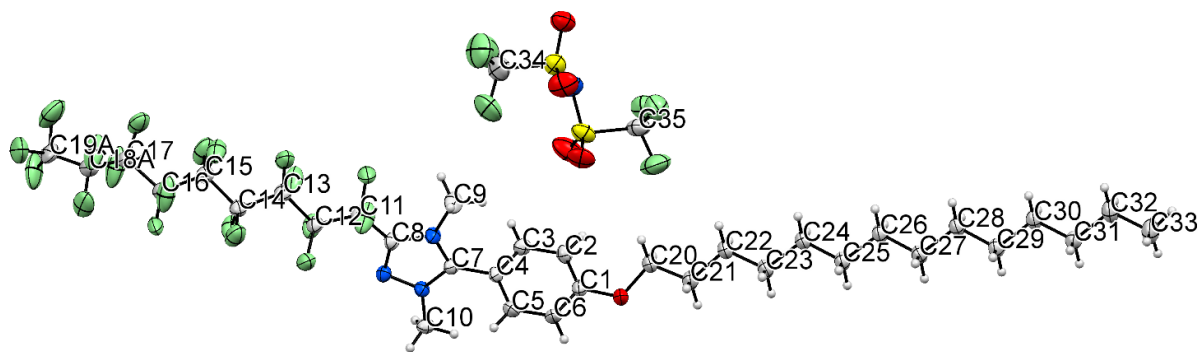


Figure A12. Ortep view of compound [TRIUM-9,14][Tf<sub>2</sub>N].

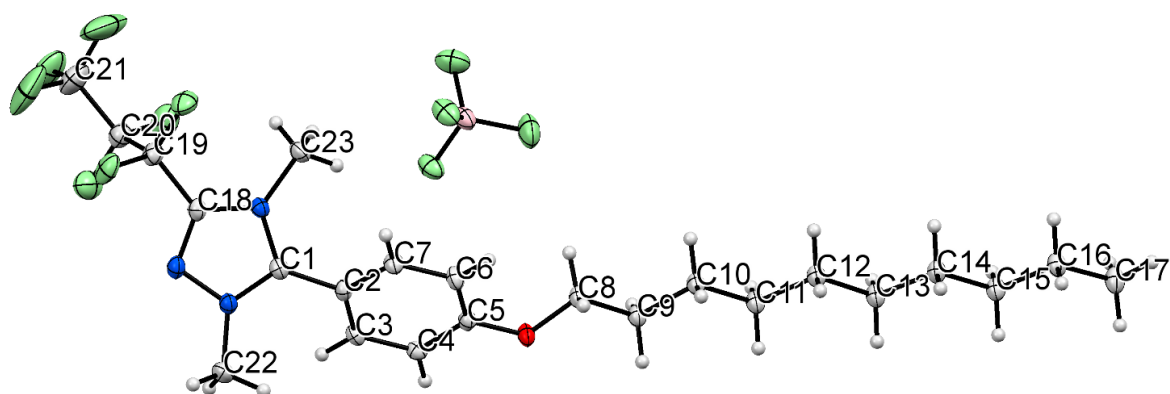


Figure A13. Ortep view of compound [TRIUM-3,10][BF<sub>4</sub>]<sup>†</sup>.

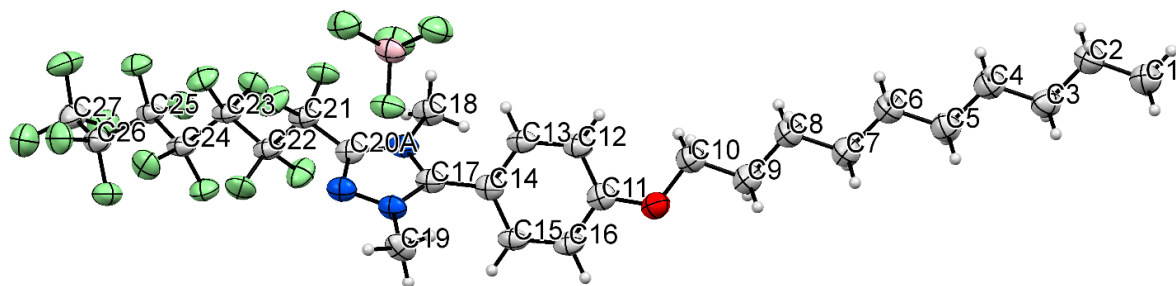


Figure A14. Ortep view of compound [TRIUM-7,10][BF<sub>4</sub>]



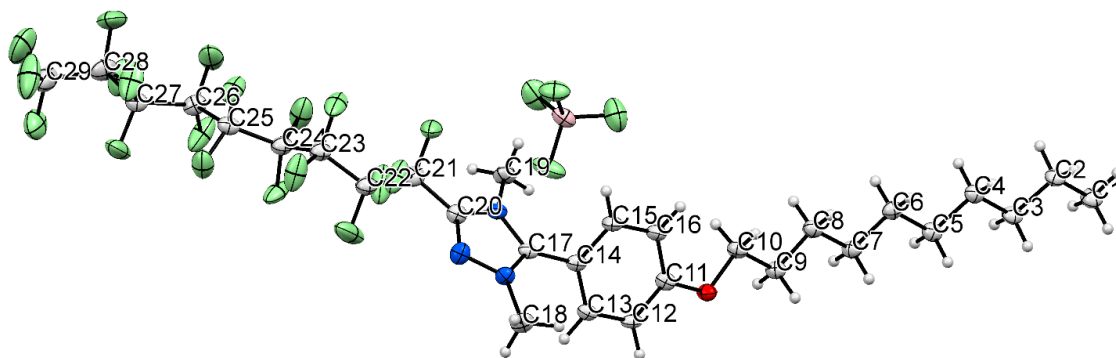


Figure A15. Ortep view of compound [TRIUM-9,10][BF<sub>4</sub>]<sup>+</sup>.

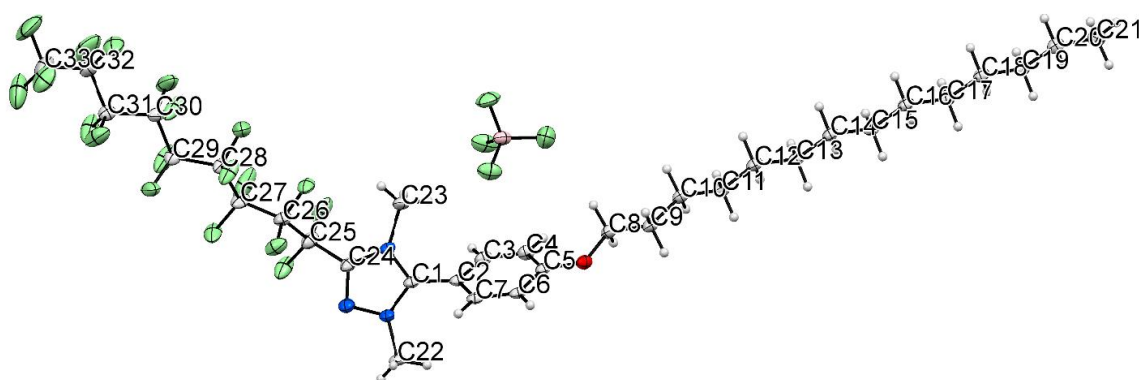
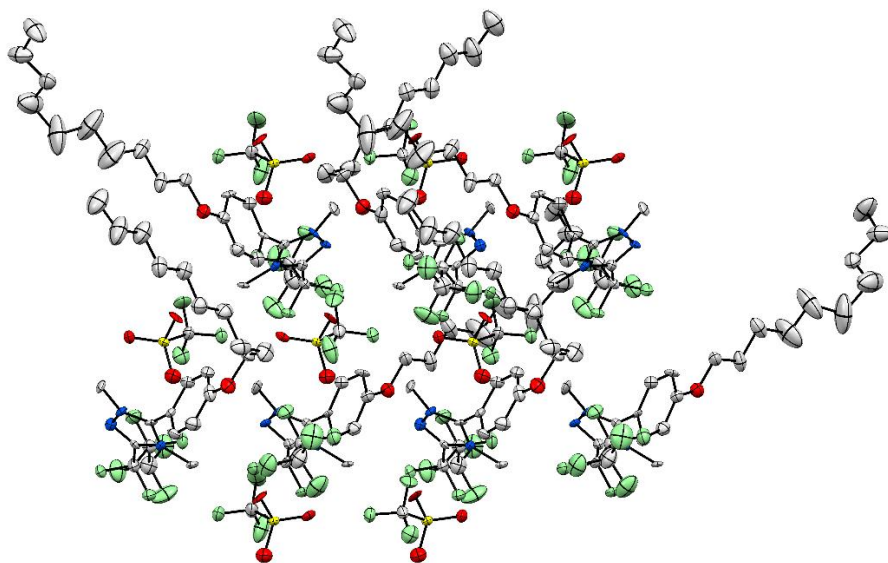


Figure A16. Ortep view of compound [TRIUM-9,14][BF<sub>4</sub>]<sup>+</sup>.

### Crystal Packings of Triazolium salts

For the sake of clarity, hydrogens are omitted in crystal packings views. Crystal packing views are orthogonal to *b* axis of the unit cell, otherwise specified. Some view can be reported with an applied depth cueing, whose brightness decreases along deepness.



**Figure A17.** Crystal packing view of compound [TRIUM-3,10][OTf] orthogonal to *c* axis of the unit cell.

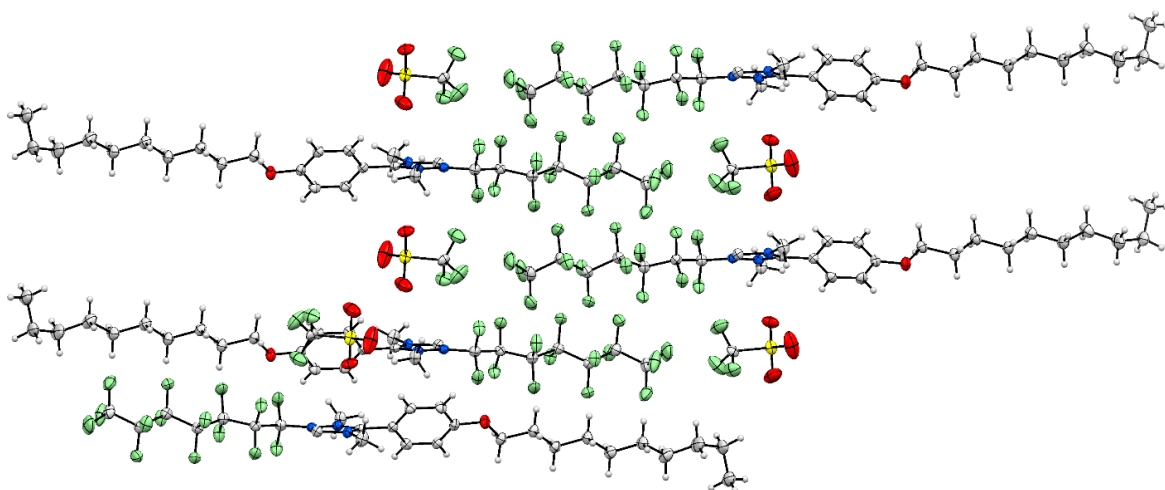


**Figure A18.** Crystal packing view of compound [TRIUM-7,10][OTf].

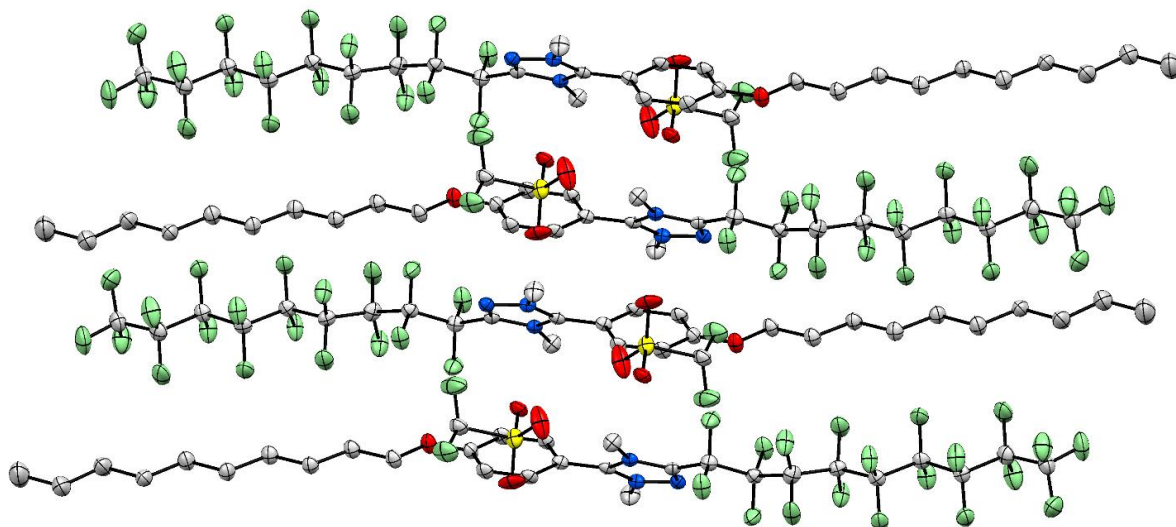


**Figure A19.** Crystal packing view of compound [TRIUM-9,10][OTf].

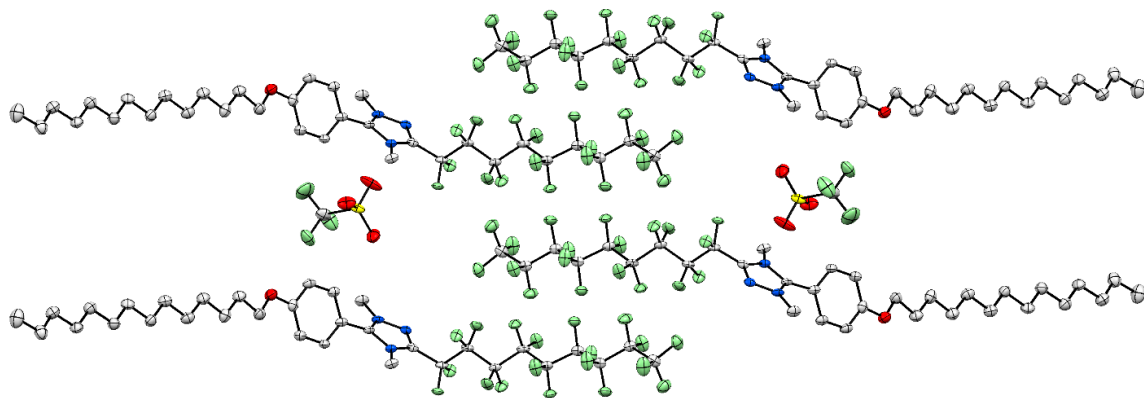


**Figure A20.** Crystal packing view of compound [TRIUM-9,14][OTf]<sup>+</sup>.

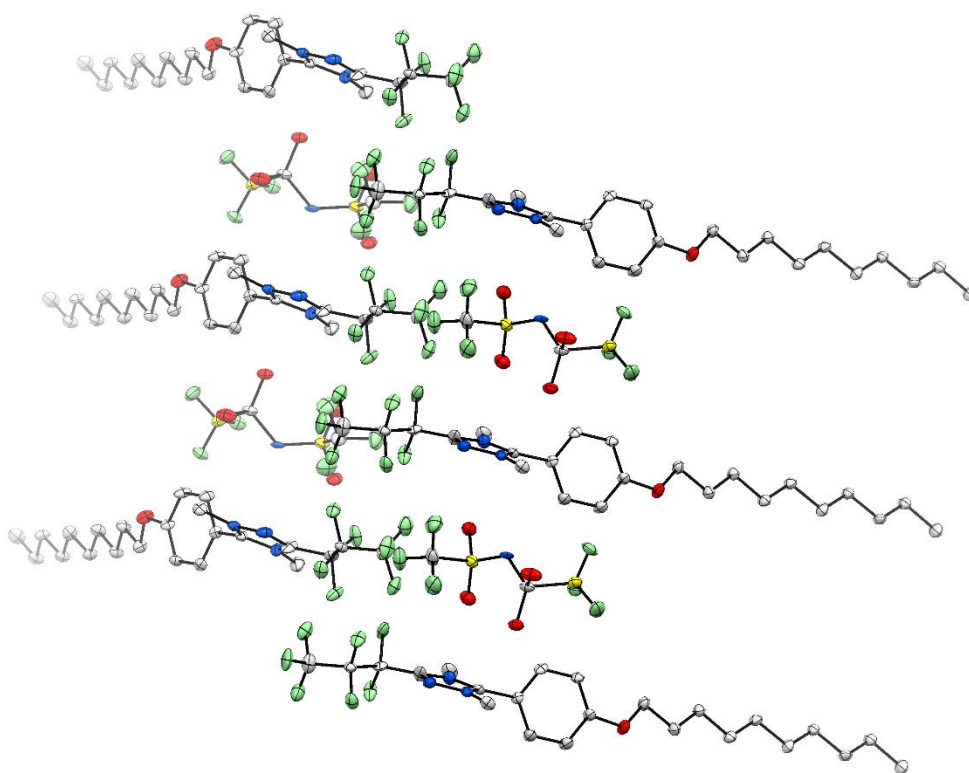


**Figure A21.** Crystal packing view of compound [TRIUM-3,10][Tf<sub>2</sub>N]. Angle view is rotated of some degrees from the orthogonal of *b* axis of the unit cell and the brightness decreases along deepness.

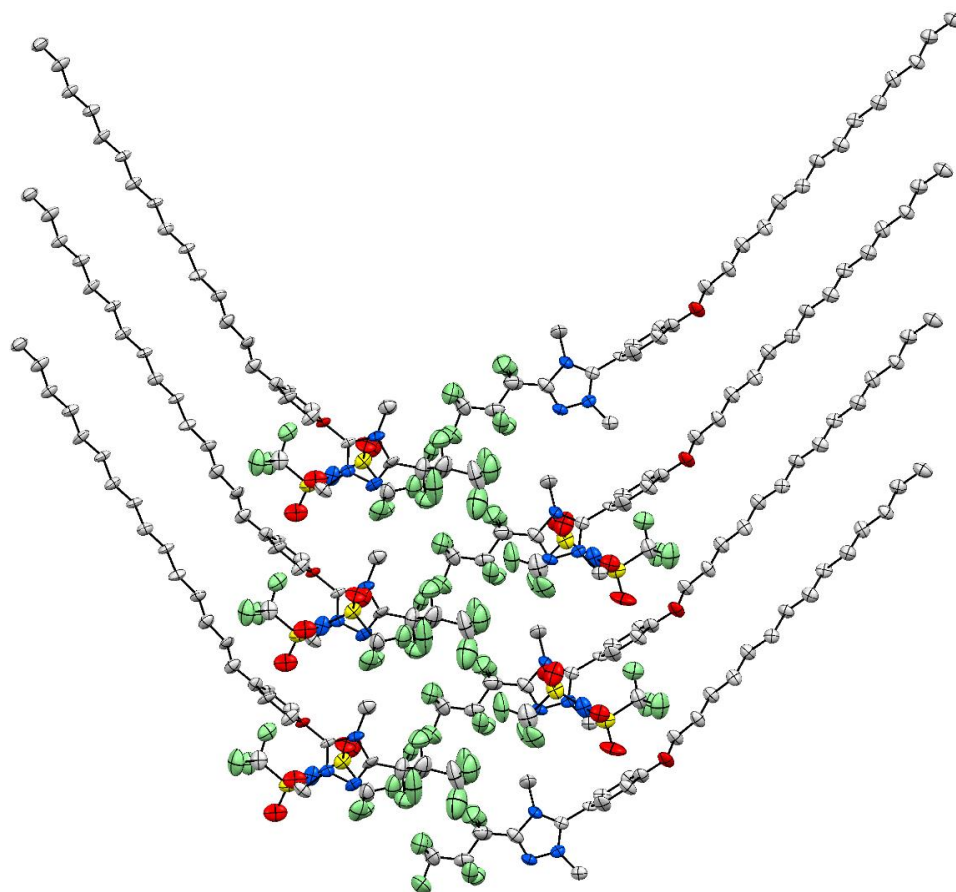


**Figure A22.** Crystal packing view of compound [TRIUM-3,14][Tf<sub>2</sub>N] orthogonal to *a* axis of the unit cell.

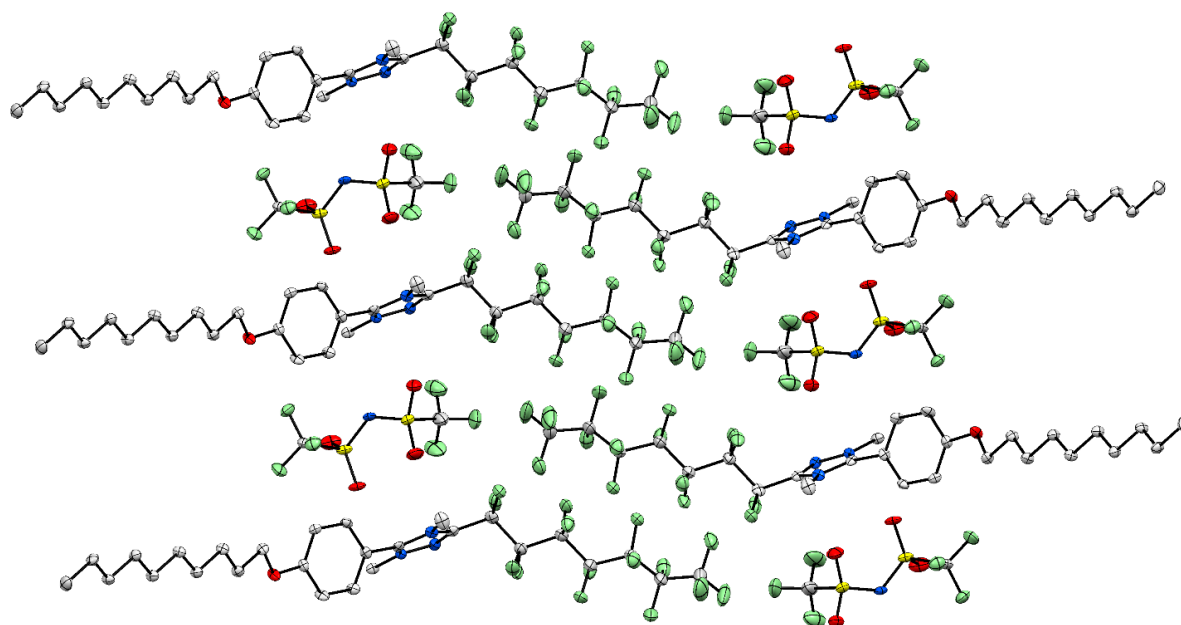


**Figure A23.** Crystal packing view of compound [TRIUM-7,10][Tf<sub>2</sub>N].

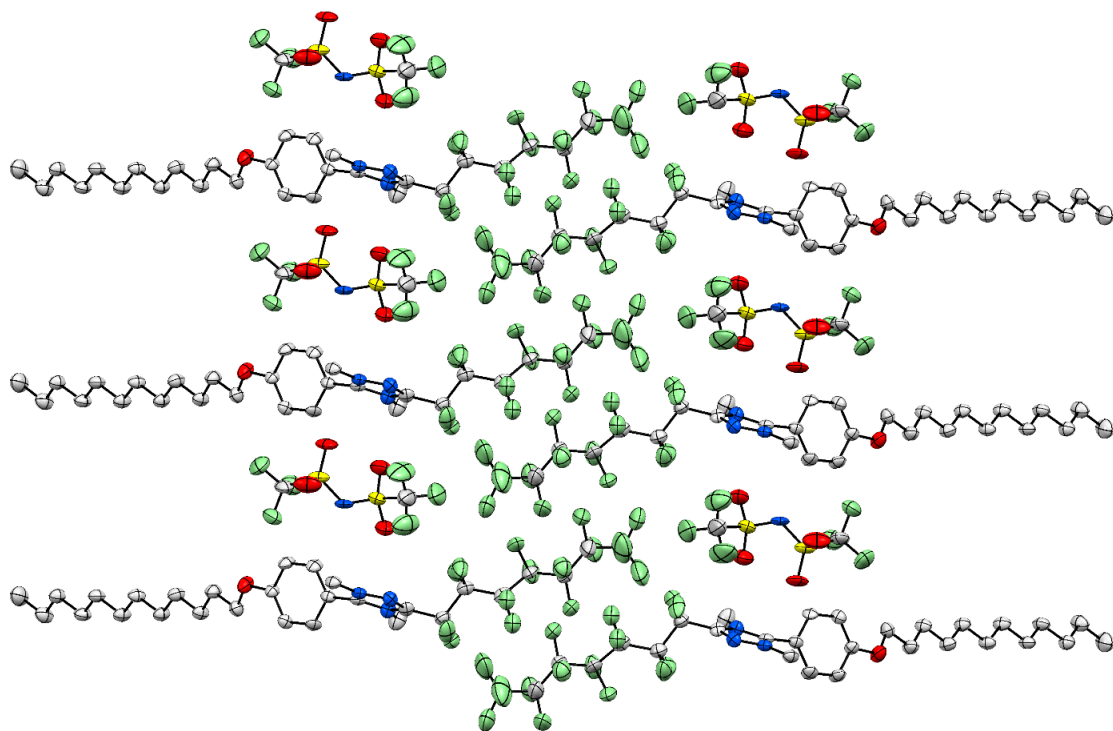


**Figure A24.** Crystal packing view of compound [TRIUM-7,12][Tf<sub>2</sub>N].

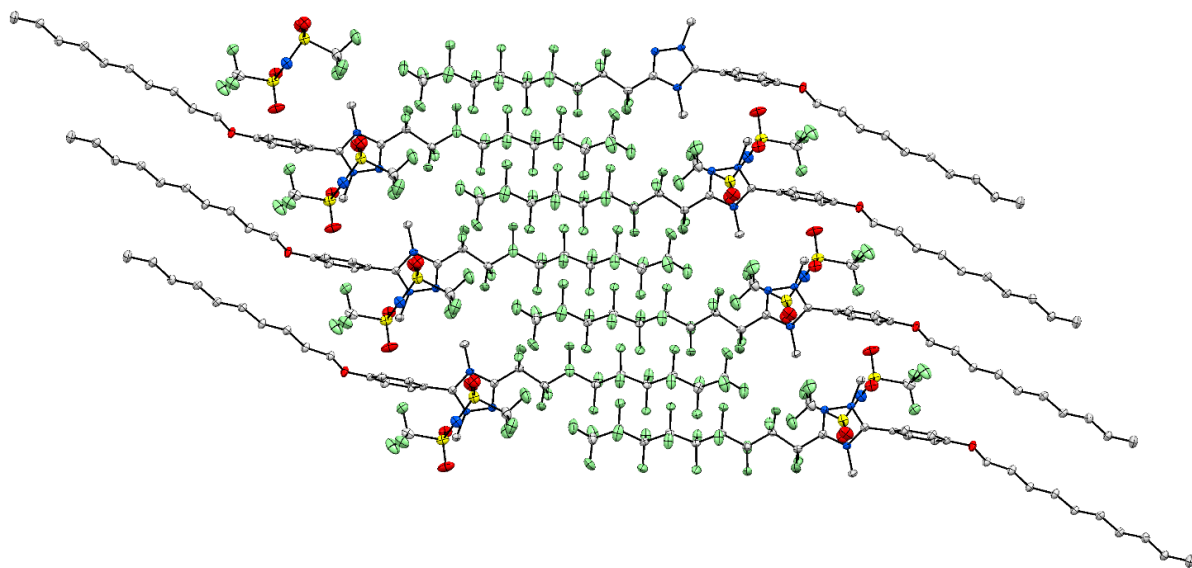


**Figure A25.** Crystal packing view of compound [TRIUM-9,10][Tf<sub>2</sub>N].

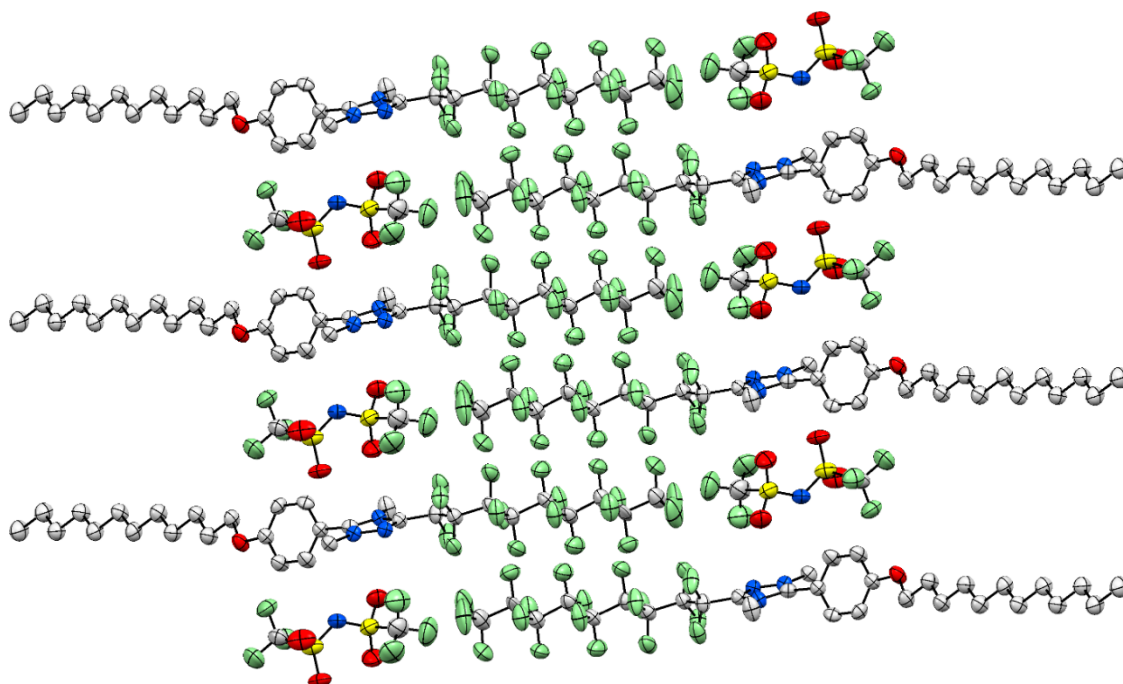


Figure A26. Crystal packing view of compound [TRIUM-9,12][Tf<sub>2</sub>N].

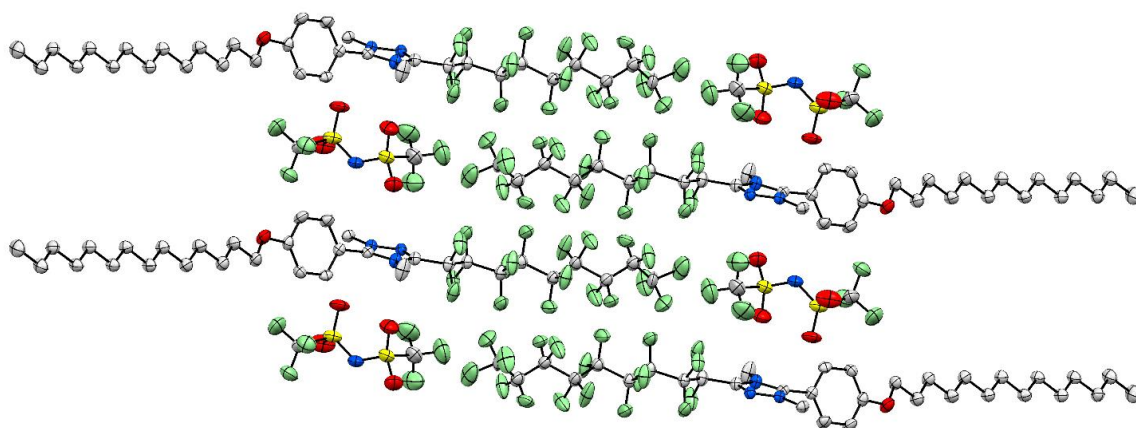


Figure A27. Crystal packing view of compound [TRIUM-9,14][Tf<sub>2</sub>N].



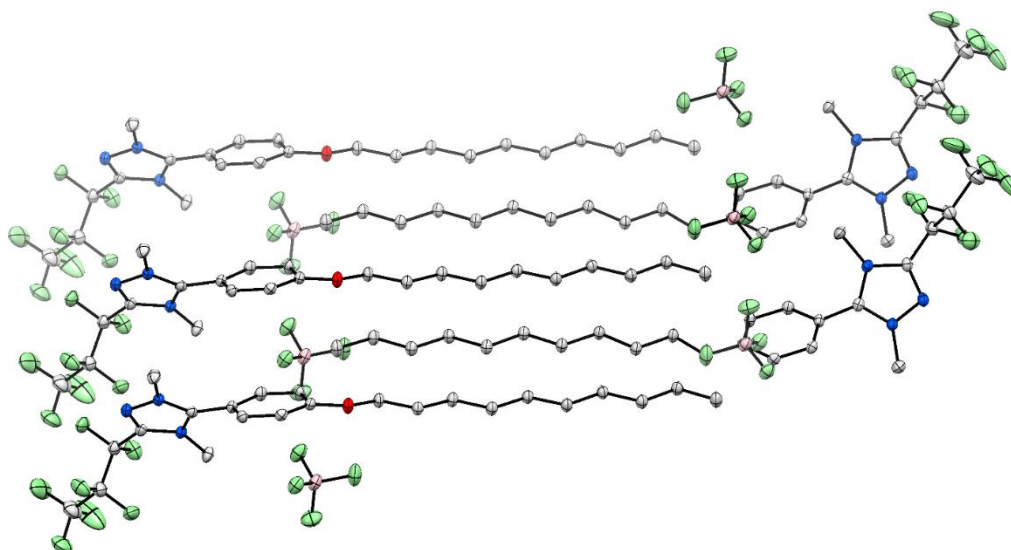


Figure A28. Crystal packing view of compound [TRIUM-3,10][BF<sub>4</sub>]<sup>+</sup>.

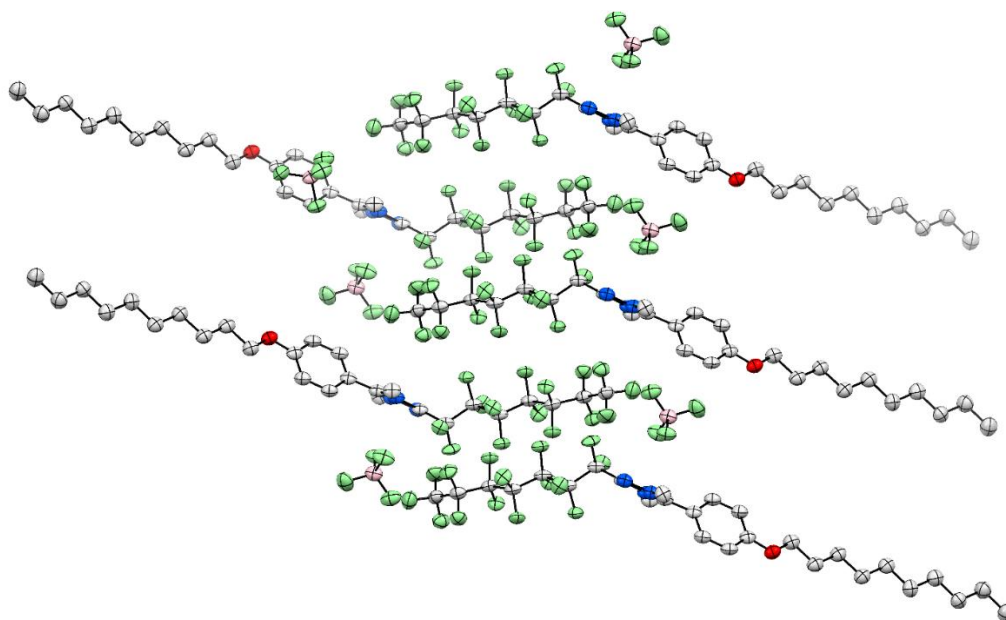
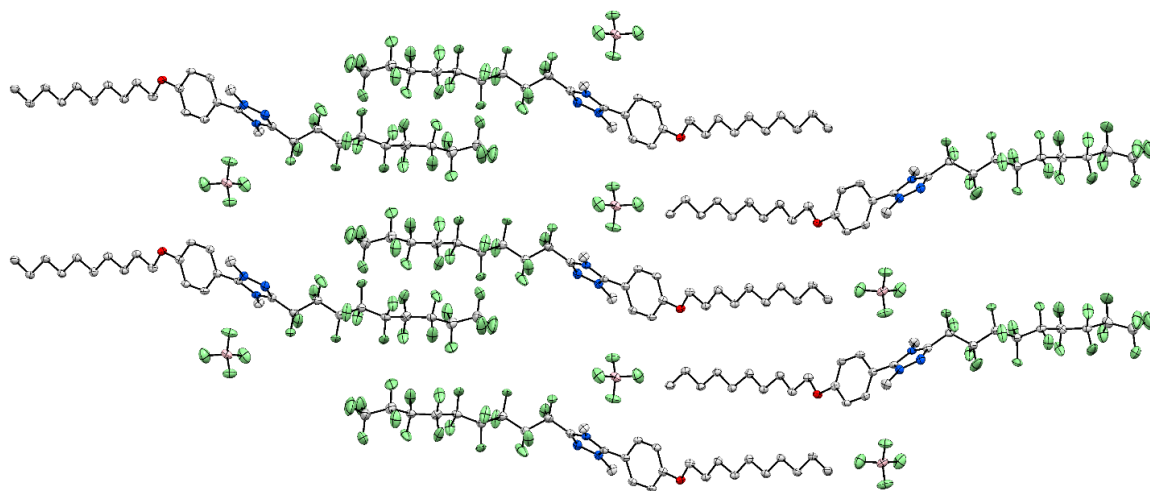
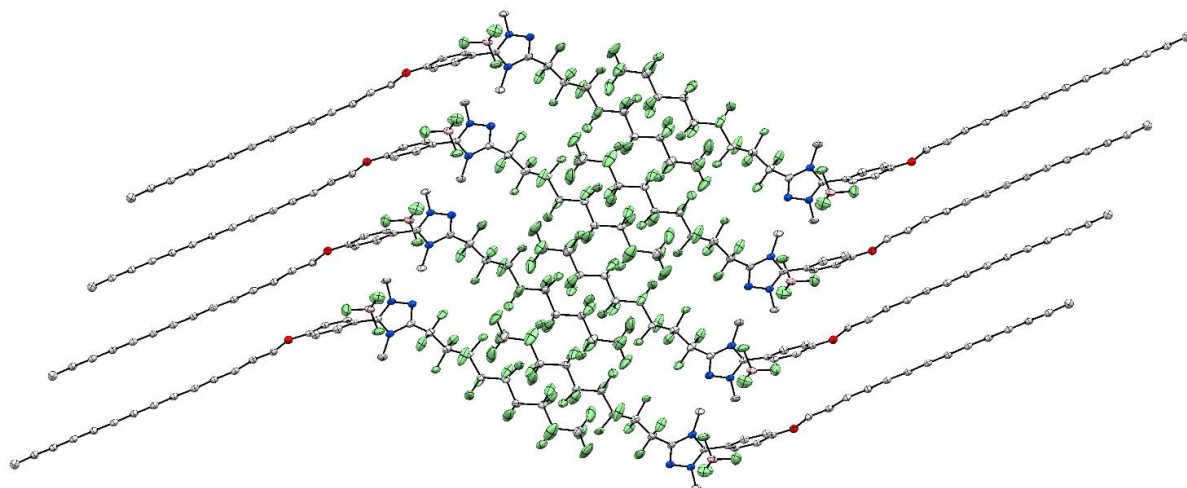


Figure A29. Crystal packing view of compound [TRIUM-7,10][BF<sub>4</sub>].



**Figure A30.** Crystal packing view of compound [TRIUM-9,10][BF<sub>4</sub>]<sup>+</sup>.



**Figure A31.** Crystal packing view of compound [TRIUM-9,14][BF<sub>4</sub>]<sup>+</sup> orthogonal to *a* axis of the unit cell.



## Appendix B – POM Microphotographs

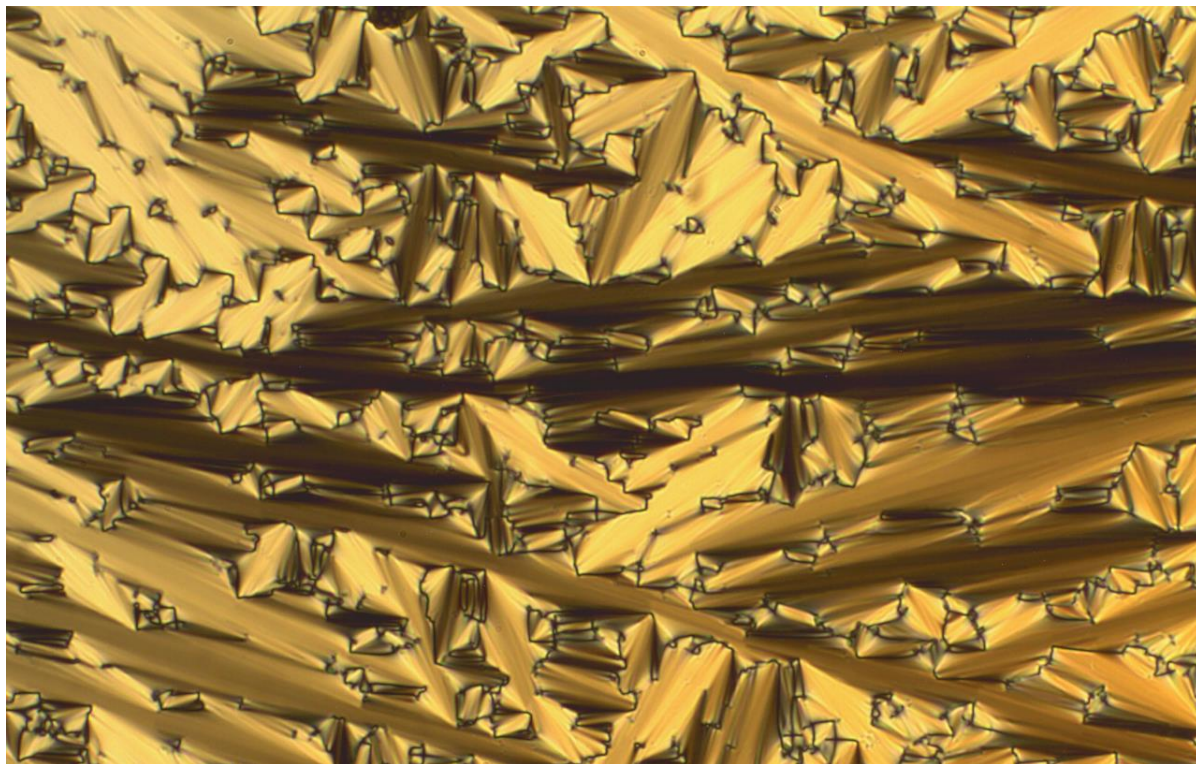


**Figure B1.** SmA phase of [TRYUM-7,10][BF<sub>4</sub>] on cooling from the isotropic liquid at 183 °C, with 100x as magnification.

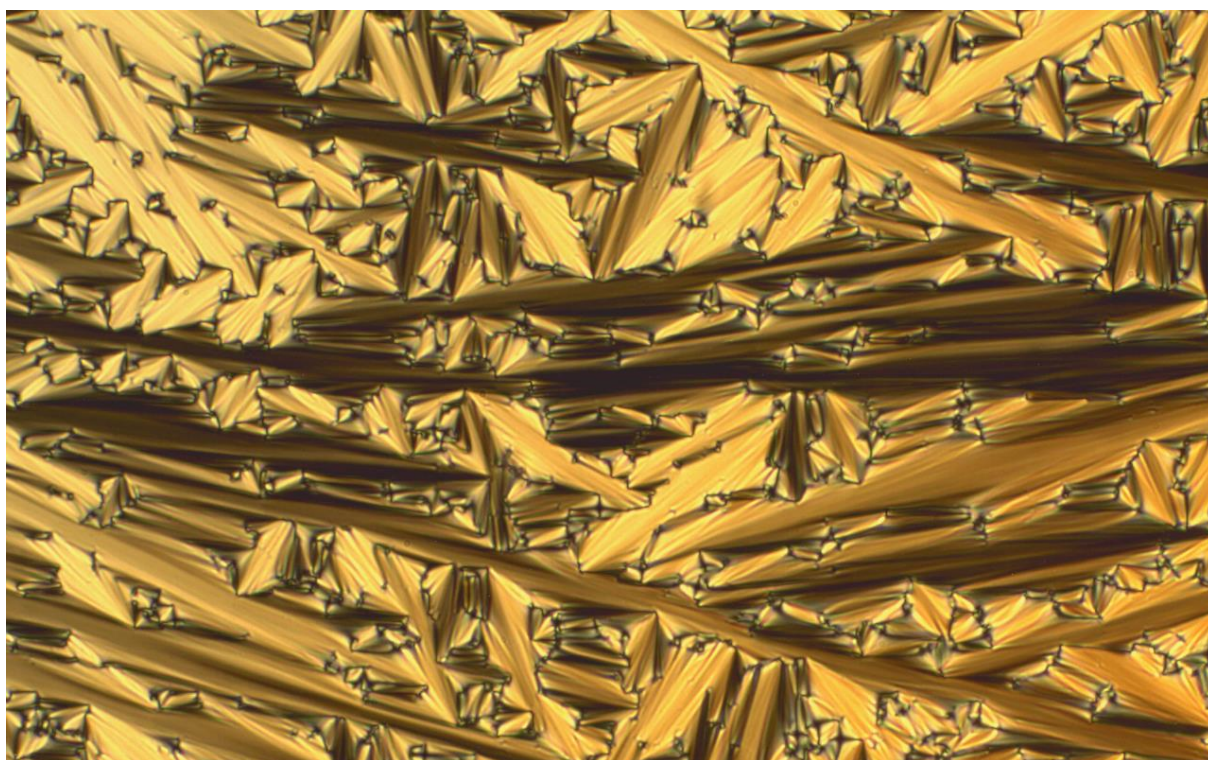


**Figure B2.** SmB phase of [TRYUM-7,10][BF<sub>4</sub>] on cooling from the isotropic liquid at 153 °C, with 100x as magnification.



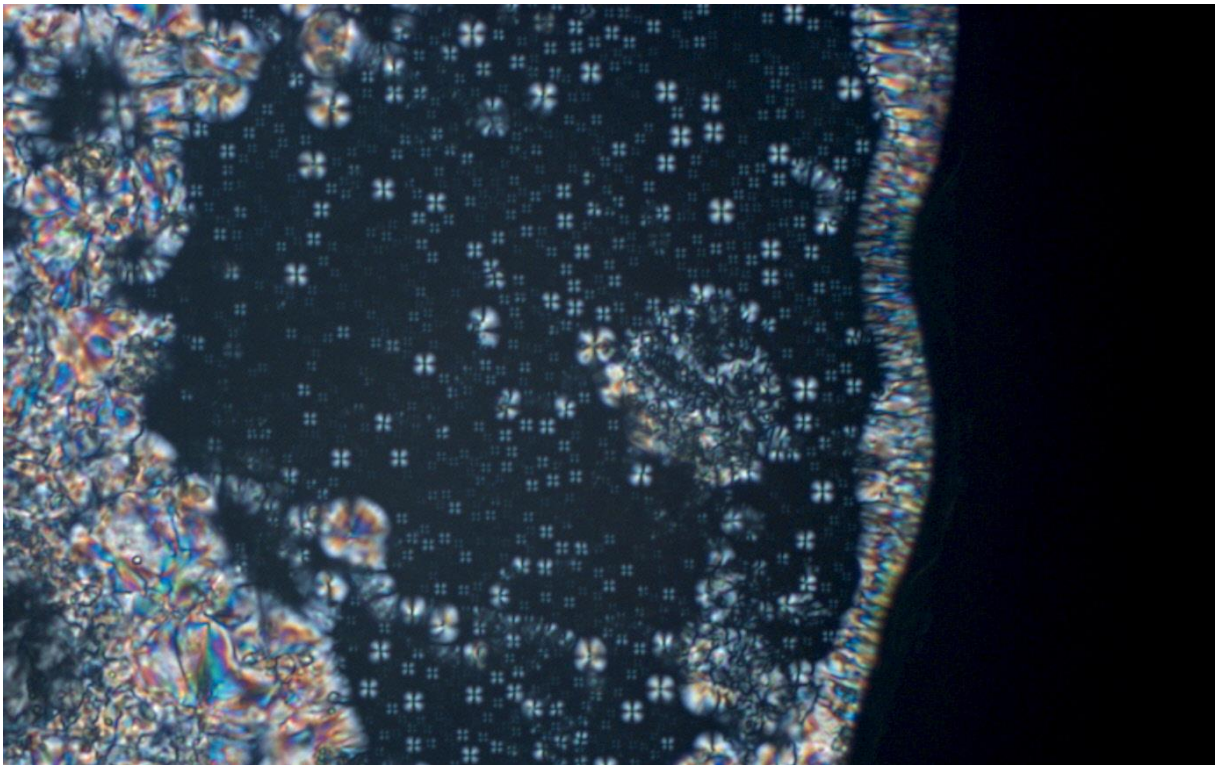


**Figure B3.** SmA phase of [TRYUM-7,12][OTf] on the 1<sup>st</sup> heating from the solid at 140 °C, with 100x as magnification.

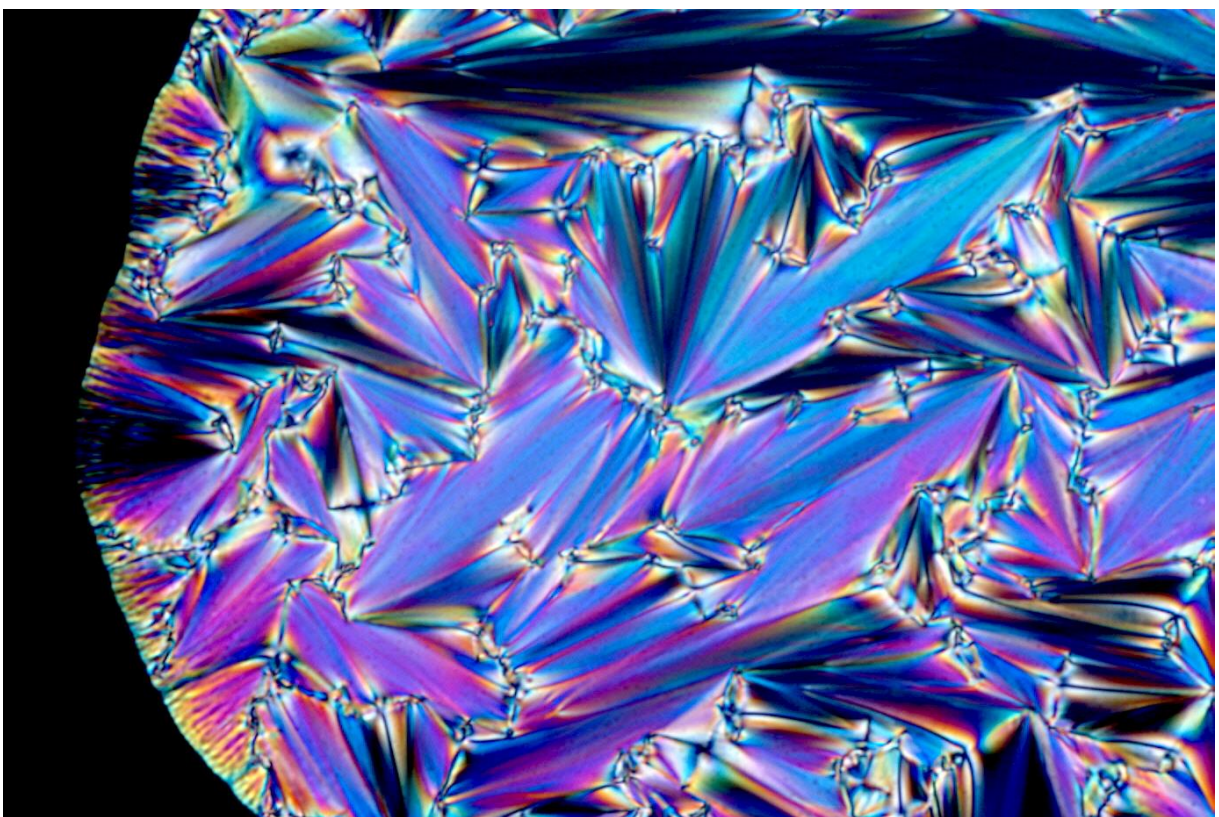


**Figure B4.** SmA phase of [TRYUM-7,12][OTf] on cooling from the isotropic liquid at 140 °C, with 200x as magnification.



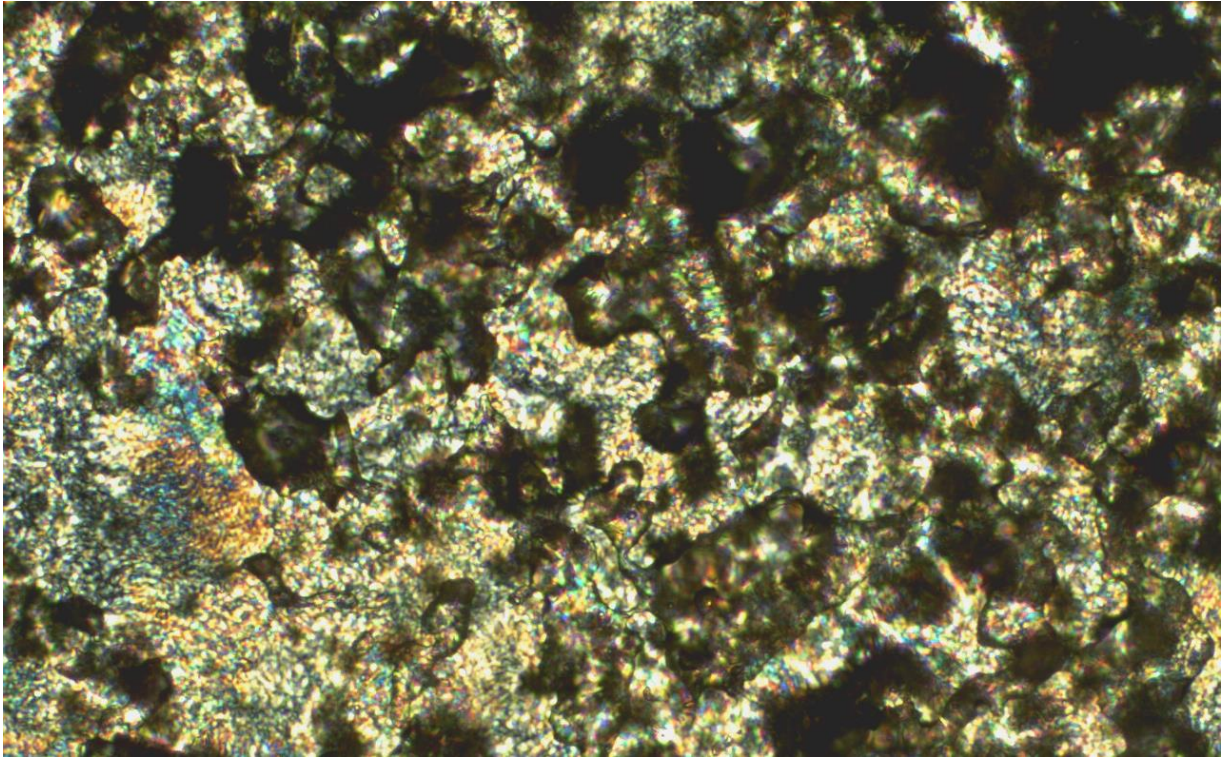


**Figure B5.** SmA phase of [TRYUM-9,14][OTf] on 1<sup>st</sup> heating from the solid at 110 °C, with 100x as magnification.

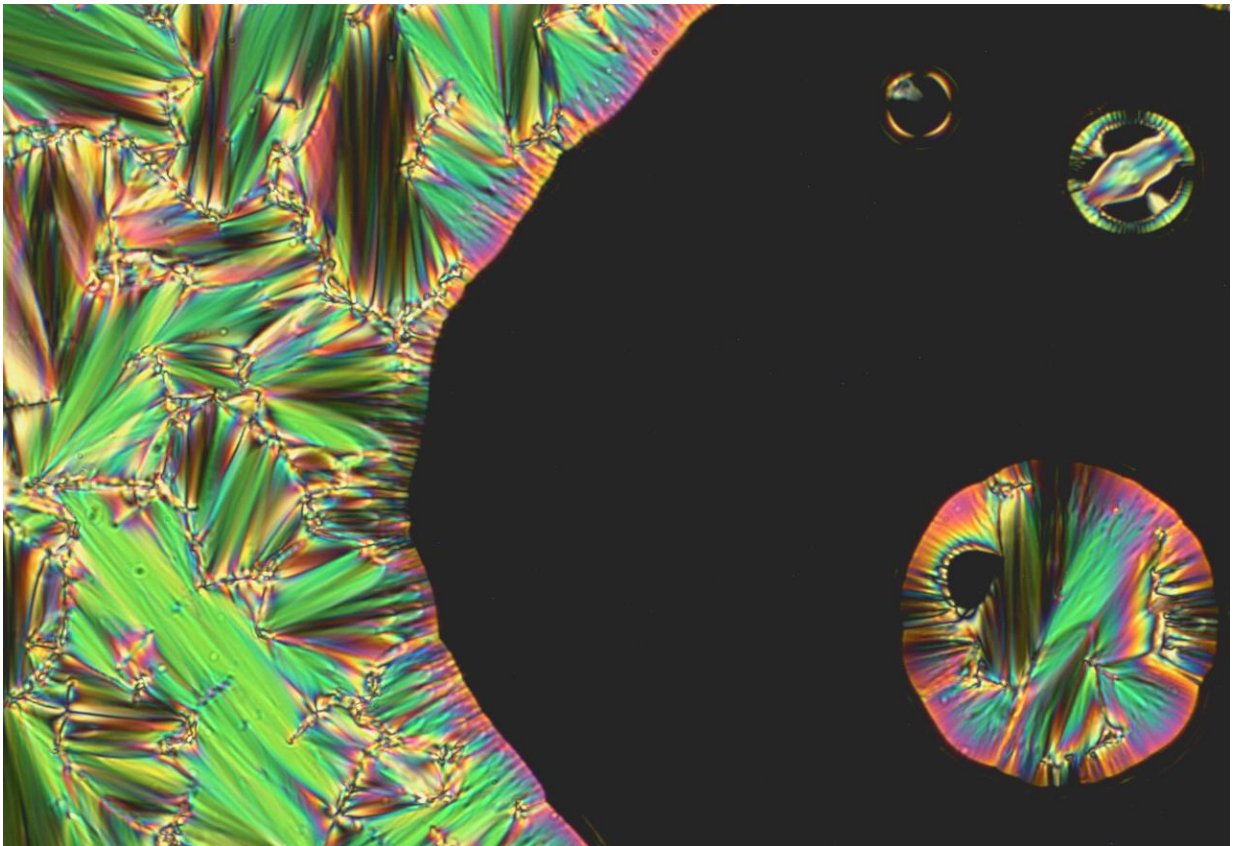


**Figure B6.** SmA phase of [TRYUM-9,14][OTf] on cooling from the isotropic liquid at 183 °C, with 200x as magnification.





**Figure B7.** Batonnet of [TRYUM-7,10][OTf] during the transition from the isotropic liquid to SmA phase at 159 °C, with 100x as magnification.

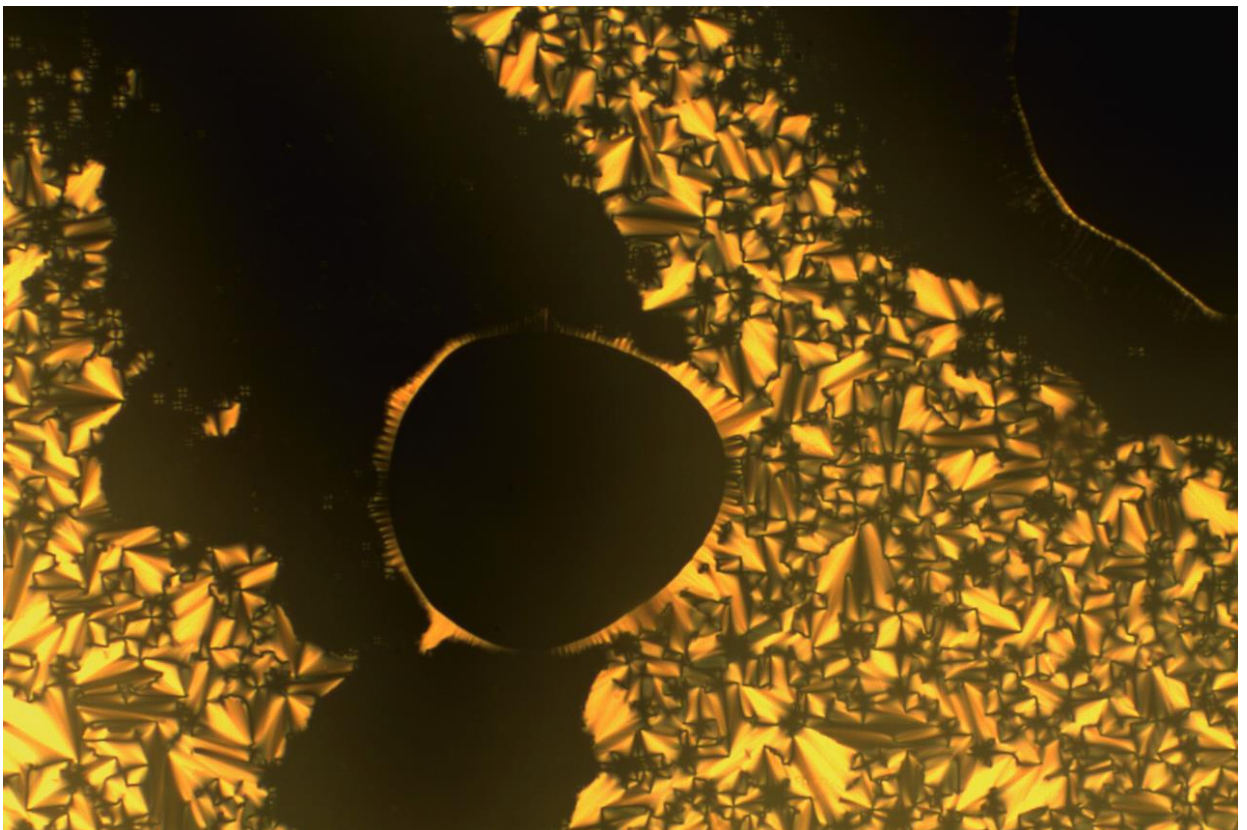


**Figure B8.** SmA phase of [TRYUM-9,12][Tf<sub>2</sub>N] on cooling from the isotropic liquid at 114 °C, with 100x as magnification.



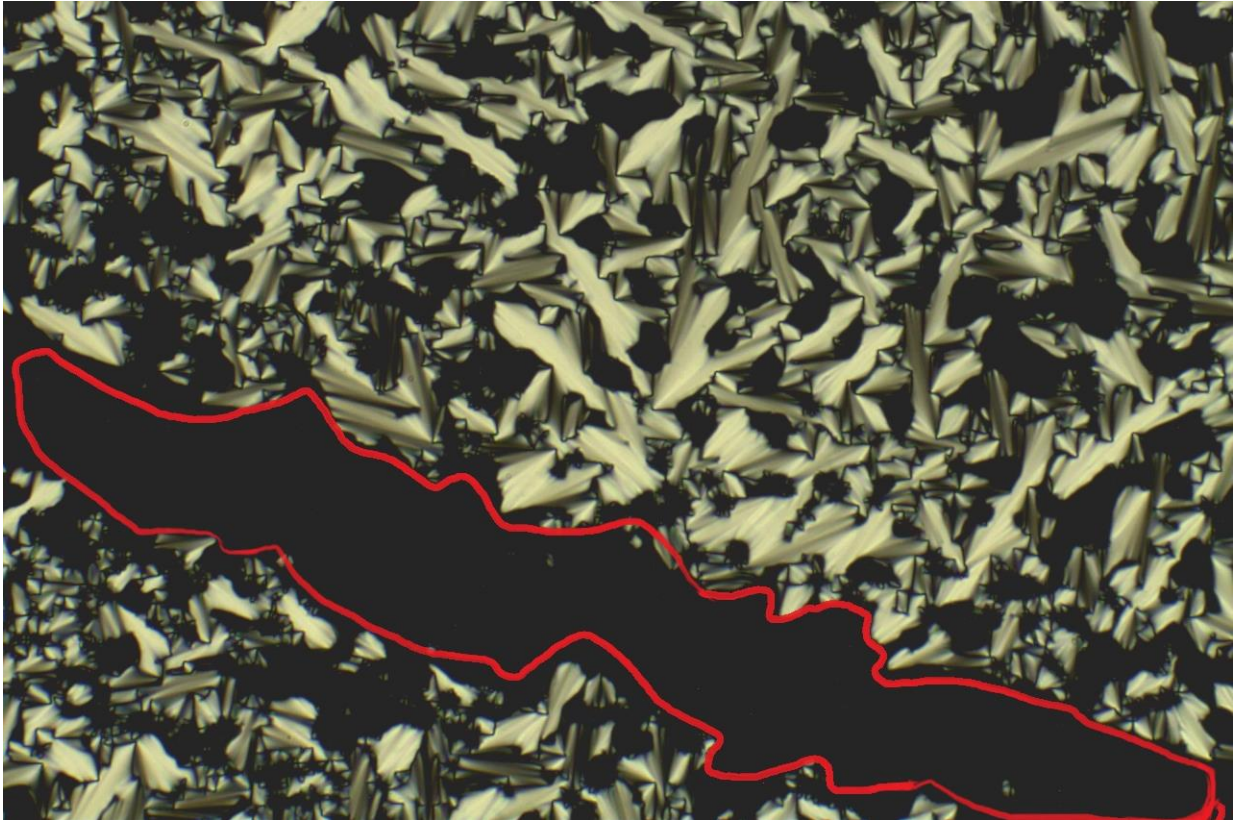


**Figure B9.** SmA phase of [TRYUM-7,10][Tf<sub>2</sub>N] on cooling from the isotropic liquid at 45 °C, with 100x as magnification. A large dark zone with homeotropic alignment is circle in red.

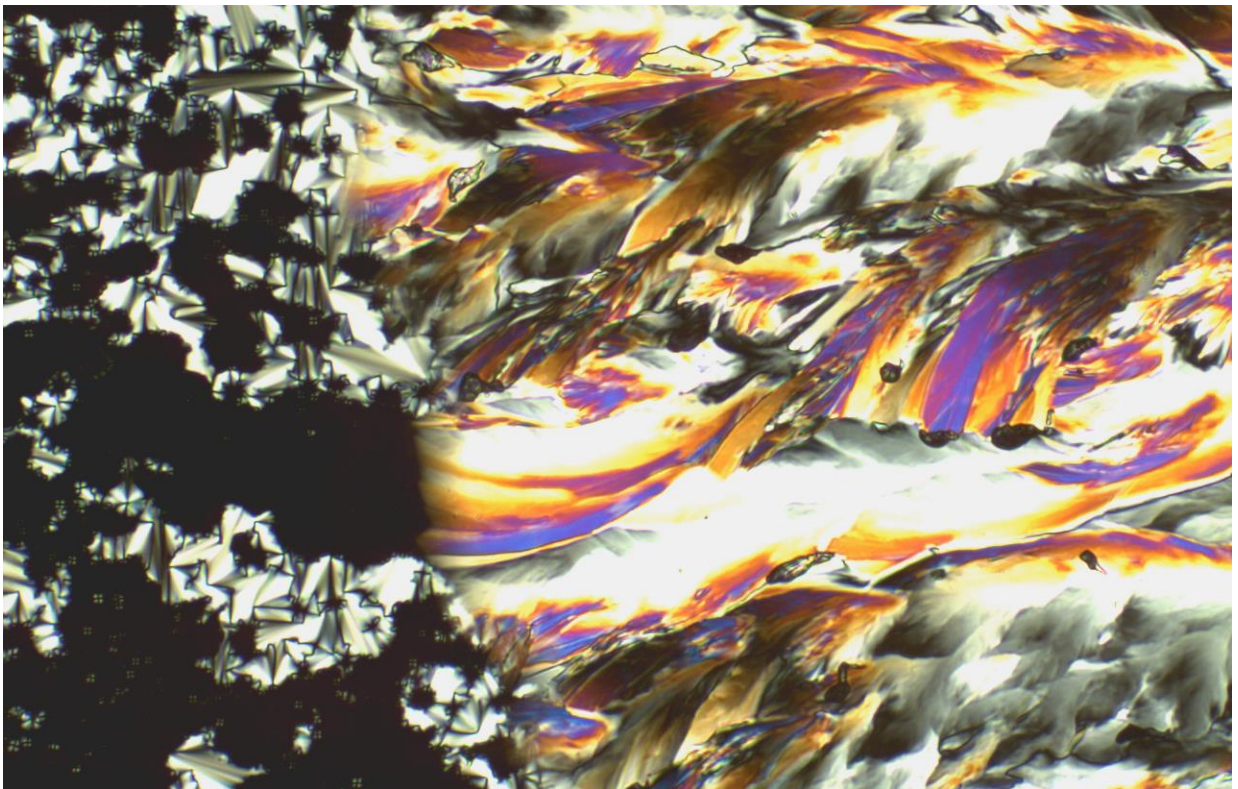


**Figure B10.** Crystallisation of [TRYUM-7,10][Tf<sub>2</sub>N] on cooling from the SmA phase at 32 °C, with 100x as magnification.

## Appendix C – SAXS and SANS plots

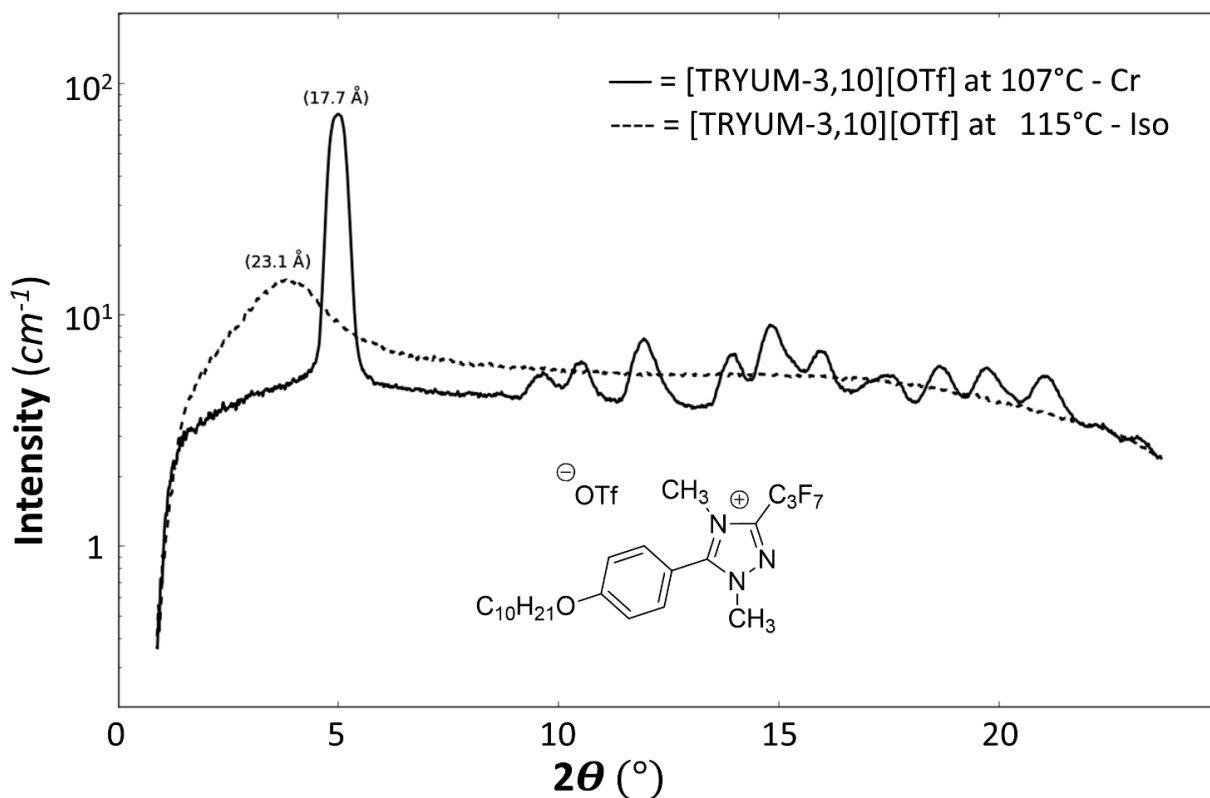


Figure C1. X-ray scattering of compound [TRYUM-3,10][OTf].

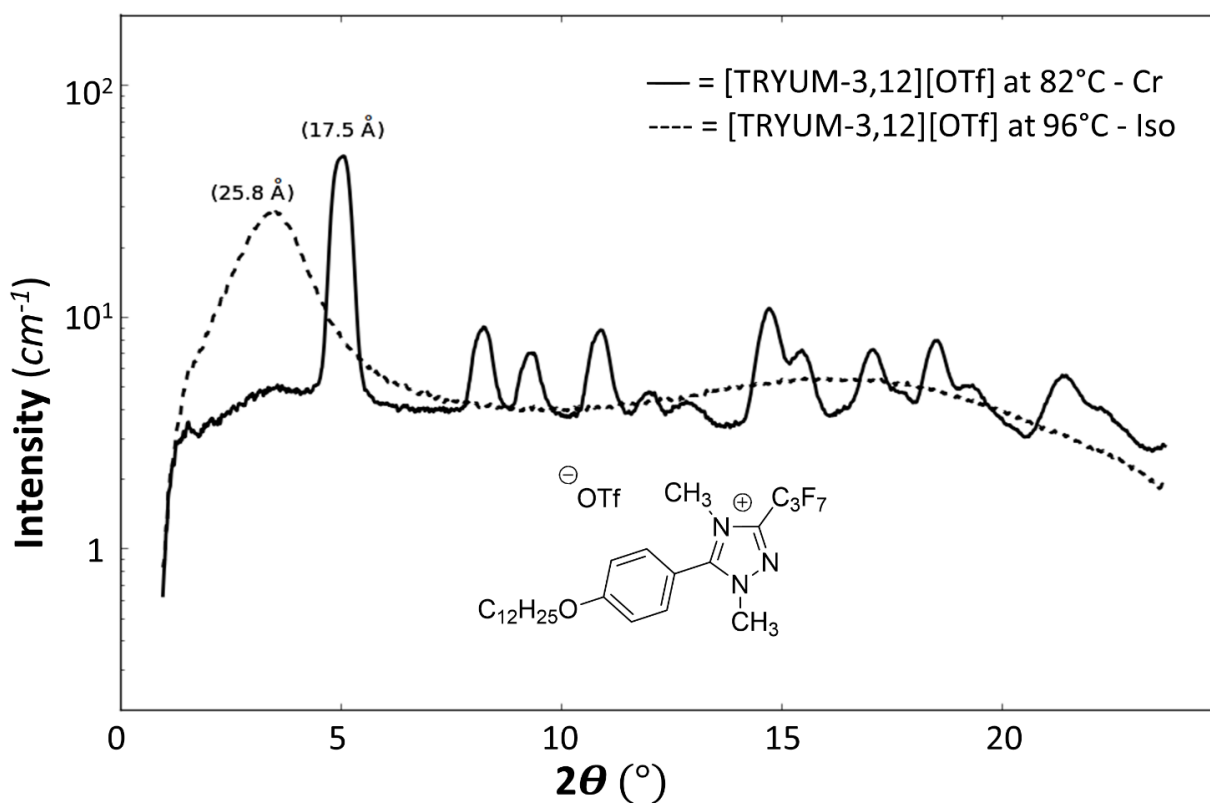


Figure C2. X-ray scattering of compound [TRYUM-3,12][OTf].

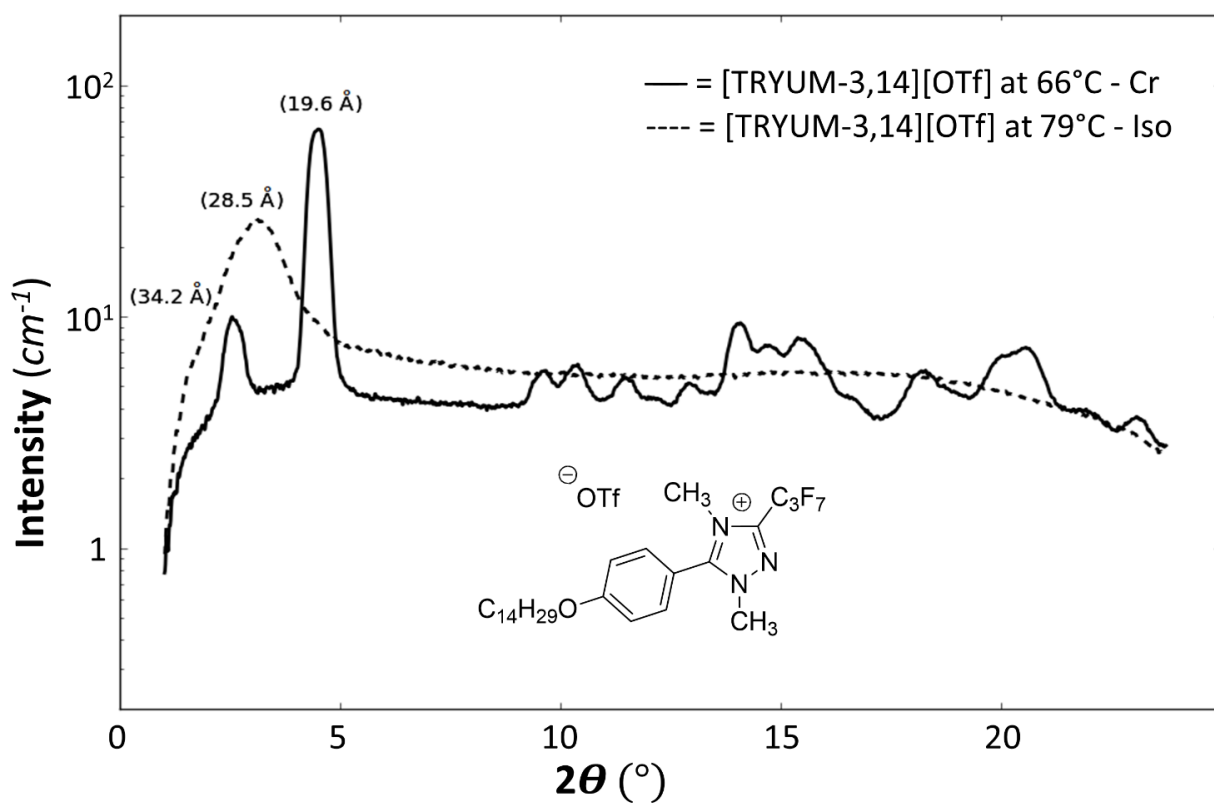


Figure C3. X-ray scattering of compound [TRYUM-3,14][OTf].

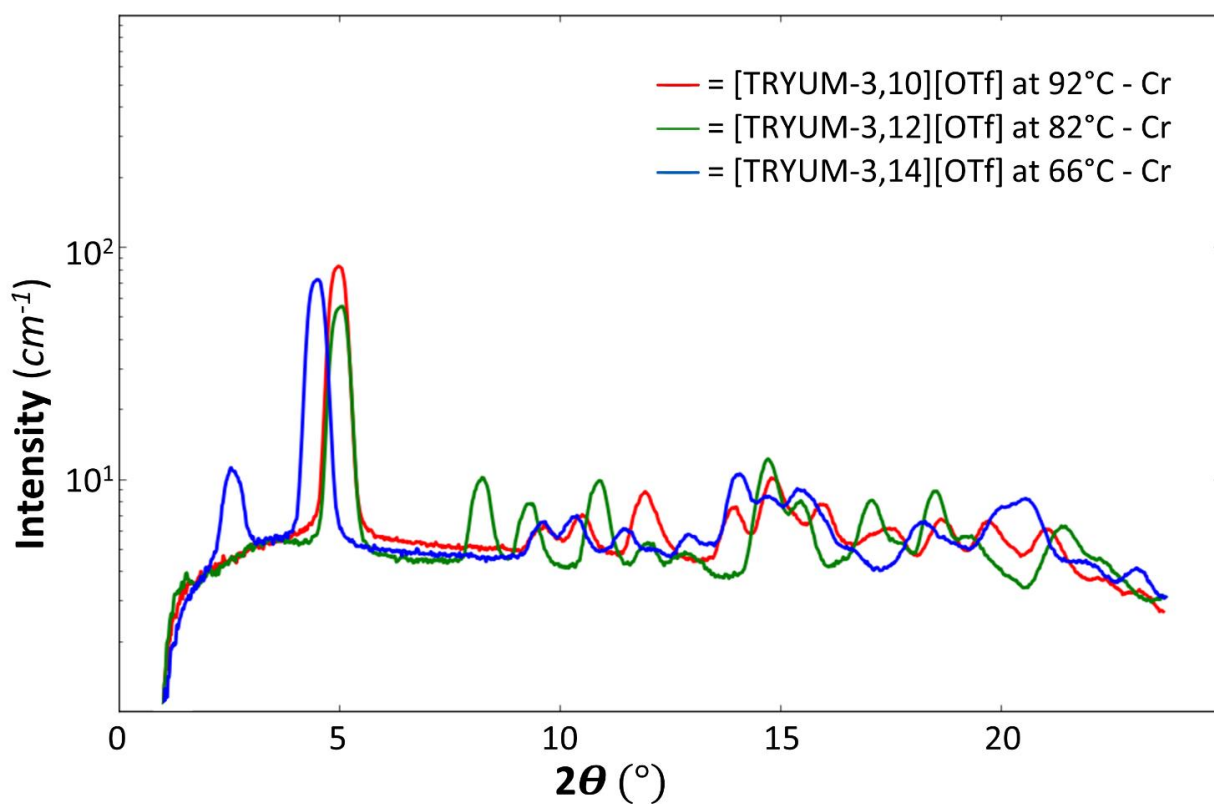


Figure C4. X-ray scattering of compounds [TRYUM-3,n][OTf] in Cr phases.

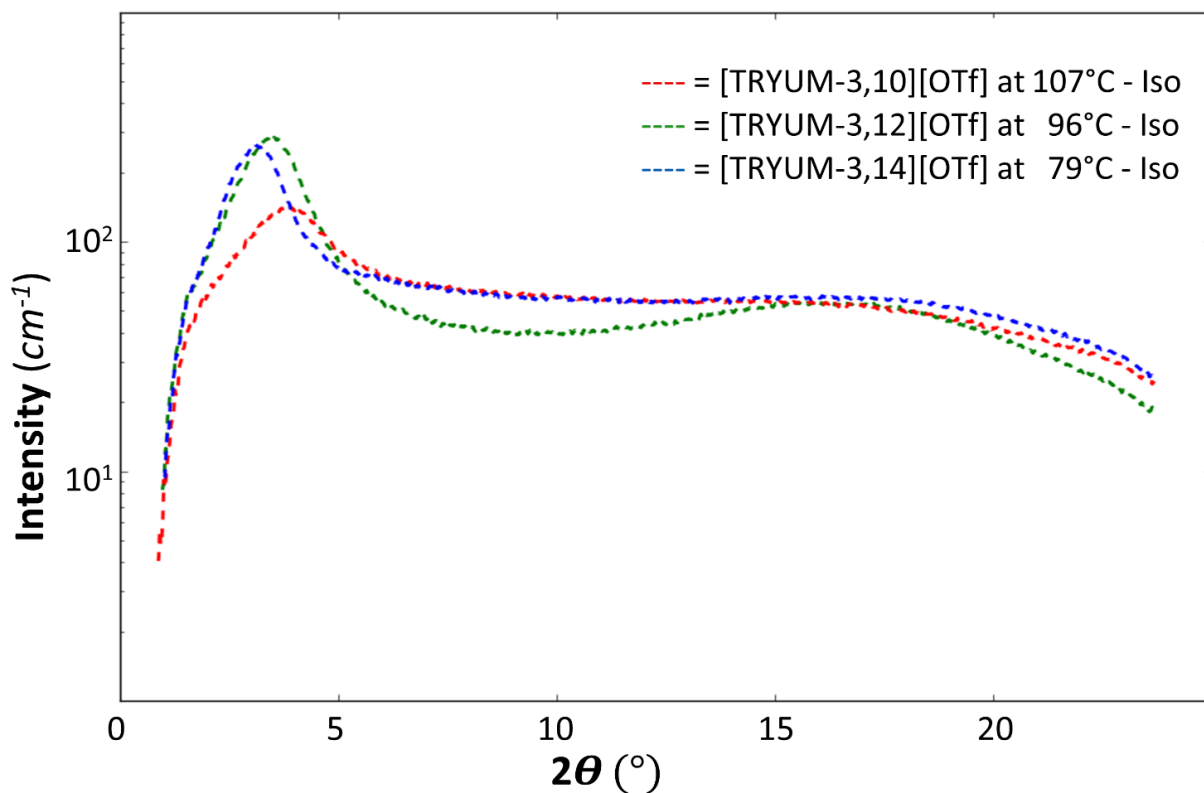


Figure C5. X-ray scattering of compounds [TRYUM-3,n][OTf] in Iso phases.

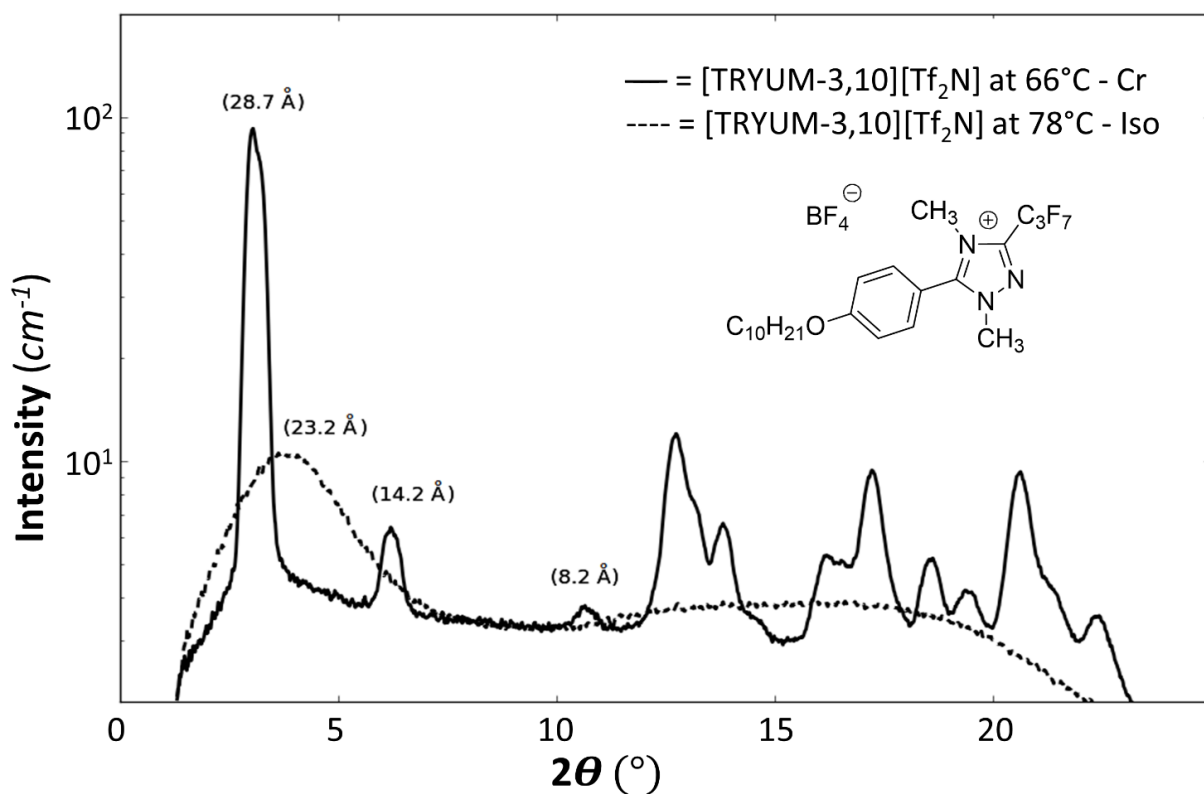


Figure C6. X-ray scattering of compound [TRYUM-3,10][Tf<sub>2</sub>N].



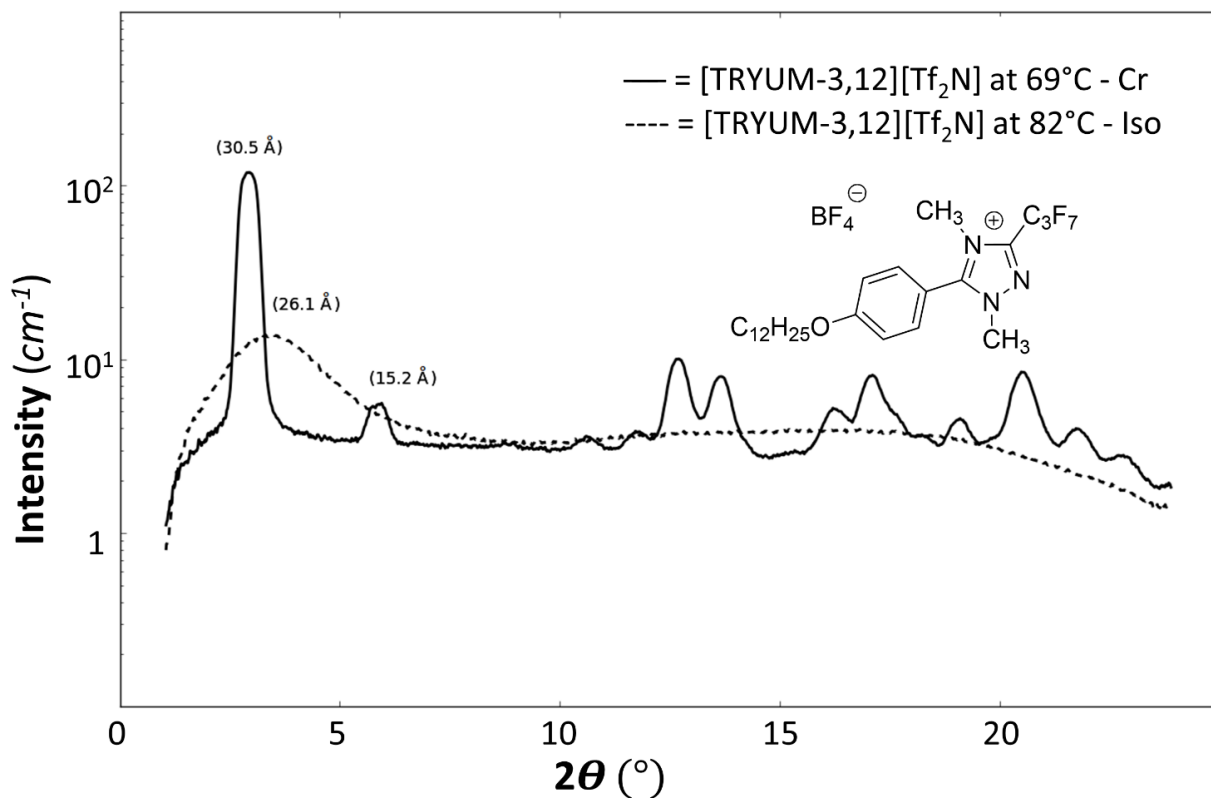


Figure C7. X-ray scattering of compound [TRYUM-3,12][Tf<sub>2</sub>N].

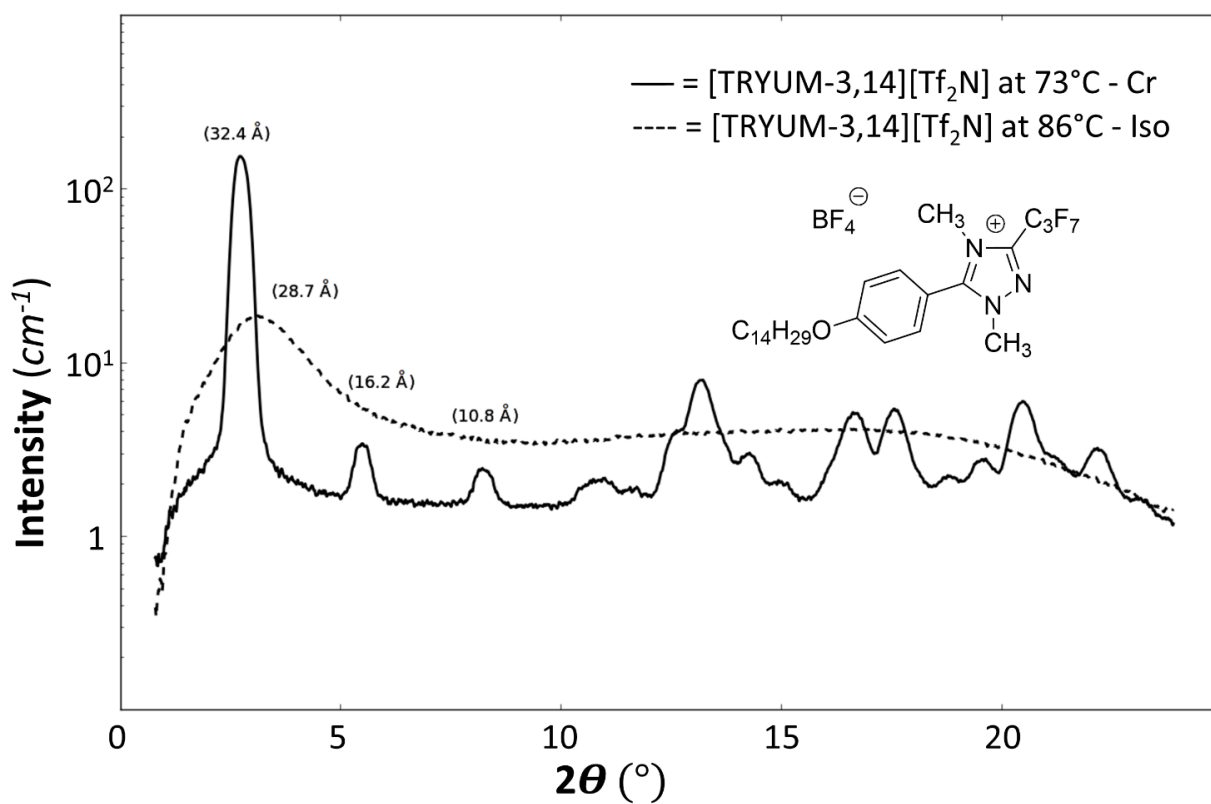


Figure C8. X-ray scattering of compound [TRYUM-3,14][Tf<sub>2</sub>N].

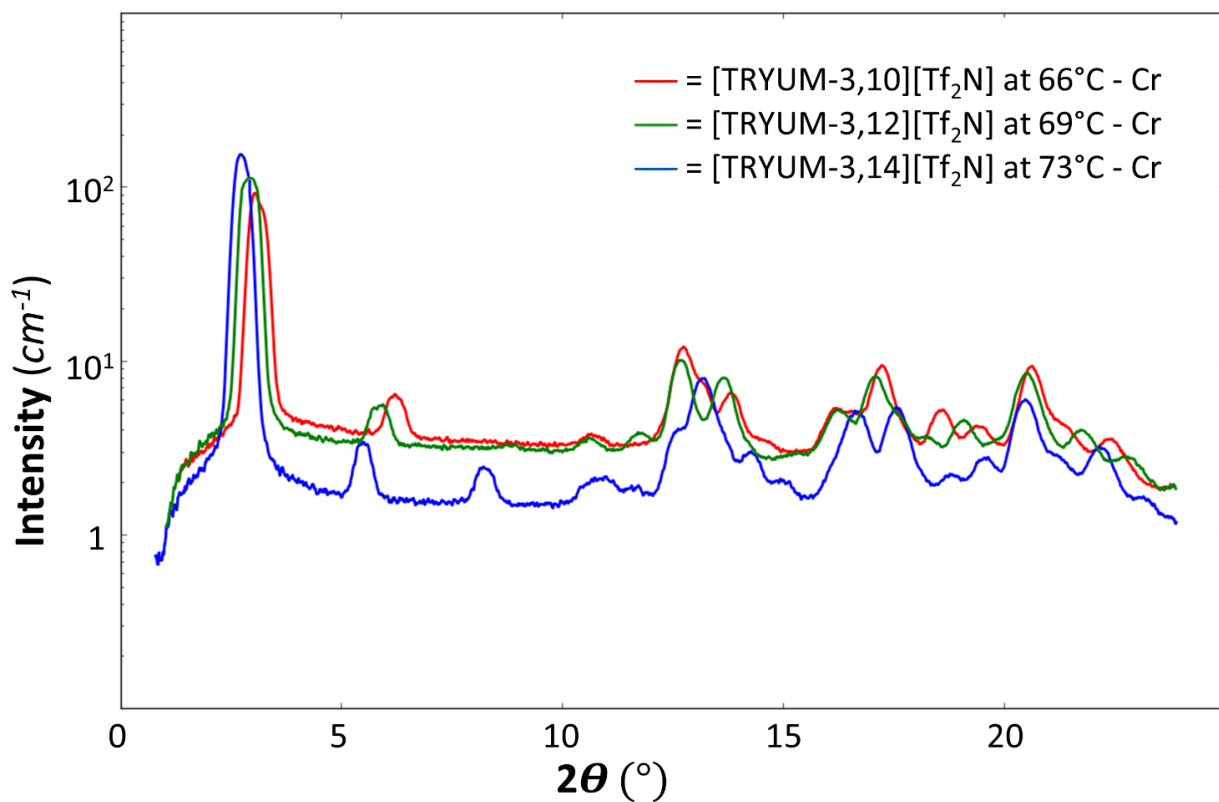


Figure C9. X-ray scattering of compounds [TRYUM-3,*n*][Tf<sub>2</sub>N] in Cr phases.

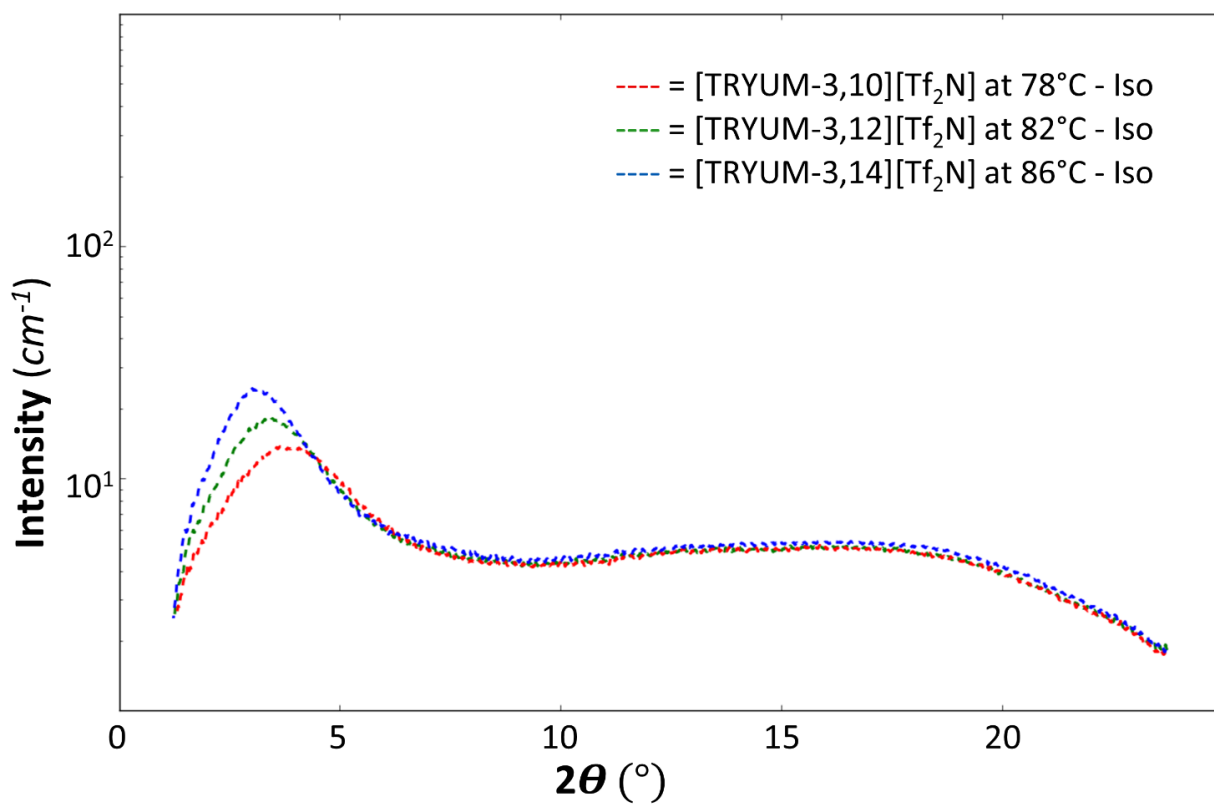


Figure C10. X-ray scattering of compounds [TRYUM-3,*n*][Tf<sub>2</sub>N] in Iso phases.

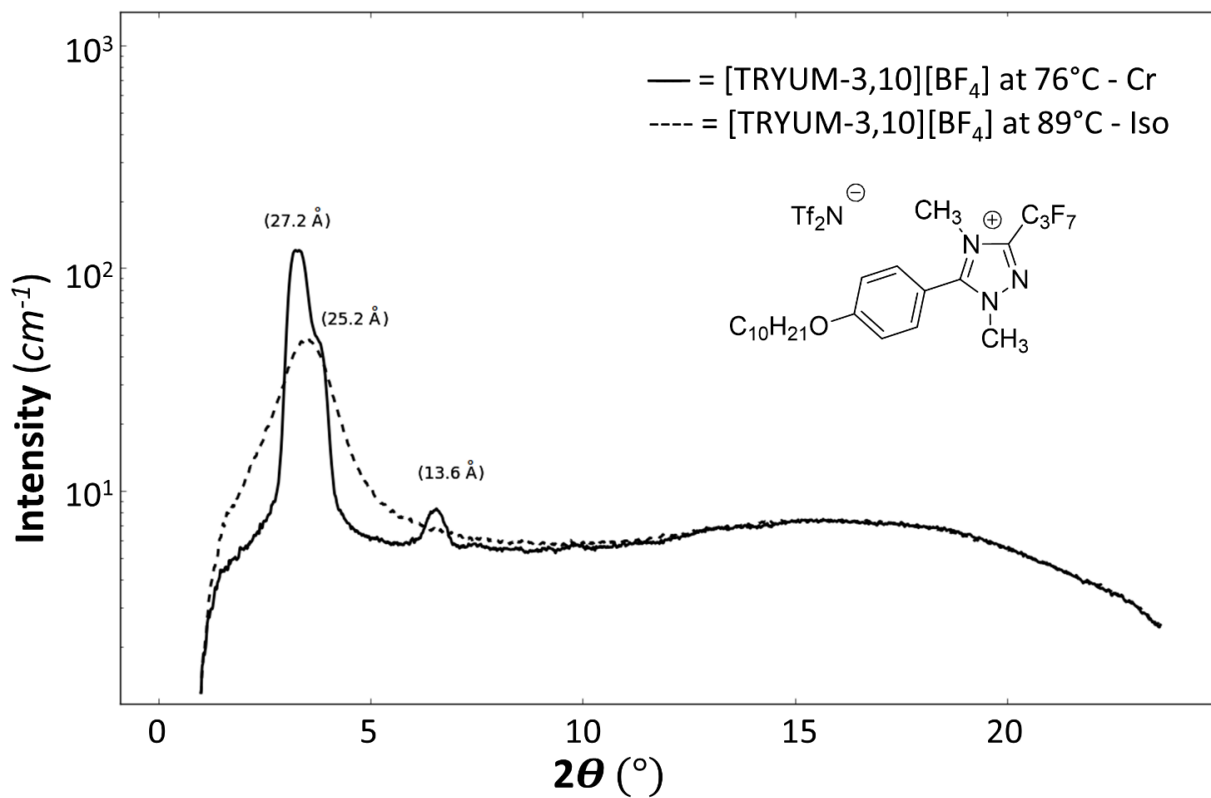


Figure C11. X-ray scattering of compound [TRYUM-3,10][BF<sub>4</sub>].

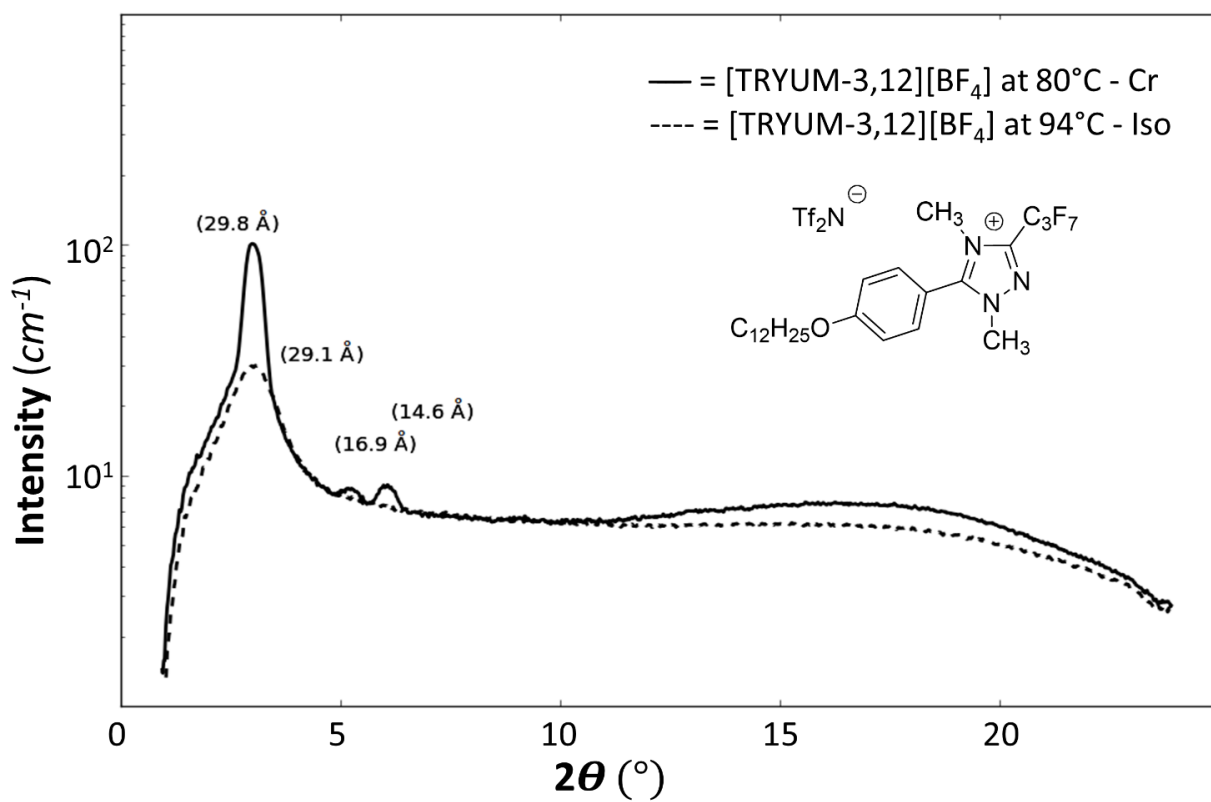


Figure C12. X-ray scattering of compound [TRYUM-3,12][BF<sub>4</sub>].

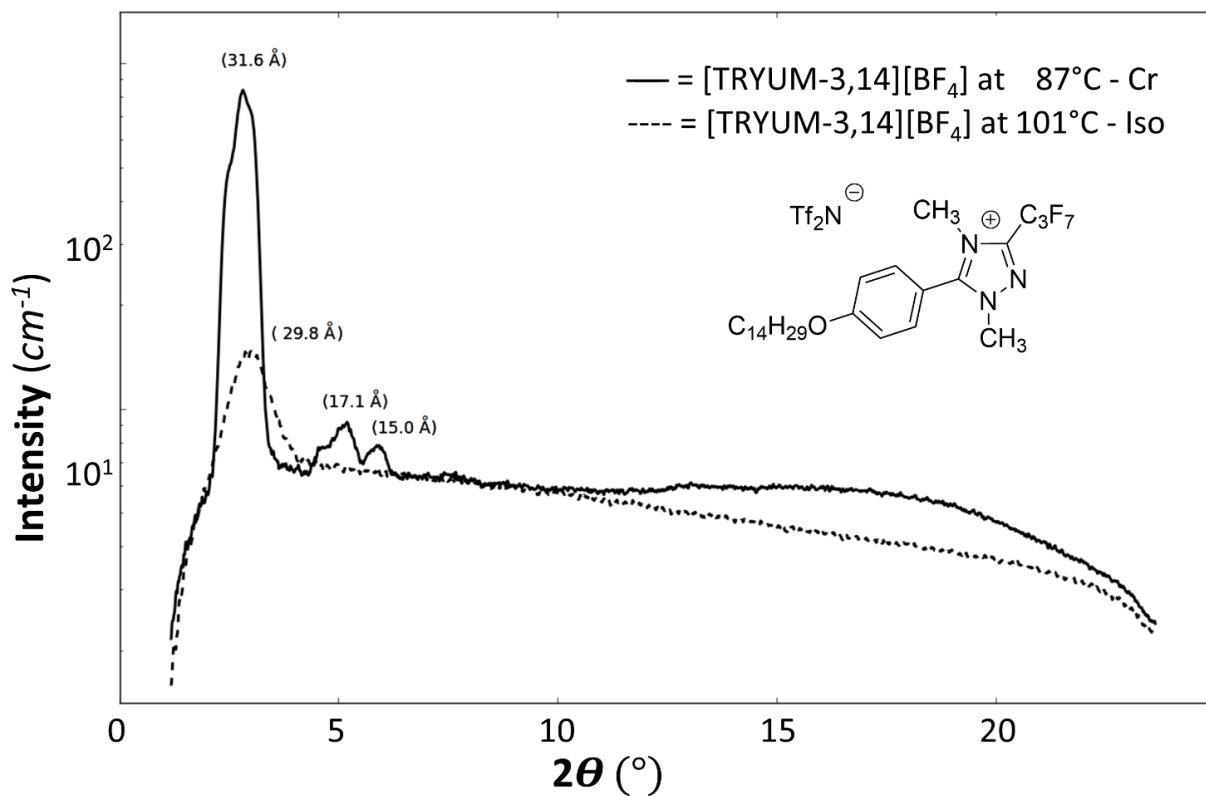


Figure C13. X-ray scattering of compound [TRYUM-3,14][BF<sub>4</sub>].

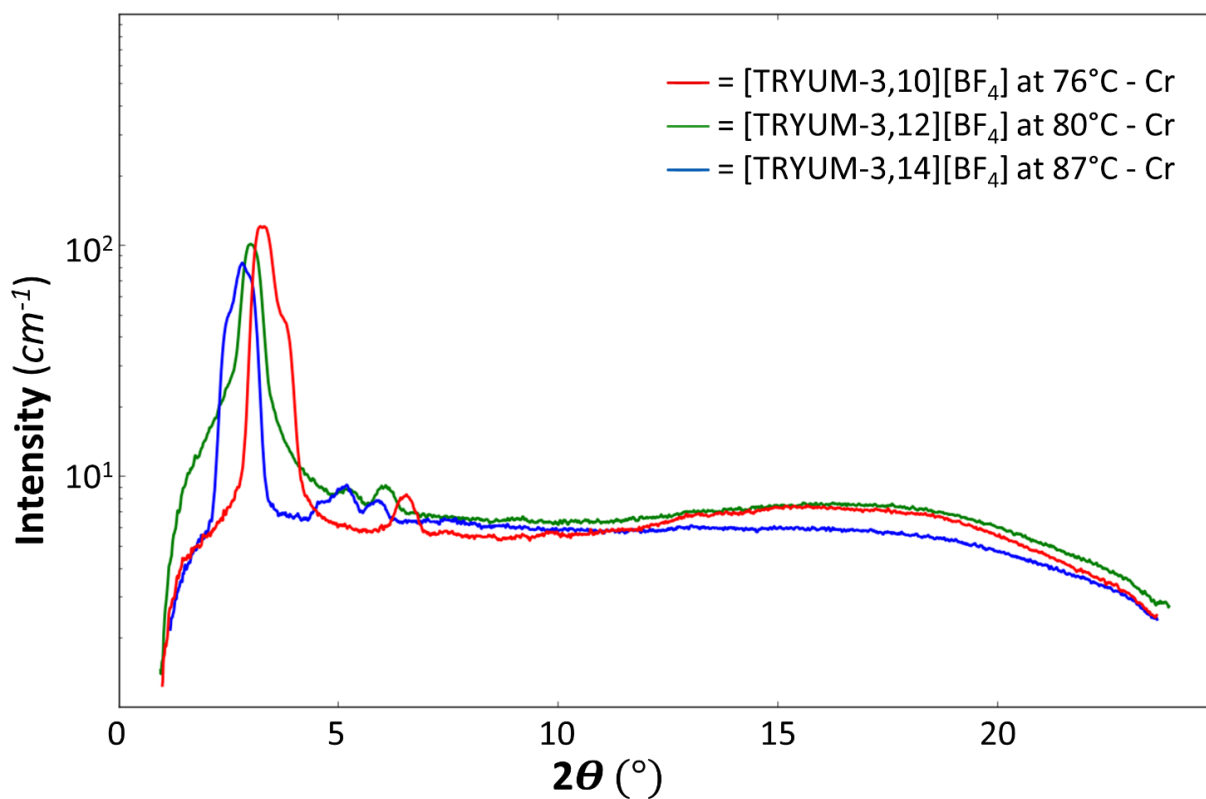


Figure C14. X-ray scattering of compounds [TRYUM-3,*n*][BF<sub>4</sub>] in Iso phases.

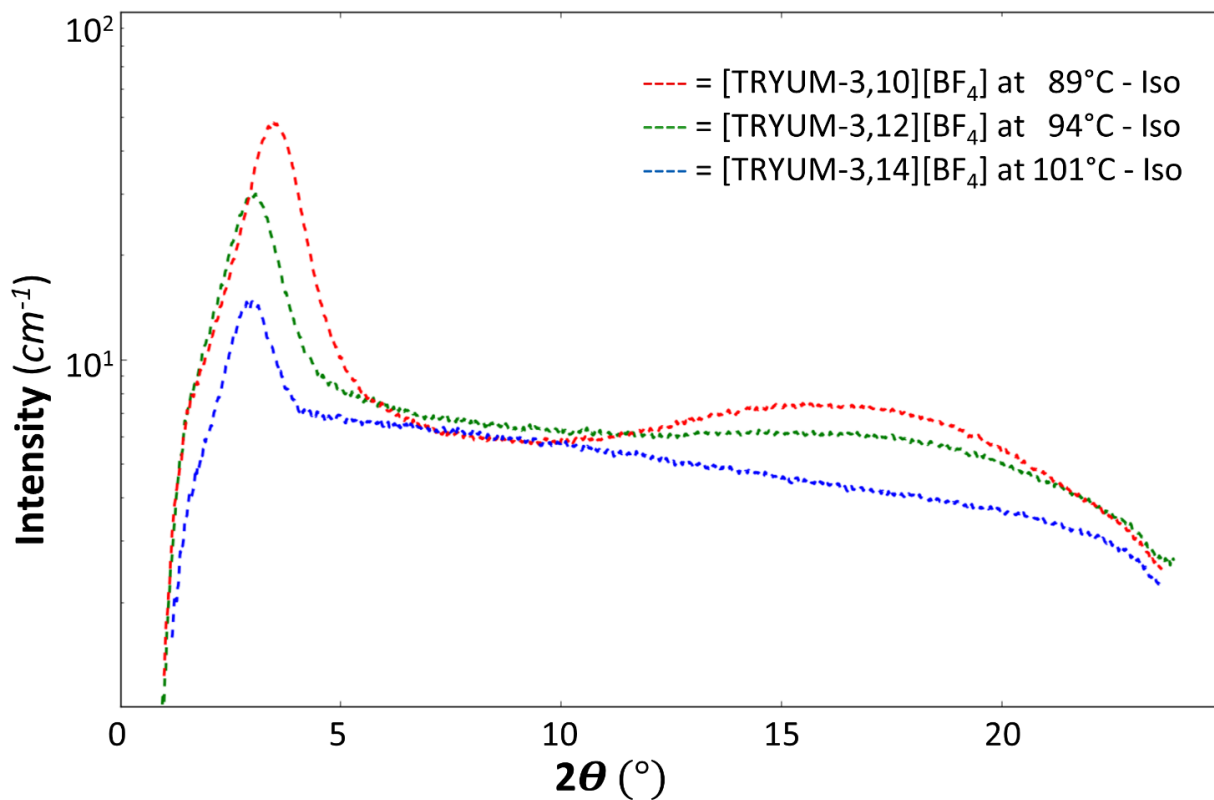


Figure C15. X-ray scattering of compounds [TRYUM-3,*n*][BF<sub>4</sub>] in Iso phases.

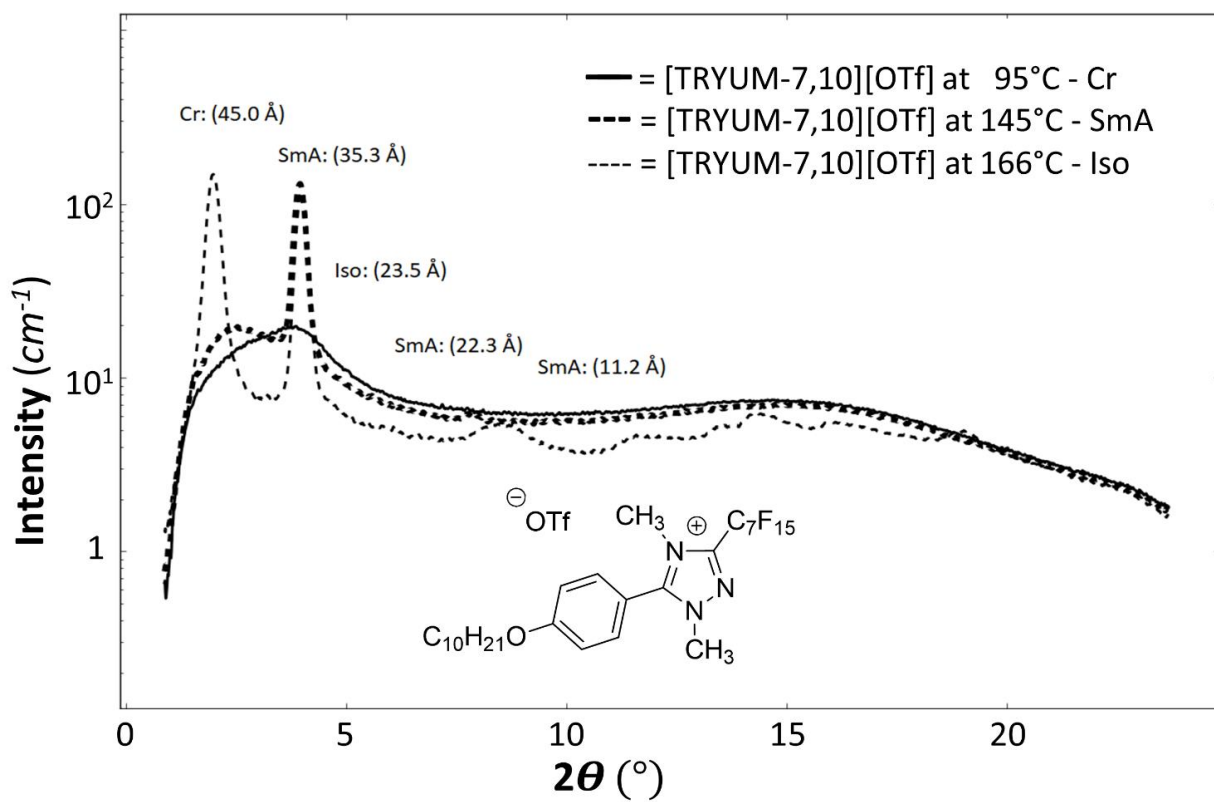


Figure C16. X-ray scattering of compound [TRYUM-7,10][OTf].

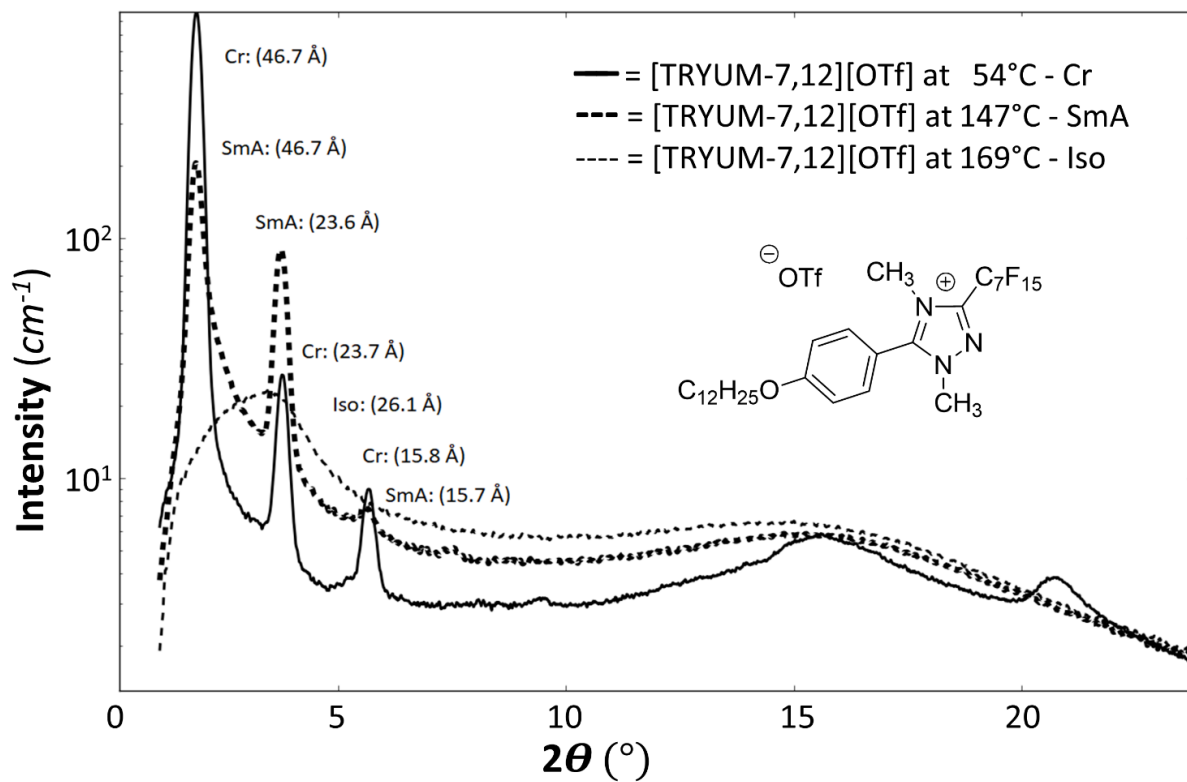


Figure C17. X-ray scattering of compound [TRYUM-7,12][OTf].

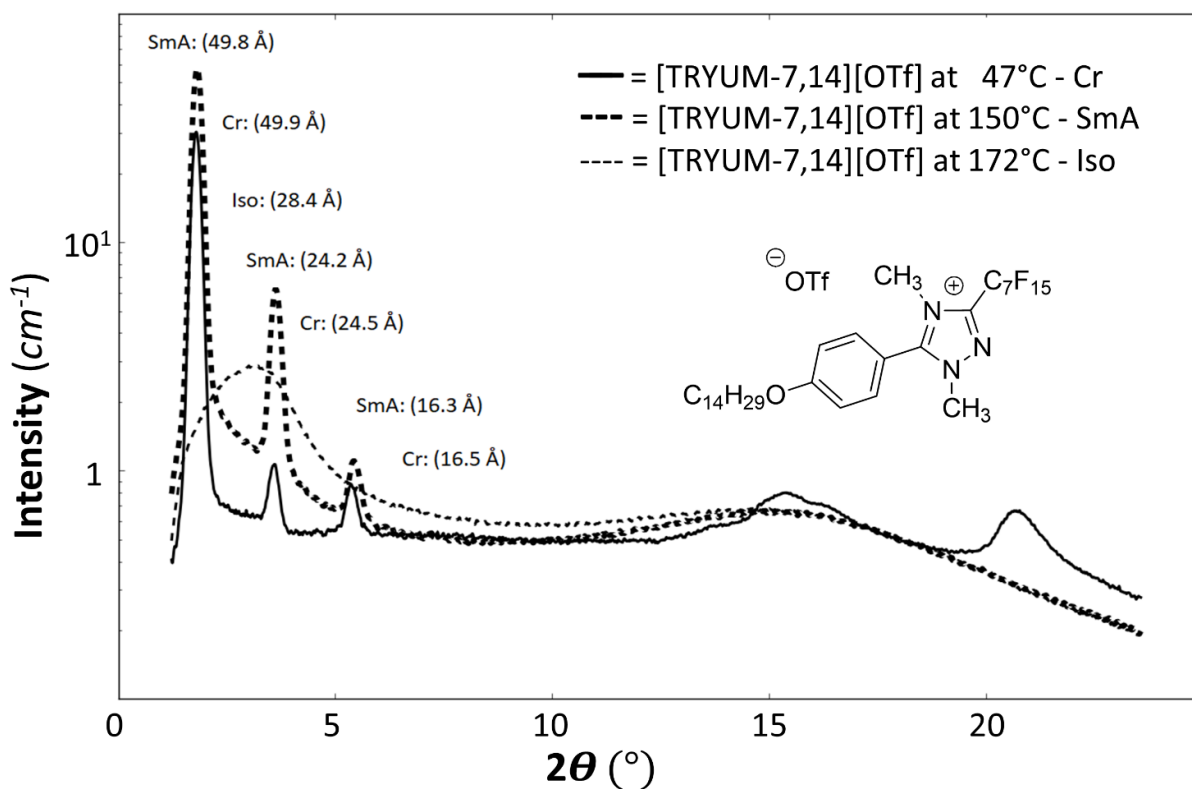


Figure C18. X-ray scattering of compound [TRYUM-7,14][OTf].

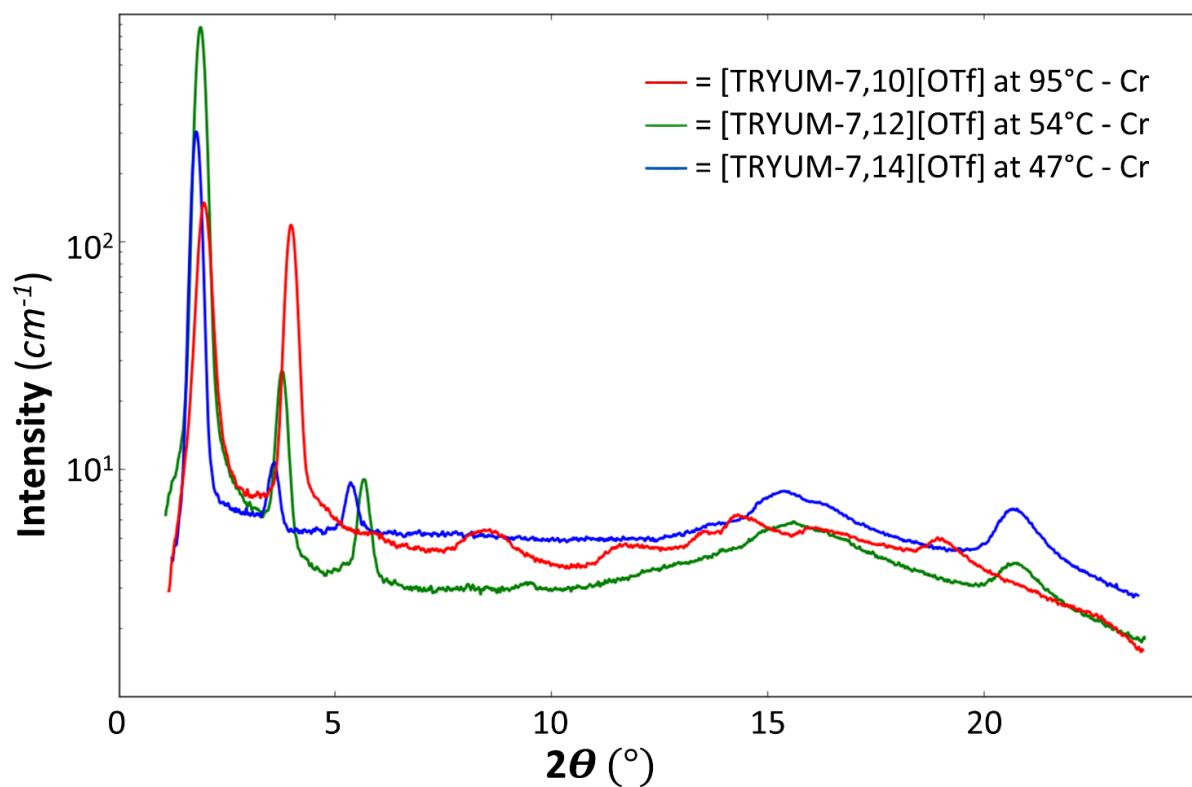


Figure C19. X-ray scattering of compounds [TRYUM-7,*n*][OTf] in Cr phases.

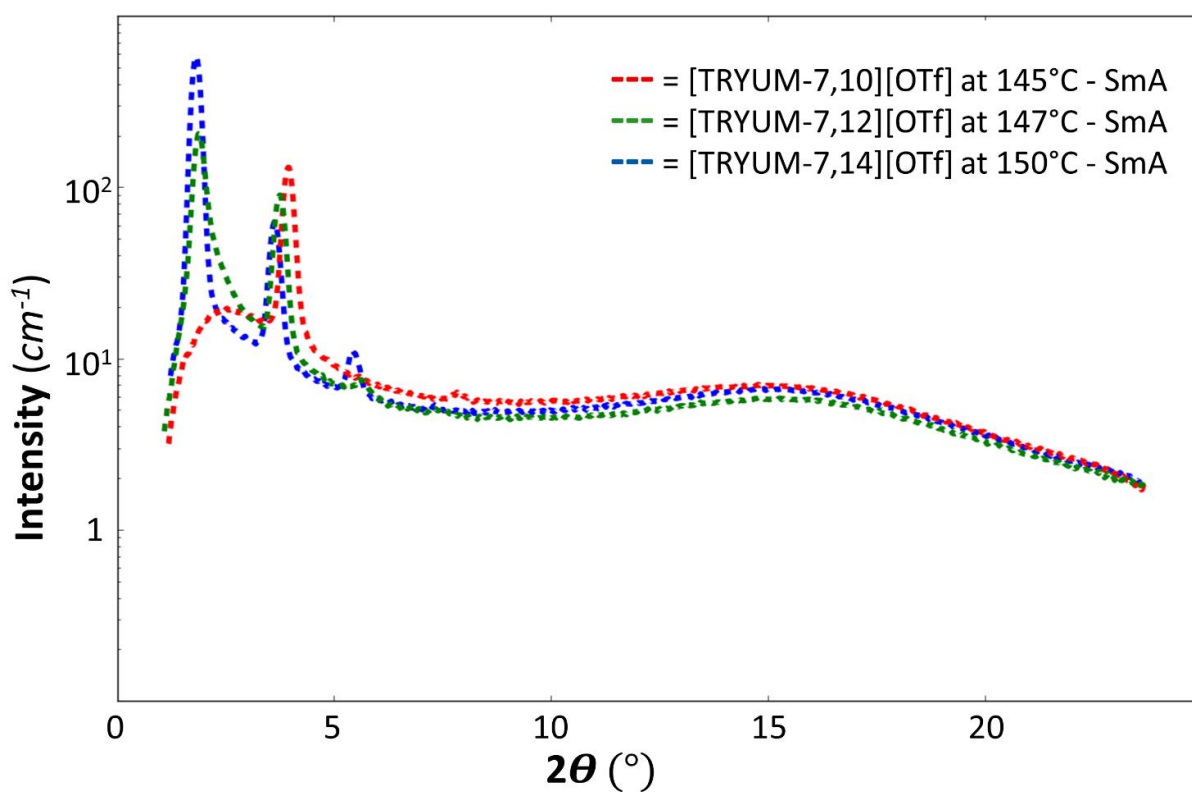


Figure C20. X-ray scattering of compounds [TRYUM-7,*n*][OTf] in SmA phases.

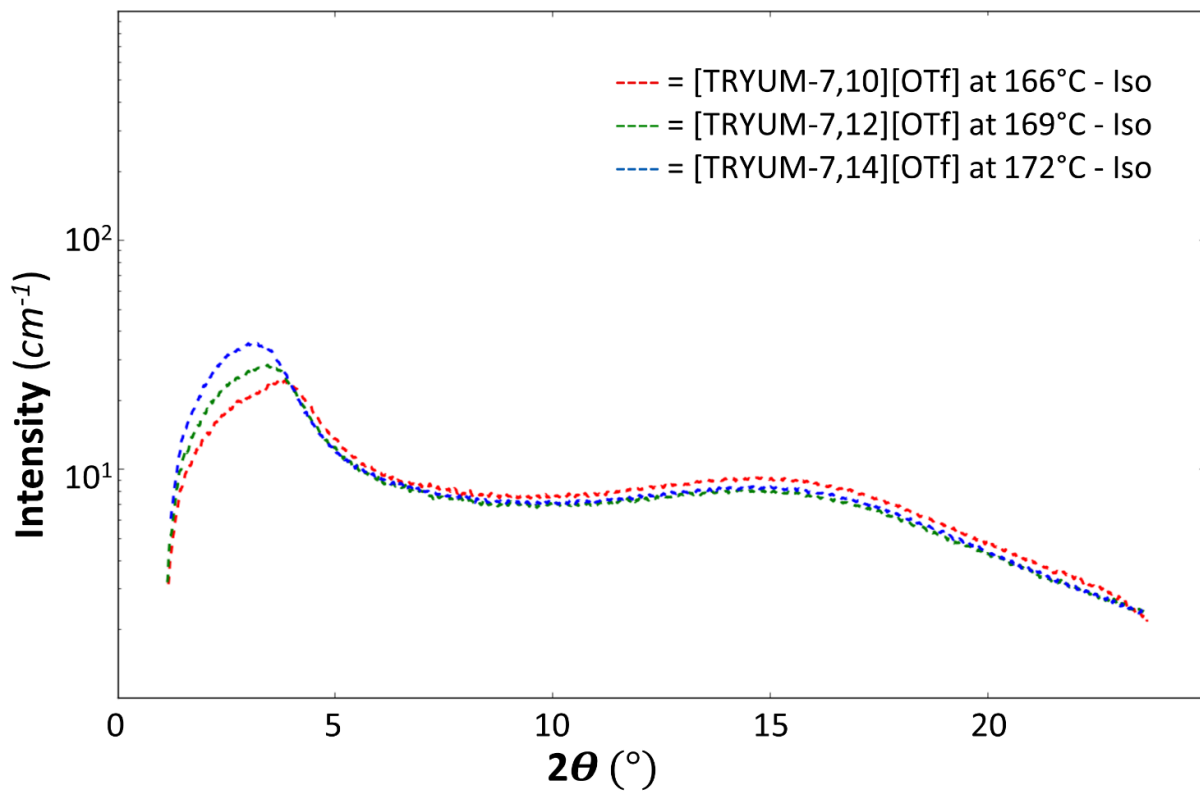


Figure C21. X-ray scattering of compounds [TRYUM-7,*n*][OTf] in Iso phases.

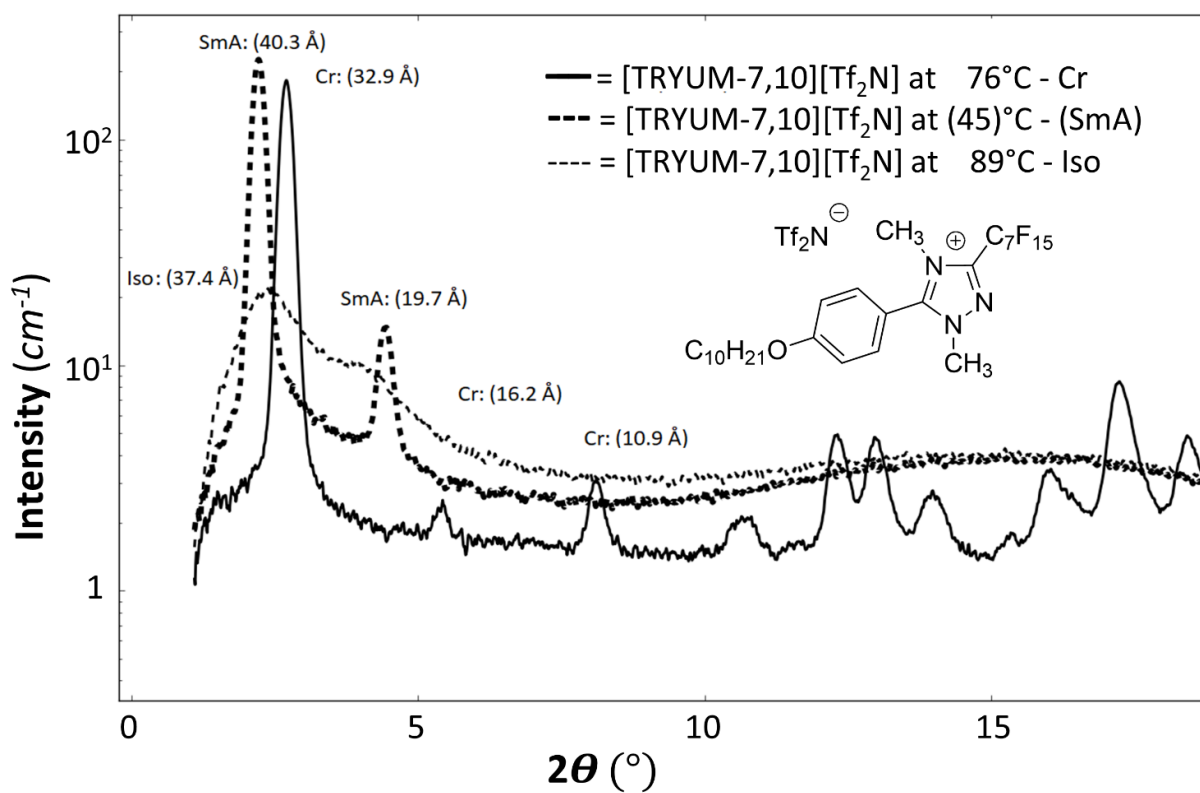


Figure C22. X-ray scattering of compound [TRYUM-7,10][Tf<sub>2</sub>N].



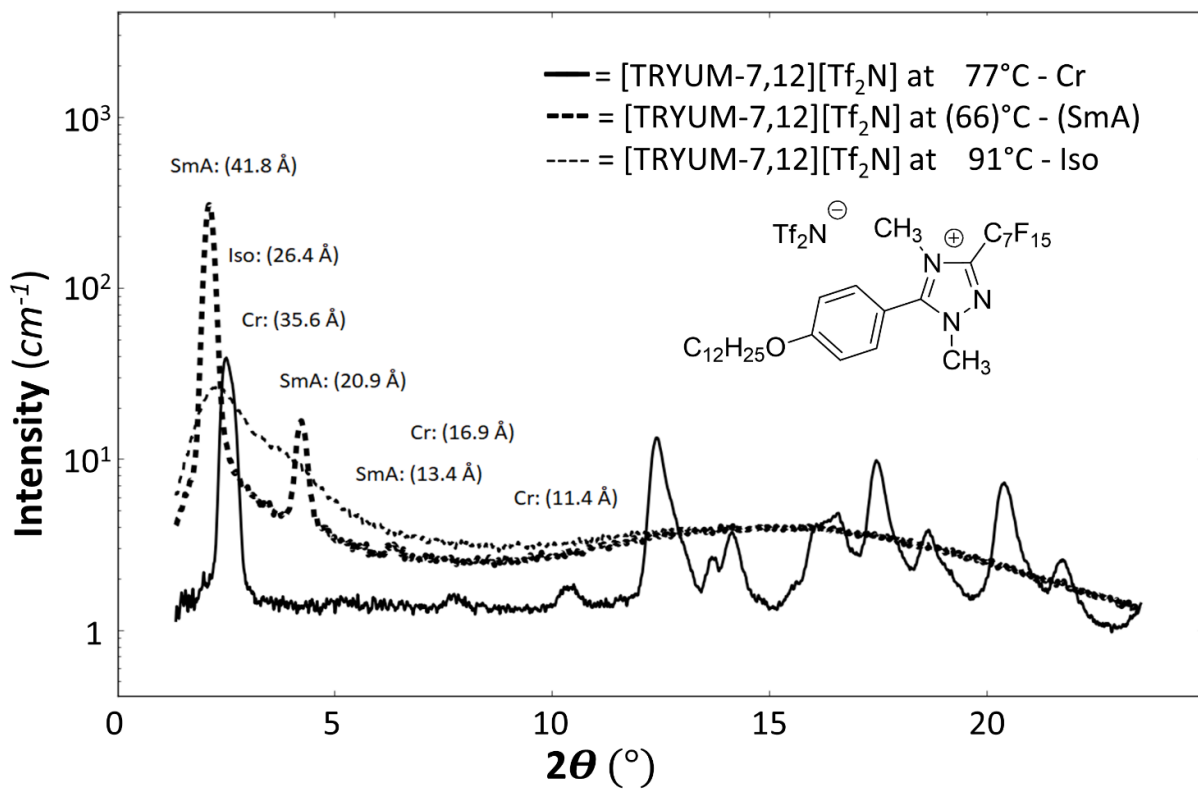


Figure C23. X-ray scattering of compound [TRYUM-7,12][Tf<sub>2</sub>N].

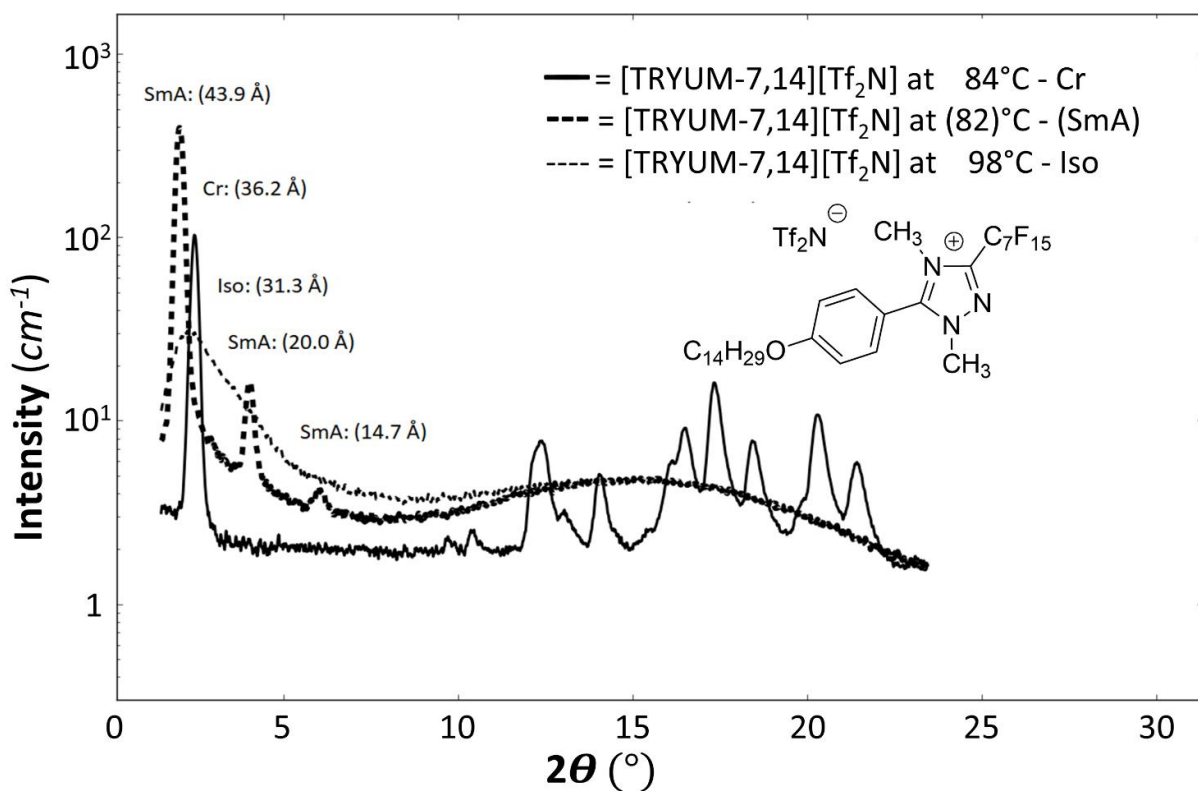


Figure C24. X-ray scattering of compound [TRYUM-7,14][Tf<sub>2</sub>N].

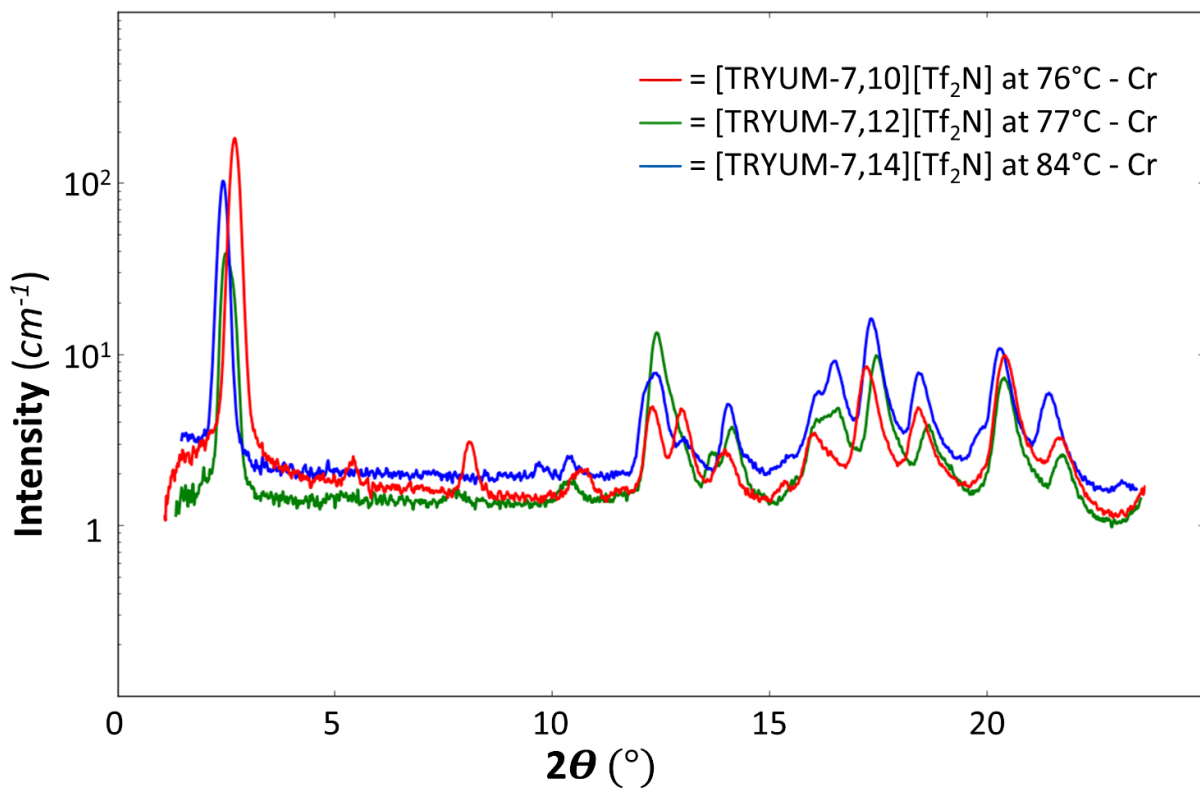


Figure C25. X-ray scattering of compounds [TRYUM-7,*n*][Tf<sub>2</sub>N] in Cr phases.

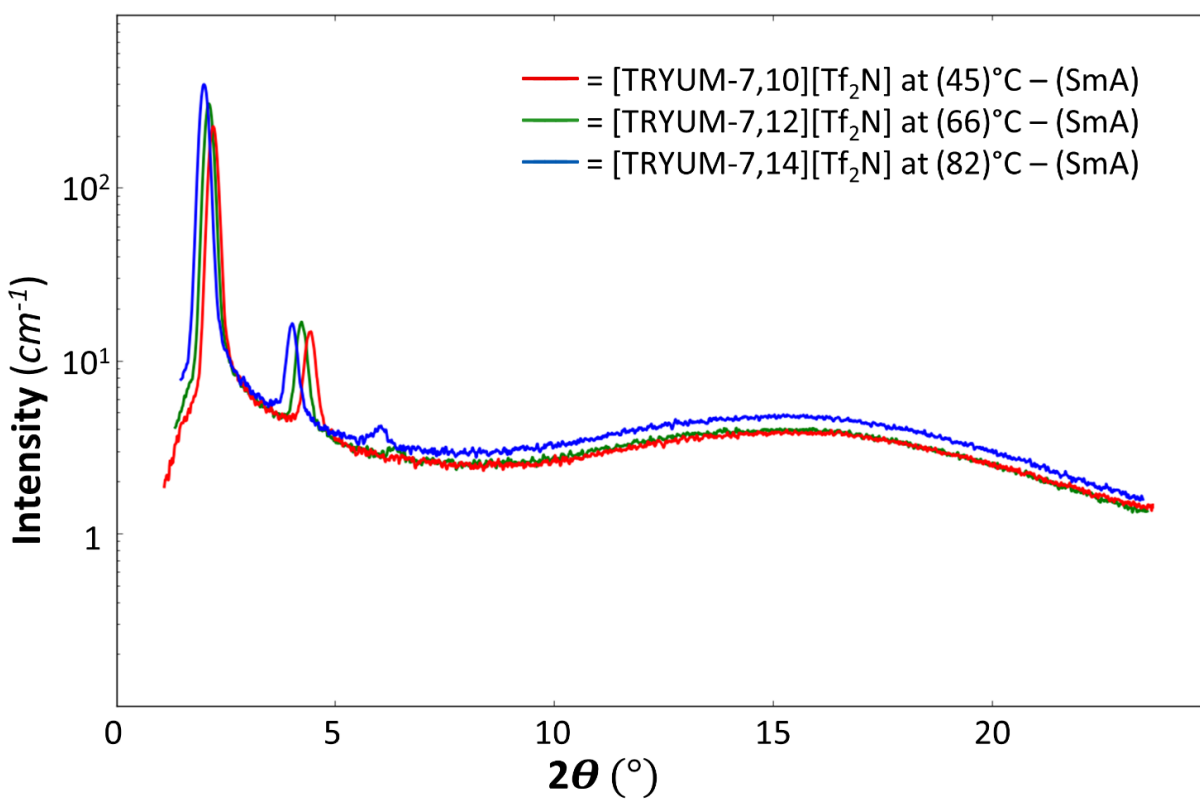


Figure C26. X-ray scattering of compounds [TRYUM-7,*n*][Tf<sub>2</sub>N] in SmA phases.

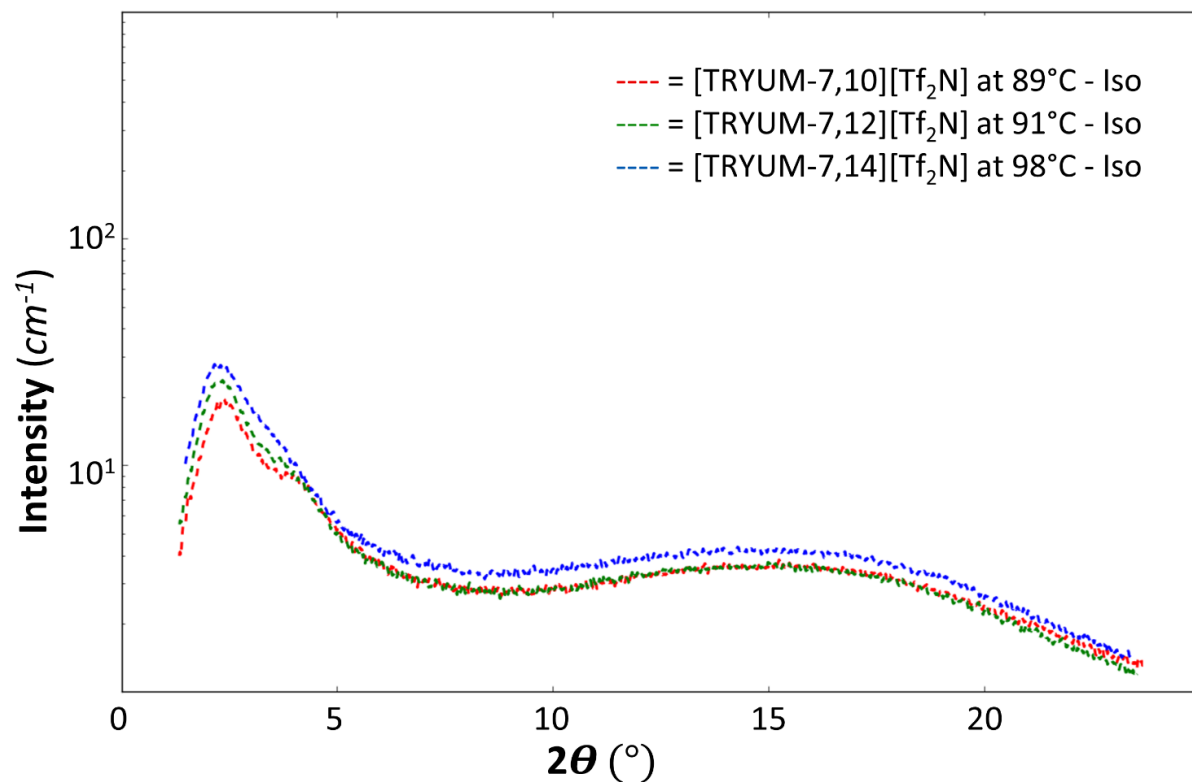


Figure C27. X-ray scattering of compounds [TRYUM-7,*n*][Tf<sub>2</sub>N] in Iso phases.

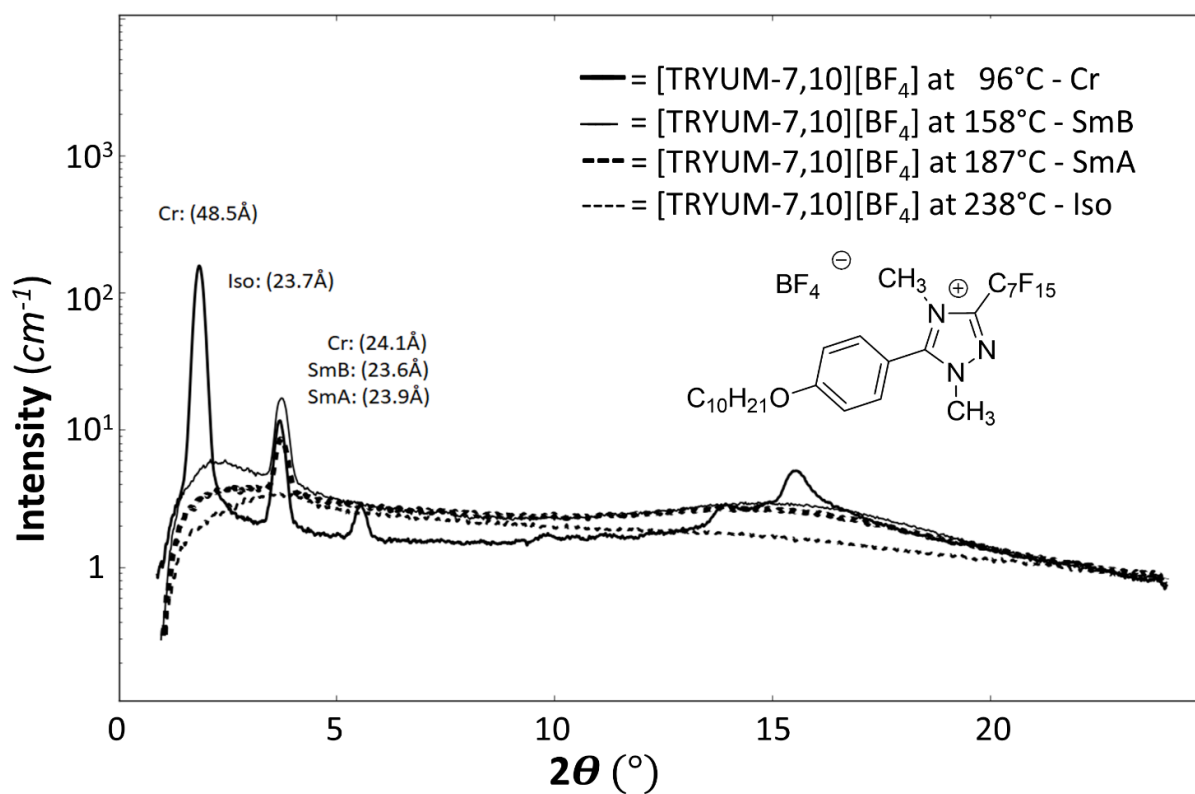


Figure C28. X-ray scattering of compound [TRYUM-7,10][BF<sub>4</sub>].

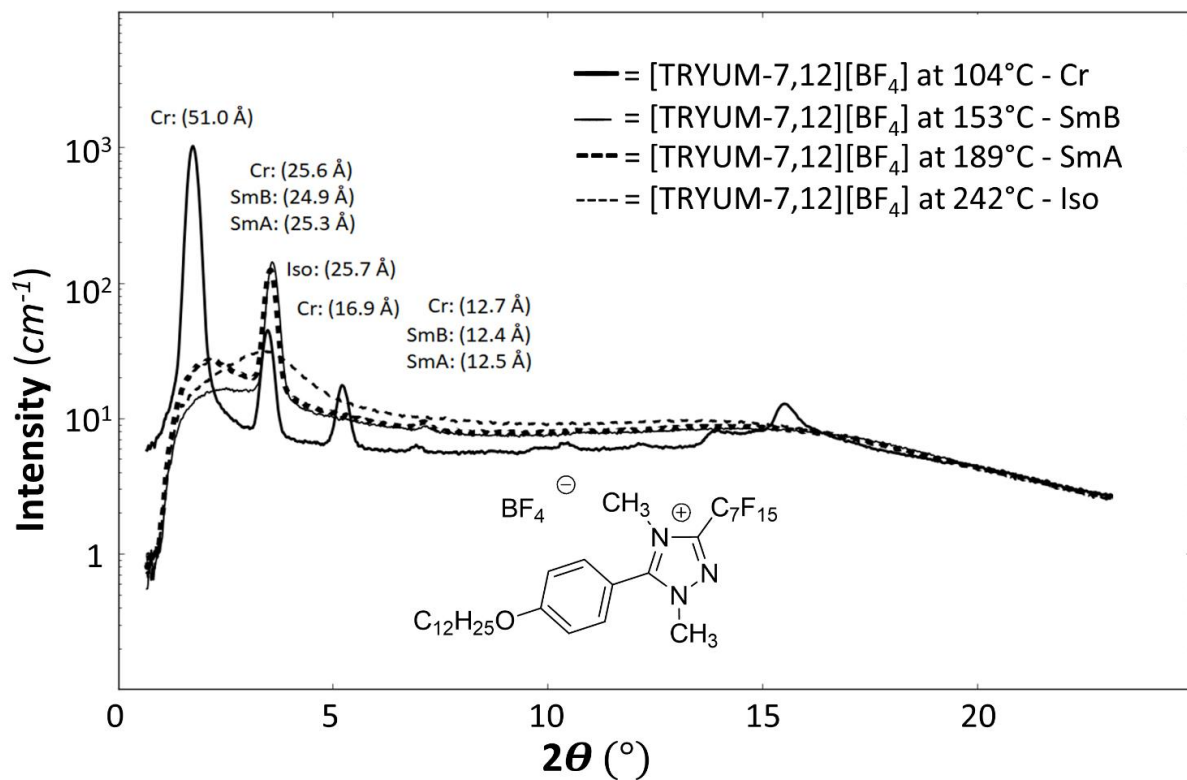


Figure C29. X-ray scattering of compound [TRYUM-7,12][BF<sub>4</sub>].

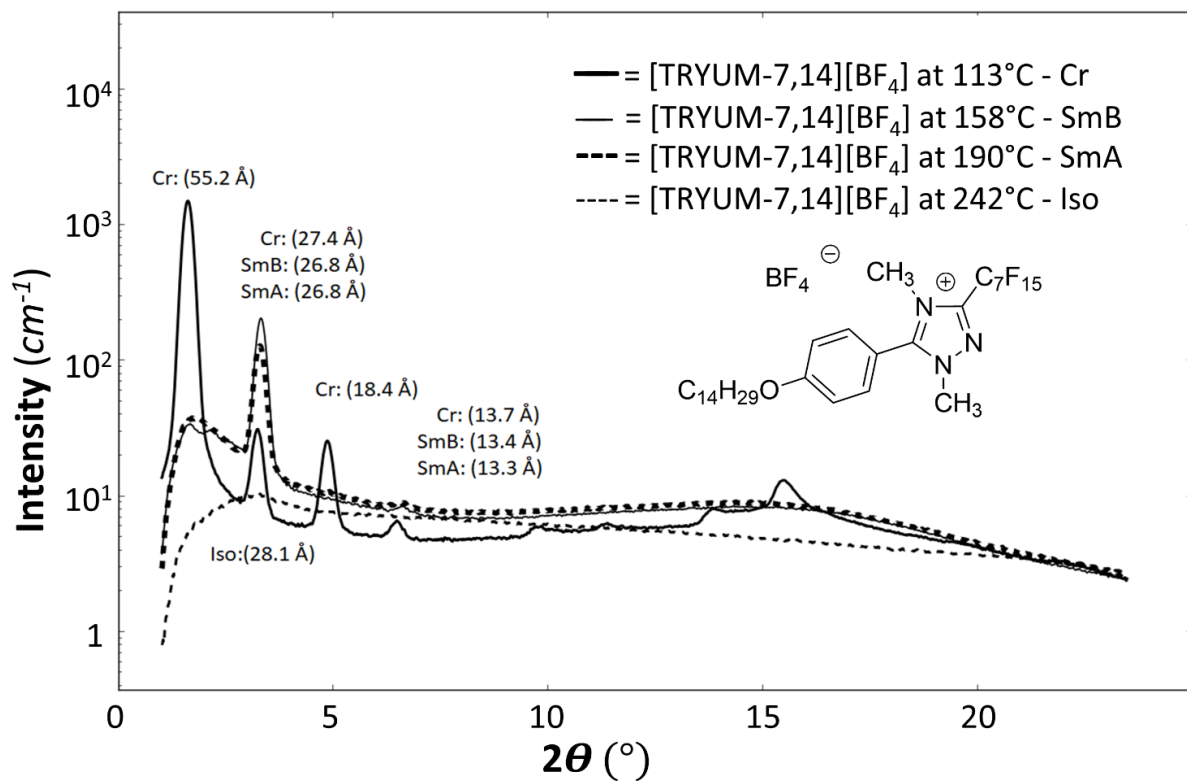


Figure C30. X-ray scattering of compound [TRYUM-7,14][BF<sub>4</sub>].

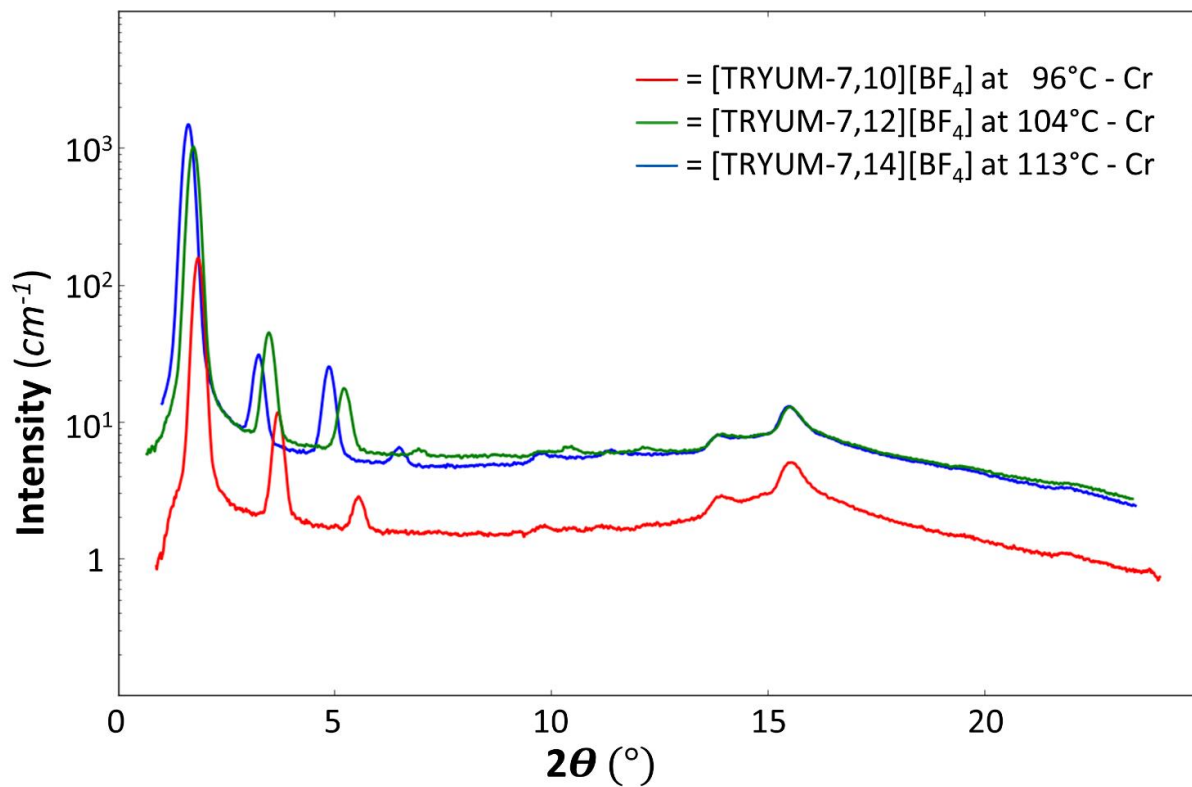


Figure C31. X-ray scattering of compounds [TRYUM-7,*n*][BF<sub>4</sub>] in Cr phases.

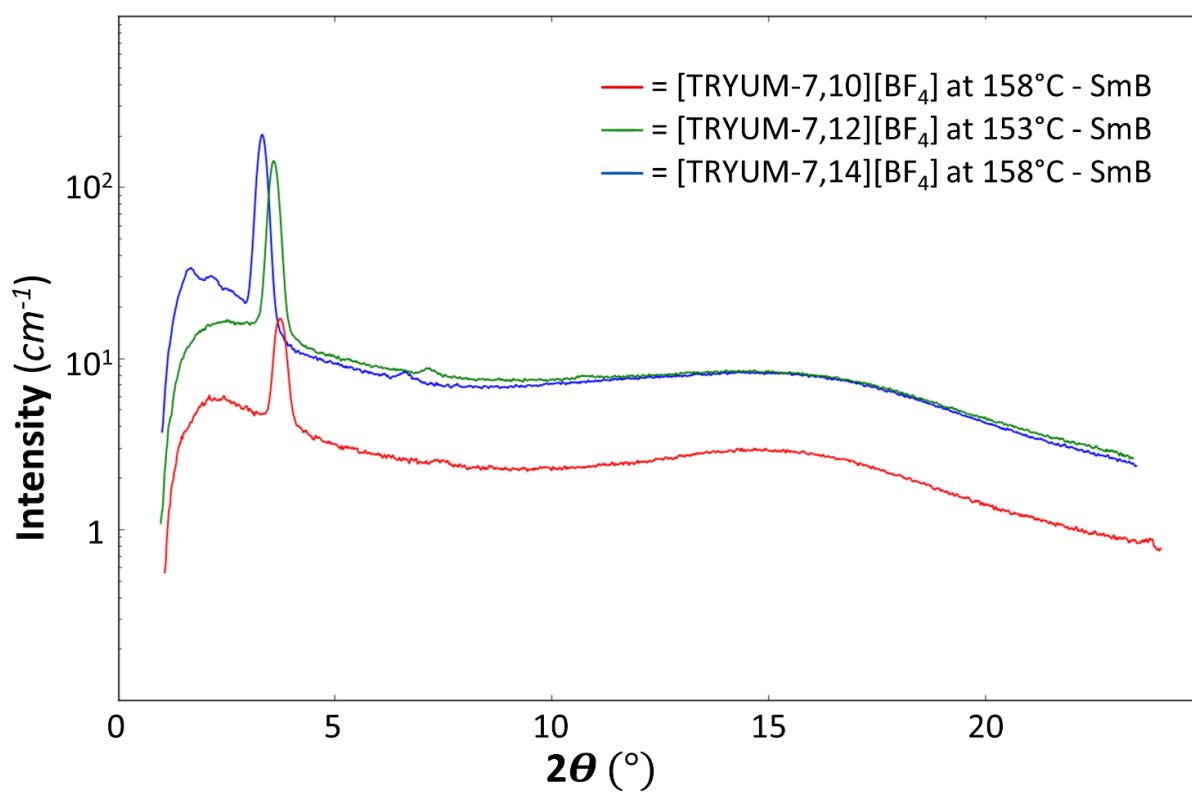


Figure C32. X-ray scattering of compounds [TRYUM-7,*n*][BF<sub>4</sub>] in SmB phases.

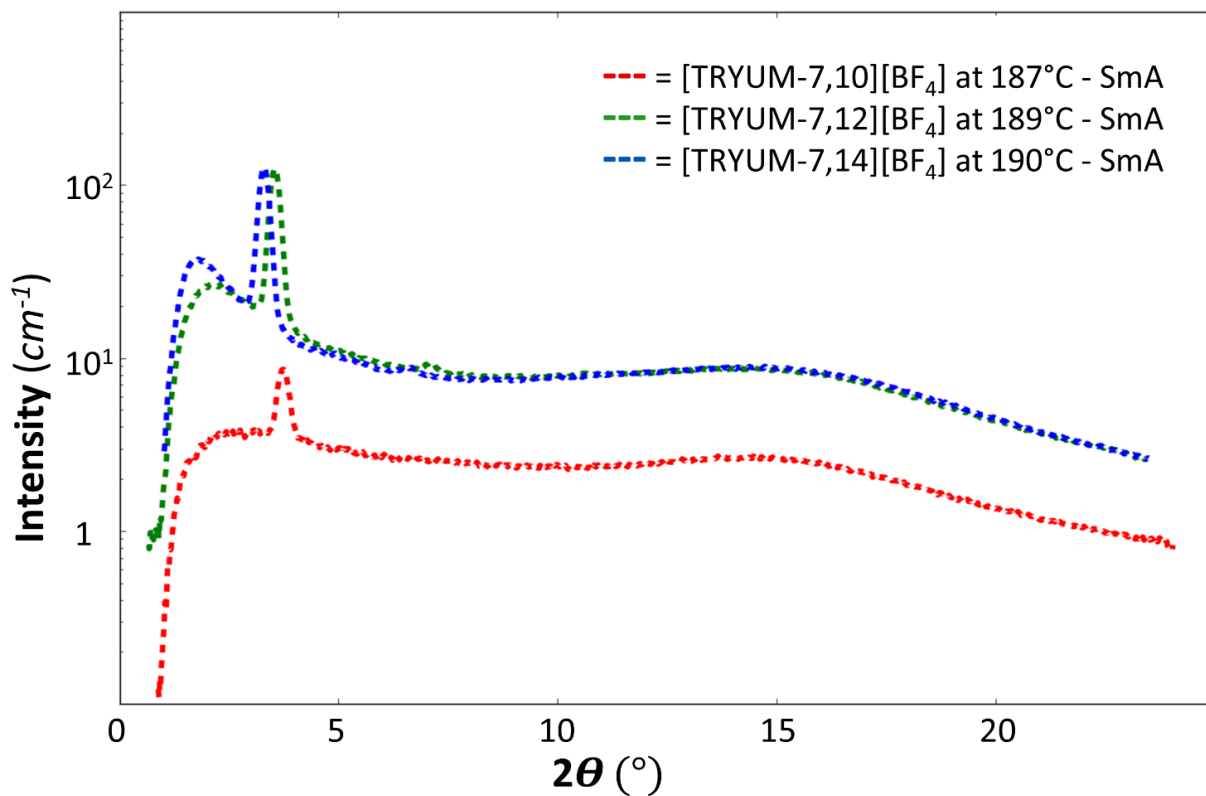


Figure C33. X-ray scattering of compounds [TRYUM-7,*n*][BF<sub>4</sub>] in SmA phases.

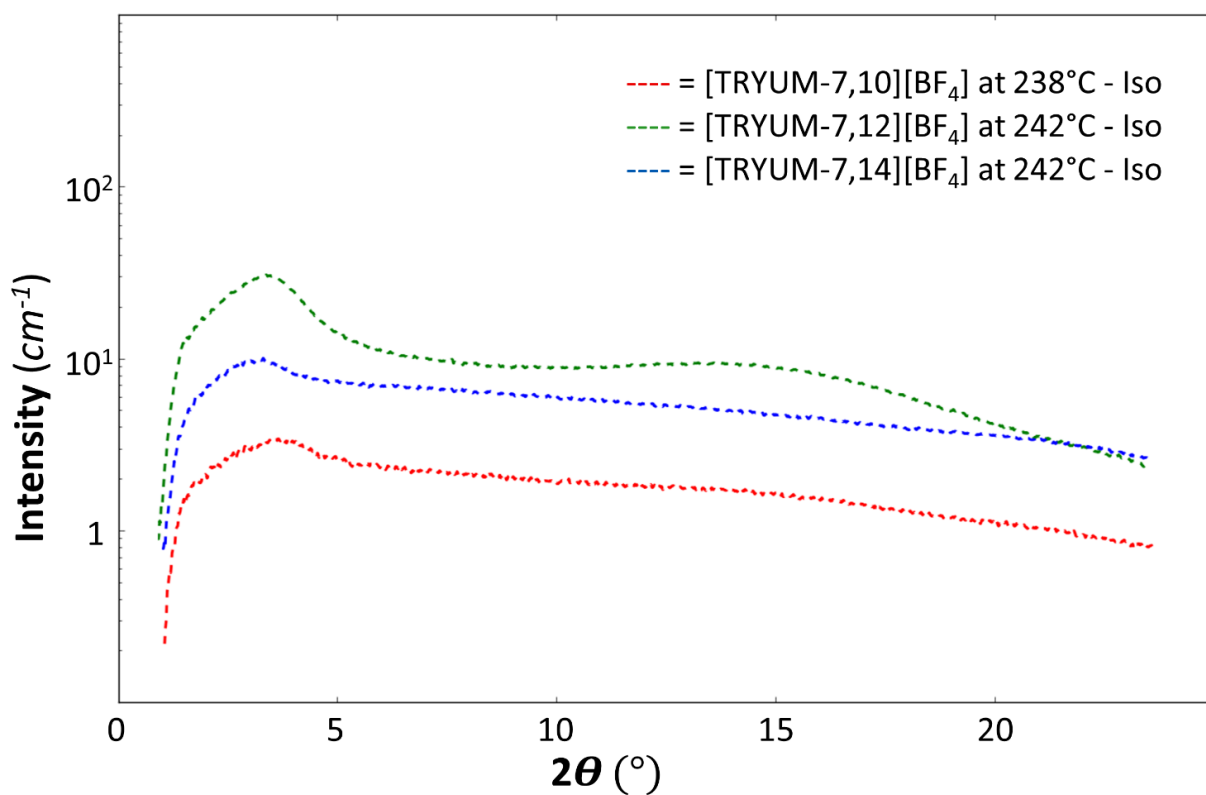


Figure C34. X-ray scattering of compounds [TRYUM-7,*n*][BF<sub>4</sub>] in Iso phases.

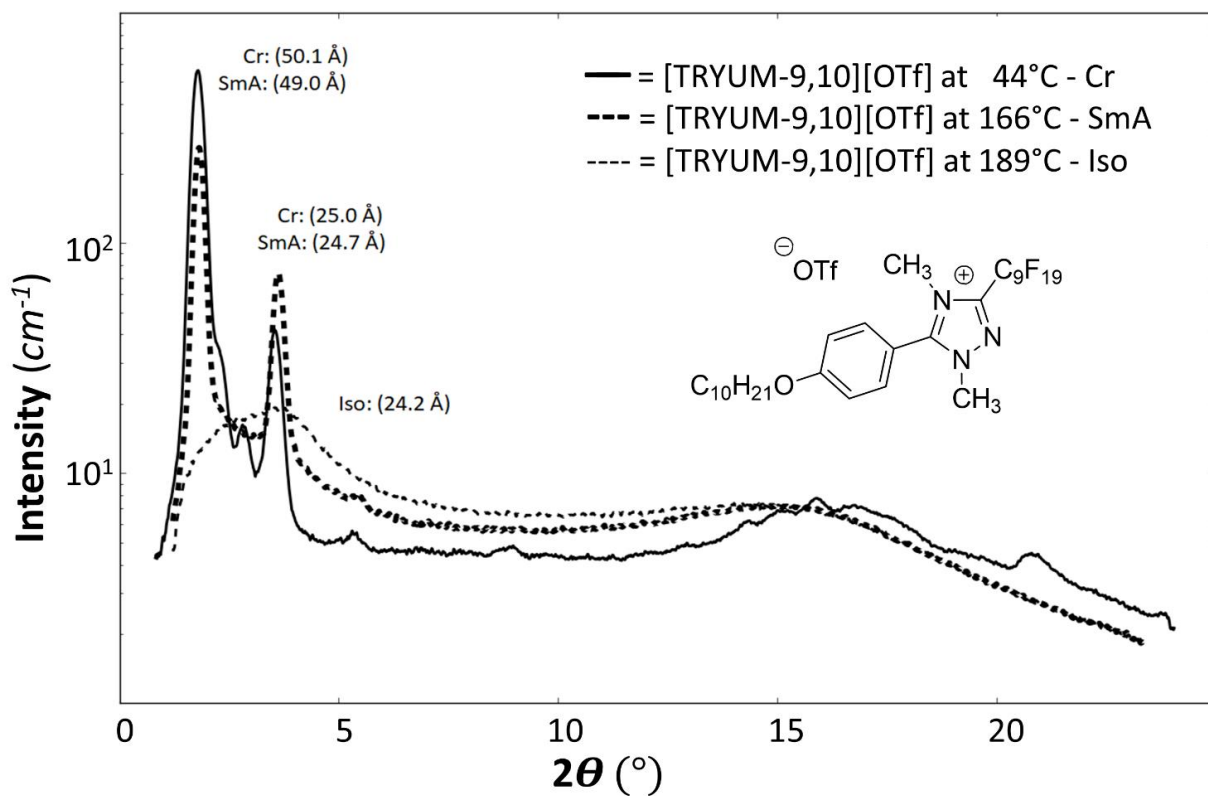


Figure C35. X-ray scattering of compound [TRYUM-9,10][OTf].

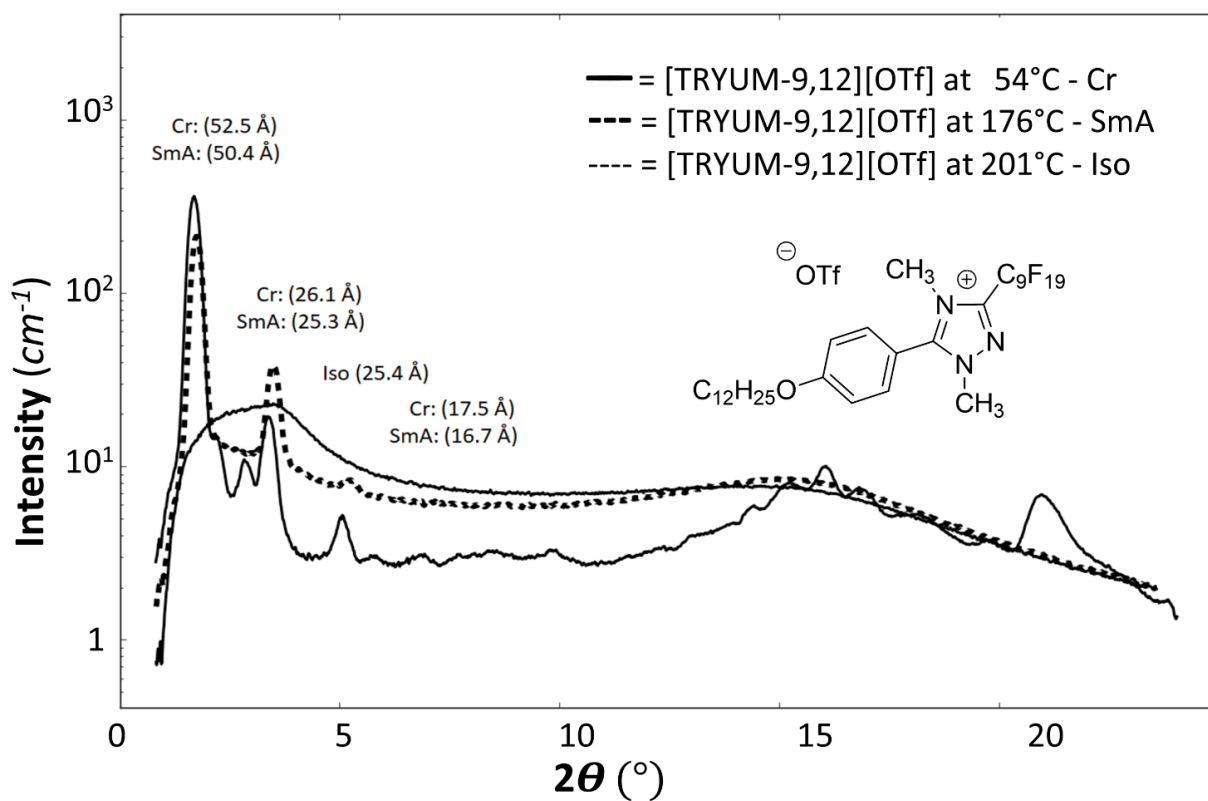


Figure C36. X-ray scattering of compound [TRYUM-9,12][OTf].

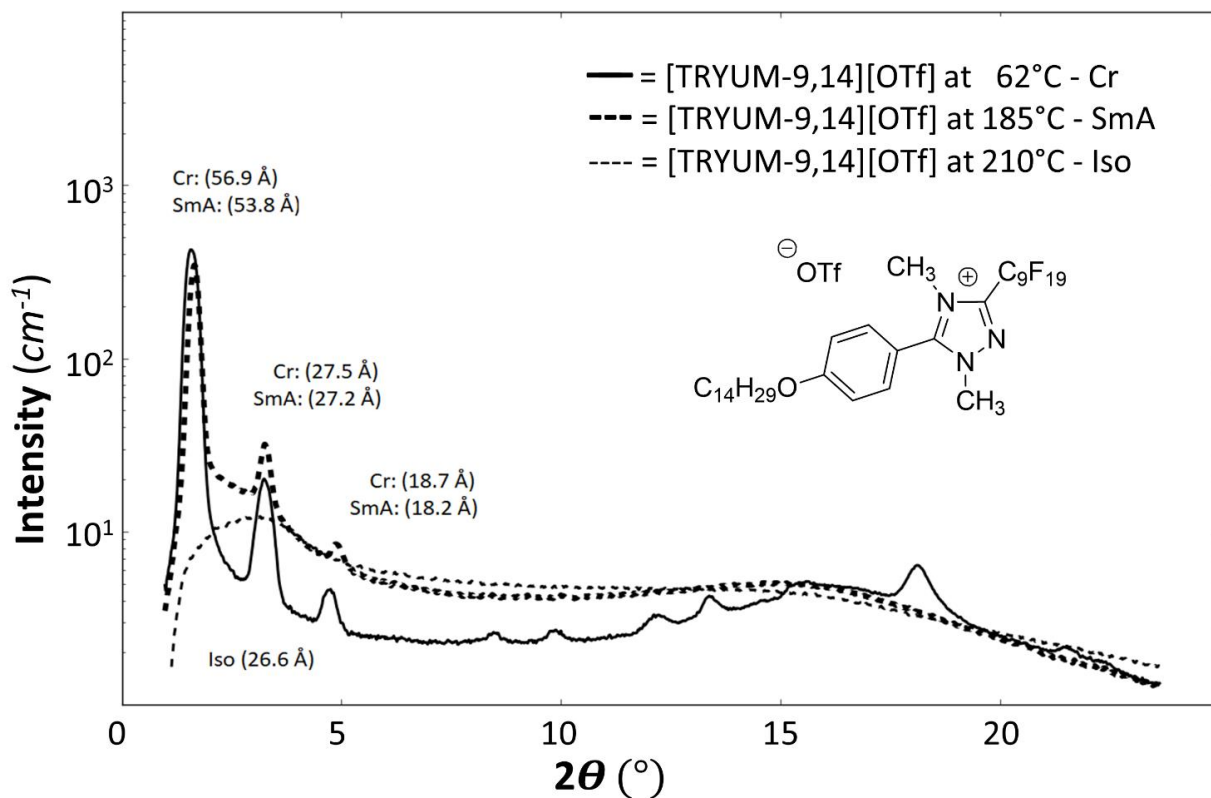


Figure C37. X-ray scattering of compound [TRYUM-9,14][OTf].

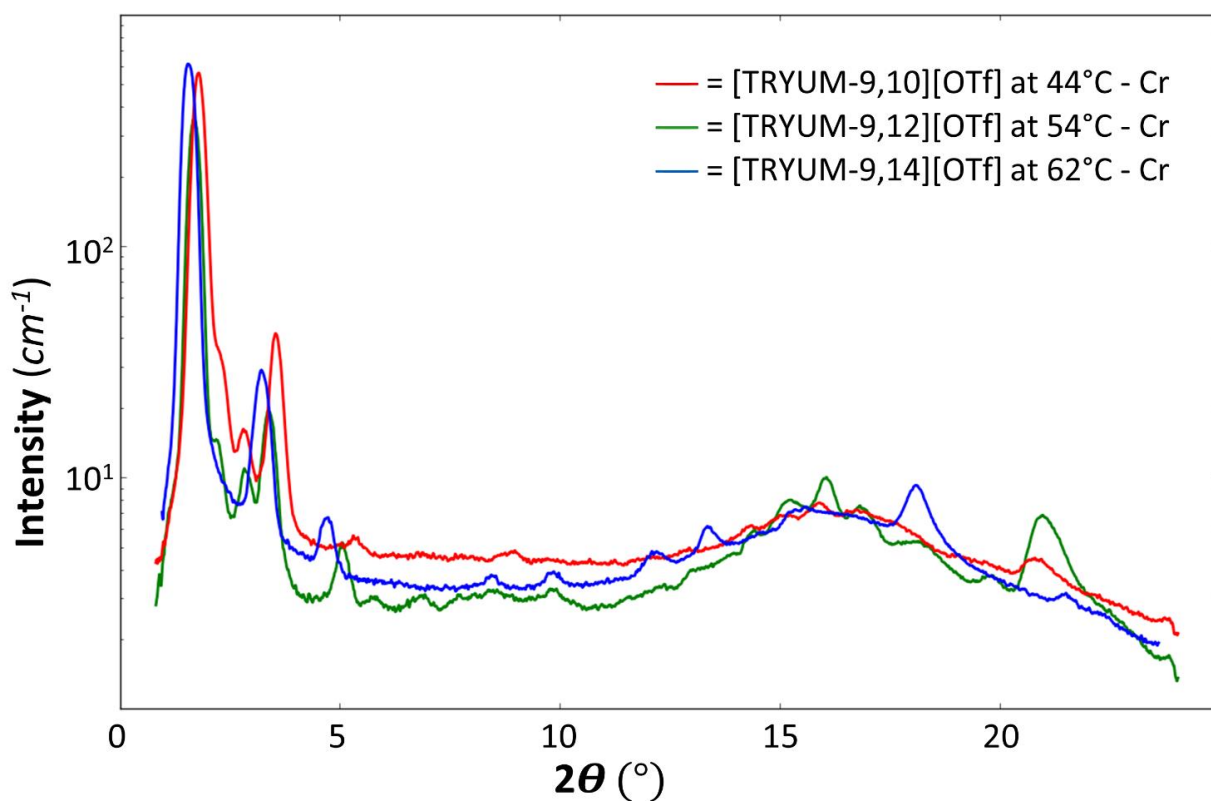


Figure C38. X-ray scattering of compounds [TRYUM-9,*n*][OTf] in Cr phases.



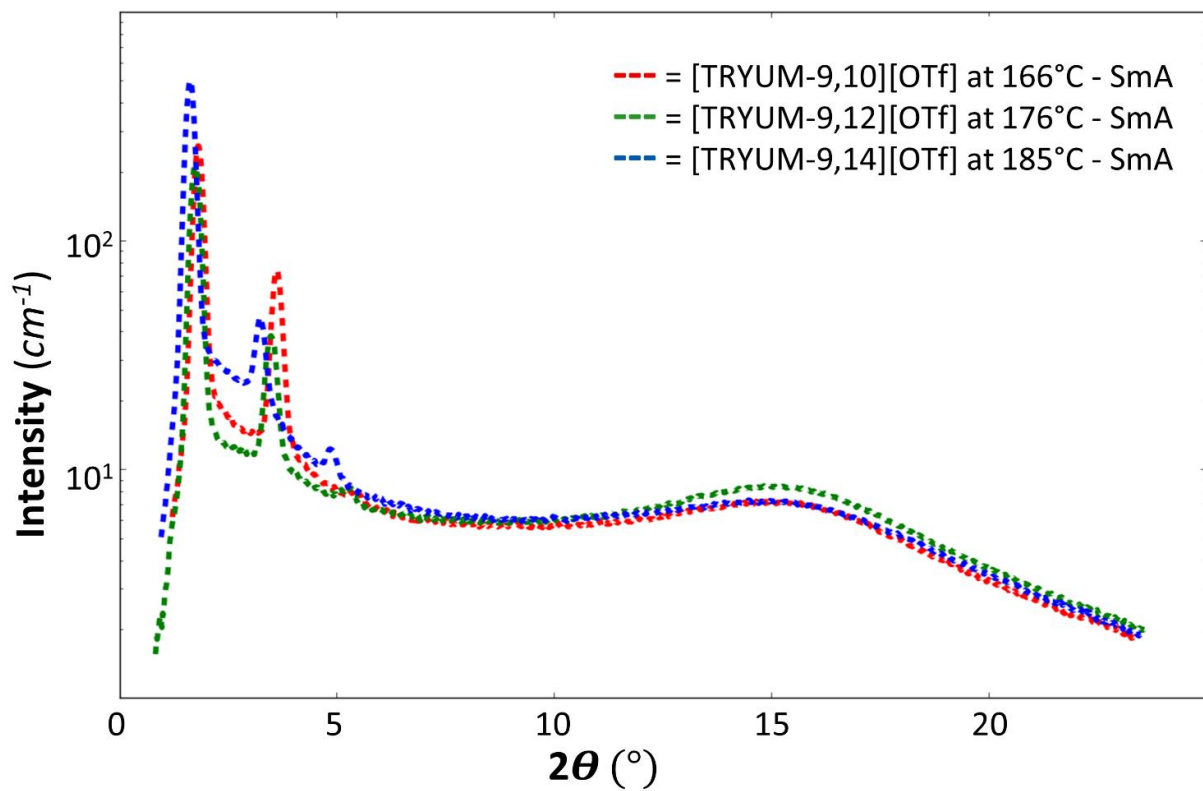


Figure C39. X-ray scattering of compounds [TRYUM-9,*n*][OTf] in SmA phases.

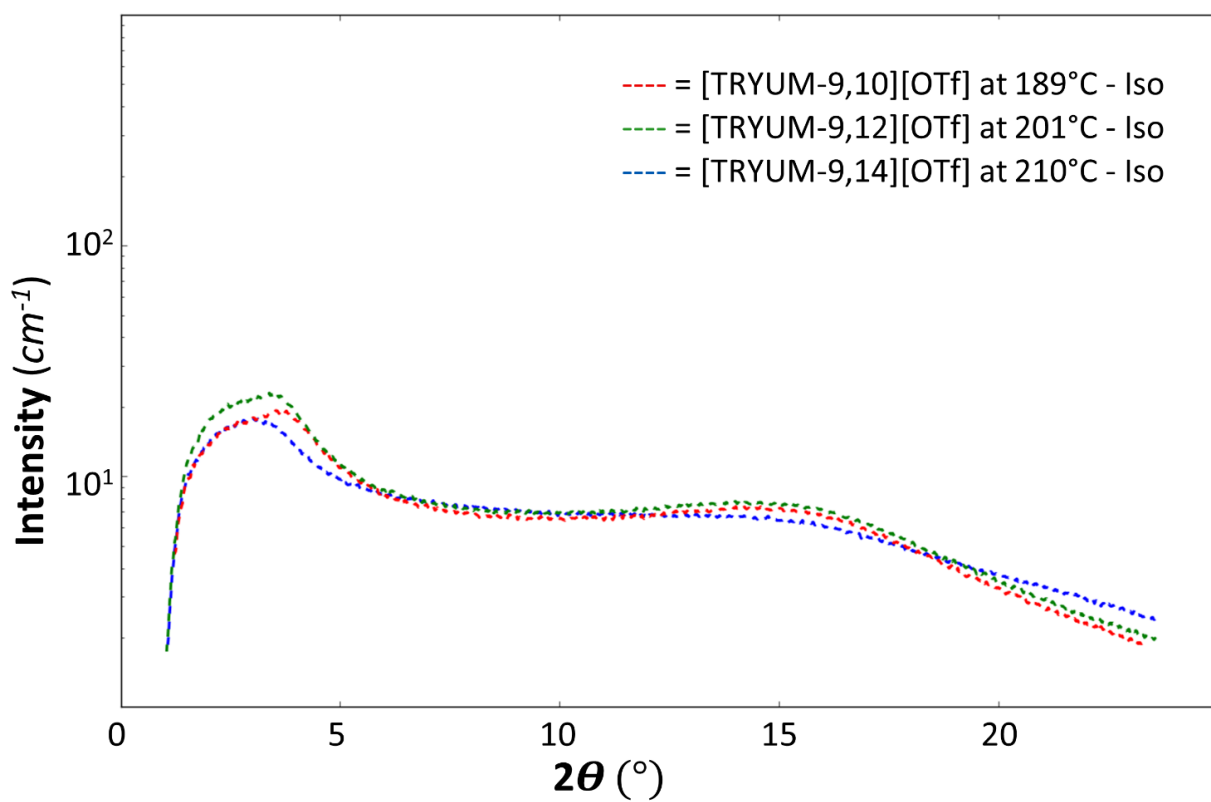


Figure C40. X-ray scattering of compounds [TRYUM-9,*n*][OTf] in Iso phases.

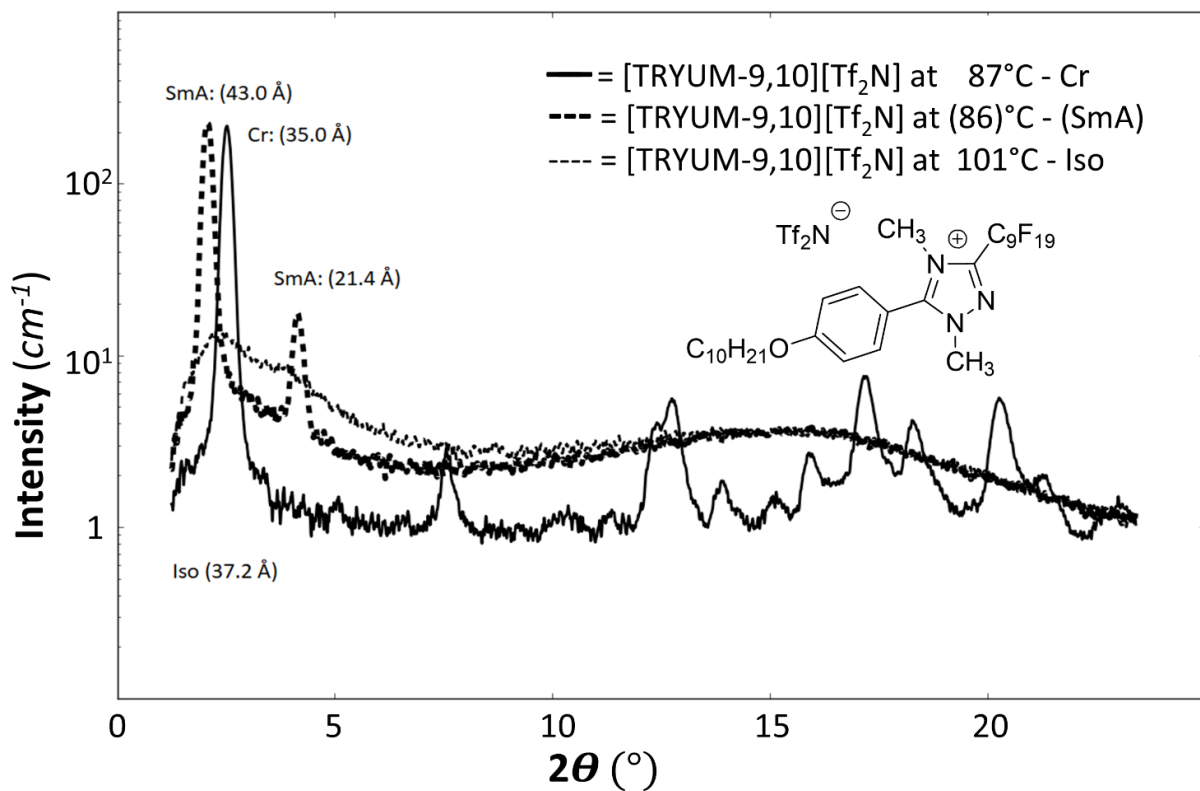


Figure C41. X-ray scattering of compound [TRYUM-9,10][Tf<sub>2</sub>N].

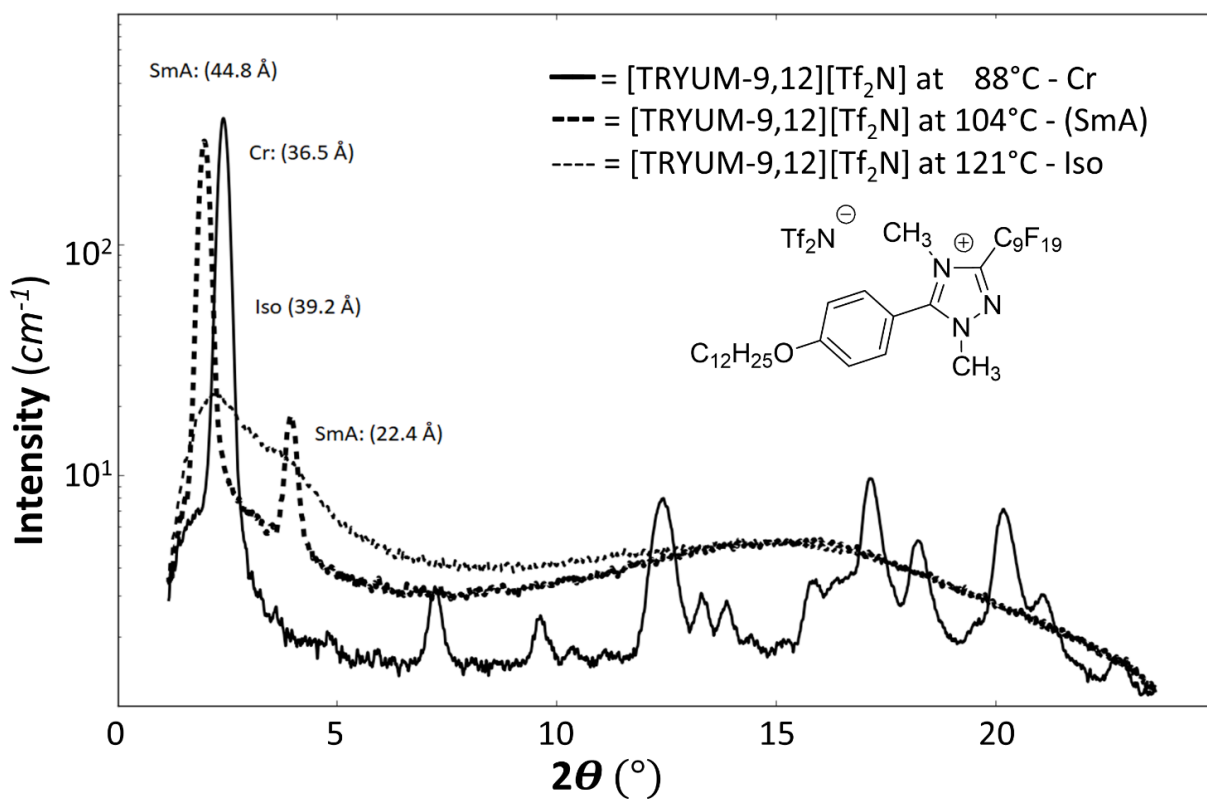


Figure C42. X-ray scattering of compound [TRYUM-9,12][Tf<sub>2</sub>N].



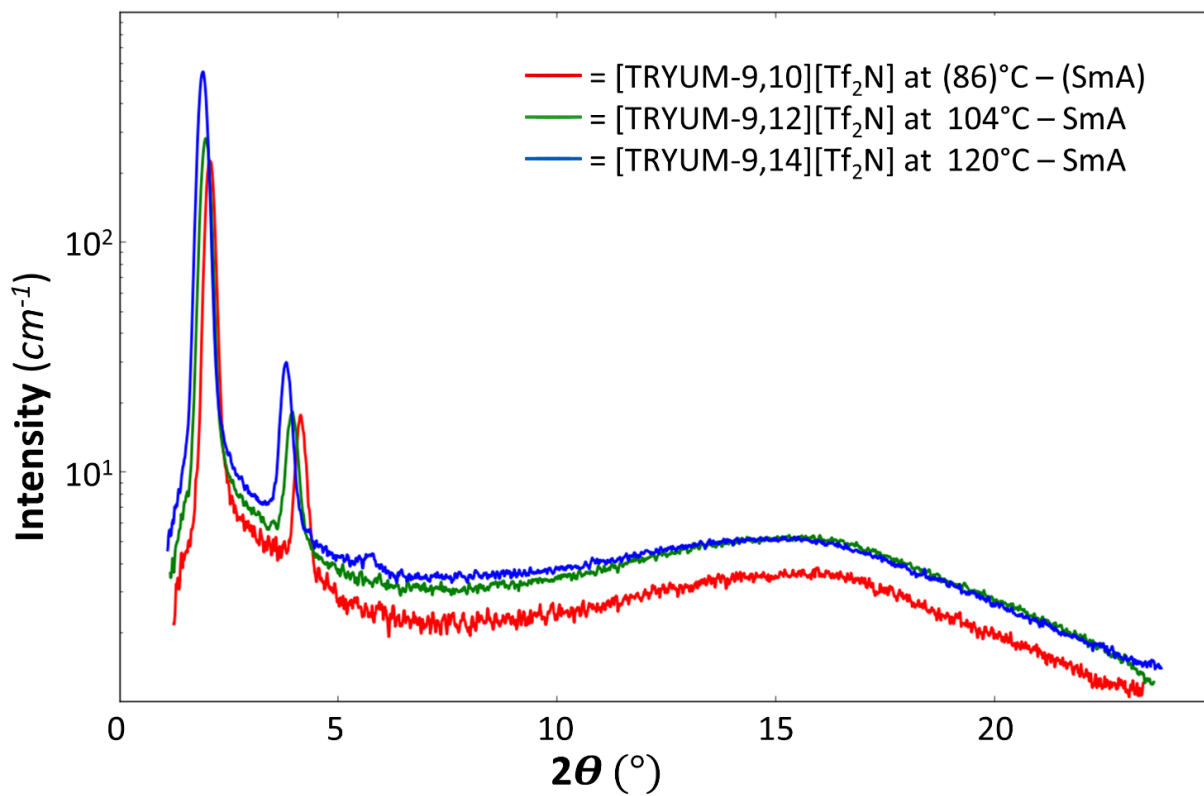


Figure C45. X-ray scattering of compounds [TRYUM-9,*n*][Tf<sub>2</sub>N] in SmA phases.

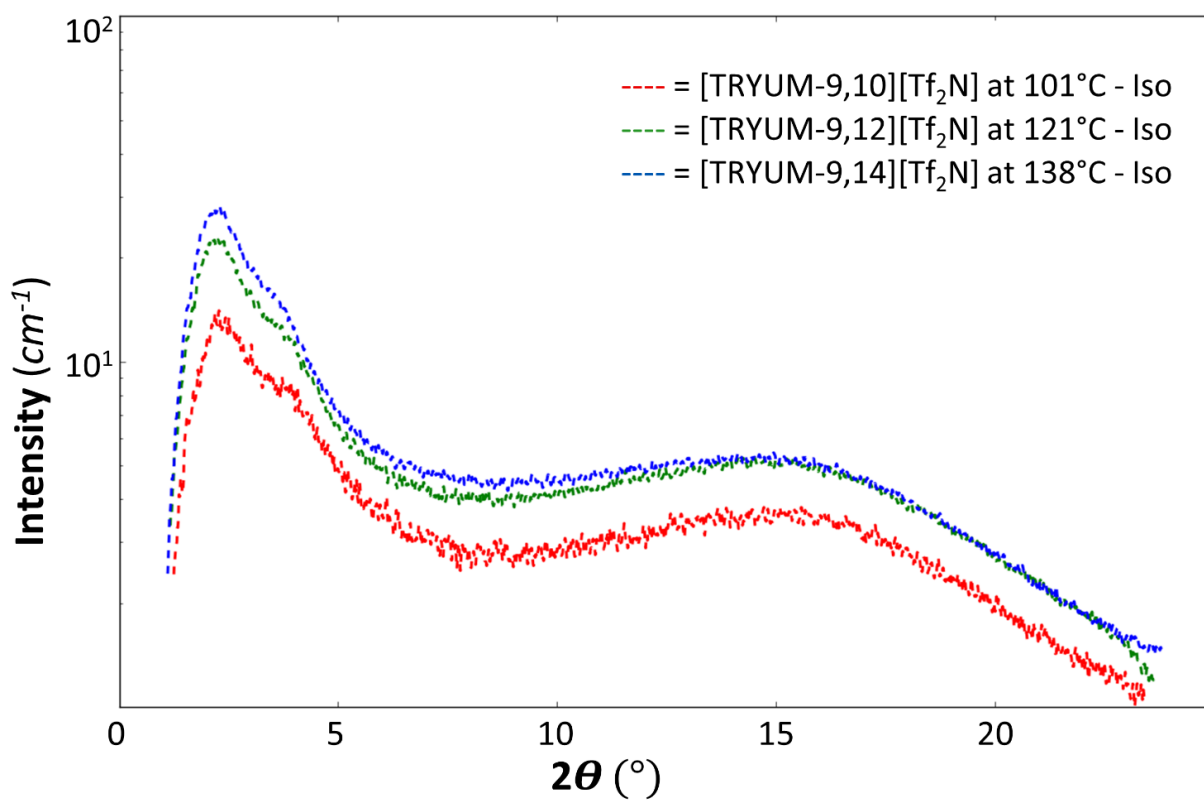


Figure C46. X-ray scattering of compounds [TRYUM-9,*n*][Tf<sub>2</sub>N] in Iso phases.

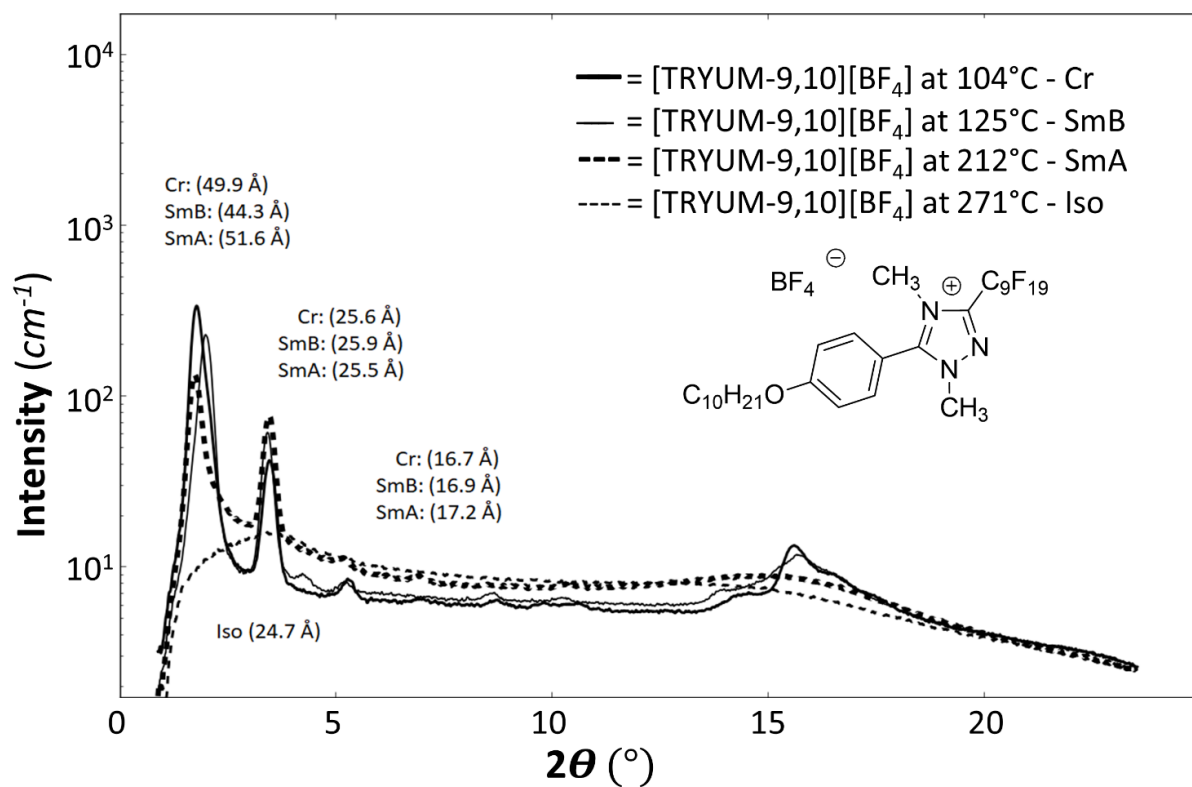


Figure C47. X-ray scattering of compound [TRYUM-9,10][BF<sub>4</sub>].

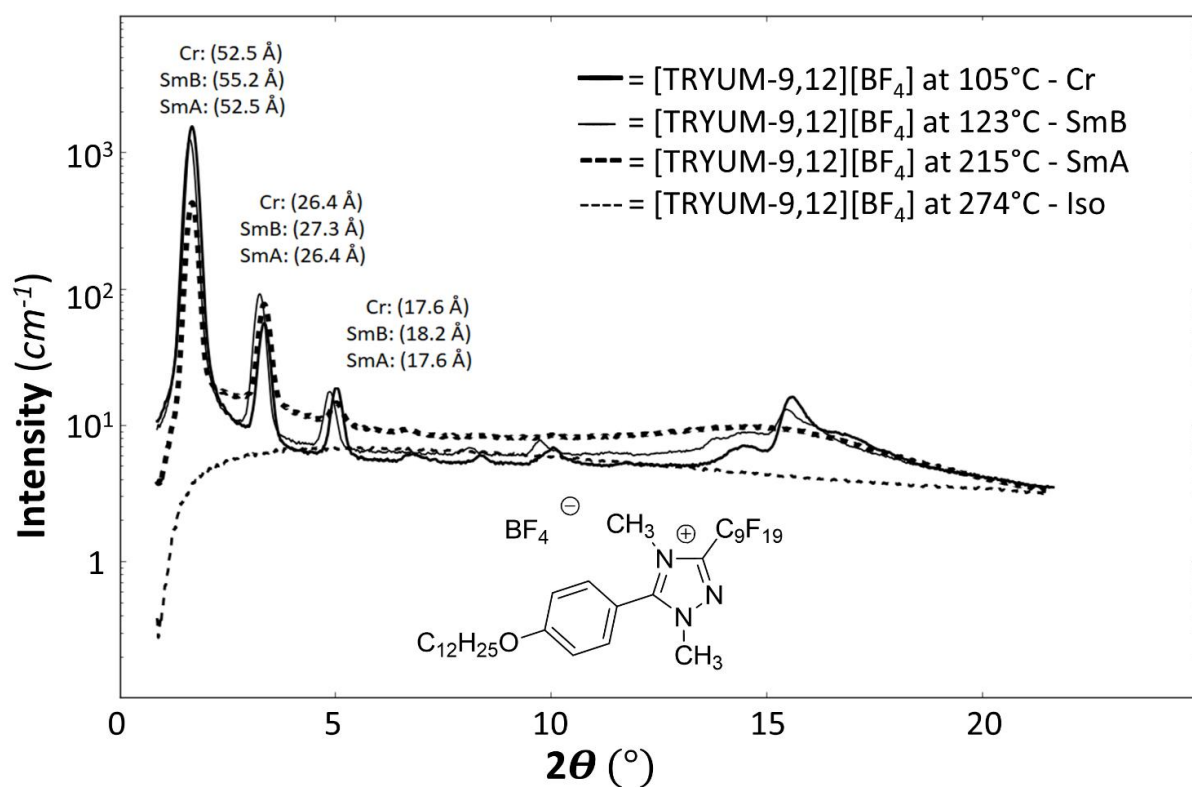


Figure C48. X-ray scattering of compound [TRYUM-9,12][BF<sub>4</sub>].

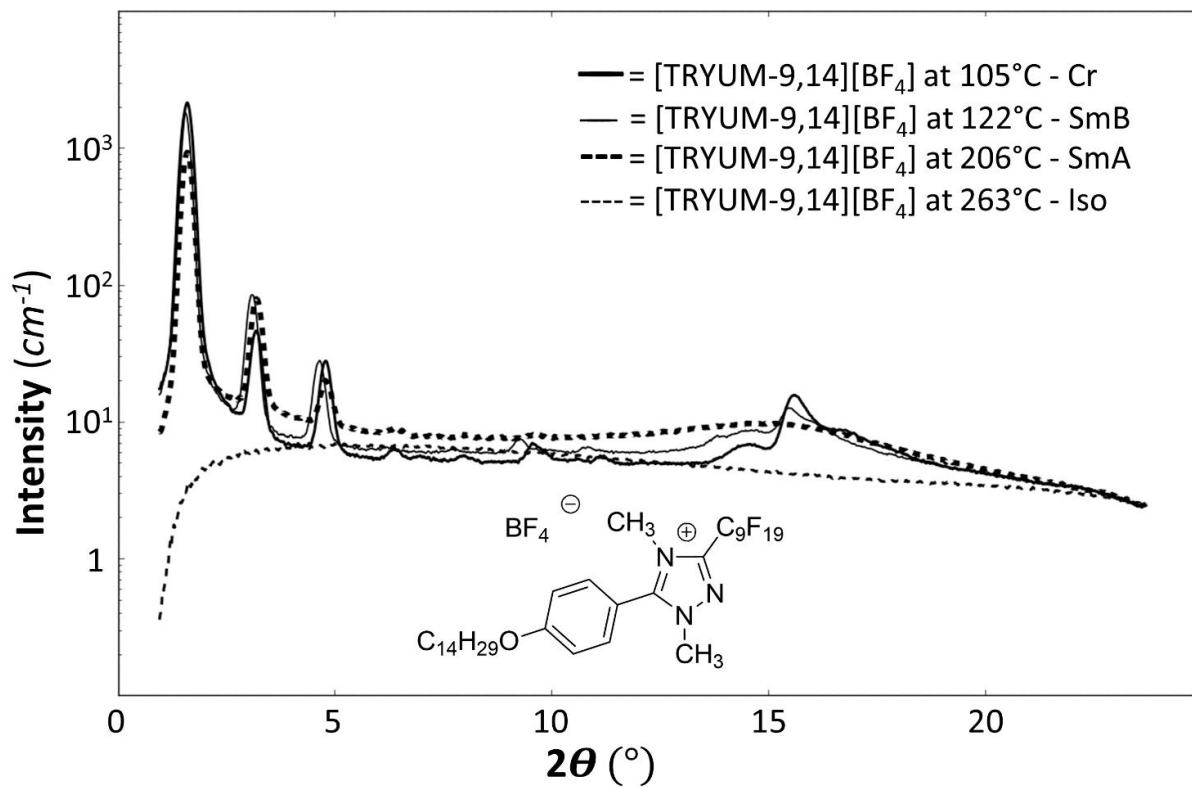


Figure C49. X-ray scattering of compound [TRYUM-9,14][BF<sub>4</sub>].

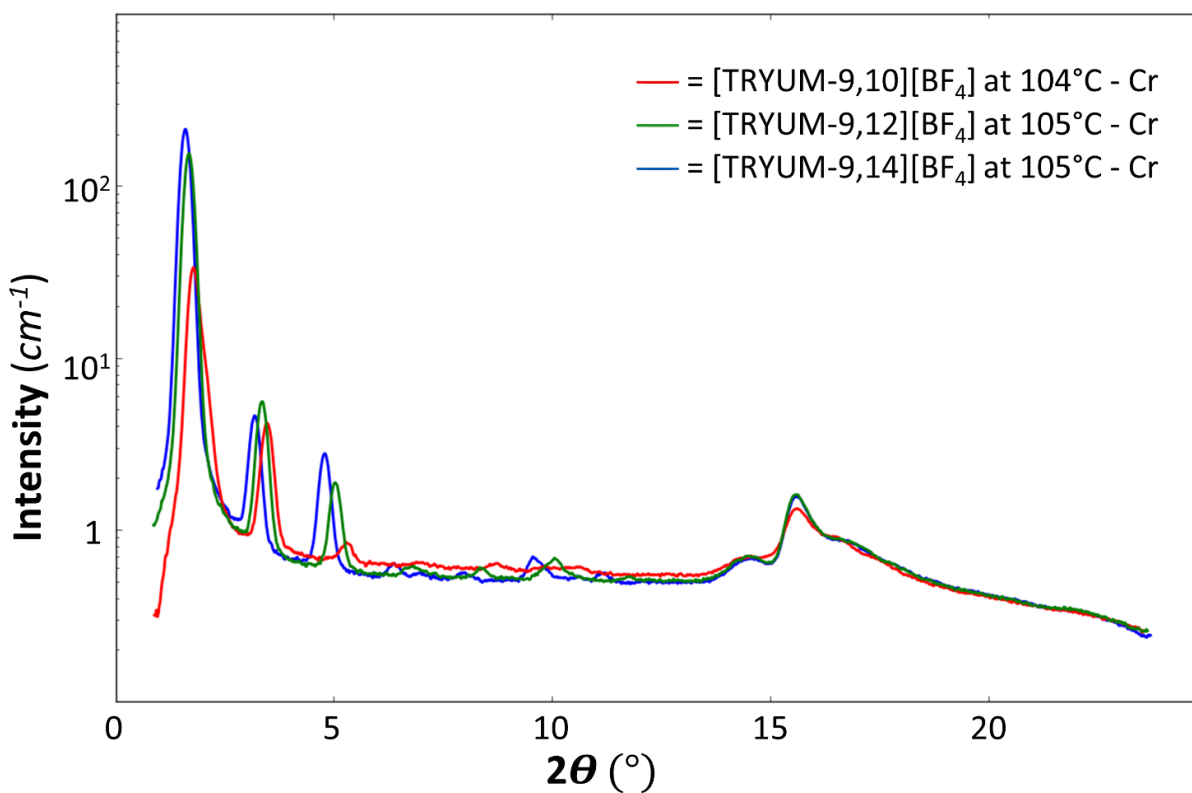


Figure C50. X-ray scattering of compounds [TRYUM-9,*n*][BF<sub>4</sub>] in Cr phases.

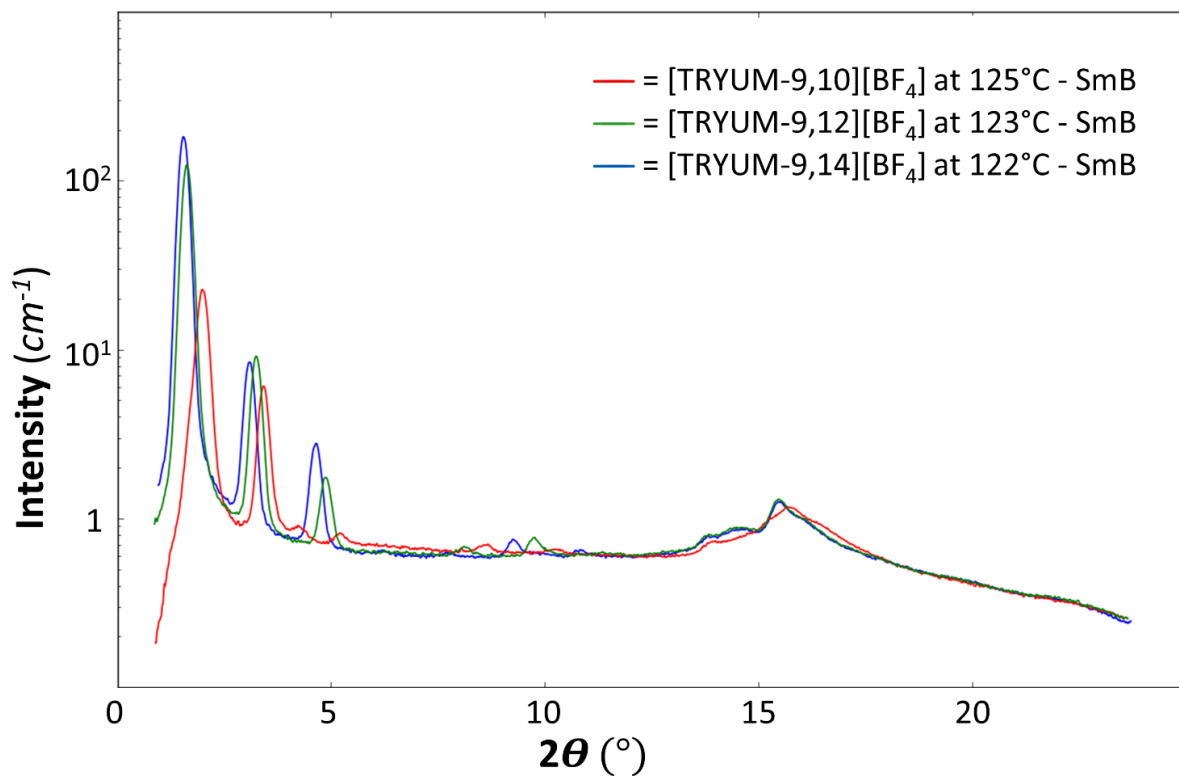


Figure C51. X-ray scattering of compounds [TRYUM-9,*n*][BF<sub>4</sub>] in SmB phases.

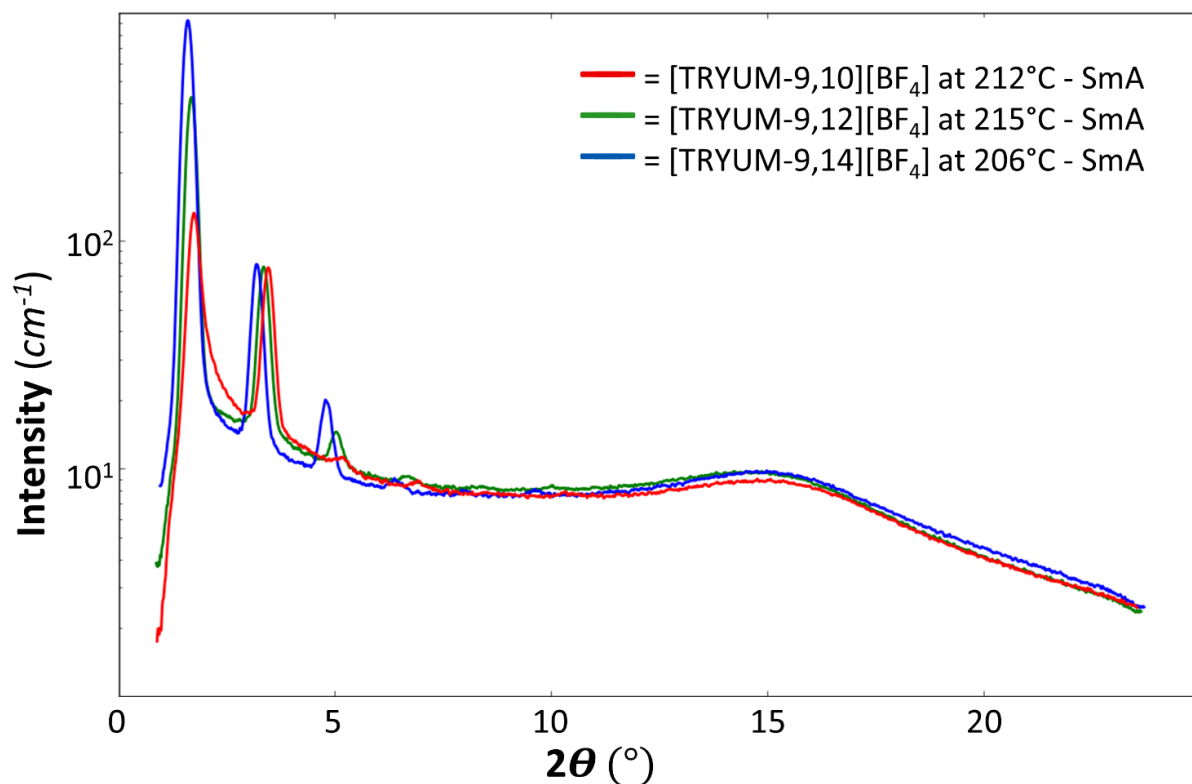


Figure C52. X-ray scattering of compounds [TRYUM-9,*n*][BF<sub>4</sub>] in SmA phases.



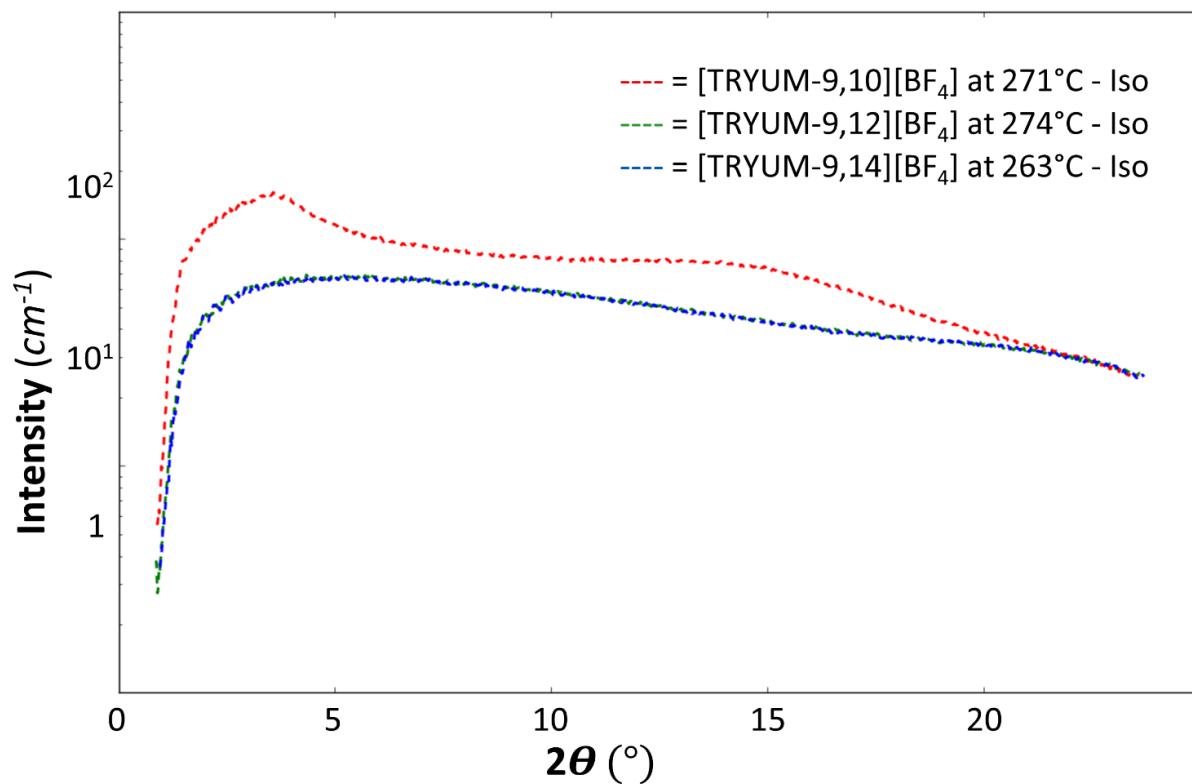


Figure C53. X-ray scattering of compounds [TRYUM-9,*n*][BF<sub>4</sub>] in Iso phases.

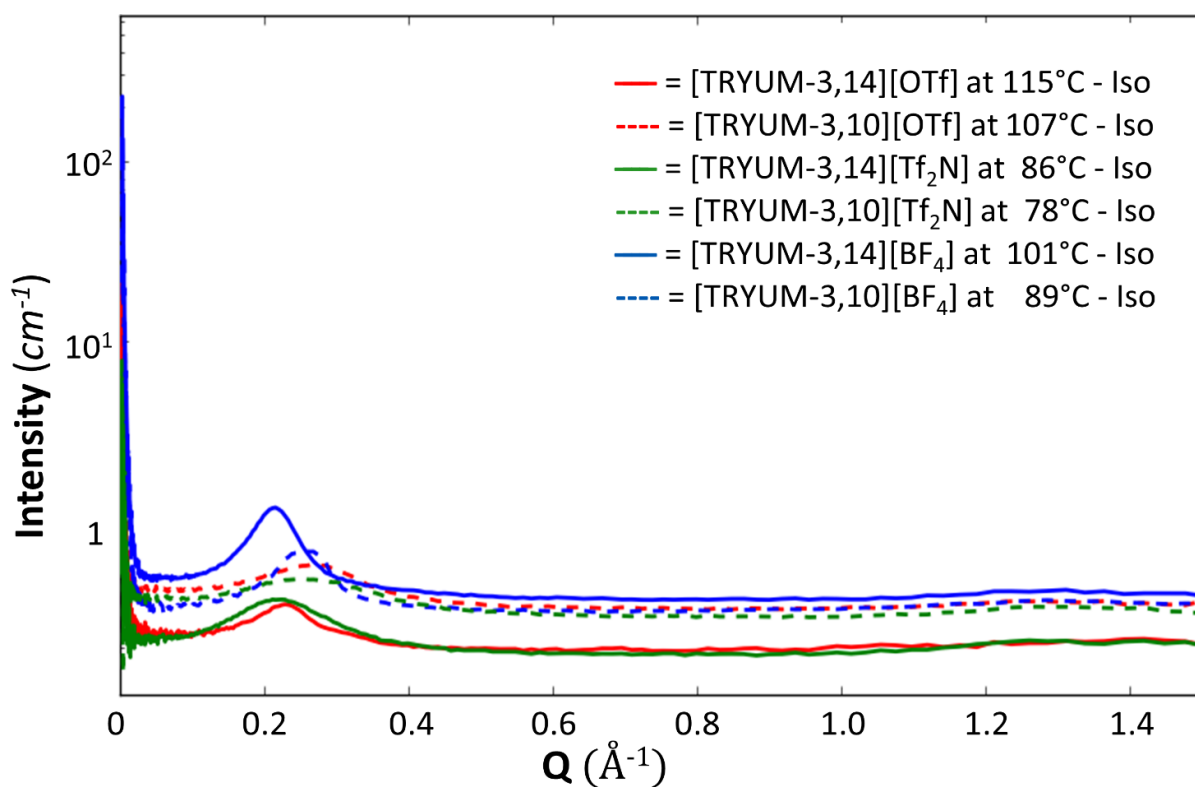


Figure C54. Neutron scattering of [TRYUM-3,*n*][OTf], [TRYUM-3,*n*][Tf<sub>2</sub>N] and [TRYUM-3,*n*][BF<sub>4</sub>] in Iso phases (*n* = 10, 14).

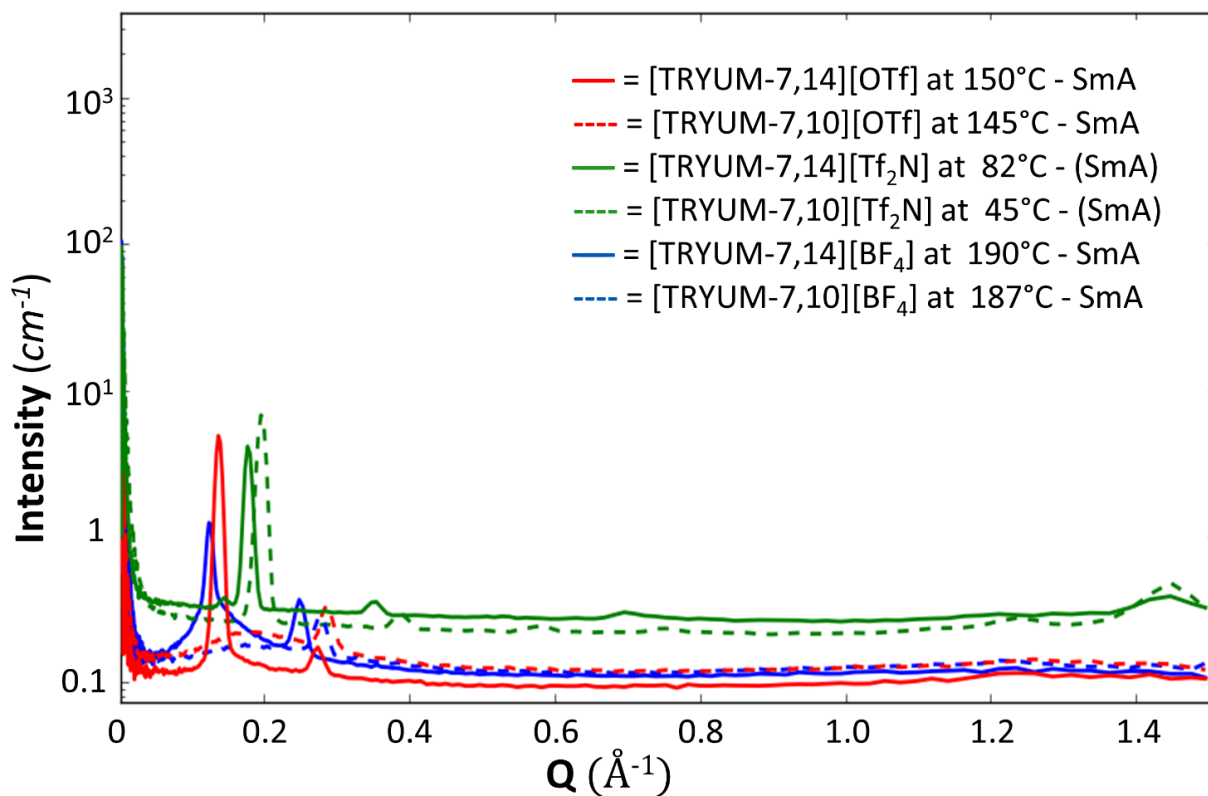


Figure C55. Neutron scattering of [TRYUM-7,*n*][OTf], [TRYUM-7,*n*][Tf<sub>2</sub>N] and [TRYUM-7,*n*][BF<sub>4</sub>] in SmA phases (*n* = 10, 14).

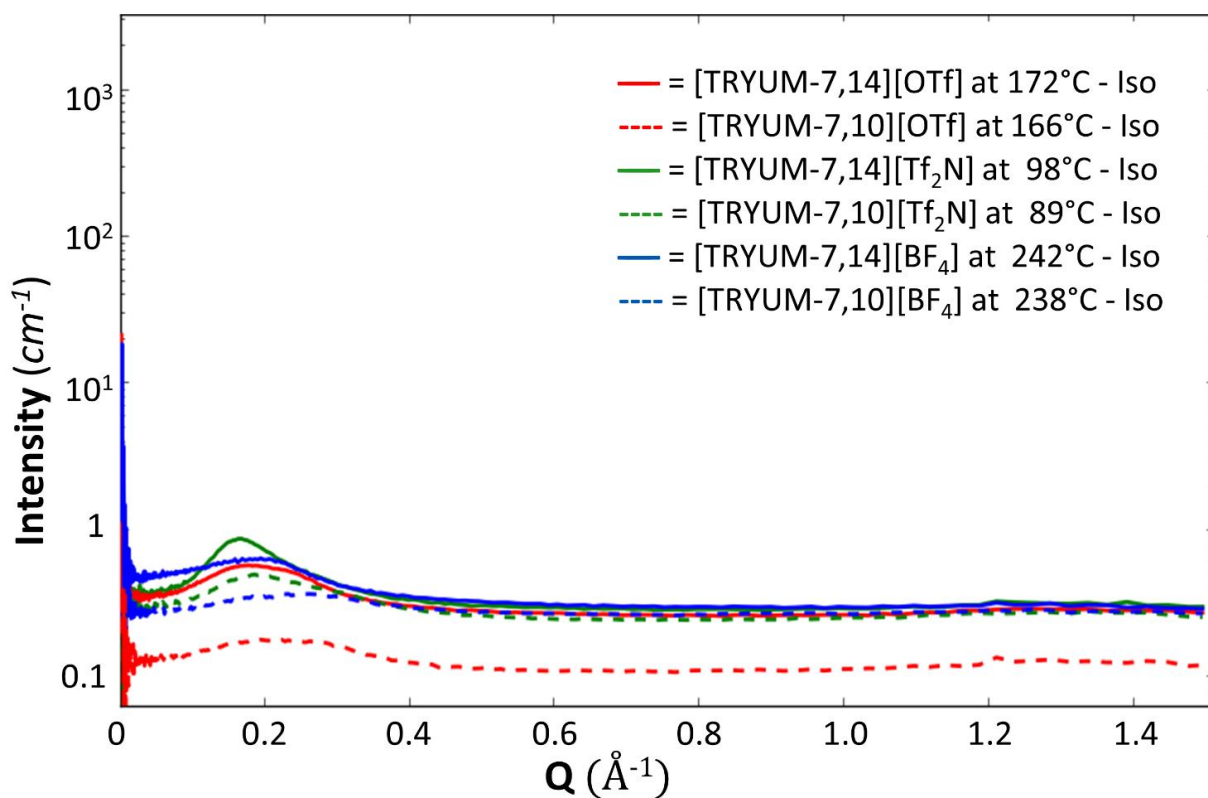


Figure C56. Neutron scattering of [TRYUM-7,*n*][OTf], [TRYUM-7,*n*][Tf<sub>2</sub>N] and [TRYUM-7,*n*][BF<sub>4</sub>] in Iso phases (*n* = 10, 14).

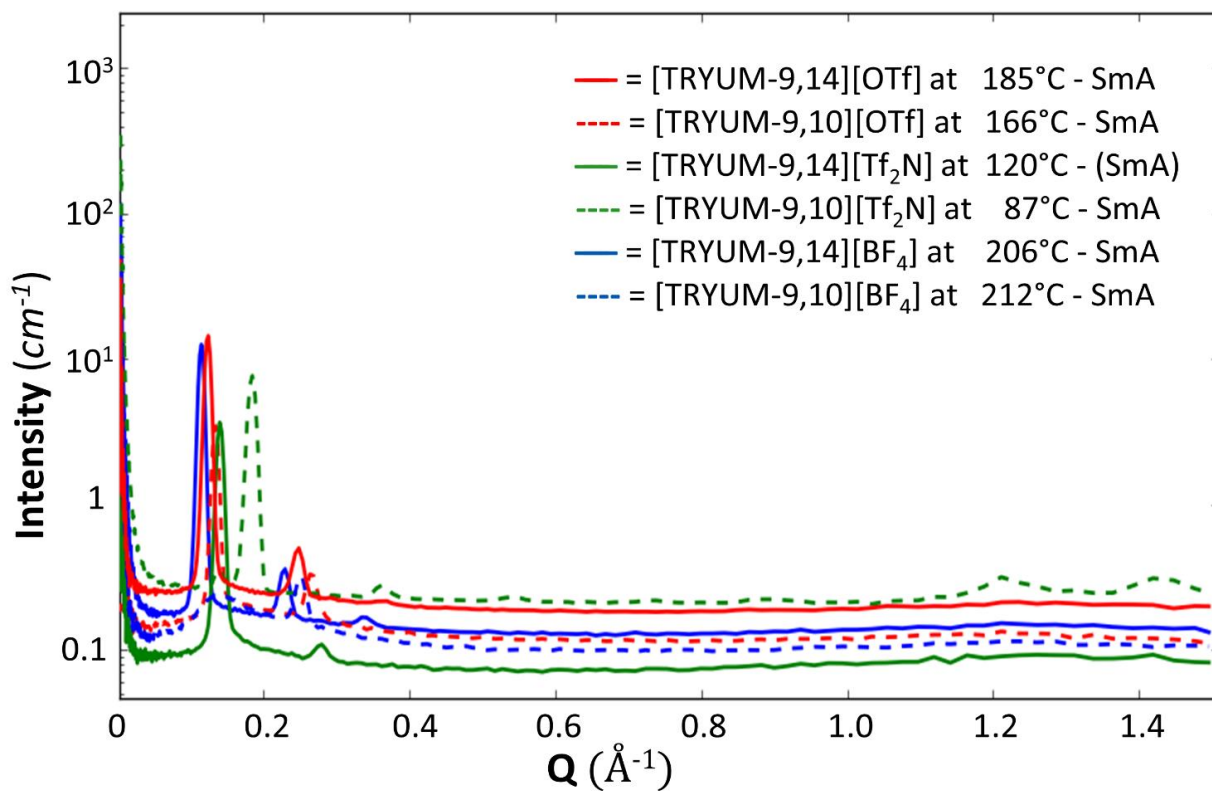


Figure C57. Neutron scattering of [TRYUM-9,*n*][OTf], [TRYUM-9,*n*][Tf<sub>2</sub>N] and [TRYUM-9,*n*][BF<sub>4</sub>] in Iso phases (*n* = 10, 14).

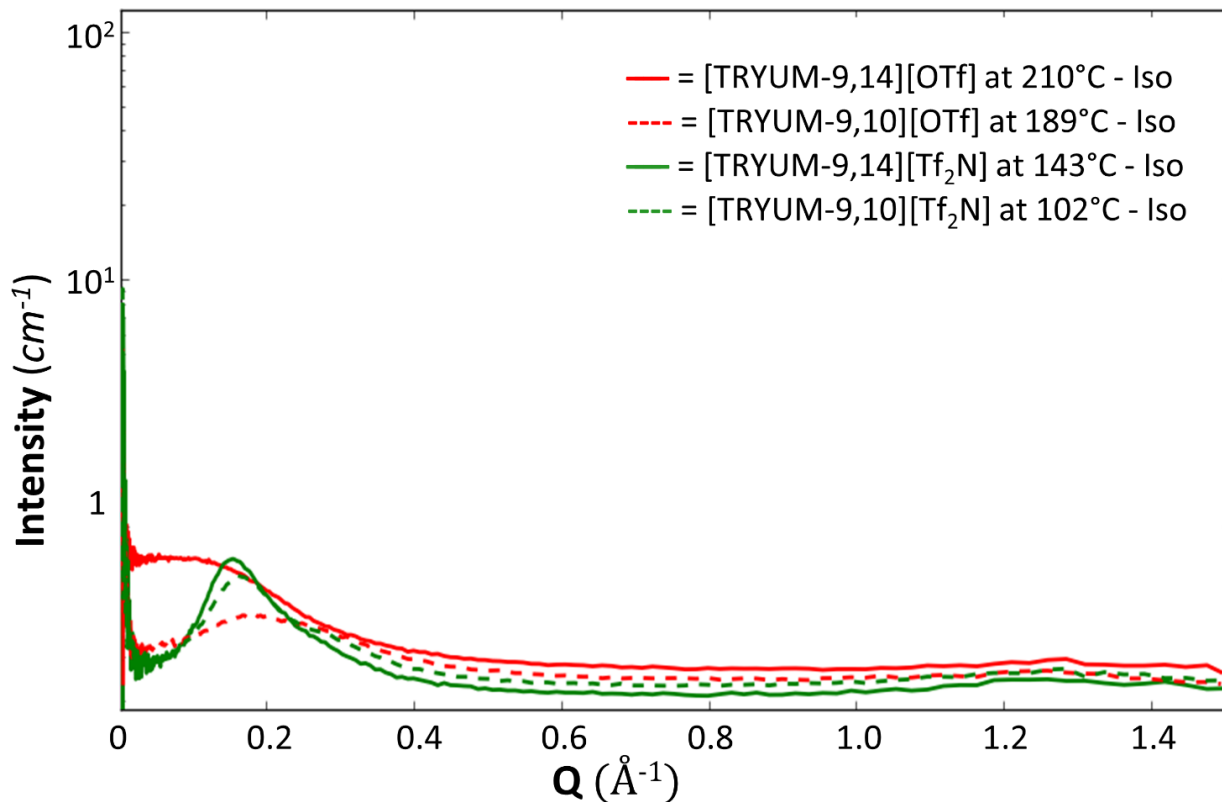


Figure C58. Neutron scattering of compounds [TRYUM-9,*n*][OTf] and [TRYUM-9,*n*][Tf<sub>2</sub>N] in SmA phases (*n* = 10, 14).

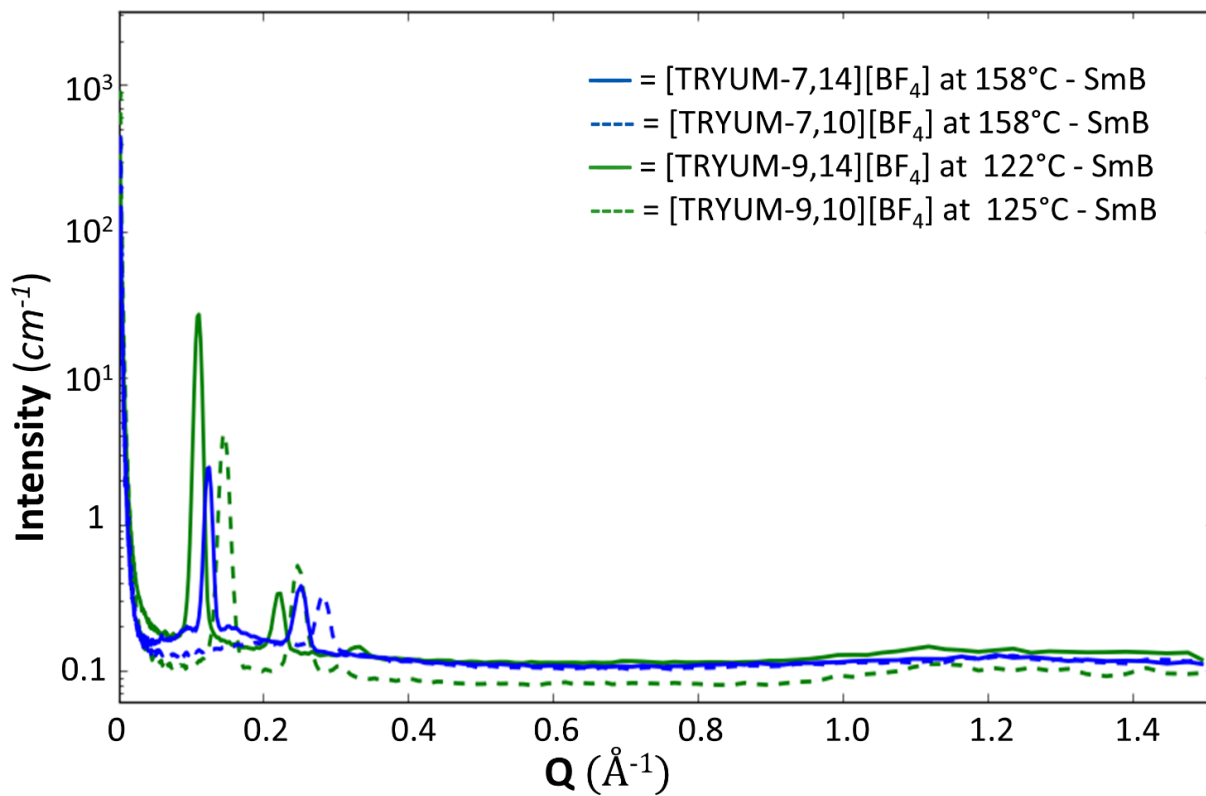


Figure C59. Neutron scattering of compounds [TRYUM-7,*n*][BF<sub>4</sub>] and [TRYUM-9,*n*][BF<sub>4</sub>] in SmB phases (*n* = 10, 14).

## Bibliography

- 1 P. Wasserscheid and T. Welton, *Ionic Liquids in Synthesis*, Wiley-VCH Verlag GmbH & Co. KGaA, Weinheim, Germany, 2007.
- 2 J. A. Boon, J. A. Levisky, J. L. Pflug and J. S. Wilkes, *J. Org. Chem.*, 1986, **51**, 480–483.
- 3 K. Behera, S. Pandey, A. Kadyan and S. Pandey, *Sensors (Switzerland)*, 2015, **15**, 30487–30503.
- 4 T. Sato, G. Masuda and K. Takagi, *Electrochim. Acta*, 2004, **49**, 3603–3611.
- 5 W. Kubo, K. Murakoshi, T. Kitamura, S. Yoshida, M. Haruki, K. Hanabusa, H. Shirai, Y. Wada and S. Yanagida, *J. Phys. Chem. B*, 2001, **105**, 12809–12815.
- 6 S. Seki, Y. Kobayashi, H. Miyashiro, Y. Ohno, A. Usami, Y. Mita, M. Watanabe and N. Terada, *Chem. Commun.*, 2006, **2**, 544–545.
- 7 H. Niedermeyer, J. P. Hallett, I. J. Villar-Garcia, P. A. Hunt and T. Welton, *Chem. Soc. Rev.*, 2012, **41**, 7780.
- 8 A. Marciniak, *Int. J. Mol. Sci.*, 2010, **11**, 1973–90.
- 9 A. B. Pereiro, J. M. M. Araújo, S. Martinho, F. Alves, S. Nunes, A. Matias, C. M. M. Duarte, L. P. N. Rebelo and I. M. Marrucho, *ACS Sustain. Chem. Eng.*, 2013, **1**, 427–439.
- 10 I. Zama, G. Gorni, V. Borzatta, M. C. Cassani, C. Crupi and G. Di Marco, *J. Mol. Liq.*, 2016, **223**, 749–753.
- 11 F. D’Anna, S. Marullo, P. Vitale and R. Noto, *European J. Org. Chem.*, 2011, 5681–5689.
- 12 J. P. Hallett, C. L. Liotta, G. Ranieri and T. Welton, *J. Org. Chem.*, 2009, **74**, 1864.
- 13 F. D’Anna, V. Frenna, S. Marullo, R. Noto and D. Spinelli, *Tetrahedron*, 2008, **64**, 11209–11217.
- 14 I. Pibiri, A. Pace, S. Buscemi, V. Causin, F. Rastrelli and G. Saielli, *Phys. Chem. Chem. Phys.*, 2012, **14**, 14306–14314.
- 15 M. Hird, *Chem. Soc. Rev.*, 2007, **36**, 2070–2095.
- 16 P. Bonhôte, A.-P. Dias, N. Papageorgiou, K. Kalyanasundaram and M. Grätzel, *Inorg. Chem.*, 1996, **35**, 1168–1178.
- 17 J. H. Davis, K. J. Forrester and T. Merrigan, *Tetrahedron Lett.*, 1998, **39**, 8955–8958.
- 18 J. N. A. Canongia Lopes and A. A. H. Pádua, *J. Phys. Chem. B*, 2006, **110**, 3330–3335.
- 19 D. Almantariotis, T. Gefflaut, A. A. H. Pádua, J.-Y. Coxam and M. F. C. Gomes, *J. Phys. Chem. B*, 2010, **114**, 3608–3617.
- 20 I. Krossing and J. M. Slattery, *Z. Phys. Chem*, 2006, **220**, 1343–1359.
- 21 J. M. Slattery, C. Daguinet, P. J. Dyson, T. J. S. Schubert and I. Krossing, *Angew. Chem. Int. Ed. Engl.*, 2007, **46**, 5384–8.
- 22 K. Binnemans, *Chem. Rev.*, 2005, **105**, 4148–4204.
- 23 K. Goossens, K. Lava, C. W. Bielawski and K. Binnemans, *Chem. Rev.*, 2016, **116**, 4643–4807.
- 24 I. Dierking, *Textures of Liquid Crystals*, Wiley-VCH Verlag GmbH & Co. KGaA, Weinheim, FRG,

- 2003.
- 25 D. W. Bruce and B. Donnio, in *Liquid Crystals II*, ed. In: Mingos D.M.P., Springer Berlin Heidelberg, 1999, pp. 193–247.
- 26 M. Kleman, *Reports Prog. Phys.*, 1989, **52**, 555–654.
- 27 J. P.-W. Wong, A. C. Whitwood and D. W. Bruce, *Chem. - A Eur. J.*, 2012, **18**, 16073–16089.
- 28 K. V. Axenov and S. Laschat, *Materials (Basel)*, 2011, **4**, 206–259.
- 29 Y. Gao, J. M. Slattery and D. W. Bruce, *New J. Chem.*, 2011, **35**, 2910–2918.
- 30 M. Yoshio, T. Kagata, K. Hoshino, T. Mukai, H. Ohno and T. Kato, *J. Am. Chem. Soc.*, 2006, **128**, 5570–5577.
- 31 A. Safavi and M. Tohidi, *J. Phys. Chem. C*, 2010, **114**, 6132–6140.
- 32 N. V. Shvedene, O. A. Avramenko, V. E. Baulin, L. G. Tomilova and I. V. Pletnev, *Electroanalysis*, 2011, **23**, 1067–1072.
- 33 M. Yoshio, T. Ichikawa, H. Shimura, T. Kagata, A. Hamasaki, T. Mukai, H. Ohno and T. Kato, *Bull. Chem. Soc. Jpn.*, 2007, **80**, 1836–1841.
- 34 M. Henmi, K. Nakatsuji, T. Ichikawa, H. Tomioka, T. Sakamoto, M. Yoshio and T. Kato, *Adv. Mater.*, 2012, **24**, 2238–2241.
- 35 T. D. Do and A. R. Schmitzer, *RSC Adv.*, 2015, **5**, 635–639.
- 36 S. Chowdhury, R. S. Mohan and J. L. Scott, *Tetrahedron*, 2007, **63**, 2363–2389.
- 37 D. W. Bruce, Y. Gao, N. Canongia, K. Shimizu and J. M. Slattery, *Chem. Eur. J.*, 2016, **22**, 16113–16123.
- 38 W. Dobbs, L. Douce, L. Allouche, A. Louati, F. Malbosc and R. Welter, *New J. Chem.*, 2006, **30**, 528–532.
- 39 W. Dobbs, B. Heinrich, C. Bourgogne, B. Donnio, E. Terazzi, M. E. Bonnet, F. Stock, P. Erbacher, A. L. Bolcato-Bellemin and L. Douce, *J. Am. Chem. Soc.*, 2009, **131**, 13338–13346.
- 40 M. Blesic, M. Swadźba-Kwaśny, J. D. Holbrey, J. N. Canongia Lopes, K. R. Seddon and L. P. N. Rebelo, *Phys. Chem. Chem. Phys.*, 2009, **11**, 4260–4268.
- 41 Q. Zhang, K. Wang, Q. Ren, L. Niu and B. Chen, *Liq. Cryst.*, 2011, **38**, 1349–1355.
- 42 X. Li, D. W. Bruce and J. M. Shreeve, *J. Mater. Chem.*, 2009, **19**, 8232–8238.
- 43 K. Lava, K. Binnemans and T. Cardinaels, *J. Phys. Chem. B*, 2009, **113**, 9506–9511.
- 44 K. Goossens, K. Lava, P. Nockemann, K. Van Hecke, L. Van Meervelt, P. Pattison, K. Binnemans and T. Cardinaels, *Langmuir*, 2009, **25**, 5881–5897.
- 45 F. Lo Celso, I. Pibiri, A. Triolo, R. Triolo, A. Pace, S. Buscemi and N. Vivona, *J. Mater. Chem.*, 2007, **17**, 1201–1208.
- 46 V. Pérez-Gregorio, I. Giner, M. Carmen López, I. Gascón, E. Cavero and R. Giménez, *J. Colloid Interface Sci.*, 2012, **375**, 94–101.

- 47 I. Giner, I. Gascón, R. Giménez, P. Cea, M. C. López and C. Lafuente, *J. Phys. Chem. C*, 2009, **113**, 18827–18834.
- 48 L. M. Antill, M. M. Neidhardt, J. Kirres, S. Beardsworth, M. Mansueto, A. Baro and S. Laschat, *Liq. Cryst.*, 2014, **41**, 976–985.
- 49 V. Causin and G. Saielli, *J. Mater. Chem.*, 2009, **19**, 9153–9162.
- 50 G. Casella, V. Causin, F. Rastrelli and G. Saielli, *Liq. Cryst.*, 2016, 1–13.
- 51 W. Li, J. Zhang, B. Li, M. Zhang and L. Wu, *Chem. Commun.*, 2009, 5269.
- 52 P. Dechambenoit, S. Ferlay, B. Donnio, D. Guillon and M. W. Hosseini, *Chem. Commun. (Camb.)*, 2011, **47**, 734–736.
- 53 D. J. Abdallah, A. Robertson, H. F. Hsu and R. G. Weiss, *J. Am. Chem. Soc.*, 2000, **122**, 3053–3062.
- 54 A. Alvarez Fernandez and P. Kouwer, *Int. J. Mol. Sci.*, 2016, **17**, 731.
- 55 K. Goossens, P. Nockemann, K. Driesen, B. Goderis, C. Görrler-Walrand, K. Van Hecke, L. Van Meervelt, E. Pouzet, K. Binnemans and T. Cardinaels, *Chem. Mater.*, 2008, **20**, 157–168.
- 56 J. Baudoux, P. Judeinstein, D. Cahard and J. C. Plaquevent, *Tetrahedron Lett.*, 2005, **46**, 1137–1140.
- 57 C. J. Bowlas, D. W. Bruce and K. R. Seddon, *Chem. Commun.*, 1996, 1625–1626.
- 58 J. D. Holbrey and K. R. Seddon, *J. Chem. Soc. Dalt. Trans.*, 1999, 2133–2139.
- 59 A. Beneduci, S. Cospito, M. La Deda, L. Veltri and G. Chidichimo, *Nat. Commun.*, 2014, **5**, 1–8.
- 60 T. Li, F. Xu and W. Shi, *Chem. Phys. Lett.*, 2015, **628**, 9–15.
- 61 A. A. Fernandez, L. T. de Haan and P. H. J. Kouwer, *J. Mater. Chem. A*, 2013, **1**, 354–357.
- 62 I. Pibiri, A. Pace, S. Buscemi, N. Vivona and L. Malpezzi, *Heterocycles*, 2006, **68**, 307–321.
- 63 A. Abate, A. Petrozza, G. Cavallo, G. Lanzani, F. Matteucci, D. W. Bruce, N. Houbenov, P. Metrangolo and G. Resnati, *J. Mater. Chem. A*, 2013, **1**, 6572–6578.
- 64 S. E. Rankin, B. Tan, H. J. Lehmler, K. P. Hindman and B. L. Knutson, *Microporous Mesoporous Mater.*, 2004, **73**, 197–202.
- 65 G. Cavallo, G. Terraneo, A. Monfredini, M. Saccone, A. Priimagi, T. Pilati, G. Resnati, P. Metrangolo and D. W. Bruce, *Angew. Chemie Int. Ed.*, 2016, **55**, 6300–6304.
- 66 S. Pensec, F.-G. Tournilhac, P. Bassoul and C. Durliat, *J. Phys. Chem. B*, 1998, **102**, 52–60.
- 67 C. Tschierske, *Top. Curr. Chem.*, 2011, **318**, 1–108.
- 68 K. Stappert, D. Uenal, B. Mallick and A. V. Mudring, *J. Mater. Chem. C*, 2014, **2**, 7976–7986.
- 69 K. Stappert, D. Unal, E. T. Spielberg and A.-V. Mudring, *Cryst. Growth Des.*, 2015, **15**, 752–758.
- 70 K. Stappert and A.-V. Mudring, *RSC Adv.*, 2015, **5**, 16886–16896.
- 71 U. G. Brauer, A. T. De La Hoz and K. M. Miller, *J. Mol. Liq.*, 2015, **210**, 286–292.
- 72 M. Lartey, J. Meyer-Ilse, J. D. Watkins, E. A. Roth, S. Bowser, V. A. Kusuma, K. Damodaran, X.



- Zhou, M. Haranczyk, E. Albenze, D. R. Luebke, D. Hopkinson, J. B. Kortright and H. B. Nulwala, *Phys. Chem. Chem. Phys.*, 2015, **17**, 29834–29843.
- 73 F. Yan, M. Lartey, K. Jariwala, S. Bowser, K. Damodaran, E. Albenze, D. R. Luebke, H. B. Nulwala, B. Smit and M. Haranczyk, *J. Phys. Chem. B*, 2014, **118**, 13609–13620.
- 74 Y. R. Mirzaei, B. Twamley and J. M. Shreeve, *J. Org. Chem.*, 2002, **67**, 9340–9345.
- 75 K. Funabiki, N. Noma, G. Kuzuya, M. Matsui and K. Shibata, *J. Chem. Res. - Part S*, 1999, **0**, 300–301.
- 76 S. Buscemi, A. Pace, I. Pibiri, N. Vivona and D. Spinelli, *J. Org. Chem.*, 2003, **68**, 605–608.
- 77 J. B. Fournier and G. Durand, *J. Phys. II*, 1991, **1**, 845–870.
- 78 John M. Cowley, *Diffraction physics*, 1975.
- 79 W. L. B. W. H. Bragg, *Proc R. Soc. Lond. A.*, 1913, **88**, 428–38.
- 80 D. Demus, J. Goodby, G. W. Gray, H.-W. Spiess and V. Vill, *Physical Properties of Liquid Crystals*, Wiley-VCH Verlag GmbH & Co. KGaA, 2007.
- 81 N. W. Ashcroft and N. D. Mermin, *Solid state physics*, 1976.
- 82 H. Xue, B. Twamley and J. M. Shreeve, *J. Org. Chem.*, 2004, **69**, 1397–1400.
- 83 T. Liang, C. N. Neumann and T. Ritter, *Angew. Chemie Int. Ed.*, 2013, **52**, 8214–8264.
- 84 G. L'abbé, *J. Heterocycl. Chem.*, 1984, **21**, 627–638.
- 85 A. M. Boulton, A.J., Katritzky, A.R., Hamid, *J. Chem. Soc. C Org. Chem.*, 1967, 2005–2007.
- 86 L. B. Clapp, *Adv. Heterocycl. Chem.*, 1976, **20**, 65–116.
- 87 S. Buscemi, A. Pace, A. P. Piccionello, G. Macaluso, C. Organica, D. Spinelli and G. Giorgi, *J. Mater. Chem.*, 2005, **70**, 3288–3291.
- 88 H. C. Van der Plas, *Adv. Heterocycl. Chem.*, 1999, **74**, 9–240.
- 89 S. Buscemi, A. Pace, I. Pibiri, N. Vivona, C. Z. Lanza and D. Spinelli, *European J. Org. Chem.*, 2004, **2004**, 974–980.
- 90 A. Pace, S. Buscemi and N. Vivona, *Org. Prep. Proced. Int.*, 2005, **37**, 447–506.
- 91 R. De Marco, M. L. Di Gioia, A. Liguori, F. Perri, C. Siciliano and M. Spinella, *Tetrahedron*, 2011, **67**, 9708–9714.
- 92 M. Kadjout, M. Smietana, J. Leroy and C. Rolando, *Tetrahedron Lett.*, 2013, **54**, 1658–1660.
- 93 T. V. Goncharova, L. V. Zatonkaya and A. S. Potapov, *Procedia Chem.*, 2014, **10**, 485–489.
- 94 J. Keeler, *Understanding NMR Spectroscopy - 2nd Edition*, WILEY, 2005.
- 95 M. Yang, B. Mallick and A.-V. Mudring, *Cryst. Growth Des.*, 2013, **13**, 3068–3077.
- 96 B. Spingler, S. Schnidrig, T. Todorova and F. Wild, *CrystEngComm*, 2012, **14**, 751–757.
- 97 X. Wang, C. S. Vogel, F. W. Heinemann, P. Wasserscheid and K. Meyer, *Cryst. Growth Des.*, 2011, **11**, 1974–1988.
- 98 A. E. Bradley, C. Hardacre, J. D. Holbrey, S. Johnston, S. E. J. McMath and M. Nieuwenhuyzen,

- Chem. Mater.*, 2002, **14**, 629–635.
- 99 K. Shimizu, C. E. S. Bernardes and J. N. Canongia Lopes, *J. Phys. Chem. B*, 2014, **118**, 567–576.
- 100 A. Triolo, O. Russina, H.-J. Bleif and E. Di Cola, *J. Phys. Chem. B*, 2007, **111**, 4641–4644.
- 101 F. Nemoto, M. Kofu and O. Yamamuro, *J. Phys. Chem. B*, 2015, **119**, 5028–5034.
- 102 Y. Wang and H. Yang, *Chem. Eng. J.*, 2009, **147**, 71–78.
- 103 M. T. Clough, C. R. Crick, J. Gräsvik, P. A. Hunt, H. Niedermeyer, T. Welton and O. P. Whitaker, *Chem. Sci.*, 2015, **6**, 1101–1114.
- 104 A. J. R. Rennie, V. L. Martins, R. M. Torresi and P. J. Hall, *J. Phys. Chem. C*, 2015, **119**, 23865–23874.
- 105 J. Katkevics, A. Viksna, A. Zicmanis and G. Vaivars, *Solid State Ionics*, 2011, **188**, 114–117.
- 106 A. Lasia, *Electrochemical impedance spectroscopy and its applications*, Springer New York, 2014.
- 107 J. R. Macdonald, *Ann. Biomed. Eng.*, 1992, **20**, 289–305.
- 108 B. S. Instruments, Impedance , admittance , Nyquist , Bode , Black , etc ....
- 109 T. Mukai and K. Nishikawa, *RSC Adv.*, 2013, **3**, 19952.
- 110 R. Aranowski, I. Cichowska-Kopczyńska, B. Dębski and P. Jasiński, *J. Mol. Liq.*, 2016, **221**, 541–546.
- 111 D. W. Bruce, C. P. Cabry, J. N. C. Lopes, M. L. Costen, L. D’Andrea, I. Grillo, B. C. Marshall, K. G. McKendrick, T. K. Minton, S. M. Purcell, S. Rogers, J. M. Slattery, K. Shimizu, E. Smoll and M. A. Tesa-Serrate, *J. Phys. Chem. B*, 2017, **121**, 6002–6020.
- 112 J. Rault, *J. Non. Cryst. Solids*, 2000, **271**, 177–217.
- 113 J. Luo, J. Hu, W. Saak, R. Beckhaus, G. Wittstock, I. F. J. Vankelecom, C. Agert and O. Conrad, *J. Mater. Chem.*, 2011, **21**, 10426.
- 114 N. Boden, R. J. Bushby, J. Clements, M. V. Jesudason, P. F. Knowles and G. Williams, *Chem. Phys. Lett.*, 1988, **152**, 94–99.
- 115 N. Yamanaka, R. Kawano, W. Kubo, N. Masaki, T. Kitamura, Y. Wada, M. Watanabe and S. Yanagida, *J. Phys. Chem. B*, 2007, **111**, 4763–4769.
- 116 A. Hagfeldt, *Chem. Soc. Rev.*, 2011, **110**, 6595–6663.
- 117 S. R. Raghavan and J. F. Douglas, *Soft Matter*, 2012, **8**, 8539.
- 118 A. R. Hirst, I. Coates, T. R. Boucheteau, J. F. Miravet, B. Escuder, V. Castelletto, I. W. Hamley and D. K. Smith, *J. Am. Chem. Soc.*, 2008, **130**, 9113–9121.
- 119 R. Kumar and O. P. Katare, *AAPS PharmSciTech*, 2005, **6**, E298–E310.
- 120 E. Carretti, L. Dei and R. G. Weiss, *Soft Matter*, 2005, **1**, 17–22.
- 121 V. V. Tomina, G. R. Yurchenko, A. K. Matkovsky, Y. L. Zub, A. Kosak and A. Lobnik, *J. Fluor. Chem.*, 2011, **132**, 1146–1151.
- 122 O. V Dolomanov, L. J. Bourhis, R. J. Gildea, J. A. K. Howard and H. Puschmann, *J. Appl. Cryst.*

2009, **42**, 339–341.

123 G. M. Sheldrick, *Acta Cryst*, 2015, **A71**, 3–8.

124 G. M. Sheldrick, *Acta Cryst.*, 2015, **C71**, 3–8.

125 W. Massa, *Crystal Structure Determination*, Springer-Verlag, 2004.

## References Summary

### Figures Index

<b>Figure 1.</b> Graphical representation of molecular orientation in Nematic (a), Smectic (b) and Chiral Nematic (c) for calamitic LCs. ....	8
<b>Figure 2.</b> Graphical representation of molecular orientation in nematic discotic (a), nematic columnar (b) and columnar hexagonal (c) for discotic LCs. ....	9
<b>Figure 3.</b> Microphotographs showing Schlieren (a) and focal conic (b) textures. Respective defects are circled in red.....	13
<b>Figure 4.</b> Depiction of molecule orientation around Schlieren defects with 2 and 4 brushes. ....	13
<b>Figure 5.</b> Depiction of focal conics in a Dupin cycloid (a). Schematic illustration of a focal conic defect on a top view (b). ....	14
<b>Figure 6.</b> According to the $2\theta$ deviation, the phase shift causes constructive (left figure) or destructive (right figure) interferences.....	15
<b>Figure 7.</b> Graphic representation of molecular orientation in SmA (a), SmB (b) and SmC (c).....	17
<b>Figure 8.</b> Graphical representation of molecular orientation between layers in SmA <sub>1</sub> (a), SmA <sub>2</sub> (b) and SmA <sub>D</sub> (c).....	17
<b>Figure 9.</b> Planes orthogonal to the vectors with different Miller indices in cubic unit cell. ....	18
<b>Figure 10.</b> Planes not orthogonal to the vectors with different Miller indices in cubic unit cell.....	19
<b>Figure 11.</b> Planes not orthogonal to the vectors with a negative Miller index in cubic unit cell.....	19
<b>Figure 12.</b> Description of SmB molecular organisation by Miller indices. ....	20
<b>Figure 13.</b> X-ray scattering of a SmB material. Miller indices denote peaks of reflections. ....	20
<b>Figure 14.</b> <sup>1</sup> H-NMR spectrum in CDCl <sub>3</sub> of compound <b>5-7</b> isolated from ANRORC reaction with <b>4-7</b> as starting material.....	31
<b>Figure 15.</b> <sup>1</sup> H-NMR spectrum in CD <sub>3</sub> CN of <b>[TRYUM-7,12][I]</b> isolated from reaction in ethyl acetate..	32
<b>Figure 16.</b> <sup>1</sup> H-NMR spectrum cuts in CDCl <sub>3</sub> of <b>[TRYUM-7,12][OTf]</b> isolated from reaction in ethyl acetate.....	34
<b>Figure 17.</b> <sup>19</sup> F-NMR spectrum cuts in CDCl <sub>3</sub> of <b>[TRYUM-7,12][OTf]</b> isolated from reaction in ethyl acetate.....	35
<b>Figure 18.</b> <sup>1</sup> H- <sup>13</sup> C HMBC-NMR spectrum in CD <sub>3</sub> CN of <b>[TRYUM-7,12][BF4]</b> .....	37

<b>Figure 19.</b> $^1\text{H}$ - $^{13}\text{C}$ HMBC-NMR spectrum cut in $\text{CD}_3\text{CN}$ of <b>[TRYUM-7,12][BF<sub>4</sub>]</b> , between 4.40 and 3.50 ppm for $^1\text{H}$ .....	37
<b>Figure 20.</b> Stacking of spectra recorded on <b>[TRYUM-7,12][BF<sub>4</sub>]</b> in $\text{CD}_3\text{CN}$ . nOe spectrum recorded irradiating with frequency at 3.82 ppm(1, red line) and 4.01 ppm (2, blue line); $^1\text{H}$ -NMR normal spectrum (3, black line).....	38
<b>Figure 21.</b> Stacking of spectra recorded on <b>[TRYUM-7,12][BF<sub>4</sub>]</b> in $\text{CD}_3\text{CN}$ . nOe spectrum recorded irradiating with frequency at 7.64 ppm (1, red line) and 7.26 ppm (2, blue line); $^1\text{H}$ -NMR normal spectrum (3, black line).....	39
<b>Figure 22.</b> Scheme of crystal growing.....	41
<b>Figure 23.</b> View with ESDs of the triazolium core of <b>[TRYUM-7,10][OTf]</b> (left) and the triazole core of <b>5-9</b> (right). Groups in position 3- and 5- of the rings have been omitted to focus on triazolium and triazole cores, where a centroid was calculated. In this and subsequent figures, carbon atoms are coloured light grey, nitrogen atoms blue, oxygen atoms red, fluorine atoms are light green, sulfur atoms are yellow and boron atoms are pink. ....	42
<b>Figure 24.</b> Ortep view of compound <b>[TRIUM-7,10][OTf]</b> viewed down the <i>b</i> -axis of the unit cell. ....	43
<b>Figure 25.</b> Ortep view of compound <b>[TRIUM-3,10][OTf]</b> . ....	44
<b>Figure 26.</b> Crystal packing view of compound <b>[TRIUM-9,10][OTf]</b> along the <i>b</i> -axis of the unit cell. ....	44
<b>Figure 27.</b> Crystal packing view of compound <b>[TRIUM-9,14][OTf]<sup>†</sup></b> along the <i>b</i> -axis of the unit cell. Acetone of crystallisation is omitted for clarity. ....	45
<b>Figure 28.</b> Ortep view of crystal lattice of <b>[TRYUM-7,10][Tf<sub>2</sub>N]</b> showing the unit cell dimensions. ....	46
<b>Figure 29.</b> Ortep view with comparison of angles between alkyl and perfluoroalkyl-chains of triazolium bis(triflimide)s cations. Centroids are coloured red. ....	47
<b>Figure 30.</b> Crystal packing view of compound <b>[TRYUM-3,10][Tf<sub>2</sub>N]</b> .....	47
<b>Figure 31.</b> Crystal packing view of compound <b>[TRIUM-7,12][Tf<sub>2</sub>N]</b> along the <i>a</i> -axis of the unit cell... ..	48
<b>Figure 32.</b> Crystal packing view of compound <b>[TRIUM-7,12][Tf<sub>2</sub>N]</b> along the <i>b</i> -axis of the unit cell... ..	49
<b>Figure 33.</b> Ortep view of compound <b>[TRIUM-3,10][BF<sub>4</sub>]<sup>†</sup></b> . Carbon atoms are coloured light grey, nitrogen atoms blue, oxygen atoms red, fluorine atoms are light green and boron atoms are pink. Acetone of crystallisation is omitted and depth cueing is applied, where brightness decreases along deepness. ....	49
<b>Figure 34.</b> Ortep view of <b>[TRYUM-9,10][BF<sub>4</sub>]</b> (left) and <b>[TRYUM-7,10][BF<sub>4</sub>]</b> (right) along the <i>a</i> -axis of the unit cell.....	50
<b>Figure 35.</b> Crystal packing view of compound <b>[TRIUM-7,10][BF<sub>4</sub>]</b> is along the <i>b</i> -axis of the unit cell and hydrogens are omitted.....	50
<b>Figure 36.</b> Crystal structure of 1,4,5-Trimethyl-3-perfluorooctyl-1,2,4-triazolium Tetrafluoroborate. View showing the helicity of the perfluoroheptyl-chain (left). View showing numbers of cations that	

surround an anion, in which depth cueing is applied, where brightness decreases along deepness (middle). View orthogonal to the <i>b</i> axis of the unit cell, which shows the segregation of the perfluoroalkyl-chain (right). .....	51
<b>Figure 37.</b> 3D Bar Chart of transition temperatures of the triazolium salts grouped by perfluoroalkyl-chain and anion. ....	54
<b>Figure 38.</b> Microphotographs taken on cooling from the isotropic liquid with 100x as magnification. On top, compound [TRYUM-7,10][BF <sub>4</sub> ] at 152.5°C in SmB (left) and the same sample at 183.3°C in SmA phase (right). On bottom, compound [TRYUM-7,10][Tf <sub>2</sub> N] at 49.4°C in SmA phase (left) and compound [TRYUM-7,10][OTf] at 160.1°C in SmA phase (right). ....	55
<b>Figure 39.</b> Bar chart of transition temperatures of the triazolium tetrafluoroborates grouped by perfluoroalkyl-chain. ....	56
<b>Figure 40.</b> Bar chart of transition temperatures of the triazolium bis(triflimide)s grouped by perfluoroalkyl-chain. For monotropic compounds (*) both the heating and cooling segments are shown. ....	57
<b>Figure 41.</b> Bar chart of transition temperatures of the triazolium triflates grouped by perfluoroalkyl-chain. ....	58
<b>Figure 42.</b> DSC traces of [TRYUM-7, <i>n</i> ][OTf]. Traces show the 2 <sup>nd</sup> heating and the 1 <sup>st</sup> cooling cycles. ....	59
<b>Figure 43.</b> DSC traces of [TRYUM-9, <i>n</i> ][OTf]. Traces show the 2 <sup>nd</sup> heating and the 1 <sup>st</sup> cooling cycles. ....	60
<b>Figure 44.</b> DSC traces of [TRYUM-7, <i>n</i> ][Tf <sub>2</sub> N]. Traces show the 2 <sup>nd</sup> heating and the 1 <sup>st</sup> cooling cycles. ....	61
<b>Figure 45.</b> DSC traces of [TRYUM-9, <i>n</i> ][Tf <sub>2</sub> N]. Traces show the 2 <sup>nd</sup> heating and the 1 <sup>st</sup> cooling cycles. ....	61
<b>Figure 46.</b> DSC traces of [TRYUM-7, <i>n</i> ][BF <sub>4</sub> ]. Traces show the 2 <sup>nd</sup> heating and the 1 <sup>st</sup> cooling cycles. ....	62
<b>Figure 47.</b> DSC traces of [TRYUM-9, <i>n</i> ][BF <sub>4</sub> ]. Traces show the 2 <sup>nd</sup> heating and the 1 <sup>st</sup> cooling cycles. ....	63
<b>Figure 48.</b> Transition enthalpy of the triazolium salts grouped for the anion and sub-grouped for the perfluoroalkyl-chain. For the monotropic compounds (*), the graph shows the enthalpy absolute term of the transition from the isotropic to SmA phase and these values are reported by points in brackets. <sup>a</sup> the value refers to the first heating. <sup>b</sup> the value refers to the enthalpy sum between the transition identified as melting point and the previous event. ....	63
<b>Figure 49.</b> DSC traces of pure [TRYUM-7,12][OTf] and [TRYUM-7,12][OTf]/ [EtTRYUM-7,12][OTf] (9:1). Traces show the 2 <sup>nd</sup> heating and the 1 <sup>st</sup> cooling cycles. ....	65
<b>Figure 50.</b> Plotting of crystal-phase <i>d</i> -spacing of triazolium salts at reduced temperatures (0.9) versus alkyl-chain length. Symbols denote different perfluoroalkyl-chain length, while colours denote different anions. ....	67
<b>Figure 51.</b> Comparison between molecular length in crystal phase of compounds [TRYUM-7,10][OTf] and [TRYUM-7,10][BF <sub>4</sub> ] and [TRYUM-7,10][Tf <sub>2</sub> N]. ....	68

<b>Figure 52.</b> SAXS frames with the detector position at 180 mt of compounds [TRYUM-7,12][OTf] (left), [TRYUM-9,12][Tf <sub>2</sub> N] (middle) and [TRYUM-9,12][BF <sub>4</sub> ] (right), at 82.7, 108.4 and 178.4 °C respectively. ....	69
<b>Figure 53.</b> Waterfall view of X-ray scatterings recorded on compound [TRYUM-7,10][OTf] over temperatures. Frames has been recorded on cooling from isotropic liquid every 3°C. ....	73
<b>Figure 54.</b> Plotting of SmA <i>d</i> -spacing of triazolium salts at reduced temperatures (0.9) versus alkyl-chain length. Symbols denote different perfluoroalkyl-chain length, colours denote different anions and irradiating source. ....	73
<b>Figure 55.</b> Comparison between SAXS <i>d</i> -spacing and crystal structure of compounds [TRYUM-7,10][BF <sub>4</sub> ] and [TRYUM-9,10][BF <sub>4</sub> ]. ....	74
<b>Figure 56.</b> SAXS frames with the detector position at 180 mt of compounds [TRYUM-3,10][OTf] (left), [TRYUM-7,10][Tf <sub>2</sub> N] (middle) and [TRYUM-9,10][BF <sub>4</sub> ] (right), at 86.1, 52.6 and 176.6 °C respectively. ....	76
<b>Figure 57.</b> Comparison of fitting of [TRYUM-7,10][Tf <sub>2</sub> N] (left) and [TRYUM-7,10][OTf] (right) SAXS data from the isotropic liquid, between the single and double peak models. ....	77
<b>Figure 58.</b> Illustrative scheme of PNPP, COP and CP in scattering of ILs isotropic states. ....	78
<b>Figure 59.</b> Plotting of <i>d</i> -spacing of triazolium ILs (isotropic phases) versus alkyl-chain length. Symbols denote different perfluoroalkyl-chain length, colours denote different anions and irradiating source. PPNP and PPNP' of the same salts are plotted in adjacent section. ....	79
<b>Figure 60.</b> Schematic representation of a Nyquist plot. ....	81
<b>Figure 61.</b> Illustration of the chamber of the platinum electrode. Sizes of the cell are reported. ....	83
<b>Figure 62.</b> Thermo-block with sample holder in relative slot (left) and cable configuration (right). ...	84
<b>Figure 63.</b> Nyquist plot of EIS measurement on [TRYUM-3,10][Tf <sub>2</sub> N] at 78°C and relative fitting. ....	85
<b>Figure 64.</b> Nyquist plot of fitted EIS of [TRYUM-3,10][Tf <sub>2</sub> N] over a range of temperatures. ....	85
<b>Figure 65.</b> A plot of triazolium salt conductivities as function of temperature. ....	89
<b>Figure 66.</b> A plot of the extrapolated triazolium salt activation energies as function of the structure. ....	90
<b>Figure 67.</b> A plot of the extrapolated triazolium salt conductivities at the same reduced temperature. The point labels indicate the respective absolute temperature (°C) referred to the reduced temperature (0.9). ....	91
<b>Figure 68.</b> A plot of the extrapolated triazolium salt conductivities at the same absolute temperature (100 °C). ....	92
<b>Figure 69.</b> Gel phase obtained mixing [TRYUM-7,10][BF <sub>4</sub> ] with DCM and hexane. ....	93

## Schemes Index

<b>Scheme 1.</b> Main cation cores of the most common ILs. ....	4
<b>Scheme 2.</b> Main anion used in the most common IL systems and their abbreviations. ....	5
<b>Scheme 3.</b> S <sub>N</sub> 2 reaction of the trifluoromethanesulfonate and bis(trifluoromethanesulfonyl)imide salts of dimethyl-4-nitrophenylsulfonium with chloride ion. ....	5
<b>Scheme 4.</b> E-/Z-isomerisation and rearrangement of phenylhydrazones of 3-benzoyl-5-phenyl-1,2,4-oxadiazole in the presence of CuCl <sub>2</sub> and Cu(ClO <sub>4</sub> ) in four imidazolium ILs [bmim][X] (X = CF <sub>3</sub> SO <sub>3</sub> , BF <sub>4</sub> , SbF <sub>6</sub> and PF <sub>6</sub> ). ....	6
<b>Scheme 5.</b> Examples of fluorinated ILs with fluorous domain in cation (left) and anion (right). ....	6
<b>Scheme 6.</b> Examples of historic rod-like and disk-like shaped molecules of LCs. ....	7
<b>Scheme 7.</b> Diagram of LCs classification. ....	8
<b>Scheme 8.</b> Cationic azoles and azides common found in ILCs. ....	10
<b>Scheme 9.</b> Fluorinated material showing different properties. ....	11
<b>Scheme 10.</b> Cationic structure of N(4)-polyfluoroalkyl-1,2,4-triazolium salts. ....	11
<b>Scheme 11.</b> Amidoxime route for synthesis of 1,2,4-oxadiazole. ....	22
<b>Scheme 12.</b> ANRORC reaction with outside leaving group. ....	22
<b>Scheme 13.</b> ANRORC reactions with inside leaving group. ....	23
<b>Scheme 14.</b> ANRORC reaction of nitro-imidazoles. ....	23
<b>Scheme 15.</b> ANRORC reaction of arylsulphonyl-nitroimidazoles. ....	24
<b>Scheme 16.</b> ANRORC reaction of 5-perfluoroalkyl-1,2,4-oxadiazoles with hydrazine. ....	24
<b>Scheme 17.</b> ANRORC reaction of 5-perfluoroalkyl-1,2,4-oxadiazoles with methylhydrazine. ....	25
<b>Scheme 18.</b> Proposal building-block. ....	26
<b>Scheme 19.</b> Proposal general structure. ....	27
<b>Scheme 20.</b> General structure. ....	27
<b>Scheme 21.</b> First synthetic pathway. ....	29
<b>Scheme 22.</b> Representation of kinetically hindered intermediate of reaction on <b>3-7.2</b> . ....	30
<b>Scheme 23.</b> Different pathways to obtain triazole <b>5-7</b> from oxadiazole <b>3-7</b> . ....	30
<b>Scheme 24.</b> Methylation of triazole <b>6-7,12</b> by methyl iodine and next metathesis reactions. ....	31
<b>Scheme 25.</b> Methylation of triazole <b>6-7,12</b> by two different methylating agent and next metathesis reaction. ....	33
<b>Scheme 26.</b> Proposal mechanism of ethylation by ethyl acetate interacting with methylating agent. ....	33
<b>Scheme 27.</b> Illustration of regiochemistry in the methylation of triazole ring. ....	36
<b>Scheme 28.</b> Illustration of spatial conformation in 1,4-dimethyl-1,2,4-triazol-4-ium salts. ....	38
<b>Scheme 29.</b> Global synthesis process. ....	40
<b>Scheme 30.</b> Equilibrium between Z and E isomers of N'-hydroxy-4-methoxybenzamidoxime. ....	41

## Tables Index

<b>Table 1.</b> Selected crystallographic properties of the triazolium triflates.....	45
<b>Table 2.</b> Selected crystallographic properties of the triazolium bis(triflimide)s.....	48
<b>Table 3.</b> Selected crystallographic properties of the triazolium tetrafluoroborates. ....	51
<b>Table 4.</b> Transition temperatures, enthalpies and entropies obtained from the DSC traces.....	52
<b>Table 5.</b> Estimated SLDs values of triazolium salts moieties. ....	66
<b>Table 6.</b> X-Ray, Neutrons and structural data for the mesophases of the triazolium salts. ....	69
<b>Table 7.</b> X-Ray and Neutrons fitting parameters for the isotropic phases of the triazolium salts. ....	77
<b>Table 8.</b> Conductivity and fitting data for the LC and isotropic phases of the triazolium salts. ....	86
<b>Table 9.</b> Scheme of gelation test of triazolium compounds in heptane. ....	94
<b>Table 10.</b> CHN Analysis results for the triazolium salts.....	114



## PhD Curriculum

ALESSIO RICCOBONO

Dipartimento di Scienze e Tecnologie Biologiche, Chimiche e Farmaceutiche

Università di Palermo

Viale delle Scienze, Parco d'Orleans

90128, Palermo, Italy

e-mail: alessio.riccobono@unipa.it

## Academic curriculum

School: 03/01/2016 – 06/01/2017 - British Liquid Crystal Society Winter Workshop at University of Hull.

Neutron scattering Experiment: 18/07/2016 – 22/07/2016 – SANS investigation of Mixture of ILs (Experiment number RB1610234) – Instrument SANS2D at ISIS pulsed neutron and muon source at Rutherford Appleton Laboratory in Oxford.

X-Ray Reflectivity Experiment: 15/09/2016 – 16/09/2016 – Investigating the surface of IL mixtures using X-ray reflectivity (Experiment number SI15237-1) – Instrument I07 (X-ray reflectivity) at Diamond light source in Oxfordshire.

Neutron scattering Experiment: 19/03/2017 – 21/03/2017 – Nanostructuring of Polyphilic Liquid Crystals (Experiment number RB1710406) – Instrument SANS2D at ISIS pulsed neutron and muon source at Rutherford Appleton Laboratory in Oxford.

Training Course: 1D NMR - 1H, 13C DEPT, 19F, 31P; 2D NMR – gradient COSY, HSQC HMBC, NOESY – Instructor: Dr. Heater Fish.

Training Course: Polarized Optical Microscopy – Instructor: Dr. Stephen Cowling.

Training Course: Differential Scanning Calorimetry – Instructor: Dr. Stephen Cowling.

Training Course: Handling of X-ray sources and Small Angle X-Ray Diffraction – Instructor: Dr. Stephen Cowling.

Training Course: Safe Handling and Dispensing of Liquid Nitrogen - Instructor: Dr. Graeme McAllister.

Training Course: Solvent system purification operation: - Instructor: Dr. Graeme McAllister.

Training Course: Fire Safety in Chemistry Laboratory and Fire Extinguisher Practice: - Instructor: Dr. Moray Stark.

## Conference communication

Alessio Riccobono, Ivana Pibiri, Andrea Pace, John M. Slattery, Duncan W. Bruce. Fluorinated azole-azine systems as new Liquid-crystalline ILs. 12th International Conference on Materials Chemistry (MC12), York, United Kingdom - July 20-23, 2015.

Ivana Pibiri, Alessio Riccobono, Andrea Pace, Antonio Palumbo Piccionello, Silvestre Buscemi, Girolamo Casella, Valerio Causin, Federico Rastrelli, Giacomo Saielli. Polyfluoroalkyl viologen-based Ionic Liquid Crystals. 12th International Conference on Materials Chemistry (MC12), York, United Kingdom - July 20-23, 2015.

Alessio Riccobono, Ivana Pibiri, Antonio Palumbo Piccionello, Silvestre Buscemi, Andrea Pace, Duncan W. Bruce, John M. Slattery. Synthesis and characterization of new azoles as building blocks for functional ionic systems. 21st International Symposium on Fluorine Chemistry & 6th International Symposium on Fluorous Technologies (21stISFC & ISoFT'15), Como, Italy - August 23-28, 2015.

Alessio Riccobono, Ivana Pibiri, Andrea Pace, John M. Slattery, Duncan W. Bruce. Ionic Liquid crystals based on 3-perfluoroalkyl-1,2,4-triazol-4-ium salts. The Symposium on Advances in Heterocyclic Organic Chemistry (SAHOC 2016), Sheffield, United Kingdom - Sep 1-2, 2016.

Alessio Riccobono, John M. Slattery, Adrian C. Whitwood, Rachel R. Bean, Duncan W. Bruce, Ivana Pibiri, Andrea Pace. Ionic Liquid crystals based on 1,2,4-triazolium rings. 14th European Conference on Liquid Crystals (ECLC 2017), Moscow, Russia - Jun 25-30, 2017.